THÈSE EN COTUTELLE

Présentée à

L'UNIVERSITÉ DE BOURGOGNE FRANCHE-COMTÉ
pour obtenir le titre de
DOCTEUR DE L'UNIVERSITÉ DE BOURGOGNE FRANCHE-COMTÉ
Spécialité Sciences pour l'Ingénieur et Microtechniques

L'UNIVERSITÉ DE SHERBROOKE
pour obtenir le titre de
PHILOSOPHIÆ DOCTOR (Ph. D.) DE L'UNIVERSITÉ DE SHERBROOKE
Spécialité Génie Électrique

Par

Juliana CHAWICH

MICROCAPTEUR À ONDES ACOUSTIQUES EN ZnO/GaAs POUR LA DÉTECTION DE BACTÉRIES EN MILIEUX LIQUIDES COMPLEXES

ZnO/GaAs - BASED ACOUSTIC WAVES MICROSENSOR FOR THE DETECTION OF BACTERIA IN COMPLEX LIQUID MEDIA

Soutenue publiquement le 28 Mai 2019 devant la commission d'examen :

Vincent HUMBLOT	Chargé de Recherche CNRS, Sorbonne Université	Rapporteur
Stéphane DURAND	Maître de Conférences HDR, Université du Mans	Rapporteur
Paul G. CHARETTE	Professeur, Université de Sherbrooke	Rapporteur
Simon LÉVESQUE	Professeur associé, Université de Sherbrooke	Examinateur
Nicolas MARTIN	Professeur, Ecole Nationale Supérieure de Mécanique et des Microtechniques	Examinateur
Andrzej LASIA	Professeur, Université de Sherbrooke	Examinateur
Céline ÉLIE-CAILLE	Maître de Conférences HDR, Université de Franche-Comté	Co-encadrante
Thérèse LEBLOIS	Professeur, Université de Franche-Comté	Co-directrice
Jan J. DUBOWSKI	Professeur, Université de Sherbrooke	Co-directeur

RÉSUMÉ

Cette thèse s'inscrit dans le cadre d'une cotutelle internationale entre l'Université de Bourgogne Franche-Comté en France et l'Université de Sherbrooke au Canada. Elle porte sur le développement d'un biocapteur miniature pour la détection et la quantification de bactéries dans des milieux liquides complexes. La bactérie visée est l'*Escherichia coli (E. coli)*, régulièrement mise en cause dans des épidémies d'infections alimentaires, et parfois meurtrière.

La géométrie du biocapteur consiste en une membrane en arséniure de gallium (GaAs) sur laquelle est déposé un film mince piézoélectrique d'oxyde de zinc (ZnO). L'apport du ZnO structuré en couche mince constitue un réel atout pour atteindre de meilleures performances du transducteur piézoélectrique et consécutivement une meilleure sensibilité de détection. Une paire d'électrodes déposée sur le film de ZnO permet de générer, sous une tension sinusoïdale, des ondes acoustiques se propageant dans le GaAs, à une fréquence donnée. La face arrière de la membrane, quant à elle, est fonctionnalisée avec une monocouche auto-assemblée (SAM) d'alkanethiols et des anticorps contre l'*E. coli*, conférant la spécificité de la détection. Ainsi, le biocapteur bénéficie à la fois des technologies de microfabrication et de bio-fonctionnalisation du GaAs, déjà validées au sein de l'équipe de recherche, et des propriétés piézoélectriques prometteuses du ZnO, afin d'atteindre potentiellement une détection hautement sensible et spécifique de la bactérie d'intérêt. Le défi consiste à pouvoir détecter et quantifier cette bactérie à de très faibles concentrations dans un échantillon liquide et/ou biologique complexe.

Les travaux de recherche ont en partie porté sur les dépôts et caractérisations de couches minces piézoélectriques de ZnO sur des substrats de GaAs. L'effet de l'orientation cristalline du GaAs ainsi que l'utilisation d'une couche intermédiaire de Platine entre le ZnO et le GaAs ont été étudiés par différentes techniques de caractérisation structurale (diffraction des rayons X, spectroscopie Raman, spectrométrie de masse à ionisation secondaire), topographique (microscopie à force atomique), optique (ellipsométrie) et électrique. Après la réalisation des contacts électriques, la membrane en GaAs a été usinée par gravure humide. Une fois fabriqué, le transducteur a été testé en air et en milieu liquide par des mesures électriques, afin de déterminer les fréquences de résonance pour les modes de cisaillement d'épaisseur. Un protocole de bio-fonctionnalisation de surface, validé au sein du laboratoire, a été appliqué à la face arrière du biocapteur pour l'ancrage des SAMs et des anticorps, tout en protégeant la face avant. De plus, les conditions de greffage d'anticorps en termes de concentration utilisée, pH et durée d'incubation, ont été étudiées, afin d'optimiser la capture de bactérie. Par ailleurs, l'impact du pH et de la conductivité de l'échantillon à tester sur la réponse du biocapteur a été déterminé. Les performances du biocapteur ont été évaluées par des tests de détection de la bactérie cible, *E. coli,* tout en corrélant les mesures électriques avec celles de fluorescence. Des tests de détection ont été réalisés en variant la concentration d'*E. coli* dans des milieux de complexité croissante. Différents types de contrôles ont été réalisés pour valider les critères de spécificité. En raison de sa petite taille, de son faible coût de fabrication et de sa réponse rapide, le biocapteur proposé pourrait être potentiellement utilisé dans les laboratoires de diagnostic clinique pour la détection d'*E. coli*.

Mots-clés : biocapteur à ondes acoustiques, bio-interface, Arséniure de Gallium, couches minces piézoélectriques d'oxyde de zinc, bactéries.

ABSTRACT

This thesis was conducted in the frame of an international collaboration between *Université de Bourgogne Franche-Comté* in France and *Université de Sherbrooke* in Canada. It addresses the development of a miniaturized biosensor for the detection and quantification of bacteria in complex liquid media. The targeted bacteria is *Escherichia coli (E. coli)*, regularly implicated in outbreaks of foodborne infections, and sometimes fatal.

The adopted geometry of the biosensor consists of a gallium arsenide (GaAs) membrane with a thin layer of piezoelectric zinc oxide (ZnO) on its front side. The contribution of ZnO structured in a thin film is a real asset to achieve better performances of the piezoelectric transducer and consecutively a better sensitivity of the detection. A pair of electrodes deposited on the ZnO film allows the generation of acoustic waves propagating in GaAs under a sinusoidal voltage, at a given frequency. The backside of the membrane is functionalized with a self-assembled monolayer (SAM) of alkanethiols and antibodies against *E. coli*, providing the specificity of the detection. Thus, the biosensor benefits from the microfabrication and bio-functionalization technologies of GaAs, validated within the research team, and the promising piezoelectric properties of ZnO, to potentially achieve a highly sensitive and specific detection of the bacteria of interest. The challenge is to be able to detect and quantify these bacteria at very low concentrations in a complex liquid and/or biological sample.

The research work was partly focused on the deposition and characterization of piezoelectric ZnO thin films on GaAs substrates. The effect of the crystalline orientation of GaAs and the use of a titanium/platinum buffer layer between ZnO and GaAs were studied using different structural (X-ray diffraction, Raman spectroscopy, secondary ionization mass spectrometry), topographic (atomic force microscopy), optical (ellipsometry) and electrical characterizations. After the realization of the electrical contacts on top of the ZnO film, the GaAs membrane was micromachined using chemical wet etching. Once fabricated, the transducer was tested in air and liquid medium by electrical measurements, in order to determine the resonance frequencies for thickness shear mode. A protocol for surface bio-functionalization, validated in the laboratory, was applied to back side of the biosensor for anchoring SAMs and antibodies, while protecting the top side. Furthermore, different conditions of antibody immobilization such as the concentration, pH and incubation time, were tested to optimize the immunocapture of bacteria. In addition, the impact of the pH and the conductivity of the solution to be tested on the response of the biosensor has been determined. The performance of the biosensor was evaluated by detection tests of the targeted bacteria, *E. coli*, while correlating electrical measurements with fluorescence microscopy. Detection tests were completed by varying the concentration of *E. coli* in environments of increasing complexity. Various types of controls were performed to validate the specificity criteria. Thanks to its small size, low cost of fabrication and rapid response, the proposed biosensor has the potential of being applied in clinical diagnostic laboratories for the detection of *E. coli*.

Keywords: Acoustic wave biosensor, bio-interface, Gallium arsenide, piezoelectric Zinc oxide thin films, bacteria.

ACKNOWLEDGMENTS

This co-supervised thesis was completed with the help and support of many people who have participated in the success of this work. First, I would like to thank my supervisors Thérèse Leblois, Jan J. Dubowski and Céline Elie-Caille, for their scientific rigor, their immeasurable support and their valuable guidance. I am grateful to them for all the thoughtful advices and insights, their time and patience for numerous fruitful discussions that led to realize major milestones in my research.

I also extend my sincere thanks to Mr. Vincent Humblot, researcher at *Sorbonne Université*, Mr. Stéphane Durand, HDR lecturer at *Université du Maine* and Mr. Paul Charette, professor at *Université de Sherbrooke*, who have accepted to review my work and take a critical look at my manuscript. I also thank Mr. Nicolas Martin, Mr. Simon Lévesque and Mr. Andrzej Lasia for being part of the jury and making themselves available to attend my defense.

I would like to express my gratitude to Ausrine Bartasyte and Samuel Margueron for their collaboration, implication and precise guidance on the deposition and characterization of piezoelectric thin films. Also, thanks to Sabina Kuprėnaitė for her help in the deposition of ZnO films.

I would also like to show my appreciation to all the members of FEMTO-ST institute, especially the MN2S department and the BioMicroDevices (BMD) team. I enjoyed all the scientific discussions as well as the excellent atmosphere in this group and I wish that their adventure continues for many years to come. Thanks to all the PhD students, ex-students and interns of the institute for the daily humour, the passionate scientific conversations or for their contribution to this work. I am thinking in particular of Vivien, Sameh, Charles-Louis, Raya, Julien, Alpha, Claude and Daniel, and I wish good luck to those who are continuing the journey. Of course, this work could not have been done without the help of the technical staff of MIMENTO. Many thanks, in particular, to Laurent Robert and Cyril Millon for the training and advices on clean room work. I do not forget to thank Fabien Remy-Martin for his help with designing and manufacturing the sample holders and the fluidic chambers.

I would also like to acknowledge all the people I met at 3IT in Sherbrooke, including all the colleagues of the laboratory for Quantum Semiconductors and Photon-based Bionanotechnology (QSPB) in which I was warmly welcomed for the second half of my PhD. I would like to thank Khalid Moumanis and Walid Hassen for their help and guidance at the scientific and personal levels. Many thanks to all my fellow MSc, PhD and postdoc colleagues: Reza, Narjes, Srivatsa, Lilian, Aman, Daniela, Hakim, Lucas and René for all the good moments that we shared together. Special thanks to Getenet Ayele.

Thank you also to my parents Arze & Toufic, whom I thank for their encouragement and unconditional love. You were my unwavering companions and supporters through this challenging journey.

Finally, my last thoughts go to my sisters Nadine & Marie and to my long-time friend Christina, for all their support over the past years and for still being there for me despite the long distances.

Thank you all for everything!

TABLE OF CONTENTS

LIST OF FIGURES

LIST OF TABLES

LIST OF ACRONYMS

Acronyme	Signification in English	Signification en français
AFM	Atomic force microscopy	Microscopie à force atomique
ALD	Atomic layer deposition	Dépôt par couche atomique
APM	Acoustic plate modes	Ondes acoustiques de plaques
BAW	Bulk acoustic waves	Ondes acoustiques de volume
BSA	Bovine serum albumin	Albumine de sérum bovin
CFU	Colony forming unit	Unité formant colonie
CVD	Chemical vapor deposition	Dépôt par voie chimique en phase vapeur
DC	Direct current	Courant continu
DNA	Deoxyribonucleic acid	Acide désoxyribonucléique
EDC	1-Ethyl-3-(3-dimethylaminopropyl)carbodiimide	
ELISA	Enzyme-linked immunosorbent assay	Méthode immuno-enzymatique
FBAR	Thin-film bulk acoustic resonator	Résonateurs à ondes de volume sur couche mince
FTIR	Fourier transform infrared spectroscopy	Spectroscopie infrarouge à transformée de Fourier
FWHM	Full width at half maximum	Largeur à mi-hauteur
GFP	Green fluorescent protein	Protéine fluorescente verte
IDTs	Interdigital transducers	Transducteurs/Peignes interdigités
LFE	Lateral field excitation	Excitation à champ latéral
LOD	Limit of detection	Limite de détection
LW	Love waves	Ondes de love
MEMS	Microelectromechanical systems	Microsystèmes électromécaniques
MHDA	16-mercapto-1-hexadecanoic acid	
MUDO	11-mercapto-1-undecanol	

NHS	N-hydroxysuccinimide	
PBS	Phosphate buffered saline	Tampon phosphate salin
PCB	Printed Circuit Board	Circuit imprimé
PCR	Polymerase chain reaction	Réaction en chaîne par polymérase
PDMS	Polydimethylsiloxane	Polydiméthylsiloxane
PEG	Polyethylene glycol	Polyéthylène glycol
PLD	Pulsed laser deposition	Ablation laser pulsé
PML	Perfectly matched layers	Couche absorbante parfaitement adaptée
PVD	Physical vapor deposition	Dépôt par voie physique en phase vapeur
QCM	Quartz crystal microbalance	Microbalance à cristal de quartz
RF	Radio frequency	Radio fréquence
SAM	Self-assembled monolayer	Monocouche auto-assemblée
SAW	Surface acoustic waves	Ondes acoustiques de surface
SH-APM	Shear horizontal acoustic plate modes	Ondes de plaque transverses horizontales
SH-SAW	Shear horizontal surface acoustic waves	Ondes de surface transverses horizontales
SIMS	Secondary ion mass spectrometry	Spectrométrie de masse à ionisation secondaire
SPR	Surface plasmon resonance	Résonance des plasmons de surface
TCO	Transparent conductive oxide	Oxyde transparent conducteur
TFE	Thickness field excitation	Excitation par champ dans l'épaisseur
TOF	Time of flight	Temps de vol
TSM	Thickness shear mode	Mode de cisaillement d’épaisseur
US	Ultrasound	Ultrasons
UV	Ultraviolet	Ultraviolet
XPS	X-ray photoelectron spectroscopy	Spectrométrie photoélectronique X
XRD	X-ray diffraction	Diffraction des rayons X

Chapter 1: Introduction

1.1 General context

The detection and identification of bacteria is a major concern for food safety and medicine. Most bacterial infections are related to the presence of bacteria in drinking water, food, and cooling or aeration systems that provide favorable conditions for their development. In order to prevent these infections, it is necessary to be able to detect and identify as soon as possible the presence of these pathogens.

Conventional analytical instruments for the detection of bacteria are generally voluminous, complex, costly and not sensitive enough for some application areas such as the agri-food sector. Moreover, the phases of sample preparation, incubation, and exploitation of the results often greatly increase the total duration of the analysis. For instance, results for an enzyme-linked immunosorbent assay (ELISA) can take about 24 hours if the test is done locally [1]. In other cases, it may take several days to weeks.

The last few decades have seen continued growth of the interdisciplinary field of biosensors due to the increased need for a rapid, sensitive and selective detection of pathogenic agents [2]. Biosensors offer interesting features such as real-time, on-site detection of pathogens utilizing the selectivity of biomolecules. They are known to provide fast and accurate results and have been found to have applications in various sectors including clinical diagnostics, environmental monitoring and food industry [3], [4].

Despite a large market potential for biosensors in these vast areas, very few commercial achievements have emerged in spite of a significant amount of research work carried out in the world [5]. The major obstacle to the industrial development of biosensors is the low sensitivity in the case of complex samples, and the environmental instability resulting in poor propagation of biosensing devices into the market [6]. To overcome these drawbacks, our research has been oriented towards the development of an acoustic wave biosensor allowing the detection of bacteria in liquid environments with high accuracy and specificity.

In this context, the thesis work presented in this document aims to develop a miniaturized ZnO/GaAs-based acoustic biosensor for the detection and quantification of bacteria on site in complex liquid media, and in particular *“Escherichia coli”* (*E. coli*). It is based on the results previously obtained in the fields of design and microfabrication of piezoelectric GaAs membranes and the development and characterization of GaAs-thiol bio-interfaces [7]–[15].

1.2 Background in the research group

We aim to develop a highly efficient GaAs based resonant biosensor. The choice of GaAs is justified by several years of development and studies within the "BioMicroDevices" research group at FEMTO-ST (*Franche-Comté Électronique Mécanique Thermique et Optique - Sciences et Technologies*) institute. The objective of this project is to develop a low-cost, resonant biosensor allowing the detection and quantification of specific biological entity.

The research was initiated by a PhD student, Alex Bienaimé, whose thesis entitled "Gallium Arsenide microsensor for the detection of molecules in a fluid" [7] was directed by Pr. Thérèse Leblois and Dr. Céline Elie-Caille, and defended in 2012. His work gave a solid foundation on the design, fabrication, functionalization and testing of these devices. In the framework of this thesis, dimensioning of the resonant structure was carried out as well as the selection of the GaAs crystallographic cut [8]. Moreover, microfabrication procedures, particularly chemical wet etching, were tested and evaluated to provide the desired surface structuration in a highly reproducible way and at low manufacturing cost [9]. However, electrical measurements have shown the limitations of the transducer in achieving the expected performances (sensitivity, quality factor ...). On the other hand, a mixed architecture of alkanethiols was selected for the immobilization of immunoreceptors [10], and several surface characterizations were performed to control the surface state, the establishment of thiolates self-assembled monolayers (SAM) and the topography of the GaAs substrate [11]. Nevertheless, further analysis was needed to better understand the phenomena at the GaAs-biomolecule interface. For that, a collaboration was established with Professor Jan J. Dubowski of Université de Sherbrooke, whose research activities in the 3IT (*Institut Interdisciplinaire d'Innovation Technologique*) institute revolve around III-V semiconductors and GaAs based biosensing devices. Consequently a co-supervised thesis was launched with a new PhD student, Vivien Lacour, entitled "Optimization of a GaAs acoustic wave microsensor and its bio-interface for the detection of pathogens in liquid media" [12]. During this thesis, two techniques were used to produce GaAs membranes: chemical wet etching and chlorinated plasma etching. Despite some masking defects, this last technique allowed, to obtain very interesting results for the etching of nearly 200 μm thick membranes. On the other hand, the SAMs based bio-interfaces were deeply analyzed using Fourier-transform infrared (FTIR) spectroscopy. The study of the self-assembly process of solubilized molecules in water/ethanol solutions showed the formation of densely packed SAMs. An extensive work was carried out on the aspects of regeneration of the bio-interface, chemically [13] and by photo-oxidation in liquid medium. This latter gave promising perspectives for SAMs patterning to attach different antibodies for a multiplexed detection [14]. The results obtained in the frame of this thesis (defended in 2016) have allowed a better understanding of the kinetics of formation of SAMs on GaAs surface, as well as the regeneration processes aiming to reduce the operating cost of the sensor. Nevertheless, the sensor still showed some limitations such as the high sensitivity to the environmental parameters [16] and the low quality factors obtained experimentally (Q = 4135 at 6.72 MHz) compared with the theoretical values (Q = 282915), which could be due to microfabrication constraints [12]. Therefore, further research was necessary to achieve better performance and reliability of the sensor, which justifies the work presented in this thesis.

1.3 Research objectives

Despite the limitations of the sensor, the outlook with respect to the estimated mass sensitivity remained promising. The theoretical sensitivity has been determined at 0.1 ng/Hz by analytical modeling for a 50 μm thick GaAs membrane at 33.36 MHz [7]. This means that the capture of 100 bacteria of *E. coli* on the surface of the sensor would generate a shift of 1 Hz of the resonant frequency. Based on literature review and preceding work in both research teams at FEMTO-ST and 3IT institutes, the following general question was formulated:

"How to improve the performances of the existing GaAs based acoustic micro-biosensor through modifications of its architecture?"

In order to answer this question, we relied on the preceding work and results in our research group to develop optimization tracks in terms of sensitivity and specificity. Through a new architecture of the transducer, we would be able to increase the quality factors and consequently the sensitivity of the sensor. Moreover, the adaptation of the processes for formation of the bio-interface would improve the efficiency of the detection. To achieve the principal objective of the thesis, it was necessary to define and fulfill specific intermediate objectives. Therefore, several aspects of research were investigated: the deposition and characterization of ZnO thin films on GaAs, the realization and characterization of the bio-interface and the testing of the sensor with the targeted bacteria.

1.3.1 Hybridization of the sensor with ZnO

GaAs-based sensor, although having many advantages, does not benefit from sufficient piezoelectric properties, which resulted in the limited performances of this transducer. Hence, to overcome this weakness point, we propose to modify the architecture of the sensor and retain GaAs for the biosensor part in contact with the liquid, profiting from its functionalization facilities and its ability to be regenerated and machined by conventional microfabrication techniques. On the other hand, we propose to combine GaAs with another material with better piezoelectric and mechanical properties: ZnO. The piezoelectric properties of ZnO have the potential to enhance the response of the GaAs membrane-based device. Consequently, the sensitivity of the sensor could be increased, while keeping low the cost of device manufacturing.

1.3.2 Modeling of the ZnO/GaAs transducer

Before proceeding to the microfabrication of the transducer, the previous hypothesis needs to be validated. Therefore, modeling of the transducer was performed analytically, using the equations of piezoelectricity. We determined the modes of bulk elastic waves that can be generated in the case of GaAs and ZnO respectively, as well as their velocities. Moreover, we calculated the resonant frequency and the electromechanical coupling coefficient for thickness shear mode. The latter was preferable because the detection needs to be performed in liquid. On the other hand, a finite elements simulation was carried out using Comsol Multiphysics® to dimension the transducer combining ZnO and GaAs together. The theoretical resonance values of the transducer with and without the ZnO layer were determined in order to evaluate the impact of ZnO on the performance of the transducer.

1.3.3 Deposition and characterization of piezoelectric ZnO thin films on GaAs

ZnO thin films with piezoelectric responses comparable to bulk single crystal ZnO are not so easy to obtain. Therefore, the deposition conditions should be optimized in order to achieve the desired performance of the sensor. Through the state of the art of the commonly used deposition techniques, we choose the one allowing to obtain well oriented and textured films reproducibly. We investigated the use of a buffer layer for promoting the growth and quality of ZnO on GaAs and compared it to direct deposits. Moreover, we determined the effect of the crystallographic orientation of the substrate on the quality of the deposited films. A complete and systematic characterization of the deposited films was carried out to determine the optimal deposition parameters for obtaining device quality films.

1.3.4 Realization and characterization of the bio-interface

To ensure an efficient capture of bacteria, the bio-interface must be optimized. This applies to the SAM formation and the ligands immobilization. The first has been studied enough in the frame of the previous thesis and a mixed architecture has been already optimized. As for the ligands, the optimal parameters for their immobilization, in terms of concentration, pH and incubation time, were determined in this work using FTIR and fluorescence microscopy. This would allow us to achieve a maximum of recognition sites on the surface, and therefore improve the sensitivity for bacteria detection.

1.3.5 Calibration of the sensor

The evaluation of the performance of the device when it is subjected to different environments is essential to ensure the accuracy of the results. Therefore, we need to determine the impact of physico-chemical environmental parameters on the measurement, such as the impedance dependence to the pH or salt concentration of the solution to be tested. The influence of these parameters can differ according to the surface state. Hence, the measurements were performed with the following surface states: bare, chemically functionalized with SAM, bio-functionalized with antibodies and passivated.

1.3.6 Detection tests with the targeted bacteria

A lot of effort and research has been carried out in our group to develop GaAs-based acoustic transducers and to optimize the GaAs-biomolecule interface. However, the previous sensors were never confronted with bacterial models in order to evaluate their efficiency. Therefore, the continuation of the previous work must first involve the testing of the transducer combined with the bio-interface. The sensitivity and full-scale range of the sensor were determined by performing detection tests in ideal (buffer) and complex media. Different controls were performed to validate the specificity of the bio-interface.

1.4 Outline of the manuscript

This thesis manuscript is structured in 6 chapters. In the present chapter, an introduction to the research topic is provided. After a brief presentation of the project and the preceding work in the research teams, the general outline and the objectives of the thesis are expounded.

In chapter 2, we present the bacterial threats to human health and the conventional biosensing approaches applied to detect bacteria, and particularly *Escherichia coli*, in order to position beforehand the proposed biosensor in a global context and compared to other existing techniques. We exploit the relevant microfabrication potential, as well as the surface functionalization and regeneration functionalities of GaAs, constituting a real advantage for the development of a reusable biosensor. Then, we elaborate the promising properties of ZnO thin films leading to the choice of this material. After reviewing the main works involving the deposition of ZnO thin films on GaAs, the chapter concludes on the new architecture of the transducer combining these two materials.

The relations and theoretical models allowing to understand the functioning of the transducer are presented in chapter 3. After a brief overview on acoustic waves transduction, we recall the tensorial expressions and the fundamental equations of piezoelectricity, in order to develop the analytical model of the transducer. By solving the propagation equations, the velocities, resonant frequencies and electromechanical coupling coefficient are determined for both GaAs and ZnO. To dimension the ZnO/GaAs transducer, a simulation using finite elements method is carried out using Comsol Multiphysics®. Using this model, the resonant frequency for thickness shear mode is determined. The shear mode has been preferred in this work since it allows the operation of the transducer in liquid medium with minor losses.

In chapter 4, we reveal the microfabrication procedure of the transducer. Through a review of the commonly used deposition methods for ZnO thin films, a sputtering technique is selected. The first part of this chapter shows the deposition of ZnO thin films on GaAs substrates. We investigate the use of a new metallic buffer layer for promoting the growth of ZnO on GaAs as well as the impact of the substrate's orientation on the films quality and properties. For this purpose, structural (XRD, Raman) and topographic (AFM) characterization techniques are used. The chemical interactions and interfaces between the deposited layers are studied using secondary ions mass spectrometry (SIMS), and ellipsometry is employed to evaluate the thicknesses and optical properties of ZnO films. In the last part, we detail the different stages of fabrication of the transducer including the realization of the electrical contacts and the micromachining of the GaAs membrane by chemical wet anisotropic etching.

Chapter 5 presents the development of the bio-recognition interface. We detail the procedures used for surface functionalization with SAM and antibodies as well as the different surface characterization methods employed. We also test different conditions for ligands immobilization such as their concentration, pH and incubation time, in order to achieve a maximum of recognition sites on the surface, and therefore to optimize the sensitivity of the detection.

In chapter 6, we present the experimental setup for electrical characterization, which allows determining the frequency response of the transducer. Then, we study the impact of the pH and salt concentration of the biological sample on the electrical performance of the sensor. This study is carried out on different surface states of the sensor: bare, chemically functionalized with SAM, bio-functionalized with antibodies and passivated. Consequently, we demonstrate the detection of *E. coli* at different concentrations and we correlate the results with fluorescence measurements. Moreover, we present different controls performed to test the specificity of the biosensor to the targeted bacteria. After performing detection tests of the biosensor in ideal and complex media, we determine its sensitivity. Through the study of its performance, we conclude on the opportunities that the biosensor could have in comparison with its commercial equivalents and we identify the optimization perspectives.

Finally, a summary of the achieved results is provided. In addition, the perspectives and the proposed future work are presented.

Chapter 2: State of the art and positioning of ZnO/GaAs biosensor

2.1. Bacterial threat and diagnosis

2.1.1 Urgency for bacteria detection

Man lives in constant contact with bacteria, present in his daily environment but also in his own body. A bacterium is a unicellular, prokaryotic microorganism, typically measuring between 0.5 and 5 µm. It is an autonomous cell living in a colony, capable of reproducing on its own by cell division after duplication of its single chromosome.

Some bacteria are directly beneficial to us, such as those colonizing our intestines and contributing to digestion. Others, called commensals, have no (known) effect on their host. However, some strains can become pathogenic in special circumstances, especially when they have the opportunity to cross the body's natural barriers of skin or mucous membranes. In addition, certain bacteria secrete toxins to which they confer their pathogenicity.

The detection of these pathogenic bacteria is an issue of increasing importance in many fields (medical, food safety, environmental, military, etc.) [17]. In the medical field for example, a clinician often prescribes broad-spectrum antibiotics, while waiting for the results of bacteriological analysis. Sometimes, a doctor would only check the results of an analysis if there were a therapeutic failure. If the doctor knew the identity of the infectious agent responsible for his patient's disease, he/she would be able to immediately prescribe the appropriate treatment. In addition to lowering the costs of therapy, this would limit treatment failures and the number of antibiotic-resistant mutants. Moreover, in the agri-food sector, as fresh products are rapidly perishing, they are often placed on the market before the results of microbiological tests on different batches are available. Thus, the manufacturer takes the risk of making potentially contaminated food available to consumers in the sales departments, and then withdrawing them in the case of confirmation of a contamination.

Bacterial contamination of food and water resources, as well as the increasing incidence of nosocomial infections, are elements that push us today to develop new means of detection and rapid identification of pathogenic bacteria. Indeed, contamination with a bacterial pathogen is the main source of nosocomial infection [18] and the second leading cause of foodborne infections [19]. In addition, the risks of threats to personal and territorial security (military sector) make this task even more urgent. Figure 1 (a) shows the main areas of application of the research carried out in the field of pathogen detection including food industry, environment and water quality control and clinical diagnosis [17]. In this context, the development of rapid and effective bacterial detection tools has a central role in health prevention and medical diagnosis.

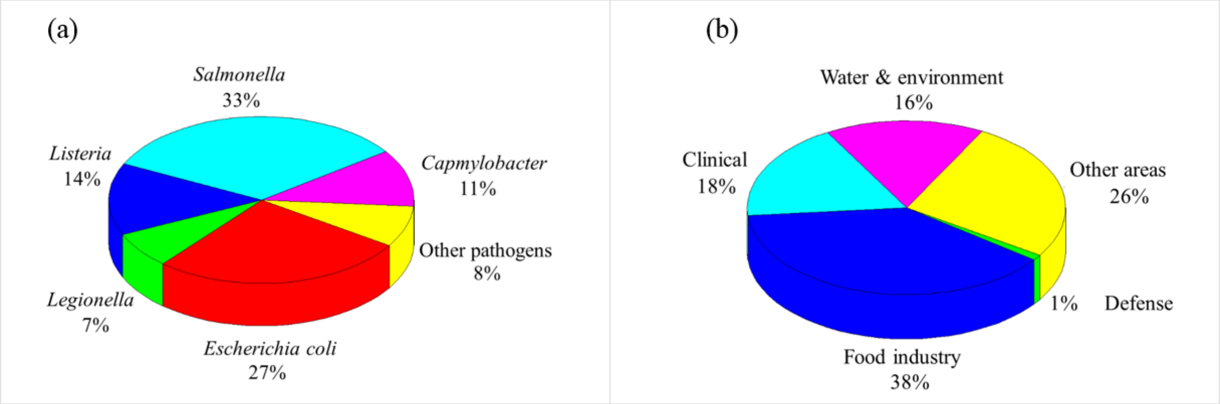

Figure 1. (a) Sectors of interest for pathogen detection, (b) Classification of studies in the literature on detection of pathogenic bacteria by micro-organism type (Source: ISI Web of Science.ca, 2500 research articles on pathogen detection over the last 20 years)

Figure 1 (b) shows the distribution of scientific literature covering the detection of pathogenic bacteria. Accounting for the second largest number of articles, *Escherichia coli* is one of the most commonly and thoroughly studied bacteria in the world, and it is the targeted bacteria in this thesis.

2.1.2 *Escherichia coli*: targeted bacteria

Regularly called into question in the epidemics of food infections, *Escherichia coli* or *E. coli* presents several facets unknown to the public. Often beneficial to the body, sometimes deadly, these bacteria continue to arouse interest.

E. coli is a bacterium naturally found in the gut of humans and most mammals, and often considered as commensal. Far from being pathogenic, it occupies about 80 % of our intestinal flora and contributes to the proper functioning of the gastrointestinal system.

While the majority of *E. coli* strains are harmless, some have acquired virulence factors that made them pathogenic causing diseases such as gastroenteritis, urinary tract infections, meningitis, etc. This is the case of so-called enterohemorrhagic *E. coli* (EHEC) strains [20]. Human infection results in serious pathologies, especially in children under the age of 3, with development of hemorrhagic colitis and/or hemolytic uremic syndrome (HUS) that can lead to kidney damage, fatal in 3 to 5 % of cases [21]. People over 60 are also considered as a population at risk. The first epidemiological data date back to 1982, when the first strain of EHEC was isolated during an outbreak in the United States caused by uncooked steaks for hamburgers. Since then, EHEC has spawned many more outbreaks and is therefore a public health problem. In 2018, the centers for diseases control and prevention (CDC) investigated three multistate outbreaks of Shiga toxin-producing *E. coli* O26 infections in the United States. One of the outbreaks was caused by ground beef contamination. Out of 18 reported cases, 6 were hospitalized, including one person who died. The other two outbreaks were linked to romaine lettuce contaminated with *E. coli* O157:H7. As a result, in June 2018, 96 people were hospitalized, including 27 people who developed a type of kidney failure and 5 deaths [22].

The public health implications of failing to detect bacteria can be fatal, and the consequences easily make the news. Therefore, threshold values were set by governmental health organizations to determine if a sample is contaminated. The Canadian guideline for drinking water (Health Canada, 2012) and the US regulations (US EPA, 2009) state that a sample of drinking water should not contain *E. coli* at all. For swimming in lakes and beaches, the current standardized threshold for *E. coli* indicating a risk of fecal contamination of effluents in water is between 2 CFU/ml (in Canada [23]) and 23.5 CFU/ml (in USA [24]). As for urine samples, the presence of *E. coli* at a concentration greater than 10^5 CFU/ml represents urinary tract infection [25].

The determination of the concentration of bacteria present in a sample requires rapid and effective tools. In the next section, we will present the conventional methods used in laboratories for the identification and characterization of these bacteria.

2.1.3 Conventional bacteria characterization techniques

Public and private surveillance systems use essentially conventional methods for recognition and characterization of pathogens, which rely primarily on microbiological and biochemical identifications. These methods usually require a pre-enrichment of the sample before proceeding to the analysis stage, which allows the pathogens possibly present in the sample to multiply in abundance (multiplication factor ranging from 10^3 to 10^9 depending on the speed of growth) and to become detectable.

Culture and colony counting

Culture-based method is a central technique used in biology labs for bacterial identification. Traditionally, the first step is to obtain a pure culture to obtain isolated colonies. From this culture, a number of morphological, cultural and biochemical characters of this unknown organism is confronted with those of many known species until finding a similarity. The origin of the organism often provides indications which, added to some simple observations and tests, can lead to the possible identity of the organism or at least, to circumscribe the research to one of the main bacterial groups. This phenotypic identification of bacteria has been used for more than a hundred years in microbiology laboratories to identify pathogens. Since these methods are based on the growth properties of microorganisms, an incubation of 18 to 24 hours is required for the identification of bacteria, and typically a minimum of 36 to 48 hours elapses before the results of the sample analysis are obtained. For some species, it may require up to 7 days to yield results, as it relies on the ability of microorganisms to multiply and to give colonies visible by the eye. In the past ten years, the matrix-assisted laser desorption ionization time of flight mass spectrometry (MALDI-TOF MS) has emerged in microbiology labs, particularly in hospital laboratories. Thanks to this technology, specific identification can be obtained from a single colony on agar in a few minutes. It is certain that the initial culture step is still necessary, but once the culture is positive, the identification is very fast. Nevertheless, the use of conventional culture-based techniques poses big problems of delay in response [26].

Methods based on immuno-recognition

These methods are based on the antibody-antigen interaction and are widely used for the detection of foodborne pathogens. In these techniques, probe antibodies, either in solution or immobilized on a surface, recognize specific antigens of the pathogen to be detected in the test solution. The antibody-antigen interaction, in the presence of the pathogen, causes a modification of the medium: formation of aggregates for serological agglutination tests, precipitates for immunoprecipitation tests or even radiation absorption for enzyme linked immunosorbent assay (ELISA) tests. The typical detection times for these techniques are more than 24 hours, so it is not a real-time detection. In addition, the detection limit is typically 10^3 - 10^4 CFU/ml, which makes the pre-enrichment phase mandatory [1].

Polymerase Chain Reaction (PCR)

DNA based method, such as PCR are fast and specific techniques that allow the analysis of several bacterial strains simultaneously [27]. PCR is based on the exponential synthesis of copies of a specific DNA sequence which doubles at every cycle. Monitoring the melting curves during successive cycles makes it possible to identify the amplified sequence, i.e. the bacteria. It is very accurate because it detects the organism by amplifying the target rather than the signal and is therefore less prone to producing false-positives. An important disadvantage of this technique is that PCR amplifies all the DNA present in solution, which implies that the dead bacteria are also detected. This characteristic can be quite inconvenient, typically for the study of sterilized samples [28].

Flow cytometry

It is a popular technique that utilizes light to count and profile cells in a heterogeneous fluid mixture. The basic principle of flow cytometry is the passage of cells in front of a laser so they can be detected, counted and sorted. When additional information is required, antibodies tagged with fluorescent dyes, and raised against the targeted cells can be used and then excited by the laser to emit light at varying wavelengths. The fluorescence can then be measured to determine the amount and type of cells present in a sample. However, this preliminary stage of fluorescent labeling may be an obstacle to practical applications. The results are usually obtained within 2 hours, with an LOD of 10^5 CFU/ml. The advantage of cytometry is that it is free from the volume of the sample to be tested, which also eliminates the enrichment phase of the solution [29].

Although these methods provide both qualitative and quantitative information of the tested entity, they are greatly limited by the time required for the identification of the bacteria or require labeling. The sectors of food industry, water treatment and clinical diagnosis in which these techniques are used, are demanding of new technologies that would be faster, reliable, specific, sensitive and simple to implement while maintaining low costs of manufacture and operation. The ability to perform real-time analysis is also a key feature for these detections.

Biosensor technology can meet these requirements and reduce the analysis time while offering detection similar to conventional techniques in terms of sensitivity and specificity. They present an attractive alternative as their capability of being used *in situ* allows reduced detection times, from several days to hours, or even minutes.

2.2. Biosensors for the detection of bacteria

2.2.1 Biosensors: definition, history and development

According to the International Union of Pure and Applied Chemistry (IUPAC), a biosensor is an integrated device capable of providing specific quantitative information through a biological recognition element in direct contact with an element of transduction. The term biosensor therefore includes any measurement device defined by a biological ligand connected to a transduction device designed to transform a molecular recognition phenomenon between the ligand and its target into a physically measurable signal [30].

Thereby, a biosensor is composed of three components: the bio-recognition interface for detecting a targeted substance in a medium, the transducer for converting the physicochemical changes induced by the biological recognition into a physically measurable signal, and the signal processing interface for the conversion/transmission of the signal.

Two classes of biosensors can be differentiated: those with direct detection (no use of labeling molecules), and those with indirect detection requiring the addition of a probe (fluorophore, enzyme, etc.).

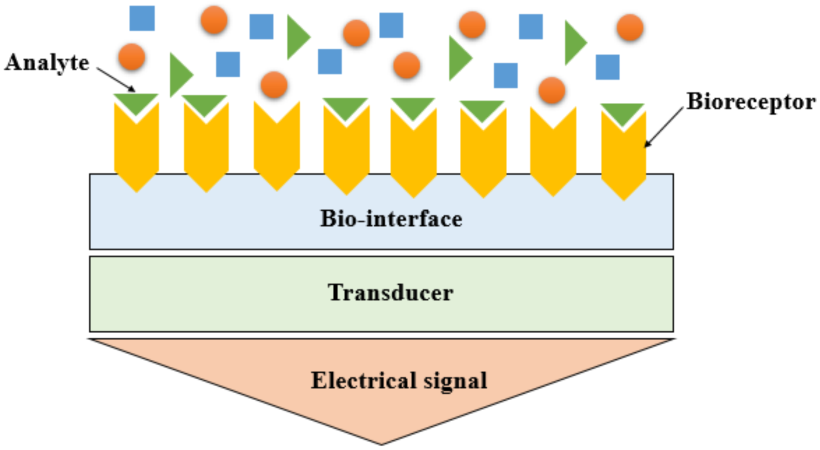

Figure 2. Diagram illustrating the components of a biosensor

The history of biosensors began in the 1962 with the development by L. Clark of the first enzyme electrode capable of measuring the concentration of dissolved oxygen in blood. The coupling of this oxygen electrode to an enzymatic membrane subsequently allowed the determination of the glucose content in the blood and in various other biological solutions [31]. At the beginning of the 1970s, Guilbault created a device to measure urea in blood and urine [32]. Since these first achievements, biosensors have continued to attract research interest and they are still experiencing increased momentum. Indeed, the number of publications on biosensors has been growing exponentially over the last 20 years, showing the emergence of these technologies [33]. Due to their many advantageous characteristics (small size, speed, ease of use, low cost, etc...), the development of biosensors is booming in various fields such as the agri-food sector [5], environmental control [34], health and military [35]. All this adds up to a prediction of a strong commercial future for biosensor technology. In this context, figure 3 shows the value of the evolution of the biosensor market over the years.

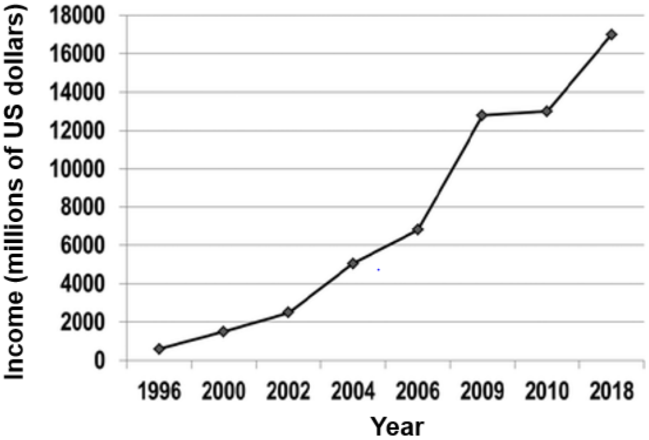

Figure 3. Evolution of the world market for biosensors in millions of US dollars, modified from [33]

2.2.2 Characteristics of a biosensor

The objective of developing a biosensor is to achieve a device of reduced size (potentially portable) that detects, alerts or even directly assays the analyte of interest, quickly and preferably without requiring additional reagents or sample pre-treatment. The performance of a biosensor is generally evaluated experimentally by their sensitivity S, limit of detection (LOD), full-scale range, specificity and response time [36].

The sensitivity: It is the ratio of the incremental change in the sensor's output to the incremental change of the measurand in input. It describes how the output signal varies with changes of a certain measurand property such as mass attachment. The slope of the calibration curve, which represents the relationship between the measurand property and the signal generated by the system, can be used for the calculation of sensitivity.

$$S = \frac{\Delta \text{ Output signal}}{\Delta \text{ measurand property}} \tag{2.1}$$

The overall sensitivity depends on three essential parameters, resulting from the decomposition of a biosensor shown in Figure 2. The first one is the affinity of the bio-interface to the targeted species. The second is determined by the nature and the respective value of the various physico-chemical changes that may occur at the level of the bio-interface during the immobilization of the compound: mass variation, modification of the visco-elastic behavior, etc. The third is related to the sensitivity of the transducer to the change of the intermediate variable.

The LOD: It represents the lowest concentration of an analyte in a sample that can be quantified and distinguished from the absence of the analyte, under the stated experimental conditions. The LOD is reached when the output signal goes three times above the noise level, where the noise is quantified by the standard deviation of the signal. At this low input change, no quantitative measurements are possible, and the sensor can only act as a probe to measure whether the measurand is present or not. At around three times the LOD, one can start to make quantitative measurements.

The full-scale range: It represents the range over which the sensor is usable with measurements that are expected/correlated to the analyte concentration. It ranges between the maximum and minimum values of the measurand that can be measured with the sensing system. It is limited by the LOD at the lowest concentrations. The broader the full-scale range, the less important are dilution or enrichment steps during sample preparation. In general, a proper sensor should function over at least one or two concentration decades.

The specificity: It represents the ability of the sensor to detect the desired analyte in the presence of other potentially interfering species, to obtain the least possible false positives. It is controlled by the biological element used to functionalize the surface. Since the concentration of the analyte to be detected can be very low compared to that of several other elements, a high specificity is essential in the real applications.

Combined with these characteristics, miniaturization, accuracy, low cost of fabrication, good reproducibility, stability and reliability are essential features of the biosensors for their industrialization [37].

2.2.3 Classification of biosensors

Biosensors can be classified according to different criteria such as the reaction involved, the nature of the ligand used or the transduction type. Indeed, the choice of the biomolecule of recognition and the transducer can directly influence the performances of the biosensor. In this section, we classify biosensors based on the transduction technique [38].

The transducer is the physical element that exploits the biochemical modification resulting from the interaction between the analyte and the ligand, to transform it into an electrical signal. The adequacy between the type of transducer and the biological element makes it possible to obtain a sensitive and easily exploitable signal with a minimum of background noise. The information given by the transducer, like the ligand, must be specific and must only correspond to the biological recognition. The type of transducer is chosen as a function of biochemical changes occurring at the bio-interface. Indeed, not all transducer-ligand combinations are equivalent, some are not even possible.

Three transduction mechanisms are mainly used for designing biosensors: electrochemical, optical, or acoustic. The general principles of the most used transducers in the literature are briefly presented here, in order to understand the pros and cons of each transduction mode.

In the case of electrochemical transducers, the binding of the analyte to the ligand generates an oxidation-reduction reaction. The latter produces or consumes ions or electrons, causing a change in the electrical properties of the solution that can be sensed out and used as a measuring parameter [39]. Based on the measured electrical parameters, electrochemical biosensors can be classified as impedimetric [40], conductimetric [41], amperometric [42] or potentiometric [43]. These transducers generally include one or more electrodes functionalised by biological compounds and operate in a liquid medium. Many reports have revealed that the electrochemical biosensor has advantages such as speed, simplicity, low cost, high sensitivity, and relatively simple instrumentation [44], [45].

Optical transducers transform the recognition event in the form of an optical quantity (variation in refractive index, absorbance, fluorescence, luminescence, etc...) [46]. The main advantages of optical sensors are their insensitivity to electromagnetic interference, their high detection sensitivity and their non-destructive character, which allows *in situ* and real-time monitoring. However, their main limitation is the difficulty of complete integration on a miniaturized chip.

Among these optical methods, Surface Plasmon Resonance (SPR) is the one with the largest market share [47]. SPR technique allows quantitative recognition of biological species in real time, without any labelling and with high sensitivity. Commercial SPRs are generally capable of detecting 1 pg/mm^2 of absorbed analytes (which corresponds to 1 bacterium of *E. coli* per mm^2) [48]. However, this sensitivity is strongly dependent on the surface functionalization. The flexibility of this technique is a great advantage, because it can be used in a multiplexed format for the detection of many analytes [49]. The principle of measurement is to send, through an incident ray (Figure 4), a wave polarized in the plane of incidence on a glass-metal interface (usually gold or silver). For a definite angle, characteristic of the metal layer, the energy of the wave is partly absorbed by the excitation of the surface plasmons. The plasmon wave will play the role of probe because its amplitude and its phase will be modified following the fixation of molecules on the surface. The analysis of the amplitude or the phase of the reflected signal will allow to determine the number of biomolecules interacting on the surface. The performances of SPRs made them reference devices used by many research teams to validate bio-functionalization/detection protocols. However, the cost of these systems is high. Indeed, their prices range from tens of thousands of dollars up to several hundred thousands of dollars [50].

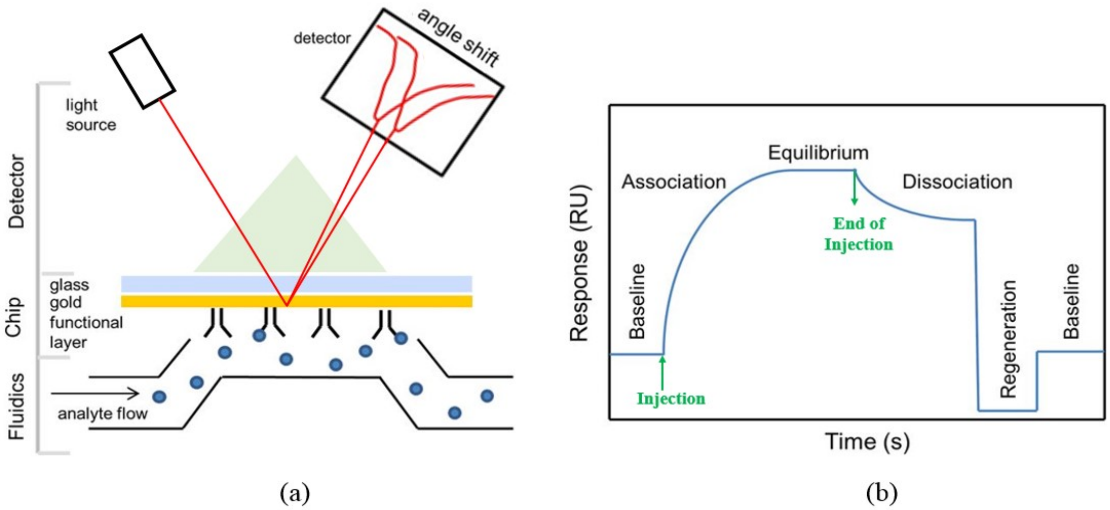

Figure 4. Principle of operation of the SPR technique (a) and typical SPR sensorgram showing the steps of an analytical cycle (b), modified from [51]

Biosensors based on acoustic waves transducers measure the physical, chemical, and/or biochemical changes that accompany the formation of the analyte-ligand complex. They can be easily integrated in a microfluidic system and the sensing area is generally coated with a biospecific layer. When a bioanalyte interacts with the sensing layer, changes in mass or viscosity of the biospecific layer can be detected by monitoring changes in the acoustic wave properties such as velocity, resonant frequency and delay time. These transducers have many advantages, namely their sensitivity, accuracy, simplicity of microfabrication, low energy consumption, as well as the possible miniaturization and integration in automated devices.

2.2.4 Positioning of acoustic wave biosensors

In this section, the important features of acoustic waves biosensors are presented and compared with other sensing technologies with respect to their qualitative advantages and disadvantages, as well as their performances (analysis time, full-scale range, LOD).

Acoustic waves-based devices offer a promising platform for the development of sensitive, accurate and portable biosensors. They could be the basis of an effective early detection system with advantages in terms of response time, possibility of integration and adaptability to a large number of applications. Since they are primarily sensitive to the effect of mass, they have a broad spectrum of applications, unlike other devices that would require the variation of a very specific parameter. Thus, any immobilization of material on its surface results in a mass variation, possibly accompanied by the variation of other parameters. Moreover, depending on its configuration, an acoustic wave sensor can respond to a wide range of physical variables such as force, pressure, temperature, mass, density or like viscosity, permittivity and conductivity in the case of a liquid.

Acoustic waves sensors do not require an expensive manufacturing process and have the particularity of being easily embeddable. They can therefore be used for nomadic applications, particularly for MicroElectroMechanical Systems (MEMS). Indeed, MEMS fabrication of acoustic waves-based sensors enables device miniaturization, power consumption reduction and integration with electronic circuits. Furthermore, acoustic biosensors are label-free which reduces their costs of operation and allows a real time detection. Additionally, they are passive sensors, so their energy consumption is very low. Another interesting feature of the acoustic wave devices compared to others is the frequency output, which has less noise than amplitude measurements, ensuring the high precision and reliability of the response. Aside from the technological advantages of acoustic waves biosensors, their performances for bacteria detection are also remarkable. Table 1 shows the detection range and analysis time for detecting *E. coli* reported in literature for different types of biosensors.

Table 1. Comparison of the analysis time, full-scale range and LOD reported for *E. coli* of different types of biosensors

Detection technique	Analysis time (min)	Full-scale range (CFU/ml)	LOD (CFU/ml)	Source
Electrochemical – Impedimetry	10 - 180	10^1 - 10^7	30	[40], [52], [53]
Electrochemical – Amperometry	6 - 30	10^1 - 10^7	16	[42], [54]
Electrochemical – Conductometry	6 - 10	10^1 - 10^5	79	[41], [55]
Electrochemical – Potentiometry	30 - 90	10^1 - 10^4	10	[43], [56]
Optical – SPR	10 - 30	10^4 - 10^8	10^4	[49]
Optical – Photoluminescence	60 - 120	10^3 - 10^5	10^3	[57]
Optical – Chemiluminescence	30	10^2 - 10^5	10^2	[58], [59]
Acoustic – Quartz crystal microbalance	30 - 60	10^3 - 10^8	10^3	[60], [61]
Acoustic – Surface acoustic waves biosensors	30 - 150	10^6 - 10^9	10^6	[62], [63]

By comparing the performances of acoustic wave biosensors to others, it is fair to say that they are well positioned with respect to the full-scale range, analysis time and LOD. Indeed, they cover a wide detection range and the analysis time averages between half an hour and three hours. In terms of LOD, it is higher than the ones achieved using electrochemical biosensors. However, the latter require much more complex fabrication and surface functionalization processes (synthesis of nanowires [64], use of nanoparticles [42], [55]). Moreover, a review by Koncki has discussed the application of potentiometric-based biosensors in biomedical analysis and concludes that bioaffinity-based biosensors using potentiometric transduction are not reliable [65]. As for amperometric biosensors, one of the limitations to their use is the potential interferences to the response in the presence of electroactive compounds in the sample, which can cause the transducer to generate a false current reading and a lack of selectivity [66]. In the case of conductometric transduction, the measurement is an additive property, hence less sensitive compared to the other electrochemical methods and strongly dependent on the used buffer [67]. Due to all these limitations of electrochemical biosensors, their fragility and their complex fabrication processes, acoustic biosensors are preferred.

As for optical biosensors, their LOD is comparable to the one of QCMs, although their cost is much higher and their integration level, although improving, still does not compare the ease of integration of acoustic biosensors.

Based on these criteria, we propose in the present work the development of an acoustic wave biosensor, for its rapid response, its ease of design, fabrication and integration, as well as its high sensitivity and specificity for the targeted application.

2.3. Gallium Arsenide for biosensing

GaAs is a microtechnical material that combines advanced MEMS technologies with possibilities for devices integration and miniaturisation. In addition, the compatibility of this material with many functionalization techniques and surface micro/nanostructuration processes makes it an ideal candidate for a biosensor application. Through the past years and thesis, our laboratory has developed a high expertise in the fabrication of GaAs membranes using chemical wet etching, the formation of SAMs on GaAs and the regeneration of its thiolated and antibody functionalized surface [8]–[10], [13], [14], [68]. In the following sections, we will present the various features of GaAs that justify the choice of this material for the sensing part of our device.

2.3.1 Microfabrication functionalities of GaAs

GaAs is a III–V compound semiconductor with a combination of physical properties that has made it an attractive candidate for many electronic applications. Most of the microfabrication processes applicable to silicon, the reference material for MEMS, are adaptable to GaAs, making this material the second most widely used in the field of microtechnology. Thus the conventional techniques of deposition, layer growth, structuring (wet or dry etching), doping (diffusion, implantation) and bonding are applicable to GaAs as well [69]. Moreover, the possibility of integrating GaAs structures with other devices is a crucial issue for the realization of MEMS, especially for bioMEMS requiring the use of fluidic cells. Thus, permanent or reversible techniques can be envisaged for producing structures, multi-material devices, generally GaAs/silicon or GaAs/glass [70]. As for permanent assembly techniques, they are identical to those proposed for Si: anodic bonding, fusion or direct bonding or thermocompression. Furthermore, GaAs could be micro-machined by wet etching in several solutions, which constitutes a batch and low-cost process of fabrication and leads to promising micro-structures for sensors [9], [71].

2.3.2 Bio-functionalization of GaAs

For a biosensor application, it is necessary to integrate on the transducer a bio-recognition layer, to detect selectively the analyte of interest. Beside its beneficial microfabrication facilities, GaAs's surface can be chemically functionalized with alkanethiols, which gives to this material very singular functionality for ligands immobilization.

Chemical functionalization of GaAs

The functionalization of GaAs surface by a monolayer of chemical molecules has the advantage of forming simple, organized and reproducible chemical interfaces. The formation of self-assembled monolayers (SAM) of chemical molecules on GaAs surface allows forming different microstructures suitable for full biofunctionalization. The self-assembly derives from the fact that the organic derivatives adsorb spontaneously and organize themselves on the substrate.

Naturally, an oxide layer forms on the surface of GaAs [72]. By deoxidizing the surface beforehand, it becomes possible to form monolayers of thiols equivalent to those obtained on gold substrate. The work of Voznyy and Dubowski has led to a better understanding of the interactions between thiols and this substrate [73], [74].

For developing the GaAs-based biosensor, Bienaimé et al. have used a mixed architecture of SAM consisting of 11-mercapto-1-undecanol (MUDO) and 16-mercapto-1-hexadecanoic acid (MHDA) [10]. The chosen molecules each possess a thiol allowing the attachment, consisting alkyl chains of different lengths (11 and 16 carbons), and respective terminal hydroxyl and carboxyl functions. These two functions make it possible to fix the proteins (reaction between activated carboxyl group and amine group of the protein) and to limit the non-specific interactions on the substrate. In his thesis, V. Lacour studied the formation kinetics of SAMs on GaAs. In his paper [14], he investigated the formation of enhanced quality mixed SAMs as a function of the molecular composition of the thiol mixture and the proportion of ethanol/water solvent used during their arrangement. His results, in addition to confirming that water/ethanol-based solvents improve the packing density of single thiol monolayers [75], demonstrate the attractive role of water/ethanol solvents in forming superior quality mixed SAMs.

Immobilization of ligands on GaAs using SAMs

Biological recognition elements, or ligands, are the key to the biosensor technology. By definition, ligands are molecular species that use a specific biochemical recognition mechanism [38]. The choice of the ligand depends on several parameters: its stability, its lifetime, the specificity of its response and the ease of its use as well as the nature of the molecules to be analyzed [33]. In our research group, we mainly use antibodies to immunocapture the targeted biological objects. Antibodies are glycoproteins produced by the immune system in response to the introduction of a foreign molecule (antigen). These complex biomolecules are composed of roughly a thousand sequenced amino acids. Particularly suitable for the recognition of analytes present in very small quantities in biological fluids, these ligands are widely used, especially for clinical diagnostic applications.

The surface of Gallium Arsenide can immobilize ligands by adsorption, trapping or covalent coupling methods. Covalent immobilization using SAMs has been found to be a strategy of choice because it allows to passivate the surface of the material while providing a high density of bonding sites for the ligands. In addition, it is a process that is simple to implement and, depending on the type of molecules, achievable at low cost. If the SAM architecture is composed of a carboxylic acid, e.g. MHDA, it is done by activation of carboxyl groups. Such is the case within the work of A. Bienaimé [10], [11]. If the SAM has biotin-terminated architecture (e.g. Polyethylene glycol (PEG) thiol), the protocol is different and requires the use of an intermediate protein (Avidin, NeutrAvidin or StreptAvidin) and biotinylated antibodies [57]. However, the non-specific interactions caused by the intermediate protein could be a limiting factor for this approach compared to the first protocol.

2.3.3 Regeneration of GaAs surface

Apart from a few expensive biosensors used in research or analysis laboratories, only the cheapest ones can be competitive to penetrate broader markets. In general, the cost of biosensors is due to the instrumentation required for its operation and to the use of materials or reagents of high quality for its manufacture. As the costs associated with the GaAs material and the fabrication of the transducer cannot be ruled out, in this situation the regeneration of the device remains the only way to reduce the cost of using the system [76].

The regeneration of the biosensor can occur on three different levels:

Level 0: It consists in removing the whole bio-interface from the surface after exposure to the target. This includes the SAM, the ligands and the targeted analyte. This strategy is the most effective, because it allows to restart the measurements with a surface state that is very close to the first one, which guaranties the reproducibility and reliability of the results.
V. Lacour used this approach for regenerating the surface of a thiolated and antibody functionalized GaAs surface using wet chemical process. The latter consists of immersing the sample in an NH_4OH: H_2O_2: H_2O (3:1:100) etching solution, that induces the chemical removal of the bio-interface. This method is fast, it can be performed *in situ*, and does not require sophisticated equipment. It allows the regeneration of the entire bio-interface, including the immunological receptors and the SAM [13]. However, on the long term or after a certain number of cycles, the gradual etching of the GaAs substrate can deteriorate the surface of the sensor (increase of the surface roughness for example). Within this thesis, another approach for regenerating the GaAs surface by UV photo-oxidation in liquid medium was tested. This method

allowed to desorb rather efficiently the thiols on the surface of GaAs by UV photo-oxidation, while preserving the surface of the material. Under exposure to a UV source, the alkanethiols adsorbed on a metal substrate oxidize to form alkanesulfonates (RSO_3^-) that can easily be rinsed with a polar solvent such as ethanol [12]. This method was found to be very promising for patterning the GaAs surface for the attachment of different antibodies, a step towards multiplexed detection.

Level 1: It consists of removing the ligands and the antigen while preserving the SAM on the surface. Although less efficient than the previous one, this strategy allows to restart the measurements with a functionalized surface and avoid the re-functionalization process which would take around 20 hours. However, after a few cycles of regeneration, the immobilization rate of ligands would not be the same, since the number of bonding sites may decrease over the cycles.

Level 2: It consists of removing only the targeted molecule. This simple and relatively fast method allows to dissociate the antigen using an antibody-antigen dissociation kit. Many commercial kits are present on the market. These agents allow to re-use the antibody without affecting the SAM or the sensor surface. However, since the regeneration is not 100 % effective, some antigens may persist from one measurement to another, and the efficiency of regeneration may decrease after a few cycles, depending on the ligand used.

As the previous works have shown, GaAs has a great potential for biosensing. Although its piezoelectric properties did not achieve the expected performances of the acoustic transducer (as mentioned in section 1.2), its surface functionalities remain very attractive. Therefore, we will keep GaAs for the biosensor part in contact with the liquid and add a piezoelectric layer of ZnO on its top side to improve the transducer's performances. In the next section, we will present the various properties and features of ZnO and compare it to other piezoelectric candidates, in order to justify this choice of material.

2.4. Zinc Oxide thin films: an overview

2.4.1 Properties of ZnO

For several years, ZnO has attracted considerable interest in a wide variety of fields. It is a semiconductor material with interesting physical properties that place it among the most promising materials in a big range of fields such as energy recovery, electronics, gas detectors, etc. [77]. The first work on ZnO appeared in 1930. The difficulties for obtaining massive crystals as for its doping slowed down its development for several years. The ZnO rebirth took place in 1995 when UV laser emissions were obtained in thin ZnO films at room temperature and was also driven by the technological interest in its thin films and nanostructures. Over the past years, the number of publications on this ion-covalent crystal has been steadily increasing. In this part, a fairly detailed discussion of ZnO properties is presented.

Structural properties

ZnO is a binary compound: it lies between ionic and covalent crystals. It can crystallize in three phases: würtzite, zinc-blende and rocksalt, as represented in Figure 5 (a). The zinc-blende phase is obtained by growth of ZnO on a substrate of cubic crystalline structure and the rocksalt structure is obtained when ZnO is subjected to high pressures (≥ 15 GPa). The würtzite phase is the most stable thermodynamically (obtained at ambient temperature and pressure), where each anion is surrounded by four cations that lie at the apexes of a tetrahedron and vice versa [78]. It is in this tetrahedral coordination that ZnO will be studied in this work.

Würtzite phase ZnO belongs to the class 6mm compact hexagonal symmetry crystal family. The indices of the faces of this structure are denoted (hkil) [79]; the value of i can be calculated from h and k using the formula: $i = -(h + k)$.

The anions and cations form two subsystems offset parallel to the direction [0001], generally called the c-axis. The mesh parameters in the plane (0001) and along the c-axis are therefore distinct, which gives this material a structural anisotropy. One of the fundamental points about Würtzite ZnO is that it does not have a plane of symmetry perpendicular to the c-axis. Therefore, ZnO of compact hexagonal structure würtzite can be described by the alternation of two compact hexagonal networks one of Zn^{2+} and the other of O^{2-} stacked alternately along the c-axis.

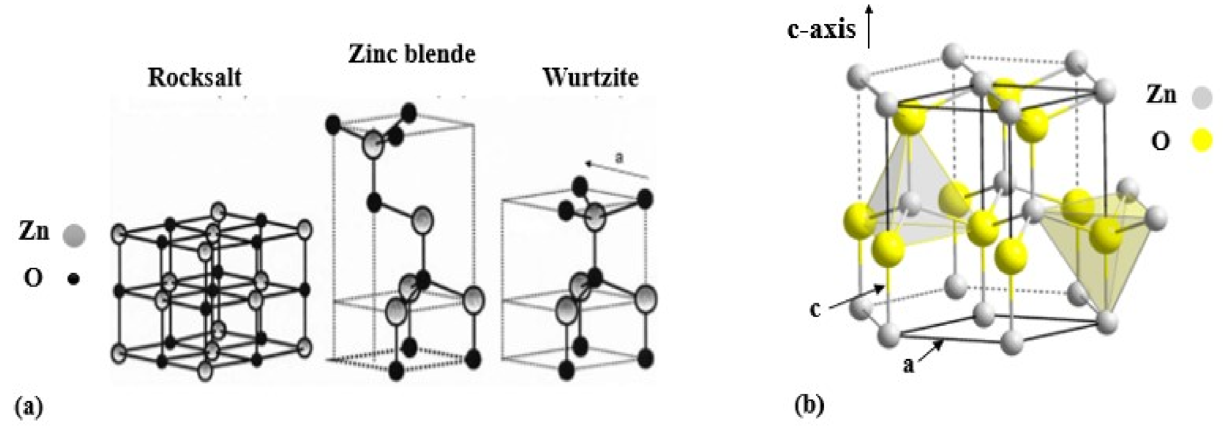

Figure 5. (a) Representation of the different crystal structures of ZnO, (b) parameters a and c of the elementary cell in the würtzite phase of ZnO, adapted from [80]

Since the {0001} planes' surface energy is higher than that of the {1010} and {1120} planes, the growth rate along the c-axis is higher. As a result, the ZnO structure promotes anisotropic growth along the c-axis, which is an advantage for obtaining one-dimensional nanostructures.

The hexagonal mesh of the würtzite structure is characterized by three constants a, c and u; a is the length of the side of a rhombus constituting the base, c is the lattice parameter along the (0002) plane referred to as the c-axis and u is an inner coordinate along the c-axis, which determines the relative position of the subnetwork of the O^{2-} anion and the Zn^{2+} cation. The coordinate u is determined using the following equation:

$$u = \frac{1}{3}\frac{c^2}{a^2} + \frac{1}{4} \tag{2.3}$$

The crystallographic vectors of the würtzite structure are:

$$\vec{a} = a\,(\tfrac{1}{2},\tfrac{\sqrt{3}}{2},0)\ ;\ \vec{b} = a\,(\tfrac{1}{2},\tfrac{-\sqrt{3}}{2},0)\text{ et }\vec{c} = a\,(0,0,\tfrac{c}{a}) \tag{2.4}$$

The parameters of the primary ZnO mesh under normal conditions of temperature and pressure are: a = 3.2498 Å and c = 5.2066 Å. These parameters depend on several factors such as the temperature and the presence of stresses, defects or impurities [80].

Electrical properties

ZnO is a II-VI semiconductor of direct band gap of 3.37 eV at ambient temperature. As a large direct bandgap material, ZnO attracts the attention of many electronic and optoelectronic applications. The advantages associated with this broad gap are the low noise generation, the high breakdown voltages and the ability to operate at high temperature (700 °C) and power and to support large electric fields [81], [82]. The electrical resistivity of ZnO in thin layer is in the range of 10^{-4} - 10^{9} W.cm depending on the deposition conditions and mainly the temperature [83]. The thermal conductivity of ZnO thin films is of the order of 15 $W.m^{-1}.K^{-1}$ [84]. However, these values are very dependent on technological parameters and in particular heat treatments.

Thermal properties

Since the deposition conditions and the heat treatment significantly influence the properties of the thin film, it is important to know the thermal parameters of the material that determine its behavior as a function of temperature. The thermal capacity of undoped ZnO has a value of 519 $J.kg^{-1}.K^{-1}$ and its thermal expansion coefficient is of 2.9 x 10^{-6} K^{-1}. To avoid the generation of thermal residual stress in ZnO films, the thermal parameters of the substrates should be also taken into consideration.

Optical properties

As a thin layer, the refractive index of ZnO varies between 1.9 and 2.2 according to the conditions of elaboration. The optical transparency of ZnO in the visible and near infrared regions is a consequence of its wide gap, the fundamental absorption threshold of ZnO being in the ultraviolet. The doped ZnO enters the class of conductive transparent oxides (TCO). Slightly doped, it can be used in photoluminescence. The wavelength of the emitted radiation extends from the near UV (0.35 µm) to the visible (0.55 µm) according to the characteristics of the oxide and the elaboration conditions. Recently, the emission of ZnO films has been extensively studied because of its high luminescence efficiency, non-ohmic property, and high excitation bonding energy (60 meV). [81].

Piezoelectric properties

ZnO of würtzite structure belongs to the class of piezoelectric materials. The piezoelectricity of ZnO originates from its crystal structure: since the barycenters of the positive and negative charges of its elementary mesh are not superimposed, an electric dipole appears inside the crystal and is modulable by the application of a mechanical stress (direct piezoelectric effect). The interaction of this electrical dipole with an external electric field can also deform the crystal (inverse piezoelectric effect).

ZnO has three piezoelectric coefficients: e_{15}, e_{31} and e_{33}. e_{15} describes the polarization induced by shear deformations. e_{33} and e_{31} connect the polarization along the c-axis to the deformation of the cell along c-axis and in the basal plane (orthogonal plane to the c-axis). In order to exhibit the piezoelectric effect, the film must be oriented along the c-axis.

The piezoelectric effect in ZnO thin films has been studied for several years and is widely applied in many fields [77], more specifically in surface and bulk acoustic wave devices for filtering and sensing [85]–[87]. Thanks to its high piezoelectric coefficients, ZnO has been renowned as a very promising material for acoustic applications.

2.4.2 Comparison of ZnO with other piezoelectric materials

Acoustic sensing devices are based on piezoelectric crystals or thin films. Of all the piezoelectric materials, only some have the ability to be deposited as thin films while conserving interesting properties. Piezoelectric thin films developed during the last decades, and in particular Aluminum Nitride (AlN), Lead Zirconate Titanate PZT and ZnO have allowed the reduction of dimensions and the increase of oscillation frequencies. Over the last few decades, there have been many improvements in optimizing deposition conditions for thin films on substrates to enhance electromechanical transduction. Control over the growth of the piezoelectric thin films can lead to good environmental stability and responses, coupled with high piezoelectric coupling coefficients [88]. This section will therefore give a comparison of these three piezoelectric thin film materials and briefly explain some of the advantages of ZnO thin films, which are used in this work. For comparison, Table 2 lists some of the main characteristics of PZT, AlN and ZnO.

PZT ($Pb\ [Zr_xTi_{1-x}]\ O_3$) is a ferroelectric material, meaning that it must be poled to exhibit sufficient coupling coefficients, i.e. the dipoles in the compacted crystals must be aligned in the same direction by subjecting them to a strong electric field. Above the Curie point, the dipole directions in ferroelectric materials disappear. PZT can be deposited in thin films form by sputtering and by the sol-gel process. Sputtered PZT films can also show a spontaneous polarity, eliminating the need of poling. Despite the difficult fabrication process, PZT-based compounds are some of the most useful electro-ceramics. Among the piezoelectric film materials, PZT has the largest piezoelectric constants [89]. However, PZT films have disadvantages for biosensing applications such as high acoustic attenuation, low quality factor, high energy loss and poor biocompatibility (high toxicity of Pb) [90], [91]. Worst of all, PZT films are not easy to fabricate [92]. The requirement for high temperature annealing and high electric field polarization also make PZT films unsuitable for integration with microelectronics as well as MEMS devices.

Table 2. Piezoelectric properties of different piezoelectric materials [93]

Material		AlN	ZnO	PZT (1-3 μm) [94]
Piezoelectric coefficients (10^{-12} m/V)	d_{33}	3.9	5.9	60 - 130
	d_{31}	-2	-5	-120 to -170
Piezoelectric stress constants (C/m^2)	e_{33}	1.55	1.22	23.3
	e_{31}	-0.58	-0.57	-6.5
Dielectric permittivity (10^{-11} F/m)	ε_{33}	10.5	10.9	300 - 1300
Thermal conductivity (W/m.K) at 300 K		285	54	1.4
Thermal expansion (/°C)		4.3×10^{-6}	6.5×10^{-6}	2×10^{-6}

Like ZnO, AlN belongs to the hexagonal würtzite crystal type, having 6mm symmetry. Its structure can be considered as two inter-inserted hexagonal structures (aluminum and nitrogen) spaced by 3/8c from each other, where c is the main symmetry axis of the crystal. Compared to AlN, ZnO has comparable piezoelectric coefficients. However, the oriented growth and crystal quality are requirements for thin film piezoelectric devices. According to the literature, controlling the stoichiometry of a ZnO thin film and its texture is much easier than for thin AlN films [78]. Deposition conditions, especially the presence of oxygen in vacuum chambers, have significant effects on AlN film growth and microstructure. Furthermore, high film crystallinity of ZnO can be easily obtained by deposition at lower temperature than for AlN [95]. ZnO normally has a low film stress and a relatively good adhesion with most substrates. Moreover, ZnO material is considered as biosafe and therefore is suitable for biomedical applications that immobilize biomolecules [96]. Hence, among the three materials, ZnO has been chosen for improving the piezoelectric performance of the GaAs-based transducer.

2.5. Deposition of ZnO films on GaAs

Regardless the deposition technique, a thin layer always tends to match the structure of the substrate on which it is deposited. Consequently, it is imperative to consider that the substrate has a very strong influence on the structural properties of the deposited layer. Thus, thin layers of some material, with the same thicknesses, may have substantially different physical properties depending on whether they are deposited on an amorphous insulating substrate such as glass, or a monocrystalline silicon substrate, for example. In this work, we investigate the deposition of ZnO thin films on GaAs substrates.

2.5.1 A brief literature review

The growth and characterization of ZnO films have been widely reported on different kinds of substrates [97]–[101]. High quality ZnO films have been deposited on Si, diamond, sapphire and glass substrates. Although the deposition of ZnO films on GaAs substrates was desirable to integrate optoelectronic devices and piezoelectric effect transducers, only a few reports were published [102]–[104]. This may be related to the possible interdiffusion of GaAs and ZnO layers, which could cause a significant degradation of the film's resistivity or in unwanted doping of GaAs during the sputtering process [105]. For instance, Ryu et al. have studied the outdiffusion of gallium and arsenic from the substrate into the ZnO film and its effect on the secondary electron emission [106]. Moreover, the oxidation of GaAs surfaces produces amorphous oxide layers that may prevent the growth of crystalline structures [72]. To address this problem, several studies have been carried out and different buffer layers between ZnO and GaAs have been tested for different applications, such as SiO_2 [107], [108], Si_3N_4 [109], ZnS [110], ZnSe [111] and Zn [112].

Indeed, the ZnO/GaAs structure has been studied by researchers for different applications. Piezoelectric ZnO thin films have been occasionally used for probing very weakly or non-piezoelectric GaAs crystal orientations [108], [113]–[115]. It has been reported that ZnO overlayer on GaAs can enhance the piezoelectric coupling strength, which increases the transducer frequency range or acousto-electric interaction efficiency. Pedros et al. reported on the dispersion of the different SAWs supported by the ZnO/GaAs heterostructure, including the fundamental Rayleigh mode and the Sezawa modes that propagate guided in the overlayer [104].

Their study showed that ZnO thin films enhance the piezoelectric field, facilitating the integration of SAW devices with GaAs electronics. On this basis, ZnO thin films were chosen to be implemented on the top side of the existing GaAs-based sensor, in order to improve its performance and achieve better quality factors. Moreover, Kim et al. studied the SAW properties of both Radio Frequency (RF) magnetron and Direct Current (DC) triode-sputtered ZnO films on (001) and (110) GaAs, and showed that the ZnO/GaAs structure can enable the monolithic integration of SAW devices and GaAs electronics [109].

These few examples show the growing interest in the ZnO/GaAs systems for different applications, and mainly for acoustic waves devices.

2.5.2 Use of buffer layer between ZnO and GaAs

As discussed in the literature, the oxidation of the GaAs substrate results in the formation of an oxide layer that affects the crystalline quality as well as the optical and electrical properties of the grown films [72]. On the other hand, diffusion effects produce unwanted phenomena at the ZnO/GaAs interface [116]. The large lattice mismatch between ZnO and GaAs and the difference between their crystallographic structures generate structural defects in the films [117]. Therefore, the use of a buffer layer, pre-deposited on GaAs substrate, can prevent these problems, and sometimes improve the quality of the grown ZnO films.

The deposition of ZnO on GaAs using a buffer layer has been investigated in the literature, and different buffer layers were tested. For example, the use of a SiO_2 buffer layer was first reported by Shih et al. who demonstrated that the SAW properties and coupling coefficient could be increased appreciably by providing a SiO_2 layer between the ZnO film and GaAs substrate [108]. Later, Kim et al. reported the use of the same SiO_2 buffer layer to obtain thermally stable ZnO films on GaAs substrates that can sustain postdeposition heat treatment [107].

Si_3N_4 passivation layer was shown to improve the ZnO film quality appreciably for both RF magnetron and DC triode sputtering methods [109]. The best quality of films observed were obtained using 1.6 µm DC triode sputtered ZnO film with 2000 Å of Si_3N_4. The authors showed that compared with bare GaAs, this particular structure has approximately 0.6 % lower SAW velocity, at least 10 times larger coupling coefficient, and -0.6 dB/µs more propagation loss.

Zhao et al. reported on the deposition of ZnO thin films by plasma-assisted MBE on GaAs substrates with ZnSe buffer layers [111]. The choice of the buffer layer was justified by the ease of control of the ZnO/ZnSe interface compared with the ZnO/GaAs interface, since ZnSe and ZnO are both II-VI semiconductors and share a common cation. They have also shown that the films grown with this buffer layer have better structural qualities.

The possibility of growing zinc-blende ZnO films on GaAs (001) substrates was studied by Ashrafi et al., and the use of a ZnS buffer layer was proposed to obtain stable ZnO films. The ZnS buffer layer prevented the formation of the amorphous oxide layer and the growth of zinc-blende ZnO of high optical quality was demonstrated on the ZnS/GaAs substrates [110]. However, for obtaining piezoelectric films, the ZnO würtzite structure is required.

Another study using Zn buffer layer between ZnO and GaAs showed a greater out-of-plane misorientation and a less compact morphology, which made us eliminate this buffer layer [112].

As for our work, aiming to develop an acoustic waves sensor, we propose to use a Platinum buffer layer, which could improve the quality of ZnO films and potentially serve as a counter electrode for thickness mode excitation within the acoustic transducer.

2.6. Proposed architecture and approach

To improve the performances of the existing GaAs-based biosensor, we propose to modify the architecture and retain the GaAs for the sensing part in contact with the liquid, profiting from its functionalization facilities and its ability to be regenerated and machined by conventional microfabrication techniques. On the other hand, we propose to add a piezoelectric ZnO thin film on one side of the GaAs membrane to improve the electromechanical coupling.

Therefore, the new geometry of the biosensor shown in Figure 6 consists of a GaAs vibrating membrane with a thin layer of piezoelectric ZnO on its top side. A pair of electrodes deposited on the ZnO film allows the generation of a bulk acoustic wave in thickness shear mode, propagating in GaAs under a sinusoidal voltage at a given frequency. The bottom side of the membrane is functionalized with a SAM of alkanethiols and antibodies against *E. coli*.

The chosen design has the advantage of separating the electrical interface from the fluidic (biological) one, which would prevent the signal attenuation due to contact with fluids.

Hence, the device fabrication by clean room techniques is divided into two main stages: the deposition of piezoelectric ZnO thin layer and the electrodes on the top side, and the micromachining of the GaAs membrane by chemical wet anisotropic etching on the bottom side.

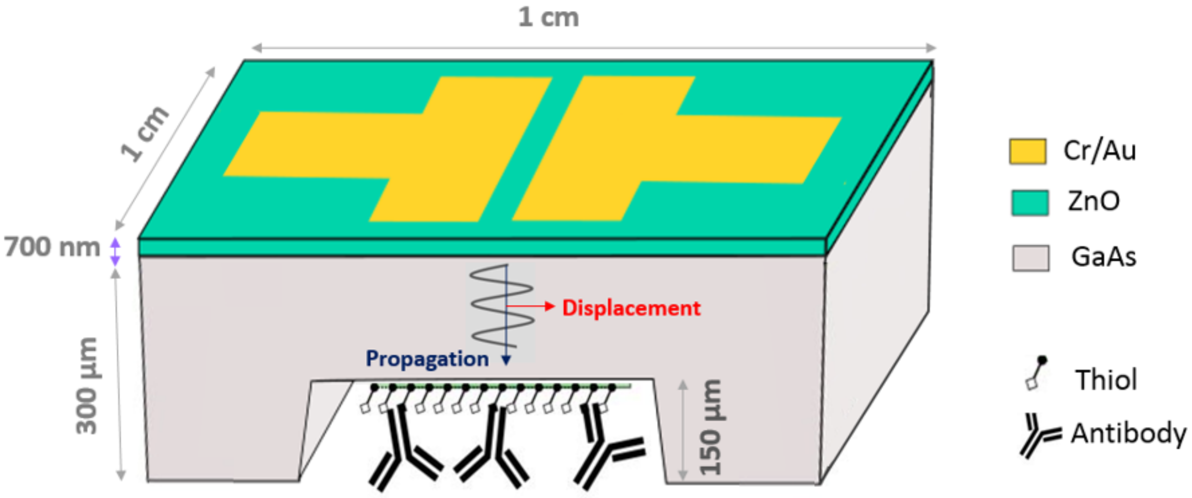

Figure 6. Architecture of the ZnO/GaAs biosensor

Before proceeding to the microfabrication of the sensor, the proposed design needs to be validated. Therefore, the next chapter presents the analytical modeling and simulation of the transducer, in order to predict beforehand its performances.

Chapter 3: Modeling & simulation of ZnO/GaAs transducer

The fabrication of acoustic wave components requires the use of so-called piezoelectric materials. The principle of acoustic wave generation is related to the electro-acoustic properties of piezoelectric materials such as quartz, AlN, ZnO and PZT. These materials allow acoustic waves devices to be designed and manufactured. In this chapter, emphasis will be placed on bulk acoustic wave (BAW) transducers designed to operate in thickness shear modes (TSM).

The present chapter consists of two main parts: the first one is a reminder of the theoretical principles governing the operation of the transducer. In this part, we will discuss the different modes of propagation of acoustic waves in piezoelectric materials, then we will establish the tensor expressions of piezoelectricity and introduce the equations describing the propagation of waves in a piezoelectric material. From these equations, and after some simplifications due to the geometry of the transducer, we will determine the velocities and directions of propagation of elastic waves in the structure, as well as the resonant frequency (f) and the electromechanical coupling coefficient (k). The second part of this chapter deals with the realization of a finite element simulation model to dimension the ZnO/GaAs transducer and determine its theoretical resonance characteristics.

3.1. Piezoelectric effect and generation of an acoustic wave

Piezoelectricity is the property of some crystals to be electrically polarized under the action of a mechanical stress. This induced polarization is proportional to the applied mechanical stress and changes sign with it. This phenomenon describes direct piezoelectricity. On the contrary, the application of an external electric field induces a mechanical deformation of the crystal: it is the inverse piezoelectric effect [118].

The piezoelectric properties of a material are related to its crystalline structure. Indeed, this characteristic is observed only in certain dielectric crystals possessing a characteristic crystalline anisotropy. In these materials, the axis of polarization is defined as the preferred axis of appearance of electric charges in the structure. Among the 32 crystallographic classes, 20 have piezoelectric properties, of which only a small number corresponds to materials of interest in piezoelectric applications.

Piezoelectric materials are particularly interesting for the generation of acoustic waves since their deformation is directly proportional to the applied electric field. In the next section, we will present the different types and aspects of acoustic waves transducers and discuss the selection of specific waves for the operation of the biosensor described in this work.

3.2. Acoustic waves transduction

An acoustic wave is a propagative disturbance of the equilibrium of a medium moving gradually and returning to a state of equilibrium thanks to its elasticity. The physical properties of the medium act directly on the propagation conditions of the wave and can affect its phase and/or amplitude velocities. There are two types of waves depending on the displacement of the particles with respect to the propagation of the wave (Figure 7).

- **Longitudinal waves (or compression waves):** the displacement of the particles is parallel to the direction of propagation of the wave. The planes perpendicular to the direction of propagation of the wave undergo a succession of compressions and dilations.
- **Transverse waves (or shear waves):** the displacement of the particles is perpendicular to the direction of the wave propagation of the wave. The planes perpendicular to the direction of propagation slide relative to each other while maintaining their distance.

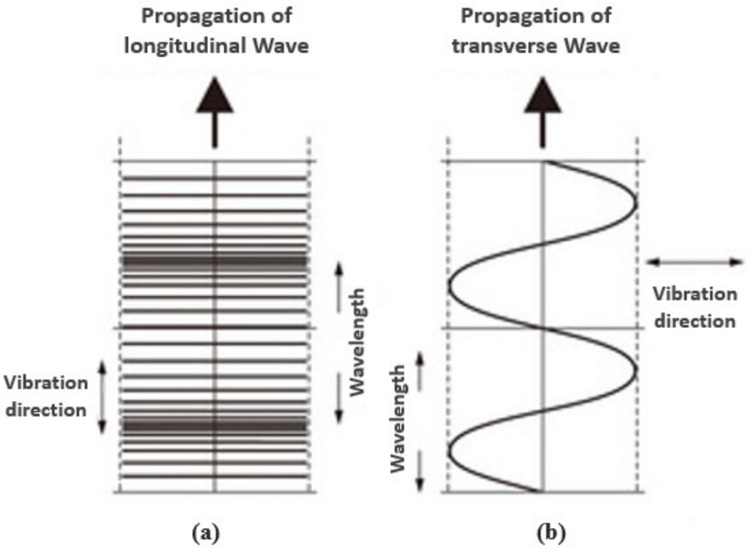

Figure 7. Longitudinal (a) and transverse (b) waves

In a gaseous environment, transducers operating in the longitudinal wave mode are appropriate, since there is not much loss of energy to the environment. However, transducers using the longitudinal wave mode are drastically affected when used for sensing in liquid phase environments. In fact, displacements normal to the surface generate compressional waves dissipating into the liquid. The resulting energy losses reduce the mass resolution substantially. In contrast, the shear mode, with a displacement parallel to the surface, allows an operation in liquids with minor damping effects due to viscous loading [119]. The excitation of shear waves requires a certain orientation of the exciting electric field with respect to the crystallographic orientation of the material.

Acoustic transducers can be classified by the type of waves generated (Figure 8) [120], [121]. If the propagation of the wave occurs through the material, it is called bulk acoustic wave (BAW). In contrast, if the wave propagates on the surface of the material where it is confined, we will observe surface acoustic waves (SAW), and if it is limited by two parallel surfaces/plates, acoustic plate waves (APM) will be generated [122].

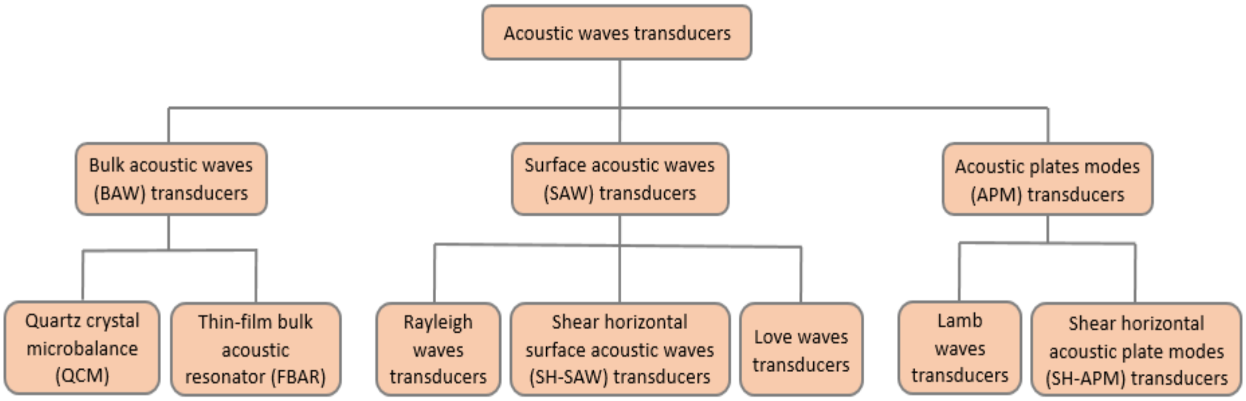

Figure 8. Classification of acoustic wave devices adapted from [120]

3.2.1 Surface acoustic wave (SAW) transducers

A SAW is an acoustic wave traveling along the surface of an elastic material, with an amplitude that decays exponentially with depth into the material. SAW transducers are components that transform an electrical signal into a surface acoustic wave, using typically an inter-digitated transducer (IDT) deposited on a piezoelectric material. When a sinusoidal voltage is applied to one of the electrodes, a strain field is generated in the piezoelectric crystal. SAW devices generally consist of a piezoelectric substrate, or a multilayer structure composed of at least one piezoelectric thin film deposited on a piezoelectric or non-piezoelectric substrate [123]. Typical substrate materials include silicon, quartz or lithium niobate ($LiNbO_3$).

The generation of SAW requires a particular configuration of the electrodes. Transducers with interdigital electrodes comprise two comb-shaped metal electrodes, usually made of gold or aluminum, deposited on the piezoelectric substrate (Figure 9). The voltage applied between two electrodes creates an electric field that generates deformations near the surface giving rise to the propagation of elastic waves. In a typical delay-line configuration, a second IDT placed at a given distance permits to sense the acoustic wave after a given time delay, explaining the name of this configuration.

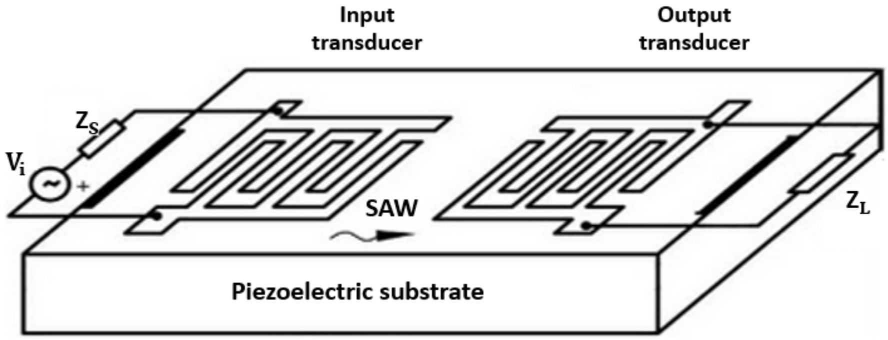

Figure 9. Basic structure of SAW device, adapted from [124]

The fact that the vibrations are localized on the surface of the device makes SAW devices more affected by the surface interactions and therefore more sensitive. This makes them widely used for detecting gases or vapors. Among SAW, we distinguish Rayleigh waves, shear horizontal surface acoustic waves (SH-SAW) and Love waves (LW).

Rayleigh transducers

Named after their discoverer, Rayleigh waves have a longitudinal component and a vertical shear component, as shown in Figure 10 (a), that can couple with a medium placed in contact with the device's surface. Rayleigh waves are mostly used in high frequency filter techniques and gas sensing (30-500 MHz), since the displacement is perpendicular to the substrate surface, which is a problem for liquid operation. Indeed, when the transducer is in contact with a liquid, the displacement component in the direction of the substrate's normal couples to the liquid, inducing energy losses and attenuation of the signal.

SH-SAW transducers

SH-SAWs have a displacement perpendicular to the propagation direction and parallel to the surface. They are horizontally polarized shear waves, generated in the range of 100-200 MHz, and adequate for sensing in liquids. Nevertheless, slight amounts of acoustic energy are lost in the bulk of the substrate, and the sensitive layer must be located on the face of the electrodes, which is not recommended for measurements in liquid medium [62].

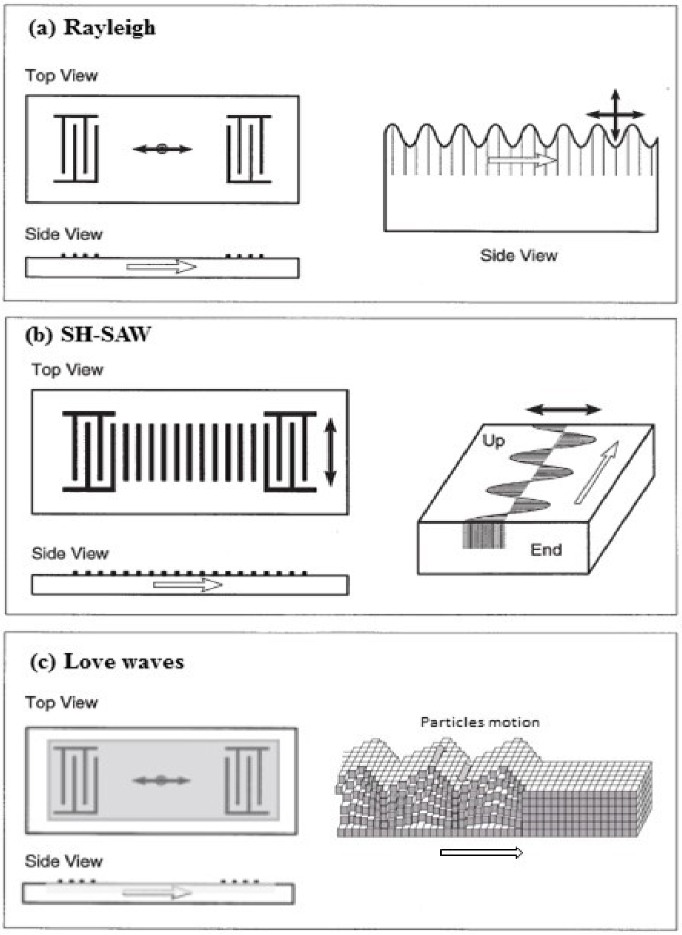

Figure 10. SAW propagation for Rayleigh waves (a), SH-SAW (b) and Love waves (c), modified from [125] (Black arrows: particle displacement, white arrows: wave propagation)

Love modes transducers

When the surface is covered by metal or amorphous SiO_2 thin films with an acoustic velocity lower than that of the substrate, LW are generated. The thin guiding layer is required to confine the surface wave and minimize the acoustic losses into the bulk of the substrate or into the liquid above the sensor surface. It also isolates the electrodes from the liquid, decoupling the electrical and fluidic interfaces [126]. LW transducers have high sensitivities and can operate in liquid medium via shear modes in the range of 100-200 MHz. Indeed, the operation in liquid environments of LW-based sensors has been profusely reported in the literature [127], [128].

3.2.2 Acoustic plates modes (APM) transducers

SH-APM transducers

Shear Horizontal Acoustic Plate Modes (SH-APM) transducers utilize a thin piezoelectric substrate or plate that serves as an acoustic waveguide, confining the energy between the upper and lower surfaces of the plate. As a result, both surfaces undergo displacement, thus, detection can occur on either side. This is an important advantage, as one side contains the IDTs that must be isolated from conducting fluids or gases, while the other side can be used for sensing. They are well suited for viscosity and bio-sensing in liquid in a frequency range going from 20 to 200 MHz, as the displacement is perpendicular to the propagation and parallel to the surface (Figure 11 (b)). However, SH-APMs have a limited sensitivity and many modes can be excited simultaneously at close frequencies [129].

Lamb waves transducers

If the substrate thickness is strongly reduced to form a membrane, APM modes become Lamb-modes, also known as guided plate waves or flexural plate wave (FPW), consisting of a longitudinal wave and a flexural wave. Lamb wave transducers are very sensitive. They operate between 5 to 20 MHz and allow real-time measurements [130]. However, they are partially attenuated in liquid medium and the membrane required for these sensors is usually very thin.

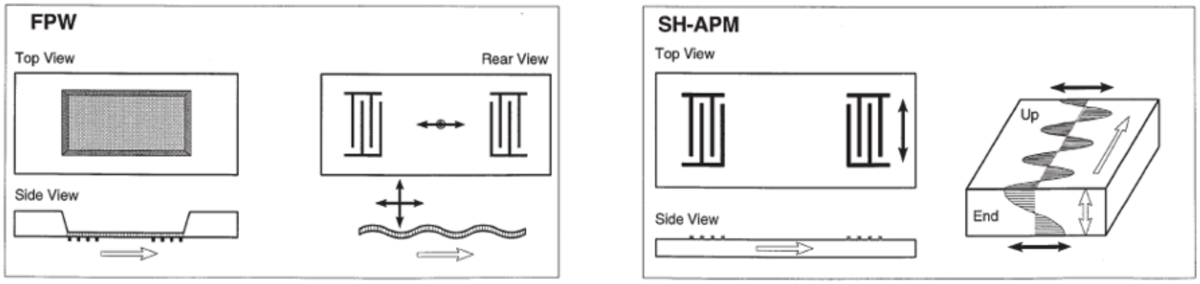

(a) (b)

Figure 11. Acoustic wave plate propagation in the case of FPW (a) and SH-APM (b), modified from [125] (Black arrows: particle displacement, white arrows: wave propagation)

3.2.3 Bulk acoustic waves (BAW) transducers

We define BAWs as the waves propagating in a homogeneous solid considered unlimited [131]. They are generated by the application of an electric potential at the resonant frequency in the range of 4 to 150 MHz.

The oldest but reference application of BAW is Quartz Crystal Microbalance (QCM). It is a piezoelectric microbalance consisting of a cylindrical quartz disk with an electrode on each of these two faces. Presented in 1959 by Sauerbrey, the initial model has been enriched by many authors to allow measurements in liquid medium and for an application as a biosensor. These devices use the piezoelectric effect of the substrate to excite and detect BAWs via electrodes deposited on the substrate (Figure 12). The retained waves operate in thickness shear modes (TSM) that allow the use in a liquid medium with a high level of sensitivity. The main advantages of QCM are the small size and ease of integration [61].

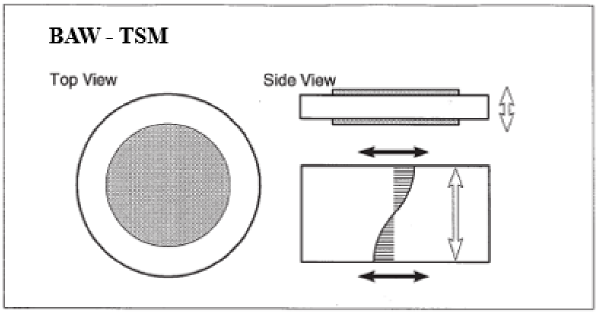

Figure 12. BAW propagation in TSM, modified from [125] (Black arrows: particle displacement, white arrows: wave propagation)

Another application is the thin-film bulk acoustic resonator (FBAR or TFBAR), which consists in a thin layer of piezoelectric material with excitation electrodes fabricated on both sides of the film (Figure 13). The acoustic waves propagate unguided through the volume of the thin piezoelectric film and the detection mechanisms occur at the opposite surfaces of the film. FBARs are popular due to their high quality factors Q that range from a few hundreds to a few thousands in air and vacuum at high frequencies (900 MHz – 1 GHz). These high Qs are achievable because FBARs create a very large acoustic impedance mismatch between the solid materials and air, thus confining the generated acoustic waves within a cavity [132].

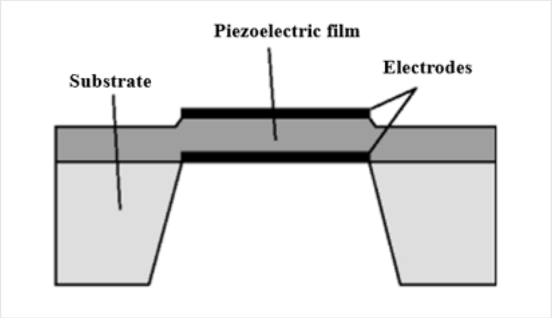

Figure 13. Example of an FBAR

To summarize, BAWs operating in TSMs have the advantage of having a fairly simple and low-cost manufacturing process, and of operating at low frequencies. Even if their sensitivity is more limited, they work perfectly in liquid medium and the electrodes (in the case of LFE) can be separated from the recognition layer. For these reasons, the proposed biosensor uses BAW in TSM. However, in order to predict its performances, an analytical study is mandatory and is presented in the next section.

3.3. Acoustic wave propagation in piezoelectric materials

A more detailed understanding of piezoelectricity is possible using the piezoelectric equations describing the coupling between electric and mechanical properties in the piezoelectric material. Displacement and stress are vectors and tensors, respectively, and the components for each can be related via the piezoelectric effect. Due to the particular structure and anisotropic behavior of the piezoelectric material, a tensor analysis is necessary. It allows to express its different physical characteristics (elasticity, permittivity, piezoelectricity) along the crystallographic axes and to establish the piezoelectric equations. These equations, presented in the following sections, were established based on references [79], [118], [133], [134].

3.3.1. Strain and Stress

During the crossing of the wave, the solid deforms (extension, shear ...) and internal stresses appear that tend to restore its initial shape. If these deformations remain below the elastic limit of the material, the deformed solid returns to its original shape as soon as the internal stresses disappear. The generalized Hooke's law translates this behavior. The stresses (T_{ij}) are therefore related to the strains (S_{kl}) by the stiffness constants c_{ijkl} specific to the material. These stiffness constants reflect the mechanical behavior of the material according to the crystallographic direction studied. The two stress and strain quantities being represented by rank 2 tensors, the tensor that connects them, called rigidity tensor, is of rank 4.

When the solid is subjected to mechanical stresses, its atoms are displaced. $u_i\,(x_i)$ represents the displacement of a point along an axis x_i (i = 1, 2, 3) with respect to its initial position. The relation between the displacement u_i and the strain S_{ij} is given by:

$$S_{ij} = \frac{1}{2}\left[\frac{\partial u_i}{\partial x_j} + \frac{\partial u_j}{\partial x_i}\right] \tag{3.1}$$

In tensorial form, Hooke's law is expressed as follows:

$$T_{ij} = c_{ijkl}\, S_{kl} \tag{3.2}$$

The indices {i,j,k,l} are taken from {1,2,3}. Similarly, the strain can be deduced from the state of the internal stresses and the compliance constants s_{ijkl} of the material:

$$S_{ij} = s_{ijkl}\, T_{kl} \tag{3.3}$$

In the previous equations, the symmetry of the tensors makes it possible to simplify the notations considerably. By adopting the Voigt notation, the tensor of rank 4 (rigidities) is reduced from 81 to 36 components, the tensor of rank 3 (piezoelectric coefficients) from 27 to 18 components and the tensors of rank 2 (strain, stress, permittivity) from 9 to 6 components. Moreover, as the tensors (T_{ij}) and (S_{kl}) are symmetrical, the elastic constants do not change during the permutation of the first two indices or the last two indices:

$$c_{ijkl} = c_{jikl} \text{ and } c_{ijkl} = c_{ijlk} \tag{3.4}$$

The simplifications of notation are obtained by replacing respectively the pairs (ij) and (kl) by an index α and β whose correspondence is given in Table 3.

Table 3. Correspondence of the indices α and β with the pairs of indexes (ij) and (kl) respectively

(ij) or (kl)	(11)	(22)	(33)	(23) or (32)	(13) or (31)	(12) or (21)
α or β	1	2	3	4	5	6

In matrix form, Hooke's law is written, after simplification, as follows:

$$\begin{bmatrix} T_1 \\ T_2 \\ T_3 \\ T_4 \\ T_5 \\ T_6 \end{bmatrix} = \begin{bmatrix} C_{11} & C_{12} & C_{13} & C_{14} & C_{15} & C_{16} \\ C_{12} & C_{22} & C_{23} & C_{24} & C_{25} & C_{26} \\ C_{13} & C_{23} & C_{33} & C_{34} & C_{35} & C_{36} \\ C_{14} & C_{24} & C_{34} & C_{44} & C_{45} & C_{46} \\ C_{15} & C_{25} & C_{35} & C_{45} & C_{55} & C_{56} \\ C_{16} & C_{26} & C_{36} & C_{46} & C_{56} & C_{66} \end{bmatrix} \begin{bmatrix} S_1 \\ S_2 \\ S_3 \\ S_4 \\ S_5 \\ S_6 \end{bmatrix} \tag{3.5}$$

Consequently, of the 36 stiffness tensor coefficients, only 21 are truly independent. Furthermore, depending on the crystalline classes considered, symmetry relations can further reduce the number of independent coefficients.

3.3.2. Tensorial expression of piezoelectricity

When the solid is exposed to electromagnetic waves, the behavior is described by the electrical boundary conditions of the solid and the Maxwell equations. Due to the high speed of electromagnetic waves compared to elastic waves in the solid (~105 times higher), we neglect these effects. Only the semi-insulating behavior of the material is taken into consideration. The electrical behavior of the material is expressed by its permittivity components ε_{ij} which link the electrical displacement D_i to the electric field E_j:

$$D_i = \varepsilon_{ij} E_j \tag{3.6}$$

E_j is the electrical field, i.e. the derivate of the electrical potential φ, which can be expressed as:

$$E_j = - \frac{\partial \varphi}{\partial x_j} \tag{3.7}$$

The preceding equations show the mechanical and electrical behavior of the structure separately. A piezoelectric solid combines these two phenomena, so we must take them into consideration simultaneously. Additional constants e_{ikl} and d_{ikl}, referred to as piezoelectric coefficients, introduced in the preceding expressions, make it possible to link the strain to the electric field or vice versa. The equations constituting a piezoelectric material are thus established as follows:

$$T_{ij} = c^{E}_{ijkl} S_{kl} - e_{kij} E_k$$

$$D_i = e_{ikl} S_{kl} + \varepsilon^{S}_{ij} E_j \quad \text{or} \quad D_i = d_{ikl} T_{kl} + \varepsilon^{T}_{ij} E_j \tag{3.8}$$

Where c^{E}_{ijkl} represents the stiffness coefficients at constant electric field, ε^{S}_{ij} and ε^{T}_{ij} represent the electrical permittivity at constant strain and stress respectively. For non-piezoelectric materials, tensors d_{ikl} and e_{ikl} are both zero, and tensors ε^{S}_{ij} and ε^{T}_{ij} are equal.

The preceding equation can therefore be expressed in the following matrix form:

$$\begin{bmatrix} T \\ D \end{bmatrix} = \begin{bmatrix} c^{E} & -e \\ e & \varepsilon^{S} \end{bmatrix} \begin{bmatrix} S \\ E \end{bmatrix} \tag{3.9}$$

Where $\begin{bmatrix} c^{E} & -e \\ e & \varepsilon^{S} \end{bmatrix}$ is the elasto-piezo-dielectric matrix, characteristic of the material.

3.3.3. Acoustic propagation and coupled wave equations

The derivation of the propagation equation of acoustic waves in an unbounded solid allows to determine the acoustic velocities and the polarization, i.e. the displacement direction, of the wave. In the absence of applied external force, the fundamental dynamic principle (Newton's law) can be written as follows:

$$\rho \frac{\partial^2 u_i}{\partial t^2} = \frac{\partial T_{ij}}{\partial x_j} \tag{3.10}$$

Where ρ is the density of the material. In the case of an insulating solid, the electrical displacement satisfies the Poisson equation:

$$\frac{\partial D_j}{\partial x_j} = 0 \tag{3.11}$$

By replacing the stress and the electrical displacement by their expressions in (3.8), and considering the formula (3.7) for the electric potential, the relations (3.10) and (3.11) become:

$$\rho \frac{\partial^2 u_i}{\partial t^2} = c_{ijkl}^{E} \frac{\partial^2 u_l}{\partial x_j \, \partial x_k} + e_{kij} \frac{\partial^2 \varphi}{\partial x_j \, \partial x_k}$$

$$e_{jkl} \frac{\partial^2 u_l}{\partial x_j \, \partial x_k} = \varepsilon_{jk}^{S} \frac{\partial^2 \varphi}{\partial x_j \, \partial x_k} \tag{3.12}$$

These partial differential equations couple the electric potential to the mechanical displacement. The solution of this system corresponds to a progressive plane wave of polarization u_i propagating in a direction indicated by the unit vector n_j at the speed V. This solution consists of the displacement and the electric potential, which can be expressed in the following form:

$$u_i = U_i \, e^{j\omega\left(t - \frac{n_j x_j}{V}\right)}$$

$$\varphi = \varphi_0 \, e^{j\omega(t - \frac{n_j x_j}{V})} \tag{3.13}$$

By substitution of the displacement and the electric potential by their expressions, the system (3.12) becomes:

$$\Gamma_{il} U_i + \Upsilon_i \varphi_0 = \rho \, V^2 U_i$$

$$\Upsilon_i U_i - \varepsilon \varphi_0 = 0 \tag{3.14}$$

Where $\Gamma_{il} = c_{ijkl}^{E} \, n_j n_k$ is the Christoffel tensor, $\Upsilon_i = e_{kij} \, n_j n_k$, and $\varepsilon = \varepsilon_{jk}^{S} \, n_j n_k$.

By eliminating the electric potential in the system (3.14), we obtain the equation of propagation of an elastic wave in a piezoelectric material called the Christoffel equation:

$$(\Gamma_{il} + \frac{\Upsilon_i \Upsilon_l}{\varepsilon}) U_l = \rho \, V^2 U_i \tag{3.15}$$

Which can also be written as:

$$\overline{\Gamma_{il}} \, U_l = \rho \, V^2 U_i \tag{3.16}$$

Where $\overline{\Gamma_{il}} = \Gamma_{il} + \frac{\gamma_i \gamma_l}{\varepsilon}$ is the stiffened Christoffel tensor.

The plane wave propagation velocities and the displacement components are determined by solving the Christoffel equation in the form of an eigenvalue problem.

For each direction of propagation, 3 velocities are determined, which correspond to the roots of:

$$\left|\Gamma_{il} - \rho V^2 \delta_{il}\right| = 0 \tag{3.17}$$

where δ_{il} is the symbol of Kronecker and V is the propagation velocity of the wave that we are looking to determine.

The corresponding eigenvectors define the polarizations of the waves u_i, which are mutually orthogonal. However, in an anisotropic medium, the polarization of the wave is not exactly perpendicular or parallel to the direction of propagation. Therefore, we define quasi-transverse and quasi-longitudinal waves. In the general case of a piezoelectric material, with propagation along an arbitrary direction, one will have coexistence of 3 plane waves with orthogonal polarization: a quasi-longitudinal wave, a rapid quasi-shear wave and a slow quasi-shear wave.

3.4. Generation of BAWs

3.4.1 Electrical excitation

The electrical excitation applied to the piezoelectric material for the acoustic waves generation can be of several types [135], [136]. As shown in Figure 14, each type of excitation requires a specific electrodes configuration.

The wave can be excited by an electric field oriented according to the thickness of the resonator, as is the case in most QCMs, referred to as thickness field excitation (TFE). In this configuration, the electrodes are placed on the two opposite sides of the piezoelectric material (Figure 14 (a)), and the electric field is oriented parallel to the thickness of the piezoelectric plate.

Lateral field excitation (LFE) is the method of interest when the transducer is used for chemical or biological sensor applications. Indeed, this configuration (Figure 14 (b)) makes it possible to separate the electrical and the fluidic interfaces of the sensor, which facilitates the electrical connections. In addition, the electrodes will not be located in the maximum displacement region, which provides better stability and a higher quality factor. Moreover, LFE enables some modes to be driven that are not available by TFE. In this work, we have chosen LFE, with electrodes placed on the opposite side of the biological capture zone.

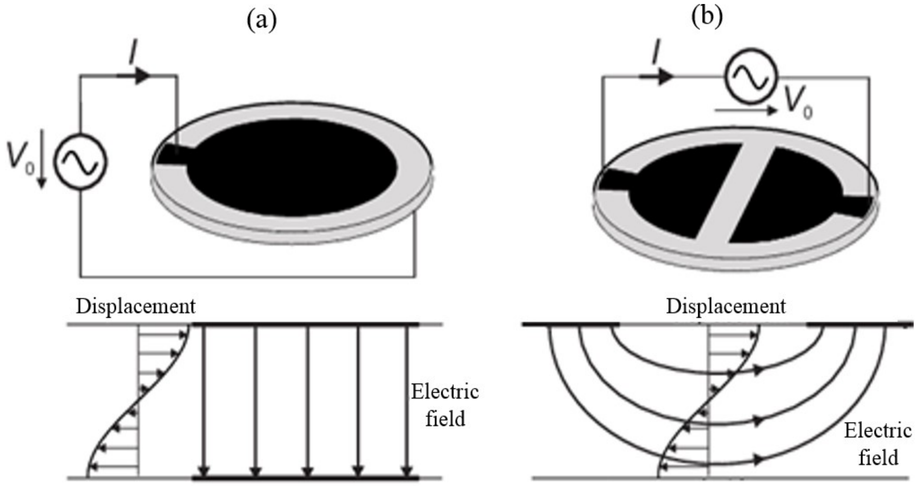

Figure 14. Thickness field excitation (a) vs. lateral field excitation (b) of waves [137]

3.4.2 Electromechanical coupling coefficient

The efficiency of the conversion process between the mechanical and electrical energies is defined by means of a coefficient called the electromechanical coupling factor k. The latter is defined as the ratio between the electromechanical energy stored in the resonator and the sum of the mechanical and electrical energies provided.

$$\mathrm{k}^2 = \frac{\text{Transformed Energy}}{\text{Provided Energy}} \tag{3.18}$$

If we consider a volume element and a transformation generating small variations of the mechanical and electrical magnitudes applied to the piezoelectric material, the energy variation δU will be the sum of the variations of the elastic (TδS) and electrical (EδD) energies:

$$\delta \mathrm{U} = \mathrm{T}\delta \mathrm{S} + \mathrm{E}\delta \mathrm{D} \tag{3.19}$$

The introduction of the fundamental relations of piezoelectricity into the expression of the variation of energy leads to the following relation:

$$\delta U = T s^E \delta T + T d\, \delta E + E d\, \delta T + E \varepsilon^T \delta E \qquad (3.20)$$

The exponents E and T above the compliance and permittivity coefficients indicate that these coefficients are given at constant electric field and stress respectively. By integrating the equation (3.20) on the whole volume, we obtain the following formulation:

$$U = \frac{1}{2} s^E T^2 + dTE + \frac{1}{2} \varepsilon^T E^2 \qquad (3.21)$$

This equation can be identified as: $U = U_E + 2U_M + U_D$, where $U_E = \frac{1}{2} s^E T^2$ is the elastic energy, $U_M = \frac{1}{2} dTE$ is the coupling energy, and $U_D = \frac{1}{2} \varepsilon^T E^2$ is the electrical energy.

The elastic and electrical energies are respectively proportional to the flexibility and the permittivity of the material whereas the coupling energy depends on the piezoelectric coefficients. The electromechanical coupling coefficient is then defined by:

$$k^2 = \frac{{U_M}^2}{U_E\, U_D} \qquad (3.22)$$

By substituting U_M, U_E and U_D by their expressions, the general formula of the electromechanical coupling coefficient becomes:

$$k^2 = \frac{d^2}{\varepsilon^T\, s^E} \qquad (3.23)$$

Note that electromechanical coupling factors are dimensionless coefficients, used for describing a piezoelectric material under a particular stress and electric field configuration for converting stored energy under mechanical or electrical action. They are mainly used to provide a useful comparison between the different piezoelectric materials for a specific wave/mode regardless of the permittivity or elasticity values.

3.4.3 Resonant frequency

In the case of TSM modes, the acoustic wave propagates in the thickness of the resonator. The resonance is obtained when a standing wave is established between the two faces of the resonator. The wavelength must have discrete values, with a maximum value equivalent to twice the thickness. The resonant frequency is therefore expressed using the following equation:

$$f_m = \frac{n\,V_m\,(1-\frac{8\,k^2}{n^2\pi^2})}{2\,h} \tag{3.24}$$

Where n is the partial rank or harmonic (n ∈ {1, 3, 5...} with n = 1 for the fundamental mode), V_m is the velocity of the wave for the mode m and h is the thickness of the resonant structure. As the value of k is relatively very small, the expression of the resonance frequency becomes:

$$f_m = \frac{n\,V_m}{2\,h} \tag{3.25}$$

3.5. Resolution of the propagation equations

In this section, we will solve the previously established equations for GaAs and ZnO separately, to determine the propagation directions and velocities of elastic waves in each material. We will determine the corresponding resonant frequency as a function of the thickness of the resonant structure, as well as the electromechanical coupling coefficient for shear modes.

3.5.1. Case of GaAs

Gallium arsenide is a blende zinc-type crystal consisting of two cubic-face-centered structures imbricated and offset by a vector a/4 according to each of the 3 crystallographic axes (a being the lattice constant). The symmetry of the crystal is of type $\bar{4}3m$ which makes it possible to simplify the tensors elastic, piezoelectric and dielectric making some of their constants equal or nil. Thus, the simplified elastic tensor is given by:

$$[c_{\alpha\beta}] = \begin{bmatrix} c_{11} & c_{12} & c_{12} & 0 & 0 & 0 \\ c_{12} & c_{11} & c_{12} & 0 & 0 & 0 \\ c_{12} & c_{12} & c_{11} & 0 & 0 & 0 \\ 0 & 0 & 0 & c_{44} & 0 & 0 \\ 0 & 0 & 0 & 0 & c_{44} & 0 \\ 0 & 0 & 0 & 0 & 0 & c_{44} \end{bmatrix} \tag{3.26}$$

Where the elasticity constants are: c_{11} = 118.8 GPa, c_{12} = 53.8 GPa, and c_{44} = 59.4 GPa [79].

The matrix of piezoelectric coefficients has only one non-zero component: $e_{14} = -0.16$ C/m^2 [138], and is written as:

$$e_{i\alpha} = \begin{bmatrix} 0 & 0 & 0 & e_{14} & 0 & 0 \\ 0 & 0 & 0 & 0 & e_{14} & 0 \\ 0 & 0 & 0 & 0 & 0 & e_{14} \end{bmatrix} \tag{3.27}$$

The dielectric matrix contains 3 non-zero dielectric constants, with a single component: ε_{11} = 9.73 x 10^{-11} F.m^{-1} [139]. It is then of the following form:

$$\varepsilon_{ij} = \begin{bmatrix} \varepsilon_{11} & 0 & 0 \\ 0 & \varepsilon_{11} & 0 \\ 0 & 0 & \varepsilon_{11} \end{bmatrix} \tag{3.28}$$

Hence, the elasto-piezo-dielectric matrix of GaAs can be written as the following:

$$\begin{bmatrix} T_1 \\ T_2 \\ T_3 \\ T_4 \\ T_5 \\ T_6 \\ D_1 \\ D_2 \\ D_3 \end{bmatrix} = \left[\begin{array}{cccccc:ccc} c_{11} & c_{12} & c_{12} & 0 & 0 & 0 & 0 & 0 & 0 \\ c_{12} & c_{11} & c_{12} & 0 & 0 & 0 & 0 & 0 & 0 \\ c_{12} & c_{12} & c_{11} & 0 & 0 & 0 & 0 & 0 & 0 \\ 0 & 0 & 0 & c_{44} & 0 & 0 & e_{14} & 0 & 0 \\ 0 & 0 & 0 & 0 & c_{44} & 0 & 0 & e_{14} & 0 \\ 0 & 0 & 0 & 0 & 0 & c_{44} & 0 & 0 & e_{14} \\ \hdashline 0 & 0 & 0 & e_{14} & 0 & 0 & \varepsilon_{11} & 0 & 0 \\ 0 & 0 & 0 & 0 & e_{14} & 0 & 0 & \varepsilon_{11} & 0 \\ 0 & 0 & 0 & 0 & 0 & e_{14} & 0 & 0 & \varepsilon_{11} \end{array}\right] \begin{bmatrix} S_1 \\ S_2 \\ S_3 \\ S_4 \\ S_5 \\ S_6 \\ E_1 \\ E_2 \\ E_3 \end{bmatrix} \tag{3.29}$$

The slowness surface represents the characteristics of propagation of the plane waves in a solid and indicates the direction of propagation of the energy. The representative surface of the slowness corresponds to the extremities of the vector: $\vec{S} = \frac{\vec{n}}{V}$

where n is the direction of propagation and V is the wave velocity. The cut of this surface by particular planes gives three outlines corresponding to the possible modes: one quasi-longitudinal and two quasi-transversals. The slowness graphs for GaAs (Figure 15) were obtained with the software “SlownessBuddy 1.4” which traces the slowness curves using the Christoffel's formulations. The dashed lines were calculated with the piezoelectricity ignored.

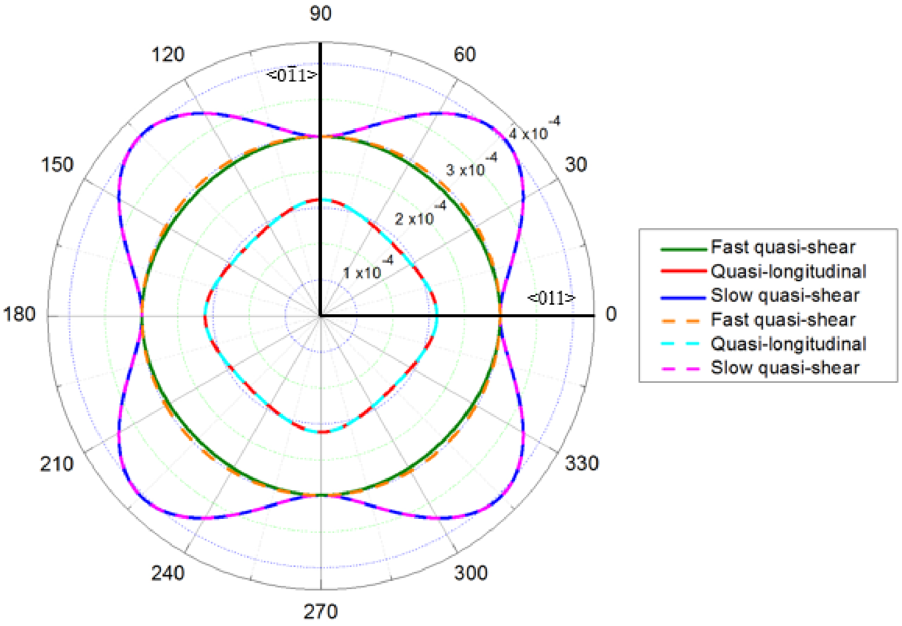

Figure 15. Slowness curves for GaAs (100) showing the two quasi-transverse shear modes (slow and fast) and the longitudinal mode; Dashed lines: piezoelectricity ignored, solid lines: piezoelectricity considered

When the piezoelectric effect is considered, the slowness surface of the slow quasi-shear mode is modified. The intersection of the slowness curves (at point A for example) with and without considering the piezoelectricity for this mode determines the orientations in which BAW can be generated. These orientations influence inevitably the electromechanical coupling coefficient k of the transducer. Therefore, in the frame of the previous thesis [7], the optimal crystalline cut for GaAs and electric field orientation were determined in order to obtain a maximum value of k. The maximum coefficient was determined using the extended Christoffel-Bechmann method [8]. To perform the calculation, the coordinate system undergoes a rotation using a transfer matrix in order to calculate the new coefficients corresponding to the directions of excitation and propagation of the wave. The membrane is considered to have infinite lateral dimensions and a finite thickness which leads to a plate model. The maximum value for k was determined for the <011> and <0$\bar{1}$1> orientations of the electric field in the crystallographic plane (100) of the GaAs. This value is equal to $k^2 = 0.43$ ($k = 0.66$) or 4.3 % for shear modes with LFE. Similar results were obtained by Söderkvist [138]. For the excitation plane (100), only the quasi-transverse modes could be excited by LFE, since the quasi-longitudinal mode has a nil electromechanical coupling coefficient in this plane.

The velocity V_b and the eigenvalue λ_b of the hardened Christoffel matrix of the quasi-transverse acoustic wave were determined using the Matlab algorithm developed for calculating the coupling coefficient:

$$\lambda_b = c_{44} + \frac{e_{24}^2}{\varepsilon_{22}} \quad \text{and} \quad V_b = \sqrt{\frac{\lambda}{\rho}} = \sqrt{\frac{c_{44} + \frac{e_{24}^2}{\varepsilon_{22}}}{\rho}} \tag{3.30}$$

By replacing the velocity and the density by their values ($V_b = 3342$ m/s, $\rho = 5.307$ g/cm^3), the resonant frequency of the GaAs structure for a rank of harmonic n can be calculated using (3.19), giving the following equation:

$$f = n\frac{1671}{h} \tag{3.31}$$

3.5.2. Case of ZnO

Due to the numerous symmetries of the würtzite structure of ZnO, the stiffness constants, the piezoelectric coefficients and the dielectric permittivity have a large number of zero or equal values. Due to these symmetries, the matrix of rigidities has only 12 non-zero constants of which 5 are different: c_{11}, c_{12}, c_{13}, c_{33} and c_{44}. The values of the parameters c_{ij} determined by Bateman in 1962 are compiled in Table 4.

Table 4. Values in GPa of the stiffness constants of the ZnO [140]

c_{11}	c_{12}	c_{13}	c_{33}	c_{44}
209.7	121.1	105.1	210.9	42.5

The matrix of rigidities is then written in the crystallographic axes in the following form:

$$[c_{\alpha\beta}] = \begin{bmatrix} c_{11} & c_{12} & c_{13} & 0 & 0 & 0 \\ c_{12} & c_{11} & c_{13} & 0 & 0 & 0 \\ c_{13} & c_{13} & c_{33} & 0 & 0 & 0 \\ 0 & 0 & 0 & c_{44} & 0 & 0 \\ 0 & 0 & 0 & 0 & c_{44} & 0 \\ 0 & 0 & 0 & 0 & 0 & \frac{c_{11}-c_{12}}{2} \end{bmatrix} \tag{3.32}$$

The matrix of piezoelectric coefficients has 3 non-zero components: $e_{15} = -0.45$ C/m^2; $e_{31} = -0.51$ C/m^2; $e_{33} = 1.22$ C/m^2, and is written as:

$$e_{i\alpha} = \begin{bmatrix} 0 & 0 & 0 & 0 & e_{15} & 0 \\ 0 & 0 & 0 & e_{15} & 0 & 0 \\ e_{31} & e_{31} & e_{33} & 0 & 0 & 0 \end{bmatrix} \tag{3.33}$$

The dielectric matrix contains 3 non-zero dielectric constants: $\varepsilon_{11} = 7.38 \times 10^{-11}$ F.m^{-1} and $\varepsilon_{33} = 7.83 \times 10^{-11}$ F.m^{-1}. It is then of the following form:

$$\varepsilon_{ij} = \begin{bmatrix} \varepsilon_{11} & 0 & 0 \\ 0 & \varepsilon_{11} & 0 \\ 0 & 0 & \varepsilon_{33} \end{bmatrix} \tag{3.34}$$

The elasto-piezo-dielectric matrix, characteristic of ZnO material, is given as follows:

$$\begin{bmatrix} T_1 \\ T_2 \\ T_3 \\ T_4 \\ T_5 \\ T_6 \\ \hline D_1 \\ D_2 \\ D_3 \end{bmatrix} = \left[\begin{array}{cccccc|ccc} c_{11} & c_{12} & c_{13} & 0 & 0 & 0 & 0 & 0 & -e_{31} \\ c_{12} & c_{11} & c_{13} & 0 & 0 & 0 & 0 & 0 & -e_{31} \\ c_{13} & c_{13} & c_{33} & 0 & 0 & 0 & 0 & 0 & -e_{33} \\ 0 & 0 & 0 & c_{44} & 0 & 0 & 0 & -e_{15} & 0 \\ 0 & 0 & 0 & 0 & c_{44} & 0 & -e_{15} & 0 & 0 \\ 0 & 0 & 0 & 0 & 0 & (c_{11}-c_{12})/2 & 0 & 0 & 0 \\ \hline 0 & 0 & 0 & 0 & e_{15} & 0 & \varepsilon_{11} & 0 & 0 \\ 0 & 0 & 0 & e_{15} & 0 & 0 & 0 & \varepsilon_{11} & 0 \\ e_{31} & e_{31} & e_{31} & 0 & 0 & 0 & 0 & 0 & \varepsilon_{33} \end{array}\right] \begin{bmatrix} S_1 \\ S_2 \\ S_3 \\ S_4 \\ S_5 \\ S_6 \\ \hline E_1 \\ E_2 \\ E_3 \end{bmatrix} \tag{3.35}$$

A thin film of hexagonal ZnO can generally excite both longitudinal and shear waves. Figure 16 shows the slowness curves of ZnO, representing the two quasi-transverse shear modes (slow and fast) and the longitudinal mode. The dashed lines correspond to the slowness calculated with the piezoelectricity ignored. It can be seen from the surface of the slowness that when the piezoelectric effect is taken in consideration, the slowness of the slow and fast quasi-shear modes is modified. The intersection of these slowness curves with and without piezoelectricity considered at certain angles/orientations indicates that the TSM of BAW can be generated in these orientations.

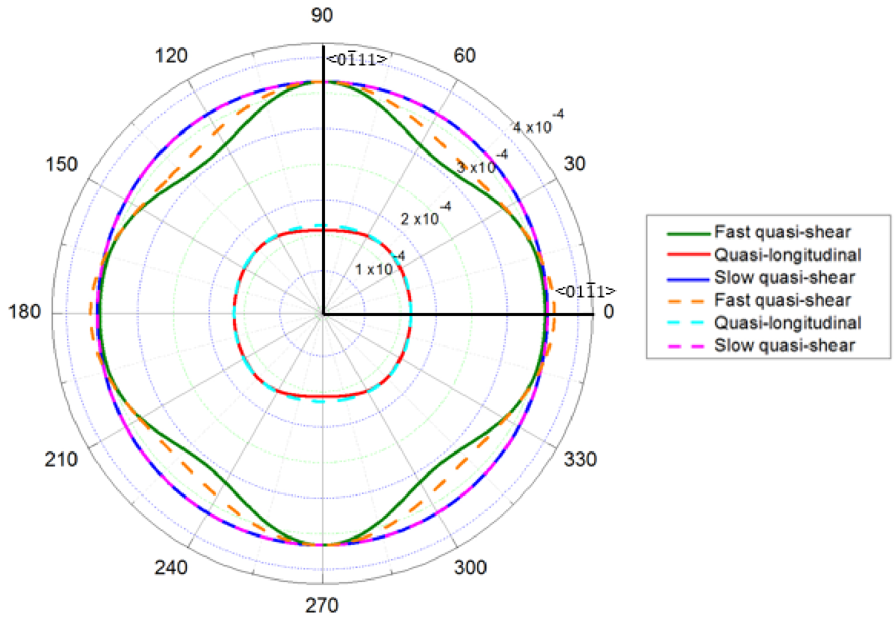

Figure 16. Slowness curves in the sagittal plane (XZ) of ZnO; Dashed lines: piezoelectricity ignored, solid lines: piezoelectricity considered

For lateral field excitation of the c-axis-oriented ZnO, we desire the electric excitation field to be orthogonal to the wave propagation. Consequently, if the wave propagation is in the direction of the Z-axis, the electric field will be in the XY plane. In this section, we will describe the coupling and the acoustic wave propagation in the general case of an electric field along any direction in the XY plane.

The normalized electric field vector m_j is of the form: $m_j = \begin{bmatrix} m_x \\ m_y \\ m_z \end{bmatrix}$

For solving the piezoelectrically stiffened Christoffel equation for laterally excited ZnO, we set: $m_z = 0$ and $m_x^2 + m_y^2 = 1$.

The resulting Christoffel matrix is of the following form:

$$\Gamma = \begin{bmatrix} c_{44} + e_{15} m_x^2/\varepsilon_{11} & e_{15}^2\, m_x m_y/\varepsilon_{11} & 0 \\ e_{15}^2\, m_x m_y/\varepsilon_{11} & c_{44} + e_{15} m_y^2/\varepsilon_{11} & 0 \\ 0 & 0 & c_{33} \end{bmatrix} \tag{3.36}$$

The eigenvalues of this matrix correspond to terms that can be used to solve for the acoustic velocity in each of the three wave propagation modes, while the corresponding eigenvectors relate to the direction of particle displacement. Solving for the eigenvectors U_i and eigenvalues λ_i of Γ (where the index i represents the mode) gives:

$$U_1 = \begin{bmatrix} -m_y \\ m_x \\ 0 \end{bmatrix}, \ \lambda_1 = c_{44}$$

$$U_2 = \begin{bmatrix} m_x \\ m_y \\ 0 \end{bmatrix}, \lambda_2 = c_{44} + \frac{e_{15}^2}{\varepsilon_{11}}$$

$$U_3 = \begin{bmatrix} 0 \\ 0 \\ 1 \end{bmatrix}, \lambda_3 = c_{33}$$

From these results, we find that only one mode is piezoelectrically excited (defined by U_2 and λ_2) and that the particle displacement will be directly aligned with the electric field, regardless of the orientation of the field with respect to the XY plane. This mode is a pure shear thickness mode and it is the mode that we are looking for. Another pure shear mode exists (defined by U_1 and λ_1) with particle displacement also in the XY plane at an angle perpendicular to that of the piezoelectrically excited mode, but it is piezoelectrically inactive. The longitudinal mode (defined by U_3 and λ_3) is also piezoelectrically inactive. Hence, an electric field in the XY plane will excite a pure TSM with particle displacement aligned with the electric field. The acoustic velocity V_2 for the shear mode can be calculated using:

$$V_2 = \sqrt{\frac{\lambda_2}{\rho}} = \sqrt{\frac{c_{44} + \frac{e_{15}^2}{\varepsilon_{11}}}{\rho}} \tag{3.37}$$

Using bulk values for ZnO [131], the theoretical acoustic velocity for the piezoelectrically stiffened thickness shear mode is approximately 2840 m/s.

The resonant frequency relationship for our resonator is therefore obtained by substituting V_2 by its value in (3.18):

$$f_s = \frac{1420\ n}{h} \tag{3.38}$$

The electromechanical coupling coefficient for this mode is then determined as:

$$k^2 = \frac{e_{15}^2}{c_{44}\,\varepsilon_{11}} \tag{3.39}$$

Which is calculated to be approximately 0.064 or 6.4 % in the case of the thickness shear mode.

By comparing the electromechanical coupling coefficient for ZnO (6.4 %) and GaAs (4.3 %), the potential of ZnO to improve the performances of the transducer is obvious.

The determined expressions and values for TSM relate to either transducers made entirely of GaAs or ZnO. However, the transducer proposed in this thesis combines the two materials. Therefore, we need to take into consideration the coupling between them, which will surely affect the resonance characteristics of the transducer. Thus, modeling of the transducer was also done using Finite Element Method (FEM) and is presented in the next section.

3.6. Modeling of the transducer using FEM

To study the performances of the piezoelectric structure, a modal analysis is required to extract the eigenfrequencies that will make it possible to identify the different modes. Therefore, a model using FEM was developed to dimension the resonant structure. The modeling was performed using COMSOL Multiphysics® finite element simulation software. The model was built using the physics "piezoelectric devices" of the "structural mechanics" module. Eigenfrequency analysis and frequency domain were the two studies used in this work. The geometric parameters introduced into the model are shown in Figure 17. For this model, we chose a membrane thickness of 200 µm corresponding to the thickness of the membrane that would make it easy to handle and not too fragile.

The set of domains created have been assigned to the GaAs and ZnO materials. The elasticity and permittivity matrices, the stiffness constants and the density of each material were adjusted in the parameters section. We did not introduce a layer of chromium or gold because of their negligible thickness (respectively 5-20 nm and 150-200 nm), and hence bending stiffness and added mass compared to that of the membrane. Two rectangular zones, of size 4 mm x 1.3 mm, were built on top of the structure to add the ground and the terminal (10 V) excitation. The geometric gap separating them is 1 mm.

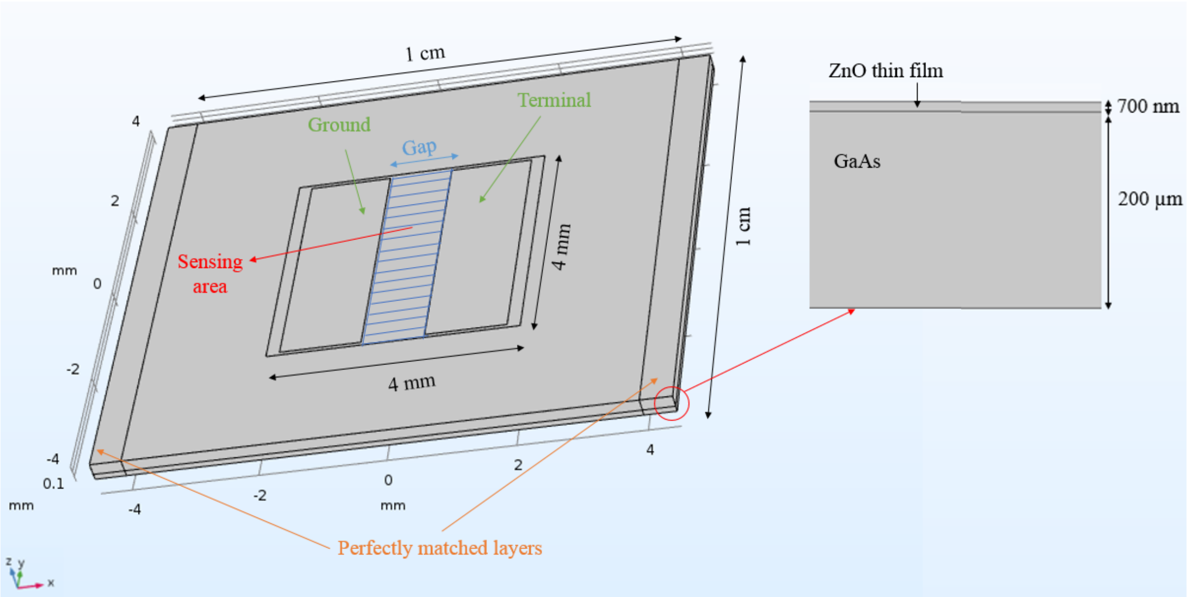

Figure 17. Geometry of the COMSOL® simulation model representing the different domains of the structure

Perfectly matched layers (PML) were added in the recessed ends of the structure. These PML domains are used to simulate the effect of propagation and absorption of elastic waves in these regions (which are not solved in real dimensions). We chose a customized free tetrahedral mesh on the plane of the membrane and the structure was divided into 8 layers to observe the evolution of the electric field locally (Figure 18).

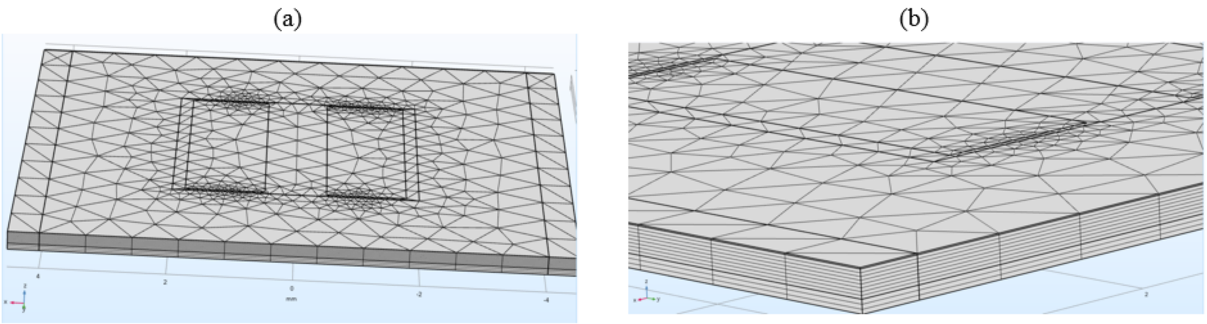
(a) (b)

Figure 18. Representation of the generated mesh in the different layers of the structure

3.6.1. Resonance characteristics of GaAs membrane with and without ZnO film

The simulations of the transducer were conducted in air at room temperature. We were able to determine the resonant frequency of the thickness shear mode at the fundamental rank, as well as its harmonics. Moreover, the material displacements in the structure along the Y-axis with and without the ZnO layer were determined for the fundamental modes (Figure 19).

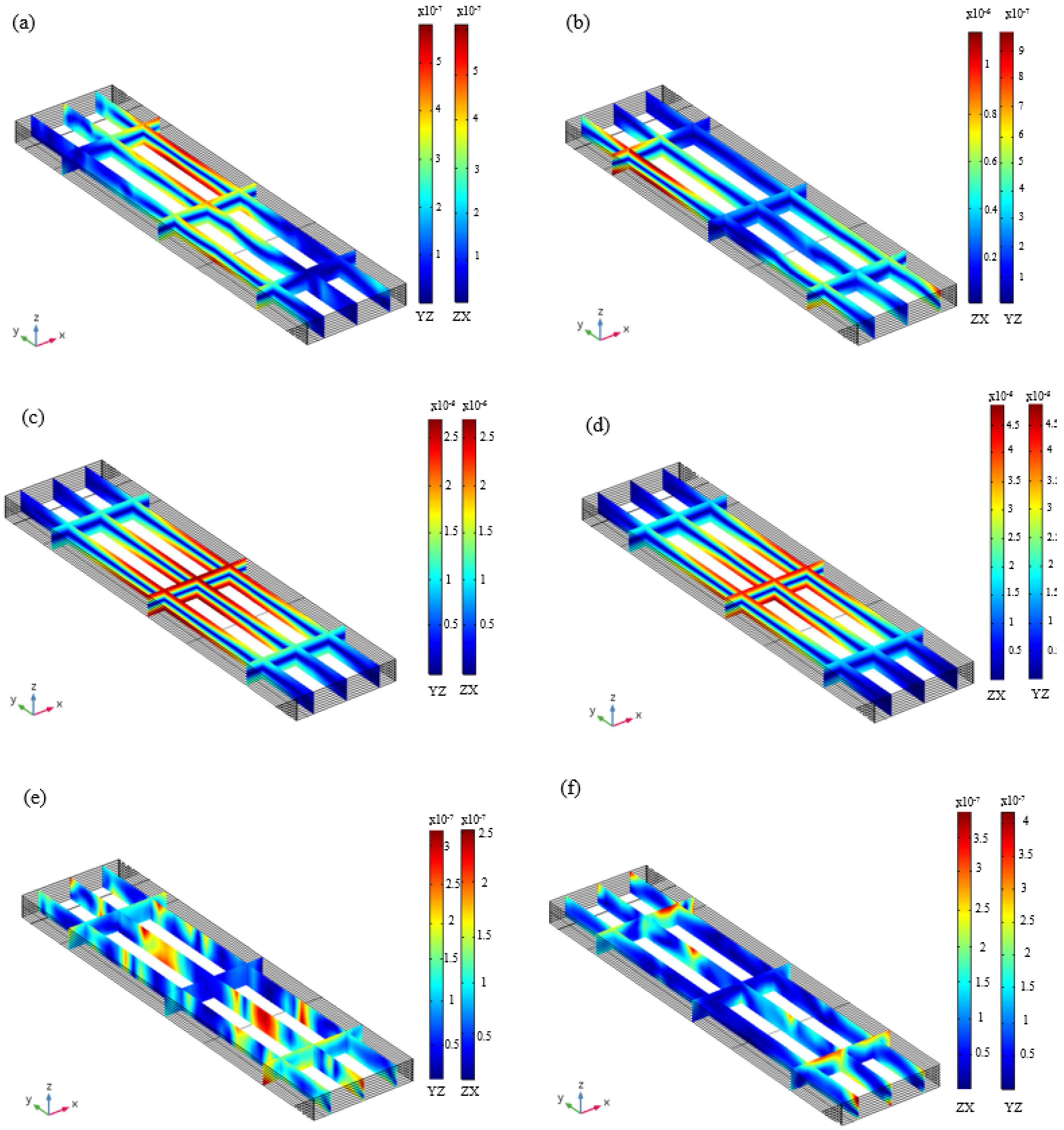

Figure 19. Sectional view of the material displacement in the sensing area along the X-, Y- & Z-axis for: GaAs at 7.9872 MHz (a), (c), (e); ZnO/GaAs at 7.9436 MHz (b), (d), (f) respectively

The material displacement along the Y-axis (Figure 19) confirms the propagation of shear mode in the structure. The displacement root mean square (RMS) as a function of the frequency was obtained by this simulation as well. It can be seen from these results that a higher displacement is obtained in the ZnO/GaAs structure, indicating a potential improvement of the performances of the transducer by addition of the ZnO film.

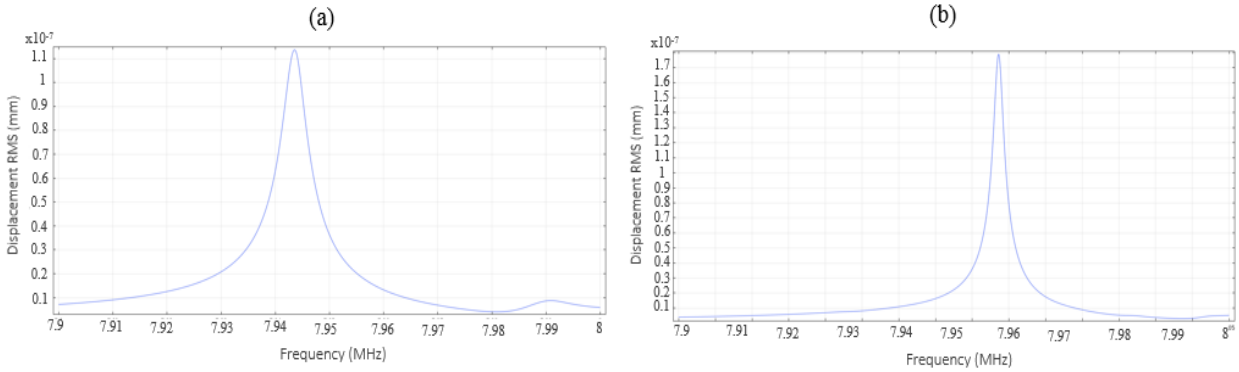

Figure 20. Displacement RMS for (a) GaAs at 7.9872 MHz and (b) ZnO/GaAs at 7.9436 MHz

To assess the correspondence between the analytical resonant frequencies and the ones determined by the FEM model, we calculated the analytical resonant frequencies of TSM for a 200 μm thick membrane made entirely of GaAs or ZnO using the equations (3.31) and (3.38) respectively. The analytical resonant frequency for the fundamental mode of GaAs is 8.35 MHz, compared to 7.987 MHz determined by FEM. This difference of 9.5 % between the two values for GaAs is due to the fact that Comsol software takes in consideration the damping, which results in a lower resonant frequency. Moreover, the analytical resonant frequency of the fundamental mode for a ZnO membrane was found at 7.1 MHz. On the other hand, the frequency of tthe ZnO/GaAs structure obtained by FEM was 7.944 MHz, which is a value comprised between the resonant frequencies of pure ZnO and pure GaAs. The electrical characterization of the device will allow the comparison of this theoretical value with the experimental one to assess the accuracy of our model.

3.6.2. Modeling of the electrodes configuration

To compare the electric field in the GaAs and ZnO/GaAs structures, and to determine the optimal inter-electrode distance, we used the previous model to examine the electrical field while varying the gap between the electrodes. Figure 21 shows the electrical displacement field in the GaAs membrane with and without the ZnO film. The values for the two structures are comparable, with more confinement in the presence of ZnO.

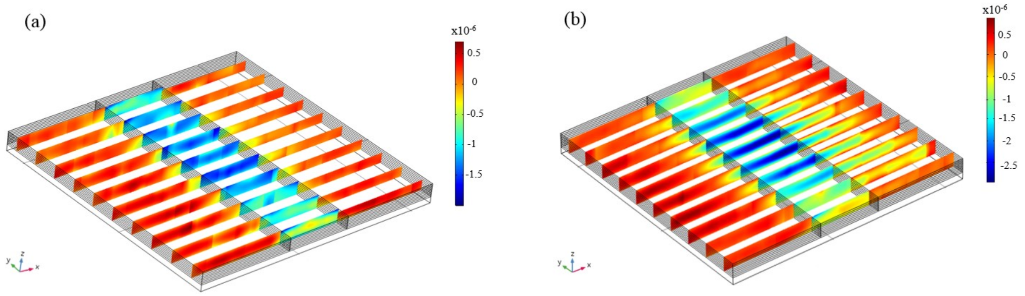

Figure 21. Electrical displacement field in the ZX plane of the GaAs (a) and ZnO/GaAs (b) structures

The simulation of the electric field observed along the X, Y and Z- axis in the ZX plane of the ZnO/GaAs structure shows a displacement along the X-axis, with a minor component along the Z-axis, as displayed in Figure 22.

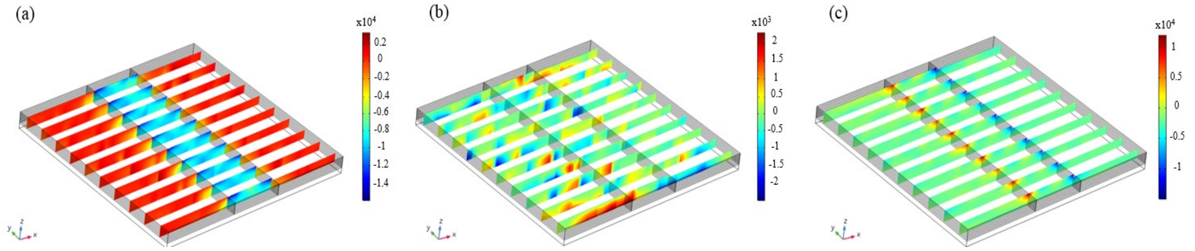

Figure 22. Electrical displacement along the X- (a), Y- (b) and Z- (c) axis observed in the ZX plane of the ZnO/GaAs structure with a gap of 1 mm

On the other hand, In order to determine the optimal inter-electrode distance, we performed simulation while changing the gap between the electrodes from 100 µm to 1 mm. The voltage supply was the same for each configuration. Figure 23 shows the electrical displacement for different gaps, for the ZnO/GaAs structure. It can be seen that the lowest electrical displacement is observed for the 1 mm gap while the highest was determined for 200 µm. The 500 µm seems to be a reasonable compromise, since the penetration of the electrical field is homogeneous. The field value is optimal at the detection surface, which would result in higher sensitivity for measurements in liquid environments.

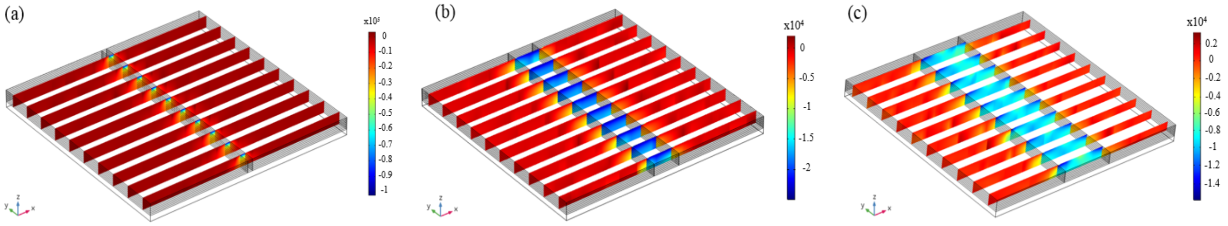

Figure 23. Electrical displacement in the ZnO/GaAs structure for different gaps (a) 200 µm, (b) 500 µm, (c) 1 mm

3.7. Conclusion

Through this chapter, we first laid out the physical fundamentals of bulk elastic waves in a piezoelectric solid. In particular, we have presented the theoretical principles of thickness shear waves transducers. After a preamble on the developed analytical models for both materials used in this work (GaAs and ZnO), a numerical FEM model was built to simulate the resonator in normal operation. The results obtained with this modelling allowed us to determine the resonant frequency for TSM and the displacement along the different axis of the GaAs and ZnO/GaAs structures. Moreover, we examined the electrical field displacement for different inter-electrode distances for the ZnO/GaAs transducer, and 500 µm was shown to be an optimal configuration to limit the penetration of the electrical field in the structure, especially in the case of measurement in liquid medium.

Chapter 4: Microfabrication of ZnO/GaAs transducer

4.1 Microfabrication strategy

The manufacture of the devices is conducted in the MIMENTO (MIcrofabrication pour la MEcanique, les Nanosciences, la Thermique et l'Optique) technology center of the Renatech network, attached to our laboratory, in Besançon - France. The microfabrication procedure is carried out in two main phases: the realization of the electrical contacts on the top side of the GaAs substrate, and the micromachining of the membrane on its bottom side. For this, both sides of GaAs wafers are used during the microfabrication.

The first step of the fabrication process is the deposition of ZnO thin film on the top face of the GaAs substrate. If this step was done after the micromachining of the membrane, the deposition-taking place at high temperature (up to 450 °C) could generate thermal stresses in the membrane, which would fragilize it. Taking into consideration the low thickness of the GaAs membrane (down to 50 µm), the latter can easily break during the deposition.

In order to improve the performance of the GaAs-based transducer, the deposited ZnO films must be of high crystalline quality. Therefore, a complete and systematic characterization is necessary to validate the following requirements:

- Orientation along the c-axis
- Strong texture & low residual stress
- Low surface roughness
- Sharp interfaces
- Ohmic contact

Moreover, several GaAs cuts are used to determine the substrate orientation that promotes the deposition of highly textured piezoelectric ZnO films. A new Pt-based buffer layer is also tested to promote the growth and the quality of ZnO films on GaAs substrates.

The second step is to produce the metallic contacts consisting of a chromium bonding layer and a gold layer, sputtered onto the ZnO film using a lift-off process. These electrodes will be used subsequently to connect the device to a network analyzer to follow its frequency response.

Afterwards, a thinning stage of the substrate is necessary to increase the sensitivity of the transducer. Indeed, the starting thickness of GaAs wafers (625 ± 25 µm) is significantly greater than 50 µm, desired for the operation of the BAW sensor. The initial thinning allows to decrease the membrane micromachining time and therefore prevents the possible defects and under-etching linked with long etching processes. The main dimension of our sensor is its thickness because this parameter will determine the resonant frequency. Indeed, the variation in the frequency f_r as a function of the thickness h is expressed by:

$$\frac{\Delta f}{f} = -\frac{\Delta h}{h} \tag{4.1}$$

However, the mass is related to the thickness by the following equation:

$$m = \rho A h \tag{4.2}$$

Where A is the piezoelectrically active surface, ρ the density and h the membrane thickness.

Therefore, the variation of the thickness can be expressed by a variation of mass. Nevertheless, if a change in the absolute value of the thickness can be compensated by working at a different frequency, the thickness variations (non-homogeneity), roughness or defects on the membrane surface will generate a strong damping of the acoustic waves and cause a significant reduction in the quality factor of the resonator. It is therefore necessary to master the etching conditions in order to control the flatness of the membrane surface and avoid defects.

The basic process requires two different masks: a first one for the electrodes and a second one containing the membrane patterns. Alignment marks present on both masks make it possible to align the membrane and electrodes patterns present on opposite faces of the wafer. For the whole process, we have selected low-cost production techniques (particularly wet chemical etching) in order to obtain an economically interesting and industrially transferable device.

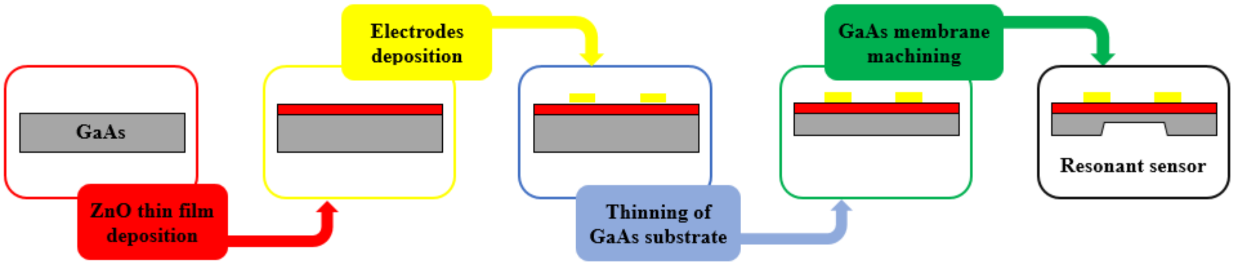

Figure 24. Diagram representing the microfabrication stages of the transducer

In this chapter, the different manufacturing stages of the device will be detailed. In particular, we will exploit the deposition and characterization of ZnO thin films on GaAs.

4.2 Deposition of ZnO thin films on GaAs substrates

4.2.1 Selection of the deposition technique

ZnO thin films can be deposited using a large variety of techniques due to the diversity of its applications [84]. To obtain device quality films with piezoelectric responses comparable to ZnO monocrystal, the selection of the deposition technique involves the following criteria:

- Crystalline quality, texture and orientation
- Adhesion to the substrate and stresses
- Purity, stoichiometry
- Deposition rate and reproducibility

Different methods have been reported for the deposition of ZnO films. They can be obtained by operating in liquid or in vapor phase, and by physical or chemical methods [141]. In liquid phase, the most frequent techniques are the sol-gel process and the electrolytic deposition. In vapor phase, chemical deposition (CVD) and physical deposition (PVD) methods are distinguished. In this section, we present and compare the most commonly used techniques for depositing ZnO thin films (Table 5), while reserving a more in-depth description to RF magnetron sputtering, a technique chosen for this work.

Table 5. Comparison of the commonly used deposition methods for ZnO thin films

	Deposition technique	Advantage	Disadvantage	Source
Liquid phase deposition	Sol-gel process	-High purity and stoichiometry -Fast process (few minutes)	Need of heat treatment to densify the deposited material and eliminate the organic solvents used in the preparation of precursor solutions	[142], [143]
	Electrolytic deposition	Control over the properties and morphology		[144], [145]
Chemical vapor phase deposition (CVD)	Spray pyrolysis	-Simplicity and reproducibility -Uniform and high-quality films		[146], [147]

	Metal-Organic Chemical Vapour Deposition (MOCVD)	-Good reproducibility -High quality films	-Contamination of layers by the metal-organic compounds -Low deposition rate (0.2 to few nm/s)	[112], [148], [149]
	Atomic layer deposition (ALD)	-Crystallization of films without annealing -Control of the composition during deposition - Uniform thickness and composition -Good adhesion	-Contamination by residues of precursors -High reaction temperature	[150], [151]
Physical vapor phase deposition (PVD)	Evaporation	-High purity -Temperature control and low pressure	-Low adhesion -Dissociation of the oxides -Defects, dislocations -Decomposition or micro-explosions of the materials to be evaporated.	[152], [153]
	Pulsed laser deposition (PLD)	-High quality of films grown at relatively low substrate temperatures (200 - 800 °C)	-High atoms energy inducing high stresses -Low deposition rate (0.1 - 0.4 nm/s)	[116], [154]
	RF magnetron sputtering	-Control of the preferred crystalline orientation -Good adhesion to the substrate -High density and texture	Low deposition rate (few nm/min)	[97], [99], [155]

The CVD deposition methods consist of decomposing on a substrate a precursor containing the elements to be deposited. The substrate being heated to several hundred degrees Celsius, the growth conditions of the layer are close to thermodynamic equilibrium. The main advantages of these techniques are the crystallization of films without any annealing treatment, the control of the composition during the deposition, and the production of a deposit of uniform thickness and good adhesion. However, these techniques have the disadvantage of giving films contaminated by incorporating by the precursor residues into the layers which is incompatible with the crystalline quality and chemical purity required for piezoelectric application.

On the other hand, PVD processes make it possible to synthesize ZnO films with high crystalline quality. PVD processes mainly include evaporation, laser ablation and sputtering in all its forms. The deposition process goes through three main steps: the creation of the species to be deposited in the form of atoms, molecules or clusters, the transport of these species in the vapor phase from the source to the substrate and finally the deposition on the substrate and the growth of the layer. Among these techniques, we have selected a sputtering technique allowing the deposition of highly c-axis oriented films ZnO thin films reproducibly.

According to the literature, this technique has received a great interest over the last years because of the easy control for the preferred crystalline orientation, the good interfacial adhesion to the substrate and the high texture and density of the grown films [155]–[157].

These properties are mainly due to the kinetic energy of the clusters given by the electric field. This energy enhances the surface migration effect and surface bonding state. The basic principle of sputtering is to bombard a target, which is introduced into a vacuum chamber. This target is fixed on a cooled electrode (cathode) and is bombarded using a neutral gas, generally Argon, in order to sputter the atoms from the target. These sputtered atoms will then be deposited on the substrate which acts as an anode.

According to the nature of the voltage applied between the two electrodes (target and substrate) and the geometrical configuration, the following modes can be distinguished, and some of them may be combined:

- Direct current (DC) sputtering, where a direct current is applied.
- Radio Frequency (RF) sputtering, for which a radio frequency voltage is applied, which makes it possible to spray insulators.
- Magnetron process, for which permanent magnets distributed around the chamber make it possible to create a magnetic confinement of the plasma and to increase the ionization efficiency of the electrons [158]. The ionized gas is usually an inert gas such as Ar for a non-reactive sputtering deposition, or a gas mixture (Ar + O_2) for a reactive sputtering deposition. Ar acts as the sputtering enhancing gas and O_2 serves as the reactive gas.

The growth of ZnO films by sputtering is usually carried out from a high-purity ZnO target using a reactive RF magnetron sputtering system (Figure 25), in the growth ambient with O_2/Ar ratios ranging from 0 to 1.

As compared to other deposition techniques, reactive RF magnetron sputtering has been a preferred method because of its simplicity, reproducibility, low operating temperature and stresses in the films. Despite the low deposition rates, it provides highly textured films with high crystalline quality and orientation, thickness uniformity and high density. Therefore, this technique is privileged in our work.

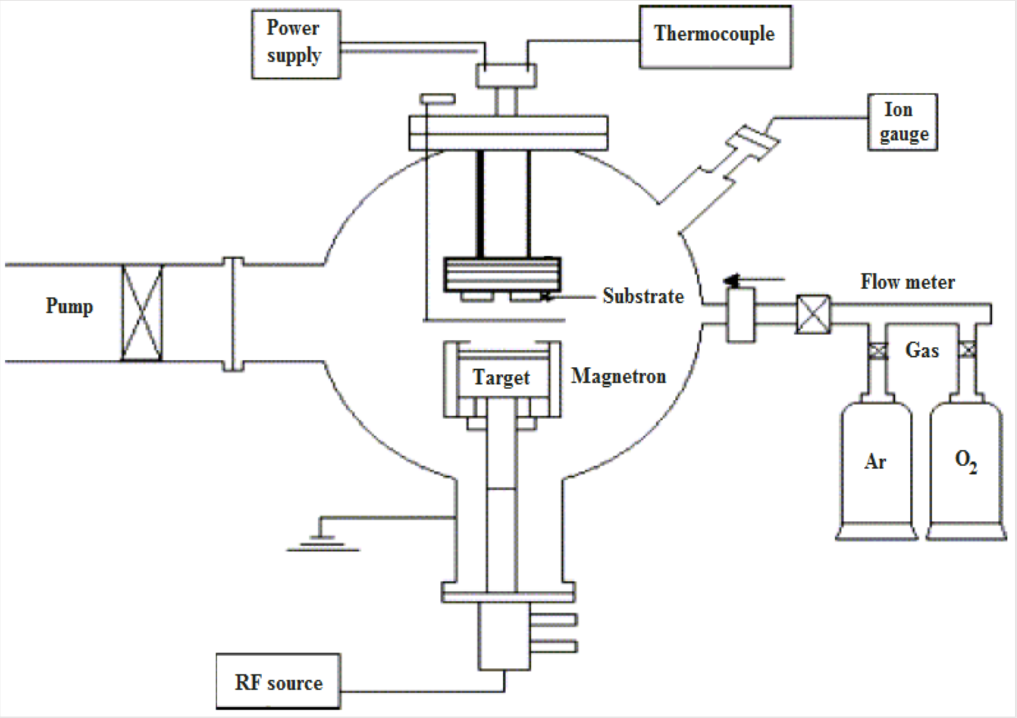

Figure 25. Schematic of an RF magnetron sputtering setup, modified from [159]

4.2.2 Preparation of GaAs substrates

GaAs is generally provided in wafers of 2, 3- or 4-inches diameter (about 50, 75 or 100 mm respectively) and thicknesses ranging from 350 µm (2 ") to 625 µm (3 ") or 635 µm (4 ").

The wafers are usually cut from an ingot in a specific crystalline direction. Therefore, the surface of the wafer corresponds to a particular crystalline plane. The orientation in the plane of the wafer is provided by one or two flats located on the contour.

In order to investigate the effect of the crystallographic orientation of the substrate on the structural and topographic properties of the grown ZnO films, GaAs substrates with different crystallographic cuts (100), (110), (111) A and (111) B were used, where A and B stand for Ga and As terminated surfaces respectively.

The two faces of the oriented wafers (111) do not have the same atomic composition:

- a face consisting solely of gallium atoms, referred to as (111) Ga or (111) A;
- a face consisting only of arsenic atoms, with the notation (111) As or (111) B.

The substrates used were commercial undoped semi-insulating GaAs wafers (AXT, Inc.) of thickness 625 ± 25 μm (double-side polished) or 500 ± 25 μm (single-side polished), a diameter of 76.2 ± 0.4 mm (3 inches) and a resistivity > 10^7 Ω.cm.

In order to remove any mineral or organic impurity present at the surface of the substrate, the wafers were successively immersed in acetone and ethanol baths for 5 minutes under ultrasound (US) at a frequency of 45 kHz and the power set on low. Then, prior to deposition, the substrates were cleaned under a plasma of argon and oxygen for 2 minutes to remove contaminants. The parameters are provided in Table 6.

Table 6. Tools and parameters used for the preparation of GaAs substrates prior to ZnO films deposition

Phase	Step	Tools	Parameters	Microstructure
Preparation of GaAs substrates	Removal of organic and mineral impurities	Acetone Ethanol	Duration: 5 min for each bath under US	GaAs
	Cleaning	Plasma of Argon and Oxygen	Power: 22 W Duration: 2 min	

4.2.3 Deposition conditions

Two sets of depositions were carried out for each substrate cut: the first is performed directly on GaAs substrates, and the second is done using a Pt buffer layer. The latter consisted of a Ti or Ta adhesion layer of thickness 15 nm, and a 150 nm thick Pt metallic layer, both deposited using cathodic sputtering. The ZnO films were deposited in collaboration with A. Bartasyte, by reactive RF magnetron sputtering (Plassys MP450S) using metallic zinc target. Prior to the deposition, the target was presputtered for 2 minutes to remove contaminants. The target-substrate distance was 54 mm. The substrate temperature and the chamber pressure were set to 450 °C and 4 mTorr, respectively. The O_2/Ar gas ratio was 1.5, providing a deposition rate of approximately 2.77 nm/min.

Table 7. Tools and parameters used for the deposition of ZnO thin films on GaAs substrates

Phase	**Step**	**Tools**	**Parameters**	**Microstructure**
ZnO thin film deposition	Presputtering of the target	Plasma of Argon and Oxygen	-Flow of O_2: 10 sccm -Flow of Argon: 10 sccm -Power: 100 W -Duration: 2 min	
	Sputtering of ZnO	-Plassys (MP450S) -6” Zinc target	-Flow of O_2: 1.5 sccm -Flow of Argon: 1 sccm -Temperature: 450 °C -Pressure: 4 mTorr -Power: 100 W -Rate: 2.77 nm/min	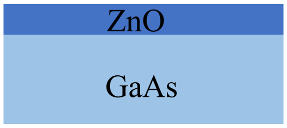

4.3 Characterization of ZnO films

Different complementary characterization techniques were used to evaluate the quality of the deposited ZnO layers. These characterizations aimed to determine the GaAs cut providing the best quality ZnO films, and to determine if the choice of the Pt buffer layer was convenient for promoting the growth of ZnO films on GaAs. X-ray diffraction (XRD) and Raman spectroscopy were used to characterize the crystalline quality (texture, mosaicity, orientation) and the residual stresses in the films. The morphology and the roughness were examined using atomic force microscopy (AFM). A study of the chemical interactions, diffusion and interface formation was also performed using secondary ion mass spectrometry (SIMS). Furthermore, the thicknesses of the films were estimated by means of ellipsometry. In this section, we present the different characterizations performed on ZnO films grown on GaAs substrates and we exploit the obtained results.

4.3.1 Structure and residual stresses by XRD

4.3.1.1 Operation principle of XRD

X-ray diffraction (XRD) is a technique frequently used to characterize the structure and crystallographic orientations of thin films. This method uses an X-ray beam to irradiate the sample resulting in the beam to scatter in specific directions. By measuring the angles and intensity of the diffracted rays, it is possible to obtain a three-dimensional image of the electron density in the sample. From this density, the average position of the crystal atoms can be determined, as well as their chemical bonds, their entropy and some other information. From the diffracted intensities and the inverse relationship (reciprocal lattice - real lattice), it is possible to determine the three-dimensional arrangement of the atoms of the crystalline structure from a series of diffraction images [160].

X-ray diffraction also makes it possible to go back to interatomic distances. The knowledge of the interatomic distances then makes it possible to determine the crystallization phase of the material. The Bragg law gives the conditions of constructive interferences according to the interatomic distances and the angle at which the measured intensity is maximum. Thus, an incident X-ray beam of wavelength λ will be reflected by a plane family (hkl) only if it encounters these planes at an angle θ that verifies the Bragg's law:

$$2d \sin\theta = n\lambda \tag{4.3}$$

Where d is the interplanar distance, θ is the half-deflection angle (half of the angle between the incident beam and the direction of the detector), n is the order of reflection (positive integer) and λ the wavelength of the X-rays used.

The experimental setup of the diffractometer (Figure 26) comprises a monochromatic X-ray tube, a sample holder, and a goniometer on which an X-ray detector moves. The incident rays are diffracted by the sample. The X-ray detector measures the intensity of the X-radiation as a function of the angle 2θ that it forms with the incident X-ray beam. Using the existing databases, it is possible to identify the phase and mesh parameters corresponding to these diffractograms.

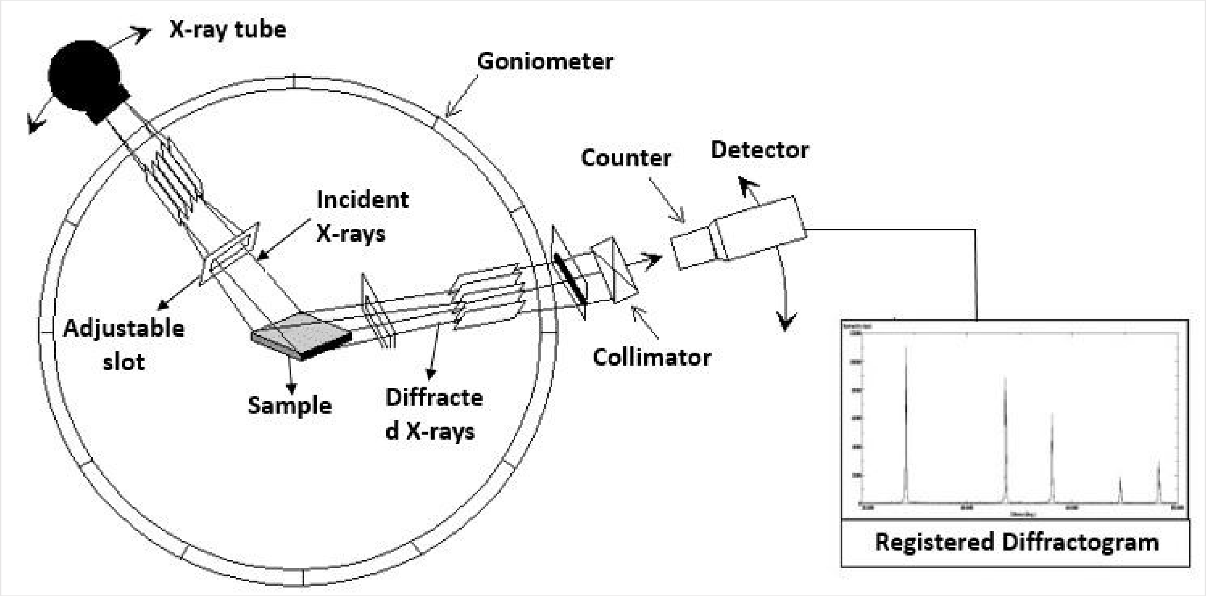

Figure 26. Schematic representation of the operation of an X-ray diffractometer

In standard XRD measurements, two configurations can be used:

Bragg-Brentano configuration: By varying the angle θ, the diffraction conditions translated by the Bragg law are satisfied by different spacing “d” in the polycrystalline materials. Only planes parallel to the surface will satisfy the Bragg's law in Bragg-Brentano geometry (Figure 27 (a)). Plotting the angular positions and the intensity of the diffracted resultant peaks produces the θ-2θ model, characteristic of the sample. In the case of thin films, the θ-2θ analyzes are used to identify the preferential phases and orientations parallel to the normal of the substrate.

Shultz configuration: Since the properties of the film are strongly related to the degree of texture, it is crucial to quantify the number and type of preferential orientation. To characterize the microstructure, rocking curves and φ-scan measurements are performed in Shultz geometry:

- Rocking Curve (or w-scan curve): to perform this measurement, a θ-2θ scan must be first executed. The angle θ and the position 2θ of the detector are set at the same value as the Bragg angle of the corresponding reflection. The measurement is carried out by varying the orientation of the sample at an angle Δω around its equilibrium position, while maintaining the position of the detector fixed. The sample is then rotated. For Δω = 0, the sample and the detector are in the exact positions of the constructive interference, and a peak will be observed. The width of this peak is a function of the interplanar distance. Therefore, the full width at half maximum (FWHM) of the peak provides information on the mosaicity and texture of the films.

- φ-scan: the measurement principle consists in turning the sample around the axis φ, while fixing the angle $\theta/2\theta$ w and Ω (Figure 27 (b)), which allows to leave the planes (hkl) not parallel to the surface at diffraction conditions. The φ-scans are generally used to highlight a possible orientation of the layer in the plane of the substrate.

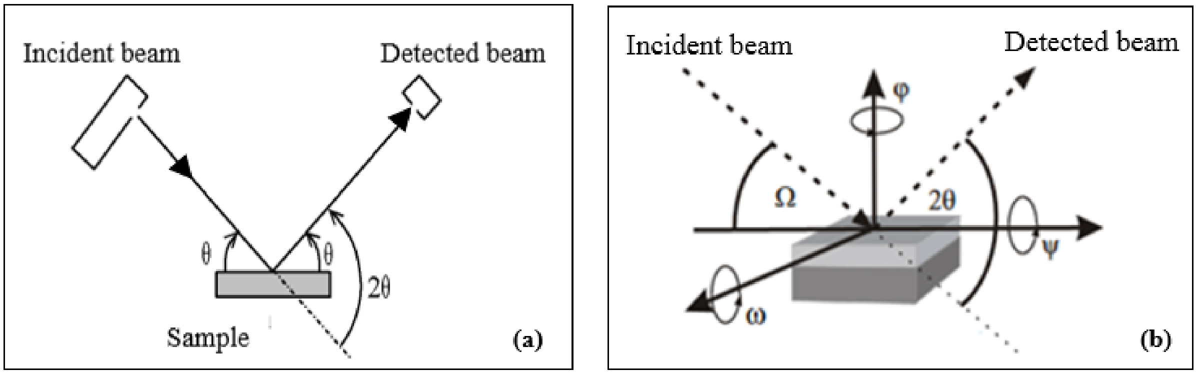

Figure 27. Definition of angles in the Bragg-Brentano (a) and Shultz (b) configurations

4.3.1.2 Measurement procedure

After deposition, the samples were sent to *Centre de Compétences X-Gamma* (Pr. P. Boulet, Jean Lamour Institute, Nancy - France) for characterization by means of XRD. The phase composition and out-of-plane orientation of the deposited ZnO films were analyzed using a Bruker D8 Advance diffractometer with monochromatic radiation CuKα (λ = 1.5405 Å). Rocking curves and φ-scans were measured using a Bruker D8 Discover diffractometer with CoKα radiation (λ = 1.79026 Å) to assess the texture quality of the films. The rocking curves were measured for (0002) ZnO reflection to determine the mosaicity of the c-axis orientation. The texture quality of the deposited layers was evaluated from the FWHM of the rocking curves fitted using a Voigt function.

4.3.1.3 Results

Structure and orientation of the films

The XRD θ /2θ patterns of the as-grown ZnO films on differently oriented GaAs substrates with and without the Pt/Ti buffer layers are shown in Figure 28.

All XRD patterns show polycrystalline Würtzite structure with dominant reflections from the (000*l*) ZnO planes. The reflections of other family planes were not observed for all substrates, confirming that the deposited layers were strongly textured along the c-axis of the hexagonal crystalline structure.

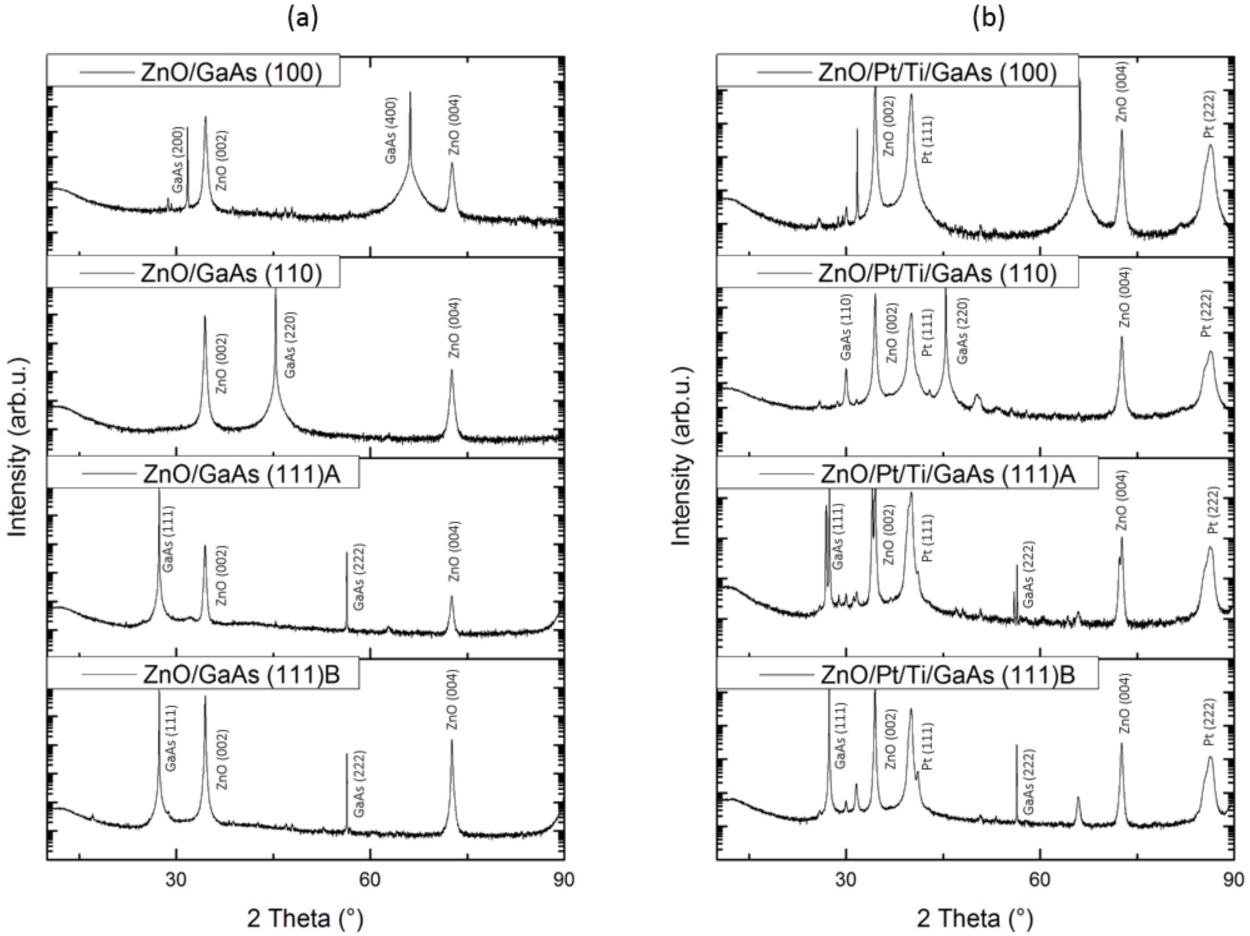

Figure 28. θ /2θ X-ray diffraction patterns of ZnO films deposited on GaAs substrates with different crystallographic orientations without (a) and with (b) the Pt/Ti buffer layer

The mosaicity of c-axis orientation was examined using rocking curve measurements. ZnO films grown directly on GaAs presented a mosaicity ranging between 5.2 and 5.8 °, represented by FWHM of (0002) reflection rocking curve, while the films grown with a Pt buffer showed a mosaicity between 1.4 ° and 1.6 ° (Table 8). Note that the instrumental resolution was 0.25 °. Texture quality is improved in the presence of the Pt/Ti buffer bilayer, making it independent of the used substrate cut. The FWHM for GaAs (110) could not be evaluated, since the rocking curve was too wide to fit. The direct growth of ZnO on GaAs substrates was highly influenced by the substrate surface orientation. The best texture quality was obtained on GaAs (100) surface (FWHM = 1.42 °). The mosaicity was also high on GaAs (111) surface and similar for both of the surface terminations A (FWHM = 1.47 °) and B (FWHM = 1.48 °). The texture on GaAs (110) was of slightly lower quality (FWHM = 1.55 °).

Moreover, the films did not present any defined in-plane orientation with respect to the orientation of the substrate, for all GaAs cuts, as confirmed by φ-scans of ZnO reflections.

Residual stresses

The effect of the stresses is reflected on the diffractograms by a displacement of the diffraction reflections. In order to determine these stresses, it is first necessary to calibrate the θ-2θ diffractograms obtained with respect to the reflections of the GaAs substrate (standard diffraction sheet JCPDS data card No. 00-014-450) provided in Appendix A. For that, we calculate the difference between the position of the reflection on the diffractogram and the one indicated in the JCPDS sheet. This difference is then subtracted from the positions of the reflections. Using the new positions, the interplanar distance of the film can be determined from the 2θ angle of the (0002)-plane reflection by using Bragg's law. The c-axis lattice constant of the films was determined using the following equation [161]:

$$c_f = n \times d_{00n} \tag{4.4}$$

Where c_f is the lattice constant for the ZnO thin film, n is a positive integer referring to the crystallographic plane, and d is the corresponding interplanar distance.

The calculated values of c-lattice constant for each thin film are reported in Table 8. Compared with a ZnO single crystal lattice constant (c_b = 5.2049 Å), it is obvious that the ZnO films present slightly extended c-lattice parameters. The shift of the diffraction reflection position from the bulk single-crystal value is mainly associated with thermal and intrinsic stresses produced within the film [162]. The 2θ position of the grown films is less than the one for bulk single-crystal, indicating that films are in a state of stress with extended c-axis. The larger value of lattice constant for the as-grown films compared to the unstressed bulk single-crystal value shows that the unit cell is elongated along the c-axis, and compressive forces act in the plane of the film.

The strain ε_{zz} in the films can be calculated from the shift of the (0002) ZnO reflection in θ /2θ X-ray patterns, using the following equation [163]:

$$\varepsilon_{zz} = \frac{c_f - c_b}{c_b} \tag{4.5}$$

Where $c_b = 5.2049$ Å is the lattice constant of bulk ZnO single crystal.

However, in the case of a thin film of hexagonal structure oriented along the axis c on a substrate of cubic symmetry, the film is under biaxial stress in the direction of the basal plane xy and stress-free in the z direction. Therefore, the main stress components are equal ($\sigma_{xx} = \sigma_{yy} = \sigma_b$), and we assume that there is no shear component. For symmetry reasons, the microdeformation is also biaxial ($\varepsilon_{xx} = \varepsilon_{yy} = \varepsilon_b$); the mechanical equilibrium relation is written as [164]:

$$\begin{pmatrix} \sigma_b \\ \sigma_b \\ 0 \end{pmatrix} = \begin{pmatrix} C_{11} & C_{12} & C_{13} \\ C_{12} & C_{11} & C_{13} \\ C_{13} & C_{13} & C_{33} \end{pmatrix} \begin{pmatrix} \varepsilon_b \\ \varepsilon_b \\ \varepsilon_{zz} \end{pmatrix} \tag{4.6}$$

By developing the 3rd line of (4.6) and isolating ε_b, the strain ε_{zz} in the films can be calculated using the following equation [163]:

$$\varepsilon_b = -\frac{C_{33}\varepsilon_{zz}}{2\,C_{13}} \tag{4.7}$$

Lines 1 and 2 are identical, which makes it possible to write:

$$\sigma_b = (C_{11} + C_{12})\,\varepsilon_b + C_{13}\,\varepsilon_{zz} \tag{4.8}$$

By substituting ε_b in (4.8), the residual stresses can be expressed as a function of ε_{zz} and can be calculated from the measured strain values [165]:

$$\sigma = (C_{13} - \frac{(C_{11}+C_{12})\,C_{33}}{2\,C_{13}})\varepsilon_{zz} \tag{4.9}$$

The sign of σ shows the type of the stress: it is either a compressive stress ($\sigma_b < 0$) or a tractive stress ($\sigma_b > 0$) depending on the orientation of the growth of the layer (c-axis).

The elastic constants of ZnO used in this calculation were: $C_{11} = 209.7 \pm 0.2$ GPa, $C_{12} = 121.1 \pm 0.3$ GPa, $C_{13} = 105.1 \pm 0.2$ GPa, $C_{33} = 210.9 \pm 0.1$ GPa [140]. The calculated stress and residual stresses for the deposited ZnO layers are provided in Table 8.

Table 8. FWHM of (0002) ZnO rocking curve, c-lattice constant, strain and residual stress in ZnO thin films deposited on GaAs substrates with different crystallographic orientations with (+) and without (-) the Pt/Ti buffer bilayer

GaAs orientation	(100)	(100)	(110)	(110)	(111)A	(111)A	(111)B	(111)B
Buffer bilayer	-	+	-	+	-	+	-	+
Rocking FWHM (° ± 0.25 °)	5.2	1.42	-	1.55	5.5	1.47	5.84	1.48
c-lattice constant (Å ± 0.003 Å)	5.218	5.215	5.208	5.207	5.207	5.206	5.207	5.204
Strain	25×10^{-4}	19×10^{-4}	6.3×10^{-4}	3.8×10^{-4}	3.7×10^{-4}	1.2×10^{-4}	3.7×10^{-4}	1.3×10^{-4}
Residual stress (MPa ± 100 MPa)	-434	-332	-108	-65	-63	-21	-63	-22

The comparison of the residual stresses for the ZnO layers shows that they are all subjected to compression stresses < 500 MPa, which is coherent with the fact that the in-plane expansion coefficient of ZnO is lower than that of the GaAs substrate. Moreover, the films deposited on the Pt/Ti buffer bilayer show slightly lower stresses than the ones deposited directly on GaAs, showing an advantage of this buffer. Although the thermal expansion of cubic GaAs is isotropic and all ZnO films presented the same crystallographic orientation, the highest residual stresses were developed in films grown on GaAs (100). The different stresses observed for the different cuts of GaAs could be explained by the difference in the interplanar distance for each cut, which could generate additional intrinsic stresses adding to the thermal ones.

4.3.2 Raman modes and stresses

4.3.2.1 Operating principle of Raman spectroscopy

Raman spectroscopy is a non-destructive analysis technique, based on the elastic interaction between the constituents of a material and the photons of an incident light radiation of defined frequency. Because of its excellent spatial resolution defined by the size of a focused laser spot, this technique is a very powerful tool for structural characterization of thin films. The information obtained by this technique concerns the position and the profile of the characteristic bands, thus making it possible to deduce the spatial distribution of many physical quantities including the crystallographic orientations and stresses [166].

The Raman effect results from the interaction of vibrational and/or rotational modes of atoms or molecules with electromagnetic radiation. It corresponds to the inelastic scattering of light by the molecules. Therefore, the observed energy (frequency) variation provides information on the energy levels of rotation and vibration of the molecule concerned and can be represented through the shift in the wavenumber (cm^{-1}), called Raman shift. Thus, in a Raman spectrum, the band positions (cm^{-1}) correspond to the characteristic vibration frequencies of the molecular bonds.

The light scattered by the molecules contains Rayleigh photons, whose energy is equal to that of excitation. It also contains weaker intensity Raman photons whose energy is modified by the molecular vibrational transitions: they are Raman Stokes or anti-Stokes photons depending on whether the material absorbs or gives energy to the incident photons. The diagram in Figure 29 represents the different energy levels involved in Rayleigh and Raman scattering.

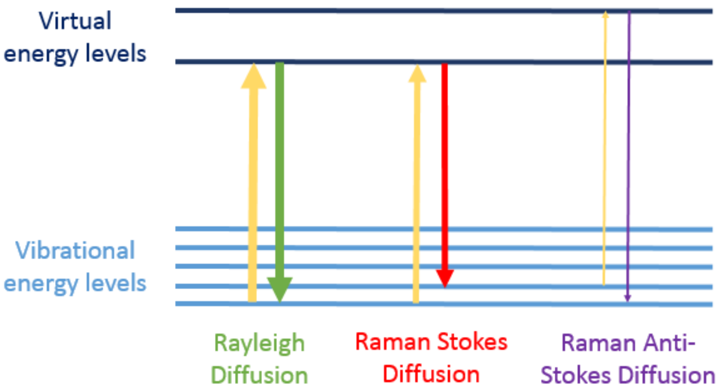

Figure 29. Diagram of the energy levels involved in Rayleigh and Raman scattering. The thickness of the lines indicates qualitatively the intensity of the signals of each transition.

The excitation source generally consists of a fine monochromatic laser line (laser source) whose energy is focused on the target to be analyzed. The Raman light is collected at a solid detection angle and then analyzed using a spectrograph whose chromatic dispersion is finally imaged on a suitable matrix detector (CCD). From the images thus produced, it is possible to plot the spectra containing all the characteristic vibration peaks of the detected targets. By the nature of the phenomenon of light scattering, Raman scattering is observable with excitation wavelengths ranging from UV to near IR, via the visible. The diagram of Figure 30 shows the elements of a Raman spectrometer and the measurement process.

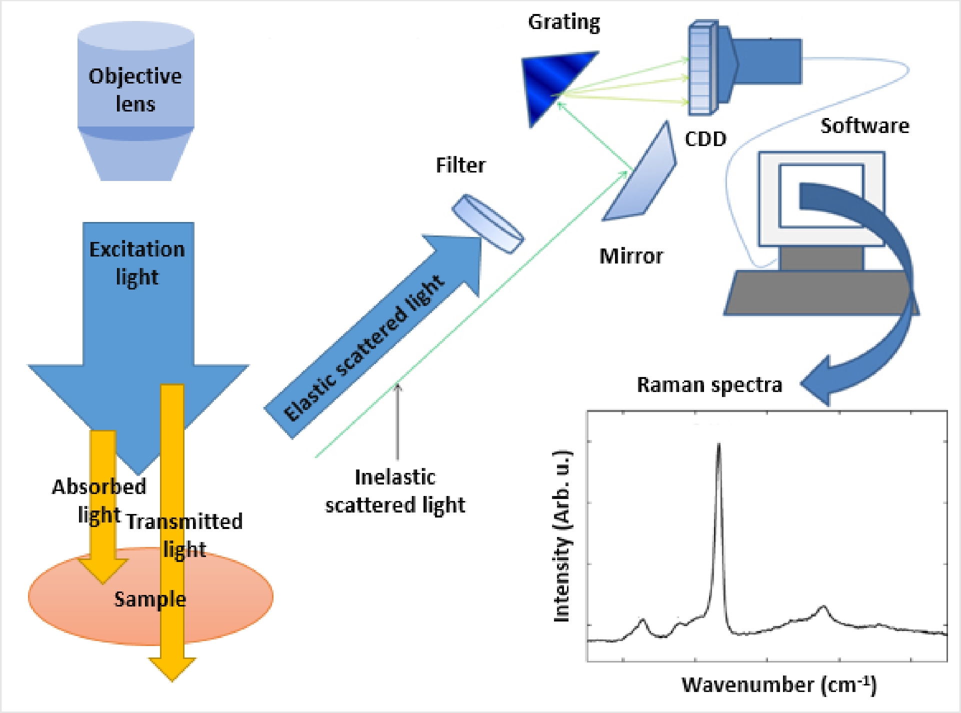

Figure 30. Process involved in collecting Raman spectra

4.3.2.2 Theoretical Raman modes of ZnO and GaAs

ZnO has a würtzite symmetry with 6mm point group. There are 4 atoms per elementary cell leading to 12 phonon branches including 9 optical and 3 acoustic. Group theory predicts that, near the center of the Brillouin zone, there is a branch A_1, a doubly degenerate branch E_1, 2 branches doubly degenerate E_2, and 2 branches B. The branches A_1 and E_1 are both active in Raman and infrared spectral range, and split into LO and TO components (longitudinal and transverse optical modes, respectively) [167]. The E_2 branches are active for Raman only, while the B branches are inactive. The symmetry and wavenumbers of the fundamental modes of ZnO are provided in Table 9 [168].

The polarization selection rules for Raman scattering in ZnO predict that it is possible to identify the peaks of the $E_{2\ (low)}$, $E_{2\ (high)}$ and $A_{1\ (LO)}$ modes in $Z(XX)\bar{Z}$ and $Z(YY)\bar{Z}$ polarization configurations, whereas for $Z(XY)\bar{Z}$ only the modes E_2 are observable.

Table 9. Frequency and symmetry of the fundamental optical modes in ZnO

Symmetry character	$E_{2\ (low)}$	$A_{1\ (TO)}$	$E_{1\ (TO)}$	$E_{2\ (high)}$	$A_{1\ (LO)}$	$E_{1\ (LO)}$
Wavenumber (cm^{-1})	101	380	413	437	579	591

On the other hand, GaAs belongs to $\bar{4}3m$ point group with zinc blende symmetry. Two modes are observable: $A_{1\ (LO)}$ and $E_{1\ (TO)}$ at 291 cm^{-1} and 267 cm^{-1} respectively. According to the Raman selection rules, it is possible to find the longitudinal modes $A_{1\ (LO)}$ for the planes (100) and (111) of GaAs, whereas this is not possible for the plane (110), and that the transverse modes $E_{1\ (TO)}$ appear for the cuts (110) and (111) and not for (100) orientation.

Raman selection rules, the frequencies and symmetries of the fundamental Raman modes of ZnO and GaAs can be found in references [168]–[170].

4.3.2.3 Measurement procedure

Raman spectra of the deposited ZnO films were collected at room temperature using S&I MonoVista Raman spectrometer with laser excitation at 532 nm. The reference spectra were obtained by measuring X- and Z- oriented ZnO single crystals and bare GaAs substrates of the following cuts: (100), (110), (111) A and (111) B. For each substrate cut, 6 samples were measured (3 with Pt buffer layer and 3 without it). For each sample, three spectra were measured using three polarization configurations noted $Z(XX)\bar{Z}$, $Z(YY)\bar{Z}$ and $Z(XY)\bar{Z}$. The measured intensities of Raman spectra of these polarization configurations are not equivalent due to difference in the optical setup.

4.3.2.4 Results

Raman modes of the deposited ZnO films

Figure 31 shows an example of Raman spectra obtained in $Z(XY)\bar{Z}$ polarization. The spectra obtained for ZnO thin films deposited directly on GaAs (Figure 31 (b)) clearly show the ZnO and GaAs Raman modes, whereas the spectra obtained for films deposited using the Pt/Ti bilayer (Figure 31 (a)) show only the ZnO modes, due to high absorption by the Pt layer. The results are similar in the $Z(XX)\bar{Z}$ and $Z(YY)\bar{Z}$ polarisations, but for simplification we chose to show the results for one polarization.

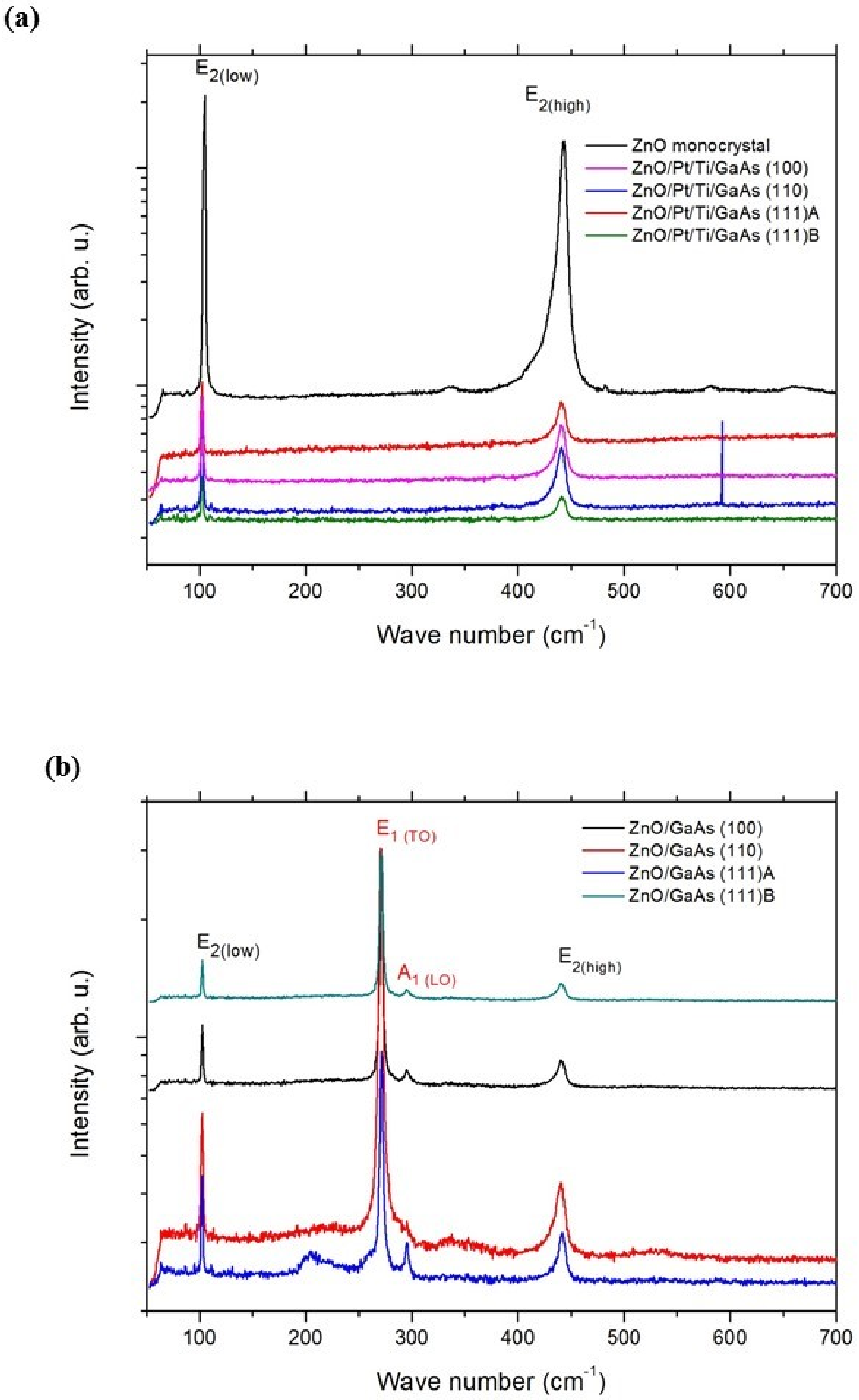

Figure 31. Example of Raman spectra collected in $Z(XY)\bar{Z}$ polarization for 8 samples (out of 32 measured) consisting of ZnO films deposited on GaAs substrates of different cuts with (a) and without (b) the Pt/Ti buffer bilayer. The GaAs modes ($E_{1(TO)}$ and $A_{1(LO)}$) are labelled in red.

For GaAs, the spectra obtained for the various orientations confirm the selection rules of a blend cubic system. The $A_{1(LO)}$ mode appears at 291 cm^{-1} and the $E_{1(TO)}$ at 267 cm^{-1}. As for ZnO films, the modes around 101 cm^{-1} and 437 cm^{-1} correspond to the $E_{2(low)}$ and $E_{2(high)}$ modes of the würtzite structure respectively, as predicted by the selection rules. The compliance with the selection rules shows that the growth of ZnO films provides high texture quality.

The observed modes of ZnO films are slightly shifted from the wavenumbers of ZnO monocrystal. These Raman shifts can provide information on the stresses acting on ZnO films.

Residual stresses

Raman spectroscopy can also provide information about the stresses in the material by the observation of the displacement of the position of the modes and by comparison with the tabulated values of the studied material in massive state.

The frequency of the modes E under constraints can be described as follows [171]:

$$w_{E\,(TO)} = a'_{E(TO)}\ (\sigma_{xx} + \sigma_{yy}) + b'_{E(TO)}\ \sigma_{zz} \pm \sqrt{c'_{E(TO)}\left(\sigma_{xx} - \sigma_{yy}\right)^2 + d'_{E(TO)}\,(\sigma_{xy})^2} \qquad (4.10)$$

Where σ_{xx}, σ_{yy} et σ_{zz} are the stresses along the axes a, b and c respectively, and $a'_{E(TO)}$, $b'_{E(TO)}$, $c'_{E(TO)}$ and $d'_{E(TO)}$ are the potential deformation constants expressed in terms of compliance (the property of undergoing elastic deformation when subjected to an applied force).

$c'E_{(TO)}$ is related to the split of double degenerate $E_{(TO)}$. If the axes a and b are affected by the different stresses or if the plane ab is subjected to shear stresses, the mode $E_{(TO)}$ splits into two components. However, the degeneration of $E_{(TO)}$ is usually quite weak and its split is difficult to identify and $c'E_{(TO)}$ is negligible. In addition, we assume that there are no shear stresses in the films, hence $\sigma_{xy} = 0$. The ZnO films, deposited on cubic substrates, are subjected to biaxial stresses σ_b in the plane of the substrate [116]. Thus, $\sigma_{xx} = \sigma_{yy} = \sigma_b$, and the shift of the modes $E_{(TO)}$ in the domain c can be expressed as:

$$\Delta w_{E(TO)} = 2\ a'_{E(TO)}\ \sigma_b \qquad (4.11)$$

Thereby, the biaxial stresses σ_b can be calculated from the shift of the position of the ZnO modes:

$$\sigma_b = \frac{\Delta wE(TO)}{2a'\ E(TO)} \qquad (4.12)$$

The values of stress for the different samples, calculated from (4.12) are provided in Table 10. The found values of the biaxial stresses are quite low (<0.25 GPa) and are close to the ones calculated from XRD data (see Table 8). Moreover, the low displacement towards high frequencies of the $E_{2(High)}$ mode is due to compressive residual stresses, is associated with a high crystalline quality of the films. The ZnO films grown on different cuts of GaAs directly or with Pt/Ti buffer layers presented compatible residual stress in the limits of the errors.

Table 10. Residual stress in ZnO thin films deposited on GaAs substrates with different crystallographic orientations with (+) and without (-) the Pt/Ti buffer bilayer

GaAs orientation	(100)	(100)	(110)	(110)	(111)A	(111)A	(111)B	(111)B
Buffer bilayer	-	+	-	+	-	+	-	+
Residual stress (MPa ± 100 MPa)	-244	-57	-98	-59	-106	-49	-41	-21

In reality, the stresses acting on our layer were thermal stresses that are generated during the cooling process following the deposition of the thin films. In general, the temperature of the substrate during the deposition T_{dep} is higher than the ambient temperature T_a. Consequently, at the end of the deposition, the thin layer undergoes a thermomechanical deformation which leads to extrinsic stresses in it. They are due to the difference of the coefficients of thermal expansion α_S and α_F of the substrate and the deposited film respectively. The theoretical biaxial deformations ε_b related to the thermal stresses were determined from the relation:

$$\varepsilon_b = (\alpha_F - \alpha_S)\,(T_{dep} - T_a) \tag{4.13}$$

Once ε_b is calculated, the theoretical values of the deformation ε_{zz} were determined using the following equation:

$$\varepsilon_b = -\frac{C_{33}\varepsilon_{zz}}{2\,C_{13}} \tag{4.14}$$

Given that the deposition of ZnO was carried out under a temperature of 350 °C, and that the coefficients of thermal expansion of ZnO and GaAs are $2.9 \times 10^{-6}\ K^{-1}$ and $5.73 \times 10^{-6}\ K^{-1}$ respectively, the biaxial stress σ_b of thermal type induced in the film was determined using equation (4.14) at -208 MPa. This value seems quite consistent with the values of the stresses estimated from XRD and Raman data in the limit of the errors (Tables 8 and 10).

4.3.3 Morphology and roughness by AFM

Since a uniform surface facilitates acoustic wave propagation and reduces losses, ZnO films possessing flat and homogeneous surfaces are preferred. Using AFM, the topography of the films deposited on different GaAs cuts and the roughness parameters are studied.

4.3.3.1 Operating principle of AFM

Atomic force microscopy (AFM) is a scanning probe analysis technique allowing, among others, to characterize the surface topography of a sample at the nanometer scale. It exploits the interaction between the surface atoms of the sample and the atoms of a probe of nanometric dimensions. The surface of the sample is scanned by a very thin tip, positioned at the free end of a flexible micro-lever, able to move in all directions of space, thanks to a piezoelectric tube (Fig. 29). The Z-movement of the tip, varying according to a feedback parameter, is recorded by a computer allowing the reconstruction of the image of the surface. The analysis of the bends of the micro-lever makes it possible to determine the exact path of the tip, as well as the measurement of the interaction forces with the sample [172].

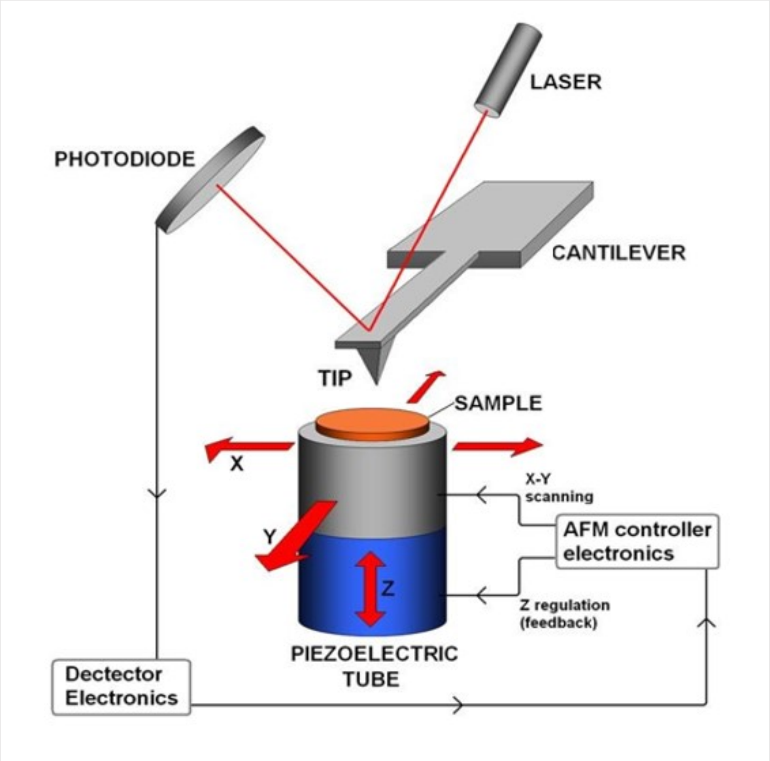

Figure 32. Schematic representation of an atomic force microscope [173]

Atomic force microscopy can be operated in three main scanning modes:

- The contact mode: it corresponds to low tip-surface distances of the order of a few Å, for which the contact forces are repulsive. When the point presses on the surface, it is pushed back according to Pauli's principle and the cantilever is deflected. The feedback is done on the measurement of the direction of the deviation.

- Tapping mode: by far the most used, it corresponds to important tip-surface distances ranging from 1 to 100 nm, for which the forces are attractive. It consists of vibrating the cantilever at its natural frequency of resonance with a certain amplitude. When the tip interacts with the surface, the amplitude decreases because the resonance frequency changes. The feedback is then on the amplitude of oscillation of the lever.

- Frequency modulation mode: This is a combination of the two previous modes. The tip-to-surface distance is between 0.3 and 100 nm. More delicate to manage, it makes it possible to separate directly the effect of the conservative and dissipative forces. The feedback is done on the deviation of the resonance frequency.

4.3.3.2 Measurement procedure

The surface topography of the films was characterized using a Nanowizard III AFM (JPK Instruments, Germany). Imaging was performed in air using Nano World NPS-10C cantilevers made from silicon nitride with a stiffness of 0.32 N/m. AFM images were collected in a contact mode, at a frequency of 0.5 lines/sec with a resolution of 512 by 512 pixels. Scans of different dimensions (100 x 100 μm^2 to 1 x 1 μm^2) were made in order to have a representative sampling of the surface.

4.3.3.3 Results

Figure 33 shows the AFM images and surface roughness of the deposited ZnO thin films. The root mean square (Rms) roughness parameters of GaAs bare substrates and of the deposited ZnO films were determined using JPK software from several 5 µm x 5 µm images (Table 11).

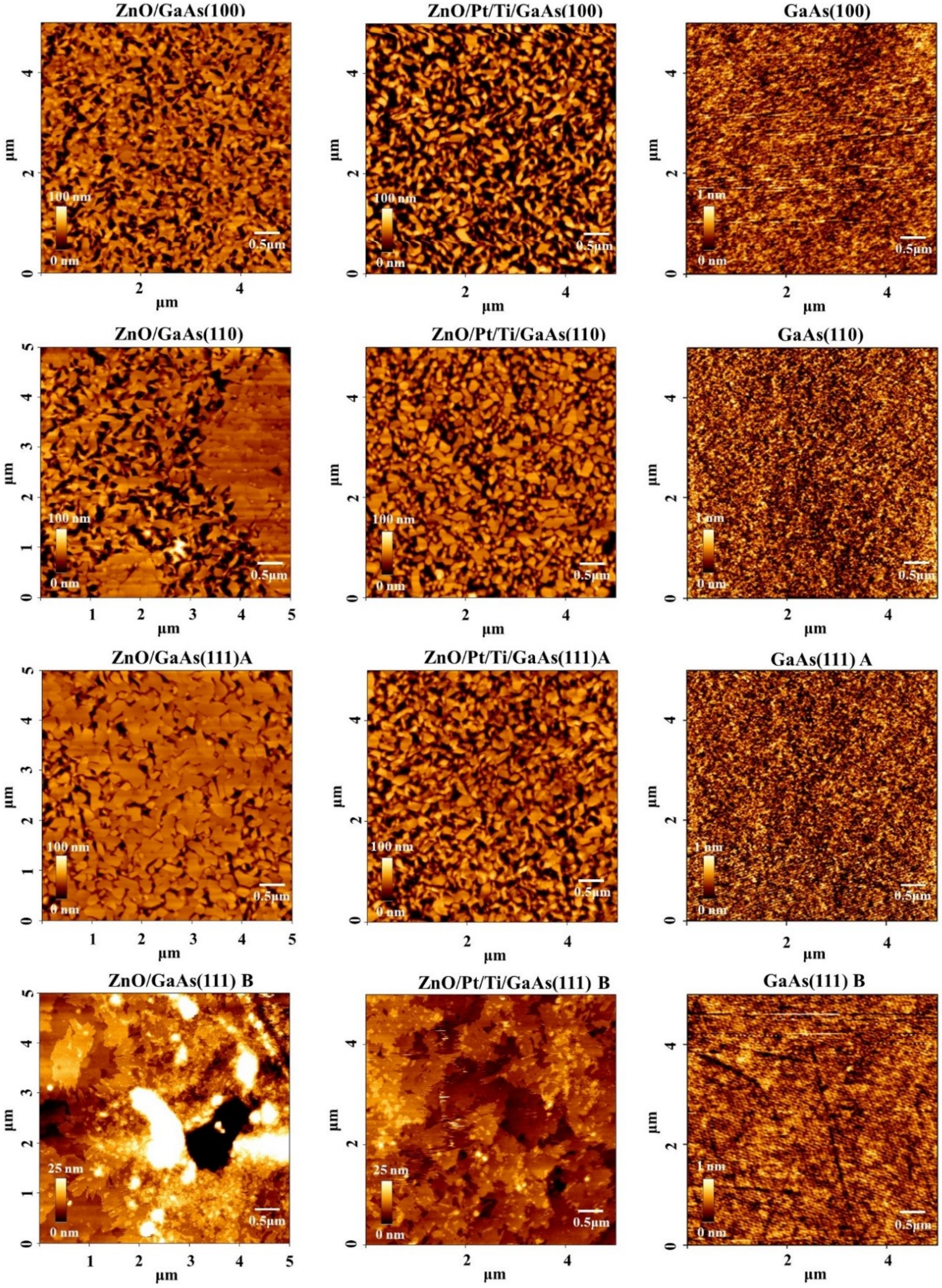

Figure 33. AFM images (5x5 μm^2, contact mode, silicon nitride tips (0.32 N/m), 512*512 pixels resolution) of ZnO thin films deposited on GaAs substrates of different cuts without and with the Pt/Ti buffer bilayer, and of GaAs bare substrates of different cuts.

Qualitatively comparing the AFM images, the dependence of the films' morphology on the substrate's plane is obvious. As seen clearly, the surface of the ZnO film deposited on GaAs (100) is the roughest, and the Rms decreasing from 26.5 ± 1.8 nm to 17.9 ± 2.1 nm when the Pt layer is added. The films grown directly on GaAs (110) showed an inhomogeneous surface, with roughness parameters varying according to the organization of the crystallites. However, that is not the case when a Pt/Ti bilayer is added, since the grains distribution becomes more homogeneous and the roughness parameters decrease from 18.9 ± 2.3 nm to 17.4 ± 3.8 nm. In the case of GaAs (111) substrates, although the surface roughness of the starting substrate is higher for GaAs (111)A than for GaAs (111)B, the surface of the ZnO thin film becomes more uniform on the Ga-terminated surface. Moreover, the roughness of the ZnO thin film changes between 13.4 ± 7.7 nm for direct growth and 2.7 ± 0.3 nm using the Pt/Ti bilayer.

The roughness parameters for all substrate orientations decrease in the presence of the buffer layer, indicating a better organization of the ZnO films. Hence, the presence of the buffer layer promotes the growth of the crystalline homogeneous structure by reducing surface heterogeneities. By comparing the Rms values for the different cuts, GaAs (111)B has shown to provide the better films quality.

Table 11. Average roughness parameters calculated from 5x5 μm^{2}AFM images of GaAs bare wafers and ZnO thin films deposited on GaAs substrates of different crystallographic orientations with (+) and without (-) the buffer bilayer

GaAs orientation	(100)	(100)	(110)	(110)	(111)A	(111)A	(111)B	(111)B
Rms for bare GaAs (pm)	187.2 ± 27.2		212.9 ± 15.1		413.8 ± 29.9		173.2 ± 13.9	
Buffer bilayer	-	+	-	+	-	+	-	+
Rms for ZnO film (nm)	26.5 ± 1.8	17.9 ± 2.1	18.9 ± 2.3	17.4 ± 3.8	12.8 ± 1.8	10.8 ± 1.9	13.4 ± 7.7	2.7 ± 0.3

For the development of the proposed sensor, GaAs (100) has also shown to promote the growth of high quality ZnO thin films, in terms of texture, flatness, homogeneity and roughness. Moreover, the micromachining of resonant membranes in GaAs using chemical wet etching has been widely studied in our research group, and GaAs (100) has shown to produce promising and reproducible microstructures for sensing [9], which is not the case for GaAs (111). Therefore, the GaAs (100) cut will be selected for the rest of the study.

Considering the possible diffusion of Ti through Pt [174], which could affect the conductivity of the latter, another set of depositions was carried out under the same conditions, on GaAs (100) substrates, using Ta as an adhesion layer. The SIMS and ellipsometry measurements were performed in order to study the interfaces quality between the different layers, the film thickness and the optical properties, respectively.

4.3.4 Interfaces and depth profiles by SIMS

For a better understanding of the ZnO/buffer bilayer/GaAs structures, a physico-chemical analysis of the layers was conducted using SIMS. This allowed to obtain depth profiles of the elements distribution of the samples at the interfaces of the constituting layers.

4.3.4.1 Operating principle of SIMS

Secondary Ion Mass Spectrometry (SIMS) is a physicochemical characterization technique, based on the detection of secondary ions torn from a sample under the effect of a bombardment of so-called primary incident ions. SIMS utilizes a beam of energetic primary ions of few keV to sputter the surface, producing ionized sputtered particles which can be detected by mass spectrometry. This technique provides in-depth information on atomic constituents by recording one or more mass peaks as the sputtering process erodes the sample, thus producing the detected signal from increasingly greater depths beneath the original sample surface. The depth resolution can be as low as 1 nm. This mode consists of alternating analysis and abrasion cycles. Successive mass spectra for each analyzed depth are thus obtained which, once processed, make it possible to reconstruct the distribution of a secondary ion in the depth of the sample. The SIMS technique provides a unique combination of extremely high sensitivity for all elements from Hydrogen to Uranium (detection limit down to ppb level for many elements), high lateral resolution imaging, and a very low background that allows high dynamic range. This technique is "destructive" by its nature (sputtering of material). It can be applied to any type of solid material (insulators, semiconductors, metals) that can be kept under vacuum [175].

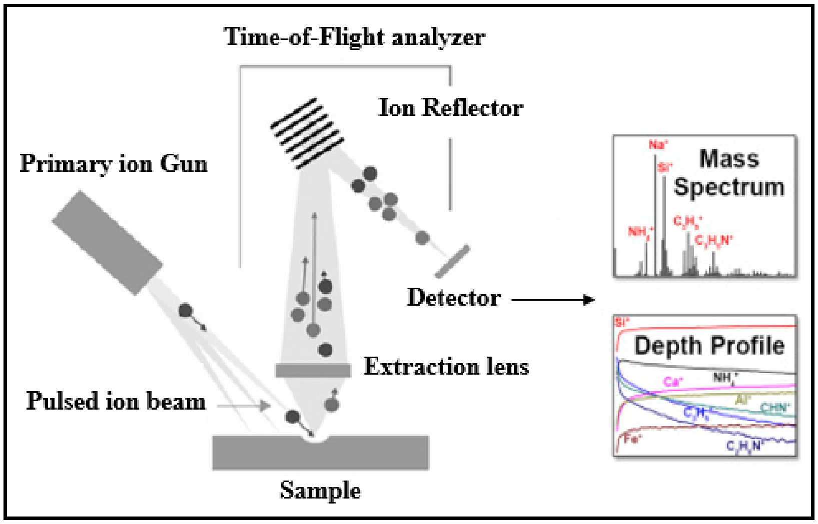

Figure 34. Schematic illustration of the functional principle of a TOF-SIMS characterization, adapted from [176]

4.3.4.2 Experimental procedure

SIMS characterization was realized at GCM laboratory of *École Polytechnique Montréal*. The depth profiles were executed in interlaced mode on a 100 µs cycle. In this mode, the sputtering source was used to remove the analyzed material for about 80 µs. During the remaining 20 µs of the cycle, the flood gun sent a pulse of low energy electrons to discharge the surface. For depth profiles, the Cs^+ sputtering source is used for negative ion profiles because Cs promotes their emission, and the O^{2+} sputtering source is used for positive ion profiles. A detailed list of the parameters used for this technique is provided in Table 12. The surface was then bombarded with the primary ions of Bi^+, and the emitted secondary ions were collected for analysis. The craters with dimensions of 300 µm x 300 µm were etched, and the analysis with the primary ions of Bi^+ was carried out in a region with dimensions of 50 µm x 50 µm located in the center of the crater to avoid the edge effect. All profiles were obtained to the interface of GaAs. The crater depth was measured using a profilometer. This allowed to determine the average erosion rate and to express the profiles as a function of depth rather than the sputtering time.

In Time-of-flight SIMS (TOF-SIMS), some species have a better detection yield in positive ions and others in negative ions. This doesn't necessarily mean that a species with a higher yield of negative ions will not be detected at all in positive ions, and vice versa, but the intensity detected would be much lower. With regards to the elements expected in the present analysis, oxides, Pt, and As have a better detection yield of negative ions. On the other hand, Ti, Ta and Ga have a better yield of positive ions. Negative ion profiles were first established for all the samples, which made it possible to observe the profiles of ZnO, Pt, As and GaAs. Then, positive ion profiles were established to observe the distribution of Zn, Ta, Ti, and Ga. The Pt was also detected, but with a decreased intensity compared to what was found in negative ions profile.

Table 12. Experimental SIMS parameters used to collect the depth profiles of the deposited ZnO thin films

Apparatus		ION-TOF SIMS IV
Ionic courant		0.5 pA
Pulse		19.1 ns
Pressure		5.0 x 10^{-9} Torr
Charge neutralization		2.35 A
Spectroscopy	Source	Bi+
	Energy	25 kV
	Analyzed surface	50 µm x 50 µm
	Spectral resolution	128 x 128 pixels
Profiles	Source	Cs+ and O_2+
	Energy	3.0 kV
	Pulverized surface	300 µm x 300 µm

4.3.4.3 Results

The examination of the depth profiles (Figure 35) of ZnO films deposited on GaAs (100) with and without the Pt/Ti and Pt/Ta buffer bilayers shows two main phenomena: the first one is the oxidation of the Ta and Ti layers during the ZnO deposition, which manifested by the presence/profile of their oxides (TaO, TaO_2, TiO, and TiO_2). The oxidation of these layers was expected since ZnO films were grown using sputtering technique at high oxygen partial pressure. The second is the diffusion of some elements up towards the ZnO film. Based on the deposition conditions used for the buffer bilayers, the thickness of Pt is expected to be of 150 nm and the one of Ti and Ta of 15 nm for each. However, Figure 35 (e) shows that Ta oxides were found across all the Pt thickness, while it was supposed to be at Pt/GaAs interface.

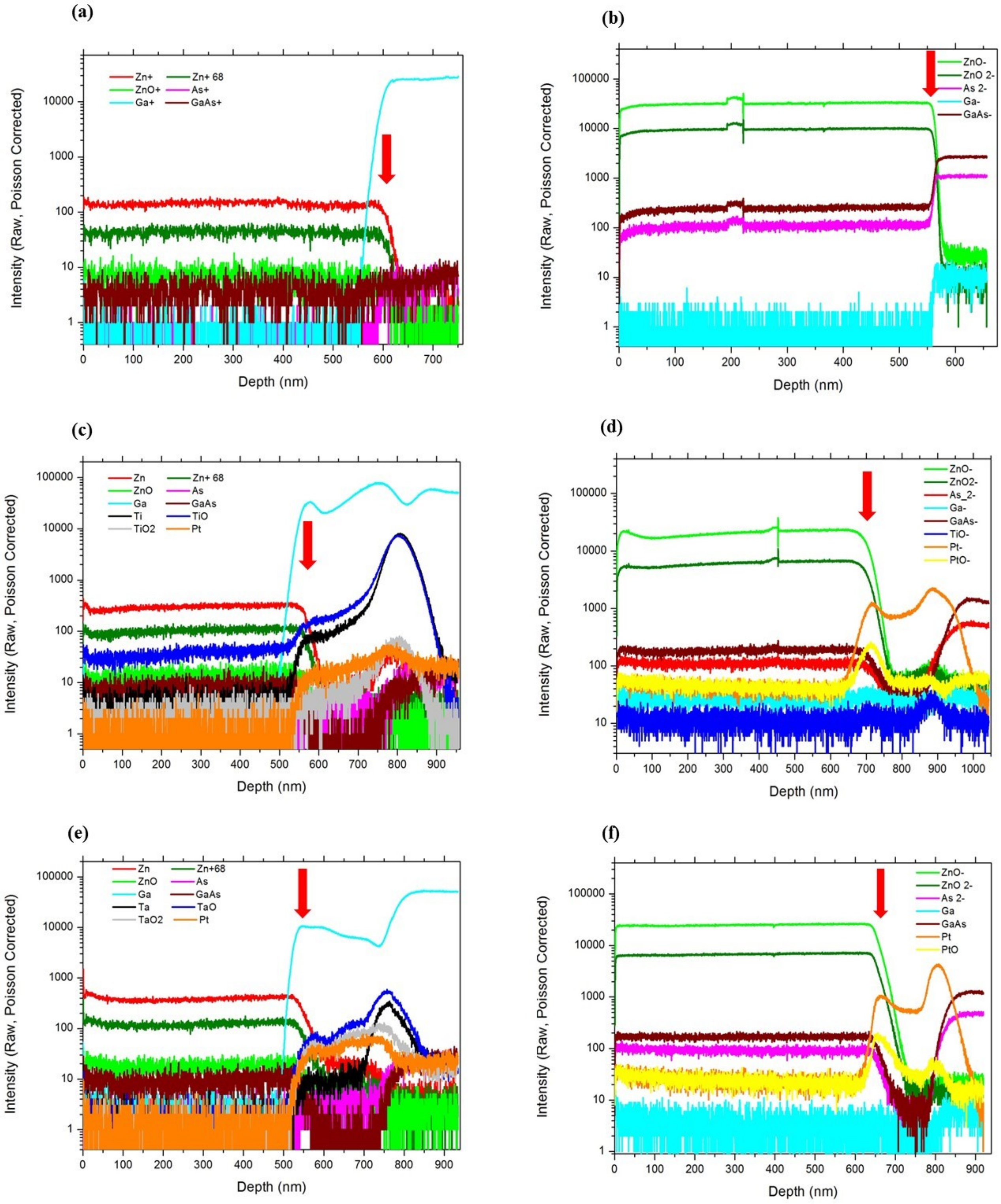

Figure 35. Positive and negative ion depth profiles measured on 3 samples by SIMS in ZnO thin films grown on GaAs (100) (a, b), on Pt/Ti /GaAs (100) (c, d), and on Pt/Ta/GaAs (100) (e, f), respectively. The red arrow indicates the interface between ZnO and other layers.

Moreover, it can be clearly observed that only Ta oxides diffuse while metallic Ta remains at the interface. As for Ti, expected to be located at Pt/GaAs interface, it diffused into Pt as well as its oxides (Figure 35 (c)). Furthermore, it was observed that ZnO tends to slightly diffuse to the Pt layer as well.

The behavior of the different elements could be explained as follows: since the deposition of the ZnO films is carried out at high temperature (350 – 450 °C), Ti and Ta have diffused into Pt in order to oxidize. However, this diffusion is less significant in the presence of Ta than that of Ti. This result is related to the fact that Ta is heavier than Ti, which is consistent with Maeder et al. stating that Ta is preferable than Ti for an adhesion layer since its diffusion is less efficient [177]. As for Ga, which tends to diffuse at room temperature in GaAs [178], [179], its diffusion stopped at the ZnO interface. However, Ga diffuses easily through Ta, Ti and Pt layers.

The inter-diffusion in the buffer layer is of a concern only if Pt is used as a bottom electrode, since it would affect the conductivity of the device. The XRD and AFM measurements confirm that this buffer improves the crystalline and structural quality of the films, in terms of texture, stress and roughness, but it promotes the diffusion of Ga, interface layers and ZnO itself. Therefore, direct growth of ZnO on GaAs should be preferred.

4.3.5 Thickness and optical properties by ellipsometry

4.3.5.1 Operation principle of ellipsometry

Ellipsometry is a well-known optical technique for the analysis of the thickness and optical parameters (refractive index, bandgap…) of materials in form of thin films of nanometric thickness. Discovered by P. Drude more than 100 years ago, it is based on the analysis of the polarization of a plane wave before and after reflection on a substrate composed of multiple layers. Ellipsometry is based on the measurement of the change in polarization state, quantified by the amplitude ratio Ψ and the phase difference Δ (Figure 36), of a light beam reflected at an angle Φ_0 by the surface. Because the signal depends on the thickness as well as the material properties, ellipsometry has become a universal tool for contact free determination of thickness and optical properties (indices n and k) of thin films [180]. The analysis and fitting of the experimental data is carried out using a mathematical model adapted according to the analyzed materials and layers.

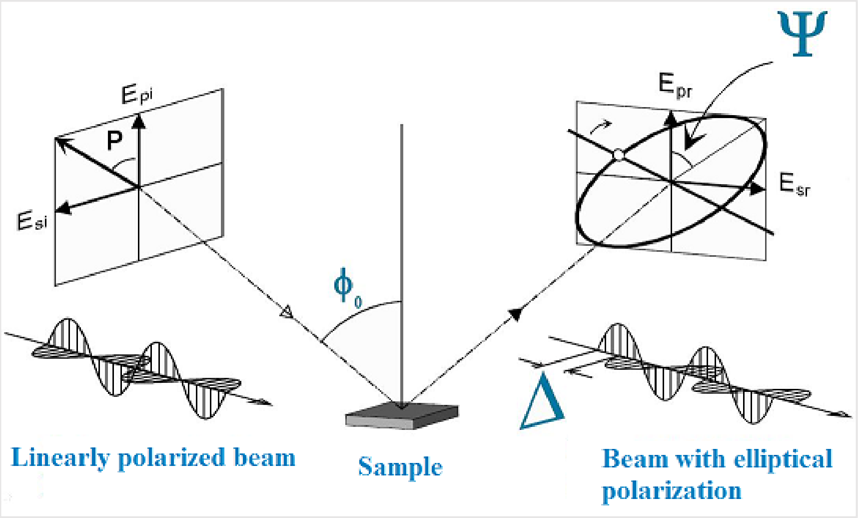

Figure 36. Operating principle of an ellipsometer

4.3.5.2 Experimental procedure & results

Ellipsometric spectra were measured using the UVISEL spectroscopic ellipsometer (HORIBA Jobin Yvon) in the range of 0.73 eV and 4.75 eV. The ellipsometric data was fitted by using a layer/substrate exitronic model proposed by K. Sato et al [181], in order to estimate the thicknesses and optical properties of the films. Three wafers were measured: ZnO/Pt/Ti/GaAs, ZnO/Pt/Ta/GaAs and ZnO/GaAs. Three measurements were carried out on each wafer, one at the center and two near the edges.

The thicknesses of the films were estimated from the ellipsometric data, which allowed to determine the location of the interfaces, and to predict at which depth each element should be located. Hence, the thicknesses of the films were determined at 758 ± 23 nm for ZnO/Pt/Ti/GaAs, 660 ± 20 nm for ZnO/Pt/Ta/GaAs and 611 ± 19 nm for direct deposit.

The bandgaps of ZnO films deposited on GaAs (100) with and without the buffer bilayers were obtained from ellipsometric measurements (an example is shown in Figure 37 (a)), by tracing the variation of the absorption coefficient (k) versus the photon energy. The determined bandgaps were 3.34 eV for ZnO/Pt/Ti/GaAs, 3.39 eV for ZnO/Pt/Ta/GaAs and 3.36 eV for direct growth, respectively, with a precision of 0.02 eV. The measured values were very close to the bandgap of ZnO single crystal (3.33 eV) [182]. The minor difference can originate from stress effect as measured by Raman and XRD. Moreover, the refractive index of the films was determined as a function of the wavelength (Figure 37 (b)), and the experimentally estimated refractive index of ZnO films were in a reasonable agreement with literature (close to 1.9 below 450 nm) [183]. Some minor difference can be observed on the intensity of the excitonic peak and in the visible absorption of ZnO. These differences may originate from intrinsic defect (oxygen vacancies) or ionic diffusion from the substrate as observed by SIMS.

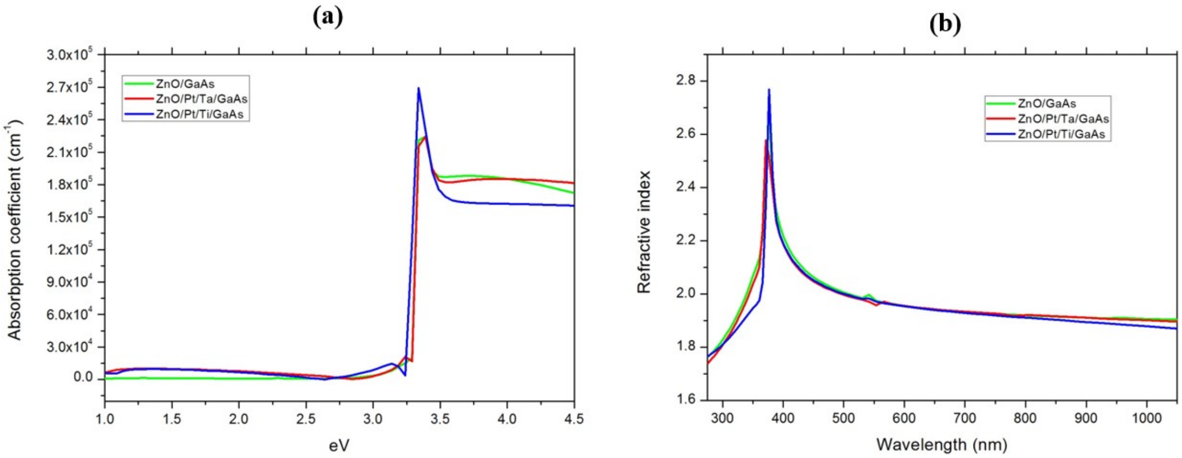

Figure 37. Absorption coefficient, k (a), and refractive index, n estimated from the fitting model for ZnO films deposited on GaAs (100) with and without Pt buffer layers

These results confirm that ZnO films present comparable optical properties (bandgap, refractive index) on the different surfaces (with and without Pt buffer layer) and that the interdiffusion between Pt/Ti/Ta/Ga did not affect the properties of ZnO.

4.4 Realization of the electrical interface

4.4.1. Production of the electrodes

After the deposition and characterization of ZnO thin films on GaAs susbtrates, electrodes were deposited on top of the ZnO films to establish the electrical contacts. This very conventional step usually consists of selectively etching layers deposited on the substrate in order to obtain the desired electrode shapes.

In the previous work [7], the electrodes consisting of a gold layer and a chromium bonding layer were deposited on GaAs. The deposition was performed on the entire surface of the substrate. Then, a resist mask was produced by photolithography for structuring the electrodes. Finally, gold and chromium were chemically etched by solutions based respectively on iodide and ammonium nitrate. However, a diffusion phenomenon was observed in the semiconductor during the deposition process which made GaAs conductive. Even by extending the etching time of metals, GaAs remained conductive. It was not possible to recover the original properties of GaAs without deeply damaging its surface.

In order to remedy this problem, the realization of the electrodes in the present work was carried out using lift-off process. This consists of depositing metal layers on the photoresist and then removing them from the areas to be protected by stripping (dissolution of the resist). After removal of the photoresist, only the electrode patterns remained on the semiconductor. No problem of inter-diffusion or penetration was observed in this situation.

For our process, we used the AZ9260 positive photoresist. Using a spincoater, a layer of photoresist was spread on top of the ZnO film. The homogeneous spreading was done by centrifugation: the wafer was fixed by suction on a rotating support, a quantity of resist was deposited on the substrate and the centrifugal force allowed the spreading of the resist uniformly in a thin film. The thickness of the resist depends mainly on its viscosity, speed and rotation time. In general, a resist is said to be positive if it becomes soluble to the developer after exposure to light, and negative in the opposite case.

A mask containing the patterns of the desired microelectrode array was designed. The design of the patterns used in the manufacture of the mask was done by V. Lacour using the software CLEWIN4. The mask allows to deposit electrodes for 21 samples at a time. Each sample has 2 pairs of electrodes: a main pair used in all the measurements and a secondary one incidentally allowing to use the device in quadrupole. Figure 38 shows the entire mask as well as the geometry of an electrode pair. The gap between the two electrodes is 200 µm, for most patterns.

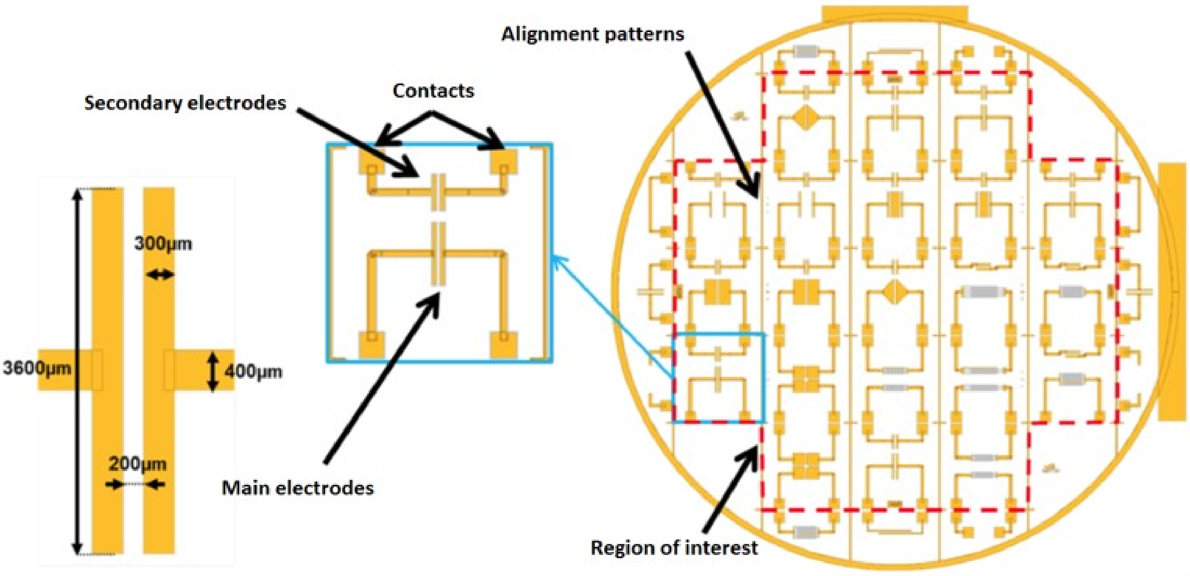

Figure 38. Patterns and mask of the electrical contacts and electrodes [12]

The mask was aligned with the resist-coated wafer using EVG aligner, and the assembly was exposed to UV light. The parameters of exposure are indicated in the Table 13.

Table 13. Tools and parameters used for the realization of the Cr/Au electrodes

Phase	Step	Tools	Parameters	Microstructure
Electrodes production by lift-off	Deposition of AZ 9260 photoresist	-Resist AZ9260 -Spin coater RC8	-Rotation time: 30 sec -Rotation speed: 3500 tr/min -Acceleration: 3500 tr/min/s	
	Annealing	Hotplate	-Duration: 6 min -Temperature: 105 °C -Rest time: 2 min	
	Insolation	-UV Lamp -Electrodes mask -Aligner DUV EVG	-Dose : 650 mJ/cm^2 -Duration = Dose/ Power -Rest time: 2 min	
	Revelation	Developer AZ 400K diluted at ¼	Revelation time: 3 min	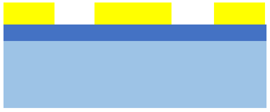
	Rinsing and drying	-DI water -Blow Gun		

	Deposition of Cr	Plassys (MP500)	-Intensity: 0.5 A -Deposition rate: 50 nm/min -Thickness: 20 nm -Duration: 30 sec	
	Deposition of Au	Plassys (MP500)	-Intensity: 0.3 A -Rate: 150 nm/min -Thickness: 200nm -Duration: 80 sec	
	Stripping	Remover 1165	-Temperature: Ambient -Duration: over night	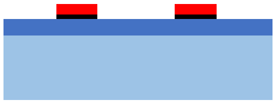
	Cleaning	Ethanol + US Spin/rinse/dry (SRD) system	Duration: 5 min Duration: 6 min	

After exposure, the mask was removed, and the substrate was immersed in a developer AZ 400K diluted 1/4 for 3 minutes to reveal the patterns. Then, a metal layer of Chromium/gold (Cr/Au, 20 nm/ 200 nm) was deposited on the surface of the sample by cathodic sputtering. After, the substrate was immersed in Remover 1165 to stripper the resin. By disappearing, it eliminates the metal that has been deposited on its surface, leaving behind the desired metallic patterns.

4.4.2. I-V characteristic of ZnO/GaAs and ZnO/Pt/GaAs devices

The I-V characteristics of ZnO/GaAs and ZnO/Pt/GaAs devices were obtained using the Keithley 3706A-S system switch and 2636B system source master, at room temperature. The voltage range was between -10 V and 10 V with a step of 0.25 V and a time delay of 0.3 sec. The Cr/Au deposited on top of the ZnO film provided the electrical contacts.

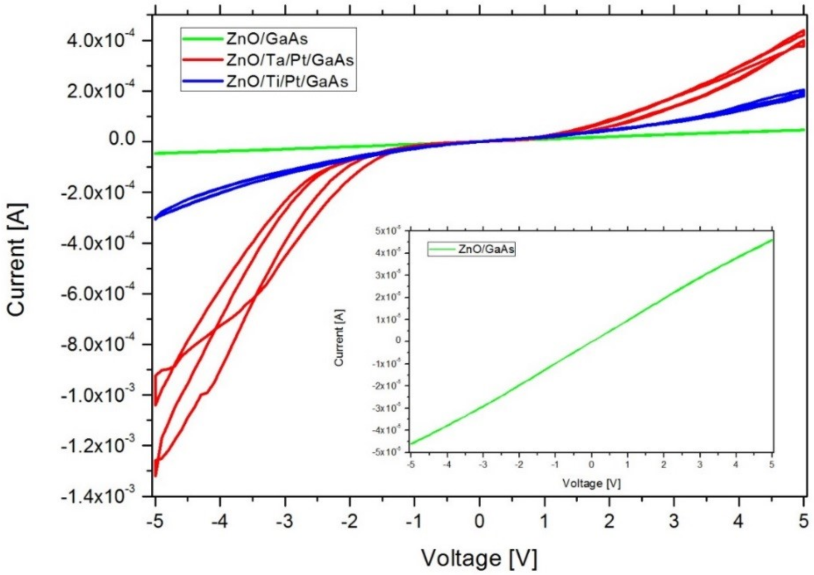

Figure 39. I-V characteristic of ZnO/GaAs and ZnO/Pt/GaAs devices

The I-V characteristic of ZnO/GaAs and ZnO/Pt/GaAs is shown in Figure 39. In the case of the direct deposition of ZnO on undoped GaAs substrate, the contact is ohmic and shows the lowest conductivity. However, in the presence of the Pt buffer layer, the conductivity is much higher and present a symmetric non-linear characteristic. It is obvious that the current flow is affected by the bottom electrode and the non-linear characteristic originates from the metal contact to the ZnO film. The symmetric characteristic arises from the symmetry of the stack structures. Some minor hysteresis is also observed that can originate from charge injection (memristive effect). For our application, the acoustic wave transducer requires the lower conductivity and the direct deposition is preferred.

4.5 Fabrication of the membrane

4.5.1 Thinning of GaAs substrates

Due to the difference in thickness between the desired membrane (50 μm) and the initial substrate (500 or 625 μm), the GaAs wafers were thinned down to 300 μm. This step does not require any masking step because we want to thin the entire substrate. To keep production at low cost, we opted for wet chemical etching. Thinning of the backside of the substrate was carried out with a solution based on orthophosphoric acid developed by Bienaimé et al. [9]. The acid is combined with hydrogen peroxide and water in the following proportions: 7 H_3PO_4: 5 H_2O_2: 8 H_2O. The process is carried at 0 °C and under normal pressure conditions providing an etch rate Er = 0.85 $\mu m.min^{-1}$. A layer of photoresist S1828 (MicroChem) was deposited beforehand on the front face of the substrate by spincoating at 4000 rpm providing a thickness of 3.8 µm. The photoresist was not developed and served to protect the ZnO film and the electrodes during the etching.

Table 14. Tools and parameters used for the thinning of the membranes

Phase	Step	Tools & solutions	Parameters	Microstructure
Thinning of the substrate	Deposition of S1828 photoresist	-S1828 photoresist -Spin coater RC8	-Rotation duration: 30 sec -Rotation speed: 1900 tr/min -Acceleration: 4000 tr/min/s	
	Annealing	Oven	-Duration: 5 min -Temperature: 120 °C -Rest time: 2 min	
	Immersion in the etching solution	-Solution: 7H_3PO_4 : 5H_2O_2 : 8H_2O -Magnetic agitator -Cryostat	-Temperature: 0 °C -Agitation speed: 300 tr/min -Etch rate: 0.85 $\mu m.min^{-1}$	
	Rinsing and stripping	-DI water -Acetone -DI water -Ethanol	At room temperature for few minutes, in the indicated order	

An assembly using a copper heat exchanger connected to the circulation circuit of a cryostat with a dedicated support for 3-inch diameter wafers has been adapted to maintain the temperature constant. The etching solution is placed in a water bath containing glycerol cooled to 0 °C. The cooling bath is temperature controlled by a submerged heat exchanger connected to a cryostat (Figure 40). The temperature of the cryostat was set at -7.5 °C to achieve a constant etch temperature of 0 °C. The tubes connecting the cryostat to the heat exchanger are isolated by a thermal sheath.

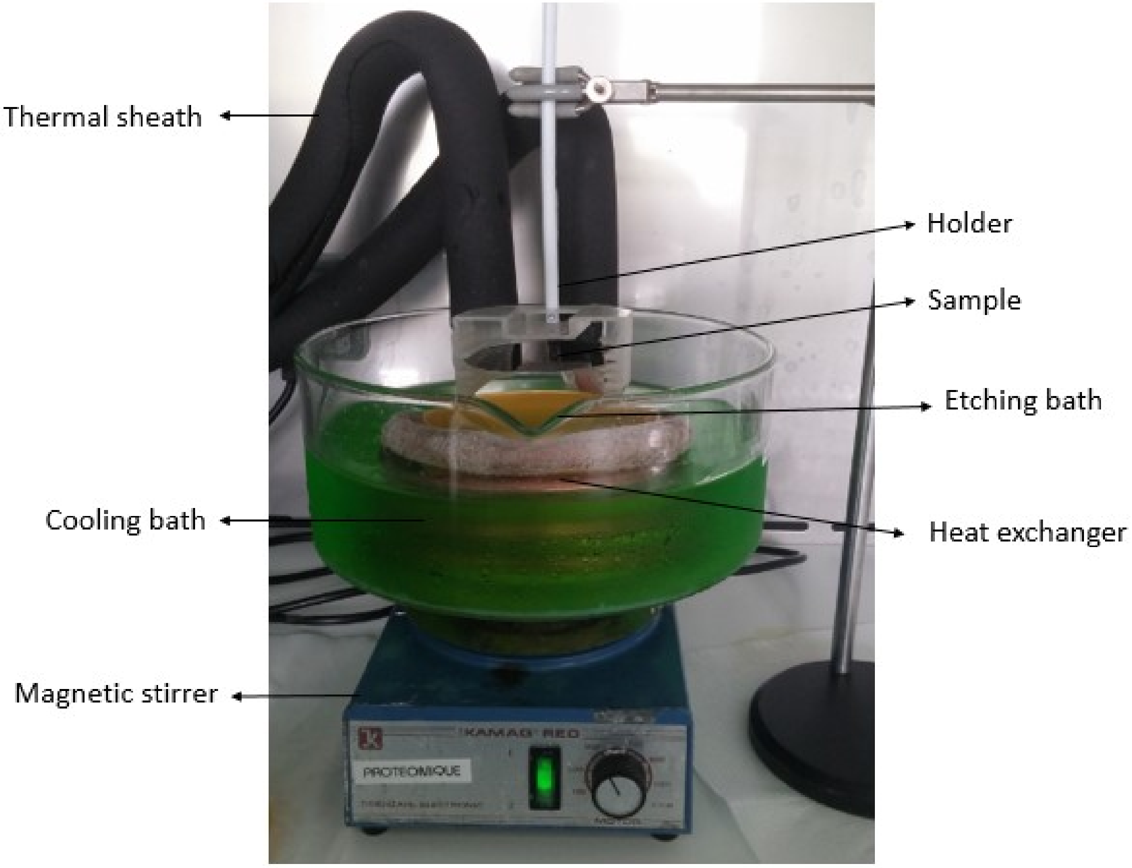

Figure 40. Assembly used for the wet etching of 3-inch wafers, with refrigerated etching bath (T = 0 °C) and magnetic stirring

The wafer to be thinned was held in the etching solution by means of a holder. It was oriented face down to the agitator to have a direct action thereof on the renewal of surface reagents. The renewal of the solution is ensured by agitation using a magnetic stirrer, with a rotation speed of 300 rpm ensuring homogeneous thinning. This strategy makes it possible to produce the electrodes on an unthinned substrate, thus not weakened. However, the flatness is not optimal especially for long engravings.

The duration D of this process was set to stop the thinning when the thickness T of the wafer reaches 300 µm using the relation: D = Er x T. At this thickness, the wafer is thin enough to avoid a long micromachining of the membrane, but thick enough to be handled without breaking. After reaching 300 µm, the wafer is removed from the etching bath and rinsed thoroughly with deionized (DI) water. Then the resist is removed by successive immersion in Acetone, DI water and Ethanol, and the thinned wafer is ready for the last step.

4.5.2 Membrane micromachining

A thick layer (3.8 µm) of photosensitive resist S1828 is deposited on both sides of the wafer. The role of this resist is, on one hand to protect the top side of the wafer (ZnO film + electrodes) and, on the other hand, to achieve the mask that will be used to structure the membrane.

Before etching the membrane, it is necessary to insolate the wafer using the mask designed for the membranes. The geometry of membranes consists of squares of 4 mm of side. In order to separate the devices, 200 µm wide cutting lines have been added to the mask. For the correct operation of the sensor, the membranes must be aligned with the electrodes, located on the other side of the wafer. It is possible to use the wafer marks (alignment flat and centering on the contours), but the precision would not be optimal. To ensure alignment between the two faces, it is necessary to first align the two masks with each other thanks to the alignment crosses provided for this purpose. Next, the electrodes of the chip are positioned with the corresponding patterns plotted on the mask of the electrodes. Once aligned, the patterns corresponding to the membranes are exposed using a double-sided aligner (DUV EVG) while switching off the lamp on the electrode side.

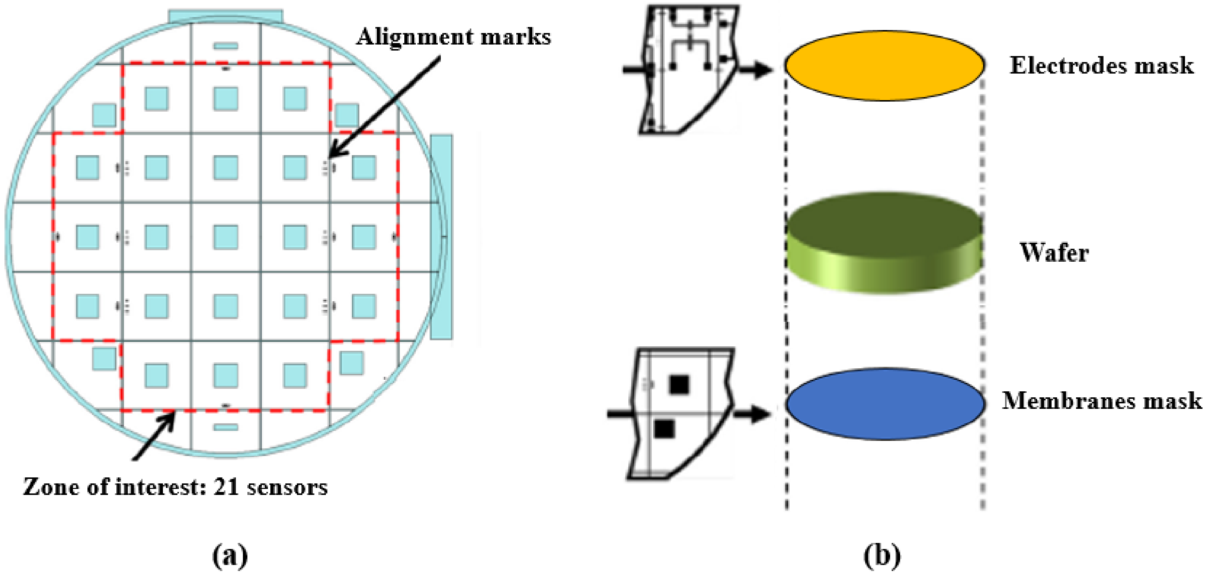

Figure 41. (a) Masks for etching membranes (b) Alignment of masks with GaAs wafer

After patterning, the wafer is immersed in the etching solution 1 H_3PO_4: 9 H_2O_2: 1 H_2O using the previous assembly. The expected etching depths are relatively high and therefore require very long etching times (5-7 hours). However, the efficiency of the reaction decreases significantly after a few hours of etching due to the depletion of the solution in reagents and to the increase of the reaction products. For the duration of the operation, the etching rate of the solution varies, in general, from 4 to 0.5 μm.min^{-1}. Therefore, it was essential to measure and control the thicknesses after each step, as well as the etching rates and defects, by means of profilometry and/or optical microscopy. For a duration of 4 hours, we obtained an average etching rate of about 1 μm.min^{-1}.

Table 15. Tools and parameters used for the micromachining of the membranes

Phase	Step	Tools & solutions	Parameters	Microstructure
Machining of the membranes	Deposition of S1828 photoresist double side	-S1828 photoresist -Spin coater RC8	-Rotation duration: 30 sec -Rotation speed: 2500 tr/min -Acceleration: 4000 tr/min/s	
	Annealing	Oven	-Duration: 5 min -Temperature: 120 °C -Rest time: 2 min	
	Insolation of the membrane	-Aligner EVG 620 -Masque designed for membranes	-Dose : 130 mJ/cm^2 -Duration : Dose/ Power -Rest time: 2 min	
	Revelation	Developer MF26A	Revelation time: 2 - 3 min	
	Etching of the membrane	-Etching solution: $1H_3PO_4$: $9H_2O_2$: $1H_2O$ -Magnetic agitator	-Temperature: 0 °C -Agitation speed: 500 tr/min -Etch rate: 1 μm.min^{-1} -Duration: D = Er x T	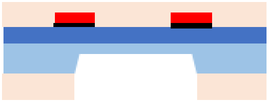
	Rinsing and stripping	-DI water -Acetone -DI water -Ethanol	At room temperature for few minutes, in the indicated order	

After etching, the wafer was rinsed several times with DI water then the resist is removed by successive immersion in Acetone, DI water and Ethanol. Figure 42 shows an example of ZnO/GaAs wafer after realization of the electrodes and the membranes.

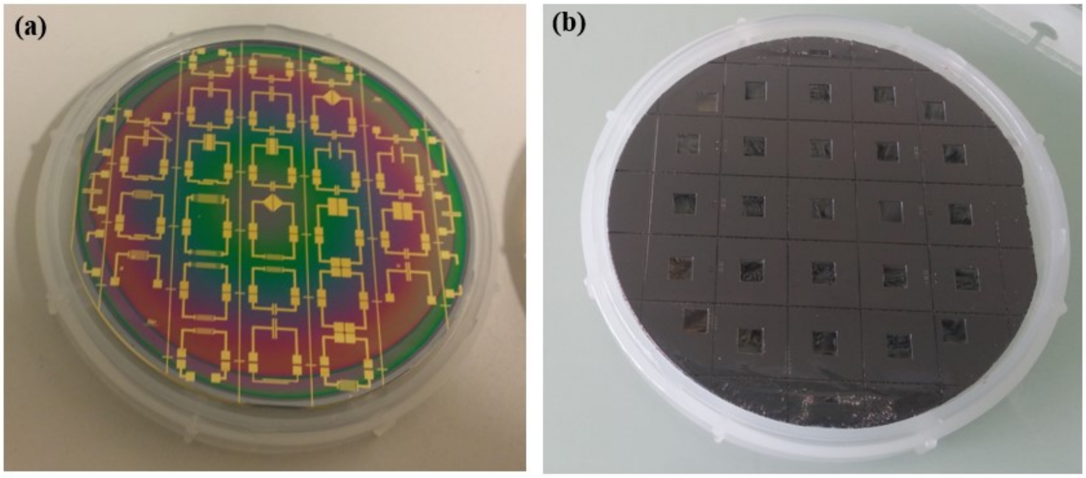

Figure 42. Photo of a ZnO/GaAs wafer (AXT – AV 503-93) after the realization of the electrodes on the top side (a) and the membranes on the bottom side (b)

After the micromachining, the obtained membranes are characterized using the profilometer Tencor Alpha-Step IQ in order to determine their thickness and roughness. For each wafer, 4 membranes were characterized (2 near the center and 2 near the edges).

For example, profilometric measurements carried out on wafer AXT – AV 503-89 indicated an average depth of 145.3 ± 3.7 µm for the central membranes and 154.9 ± 12.1 µm for the ones near the edges. These values around 150 µm differ slightly, which is certainly due to the thickness inhomogeneity caused by the thinning stage. The average arithmetic and quadratic roughnesses are respectively equal to Ra = 66.6 ± 7.6 nm and Rq = 82.3 ± 8.2 nm. These measurements have validated the machined depths.

4.6 Conclusion

Piezoelectric ZnO films were deposited on semi-insulating GaAs substrates using reactive RF magnetron sputtering, to enhance the piezoelectric performances of the existing GaAs-based acoustic wave sensor. The effect of the crystalline orientation of the GaAs substrate on ZnO films properties was studied using different characterization techniques. GaAs (100) was particularly privileged for promoting the growth of well-textured ZnO films. Furthermore, the use of a Pt buffer layer was investigated, using Ta or Ti adhesion layers. The XRD and AFM measurements confirmed that this buffer improves the crystalline and structural quality of the films, in terms of texture, stress and roughness. However, the buffer layer promotes the diffusion of Ga, interface layers (Ta, Ti) and ZnO itself into the Pt. Moreover, the ohmic contact required for our application was only observed in the ZnO/GaAs structure, making the direct deposition of the ZnO film on GaAs substrate a more adequate approach.

After the deposition and characterization of ZnO thin films and its interface with GaAs, we proceeded to the realization of the electrodes by lift off, then to the membrane micromachining. Among the different microfabrication techniques, we have opted for chemical wet etching due to the simplicity and large-scale reproducibility of this process.

After the fabrication of the structure, the bio-interface will be established on GaAs at the bottom side of the sensor and then characterized to ensure its efficiency for the capture of the targeted bacteria: *Escherichia coli*.

Chapter 5: Realization and characterization of the bio-interface on the sensor surface

The detection of biological entity, including bacteria, involves the immobilization of a specific ligand on the surface of the biosensor. The main challenge is to be able to detect the targeted bacteria present in very small concentrations and in complex liquid environments. It is therefore necessary to develop a robust and reproducible sensor bio-interface. Through the characteristics of the immobilization methods exhibited in the state of the art and based on the preceding work in the research group, the covalent immobilization of ligands via SAMs presents many advantages and suits our application. Indeed, the formation of monolayers of high organization and density allows the immobilization of the ligands in a durable, robust and reproducible way. Furthermore, this approach allows, potentially, the reusability of the biosensor by regeneration of the bio-interface.

The present chapter is divided into two main parts. The first part concerns the surface functionalization of GaAs (the bottom side of the BAW biosensor) with SAMs of alkanethiols. Given that the previous work in the research team has detailed different principles and techniques of SAMs formation on GaAs and their characterization, this section presents only the important notions and focuses on a mixed SAM composed of MHDA/MUDO (1:9 molar ratio). MHDA (16-Mercapto-1-hexadecanoic acid) of linear formula $HS\text{-}(CH_2)_{15}\text{-}COOH$ consists of a chain of 16 carbons and a carboxyl terminal group, while MUDO (11-Mercapto-1-undecanol) of linear formula $HS\text{-}(CH_2)_{11}\text{-}OH$ consists of a chain of 11 carbons and a hydroxyl terminal group. The difference in chain length facilitates the interactions between proteins and MHDA. The second part of this chapter deals with the immobilization conditions of the ligands. In order to ensure an optimal capture of bacteria, different conditions (concentration, duration, pH) for ligand immobilization were tested.

The experiments presented in this chapter were conducted in the LCSM laboratory (*Laboratoire de Caractérisation des microsystèmes et Synthèse des Matériaux*) of the 3IT institute in Sherbrooke (Canada).

5.1 Bio-functionalization strategy

The selection of the ligand is essential to achieve a sensitive and selective detection of the targeted biological element. The decisive criteria are the effectiveness of the bio-recognition (specificity, sensitivity), the conditions of detection and the type of targeted analytes (from molecules to cells). Moreover, the determination of an immobilization architecture is critical for the optimization of specific interactions with the medium to be analyzed. It can affect the orientation, the density and the accessibility of the ligands [184]. Several functionalization chemistries studied in the literature on metal substrates can be applied to deoxidized GaAs, consolidating the choice of this material.

Our strategy for capturing the biological target is based on immunological recognition. We aim to detect *E. coli* bacteria through its immunocapture using antibodies against *E. coli* immobilized covalently on the GaAs membrane via a mixed SAM of alkanethiols MHDA/MUDO (1:9 molar ratio). The chosen SAM has proved in previous studies to ensure an efficient and reproducible immobilization of antibodies [10]. Bovine serum albumin (BSA) is used to passivate the surface, and ethanolamine is employed for blocking the activated carboxyl groups that did not react with a ligand. The main stages of surface bio-functionalization are represented in Figure 43 and the used protocols will be presented in detail in the following sections.

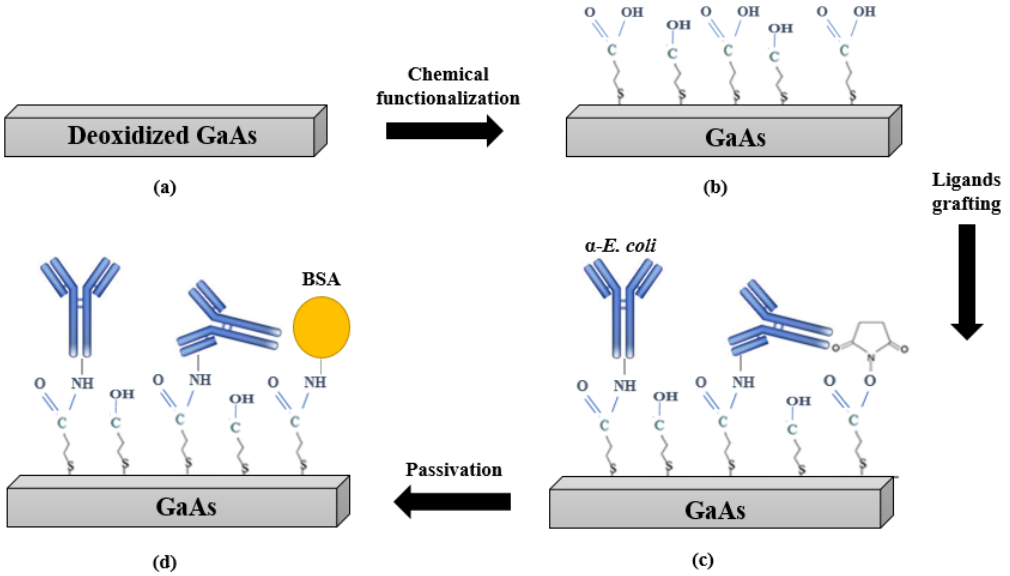

Figure 43. Schematic representation of the bio-functionalization stages: (a) bare and deoxidized GaAs surface, (b) MHDA/MUDO (1:9) chemical functionalization, (c) immobilization of antibodies anti-*E. coli*, (d) surface passivation.

5.2 Chemical functionalization of GaAs membrane

5.2.1. SAMs formation on GaAs

SAMs are organic layers that modify the chemical properties of the surface. The constitutive molecules of SAMs generally consist of a surface-active head group, a spacer and a terminal functional group (Figure 44).

- **The surface-active head group:** It is the chemical function allowing the specific adsorption of the organic molecule on the substrate. The main functional group used for deoxidized GaAs is thiol (-SH).

- **The spacer:** It constitutes a physical barrier that limits the interactions of the external environment with the substrate. It may consist of chains of different lengths and natures. The spacer commonly used for GaAs is generally constituted by an alkyl chain of at least ten carbons allowing the organization by Van der Waals interactions. Polyethylene glycol (PEG) chains have been also used in our team and seem to reduce non-specific interactions due to their hydrophilic properties [57], [185].

- **The functional group:** It determines the physicochemical properties of the monolayer. In the case of GaAs, the choice of the functional group is adapted to the required function: carboxyl for the immobilization of molecules and hydroxyl for the protection against non-specific adsorption. Several functional groups are often associated in the same self-assembled layer to obtain a mixed layer, presenting both biomolecule attachment zones and inert zones, and making it possible to reduce non-specific substrate/biomolecule interactions.

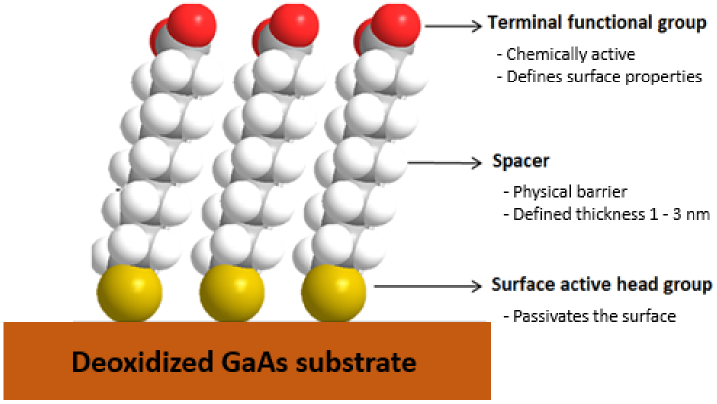

Figure 44: Organization of SAM on the surface of deoxidized GaAs substrate

Surface functionalization with SAM is a strategy of choice because it allows to passivate the surface of the material while proposing a high density of bonding sites for ligands. The functionalization of GaAs surface by a monolayer of chemical molecules is generally fast (few hours) and easy (by immersion in solution). It is a process that is simple to implement and, depending on the type of molecules, can be achieved at low cost. As mentioned in section 2.3.2., the procedure of formation of SAMs on GaAs requires the deoxidation of the surface right before the functionalization. Different chemistries can be used to deoxidize the surface of GaAs: solutions of acids (HCl, H_3PO_4 or H_2SO_4) or bases (NH_4OH). Unlike NH_4OH, acids seem to modify the stoichiometry of the GaAs surface which becomes richer in arsenic. A surface rich in arsenic is not favorable to the organization of SAMs, since it is extremely reactive and quickly re-adsorbs contaminants from the air or the etching/rinsing solutions [186], [187]. Therefore, NH_4OH is chosen in our protocol for deoxidizing GaAs.

Immunoreceptors are at least an order of magnitude larger than the molecules constituting the SAMs. The antibodies, used as ligands in this work, are 10 - 20 nm in height [188] and occupy a surface of roughly 5 - 20 nm^2, while the molecules used for SAM have a height in the range of 1 to 3 nm and occupy a surface of 0.05 - 0.2 nm^2. Thus, an antibody can cover up to 100 thiols. This means that the majority of the surface thiols will not form a covalent bond with the receptor, although some thiols may bind to different amine groups of the antibody. In order to facilitate the immobilization of the receptors, to promote their relative flexibility, to improve the stability and reproducibility, and to avoid the non-specific absorptions on the surface, it is proposed to use a so-called mixed architecture [189], [190]. Such architecture offers many advantages for immunocapture applications. Some studies on the formation of mixed SAMs on gold substrates have revealed a higher density of immobilized ligands compared to a monomolecular SAM [191], [192]. Generally, these architectures are composed of "linker" molecules that immobilize the receptors, diluted with other molecules called "diluent" that will prevent the non-specific adsorptions on the surface [189]. The alkanethiol used as diluent allows to avoid the steric hindrance associated with the immobilization of the antibodies. Indeed, the use of linker with longer chains than diluent thiols will, in the ideal case, make more accessible the head groups necessary for the immobilization of ligands. The use of an optimal diluent/linker couple is determined to offer the most degrees of freedom to the linkers while avoiding their folding. This type of effect has been studied in our research team, particularly for the functionalization of GaAs substrates for protein layer immobilization [10], [11].

The functionalization approach used in this work is composed of the following two alkanethiols: MHDA and MUDO. The carboxylic acid is used to provide a covalent bond with the antibody (amide bond), while the hydroxyl-terminated thiols passivate the substrate and space the MHDA. The covalent bond with the carboxylic acid is carried out with one of the amine groups of the protein after a so-called NHS/EDC COOH activation procedure. Compared with other terminal groups (CH_3, NH_2, PheOH), it has also been shown that hydroxyl-terminated thiols significantly limit non-specific interactions [193].

5.2.2. Functionalization procedure

The fabricated samples were placed in a holder (Figure 45) designed in Teflon to only expose the bottom side (GaAs membrane) to the solutions while protecting the top side (ZnO thin film + Cr/Au electrodes). The protection of the top side is crucial for two purposes:

1) To avoid the exposure of the ZnO thin film to the solvents and etchants during the preparation of the samples.
2) To prevent thiols from being deposited on the gold electrodes. This would result in the passivation and change of conductivity of the electrodes and influence the measured signal subsequently.

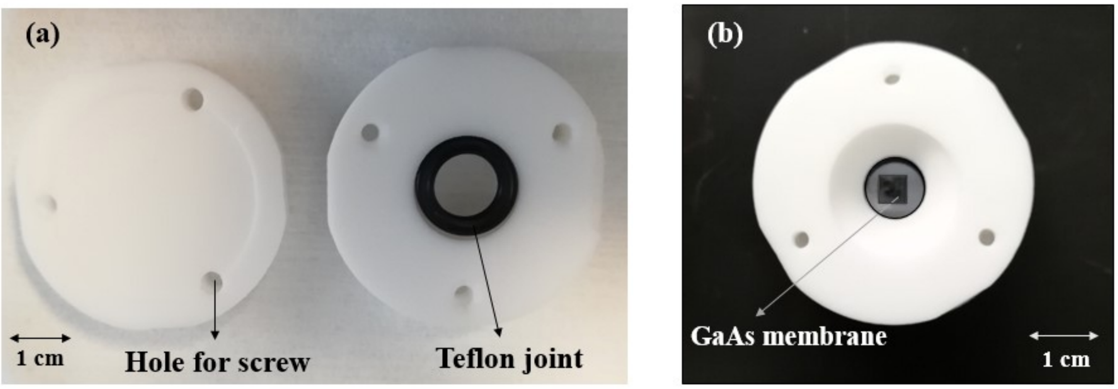

Figure 45. (a) Top and bottom sides of the samples holder, (b) positionning of the sample in the holder

Once the sample is placed in the holder, solvents were added in the following order: OptiClear, Acetone then Ethanol. After adding each solvent, the holder was placed in a sonicator for 5 minutes. Afterwards, solvent is removed, and the sample is dried.

GaAs has a high reactivity to oxygen atoms, so an oxide layer is naturally formed. Therefore, a deoxidization step is necessary before the chemisorption of the thiols on the GaAs, since the sulphide groups bind directly to the Ga and As atoms [73], [74]. Hence, the samples were exposed for 2 minutes to Ammonium Hydroxide (NH_4OH, 28 %) then briefly rinsed with deoxygenated ethanol. The latter was prepared beforehand by degassing anhydrous ethanol for 1 hour by a flow of Nitrogen. After, the samples were immediately incubated in MHDA/MUDO (1:9) at 2 mM thiol solution for 20 hours at room temperature and protected from light to avoid the photooxidation of the substrate. A reference for the measurements is always provided via a freshly deoxidized GaAs membrane incubated in deoxygenated ethanol for 20 hours.

The alkanethiols were solubilized in deoxygenated ethanol as well. This process makes it possible to minimize the presence of oxygen in the thiol solutions and to avoid the formation of oxide before and during the functionalization step. This step also makes it possible to promote the reproducibility of the process. Once degassed, ethanol is used immediately for the preparation of alkanethiol solutions, or for rinsing.

After 20 hours, the samples were rinsed thoroughly with degassed ethanol, followed by ultrasonic cleaning for 30 sec in degassed ethanol to remove the physisorbed thiols. Finally, the samples were dried under nitrogen flow.

Once mixed, the thiols have different reactivity with the surface and their proportions change when self-organizing on the surface. Indeed, the transfer of the molecules from a 3D space (solution) to 2D (GaAs surface) causes different reactivity of the molecules and is dependent on the polarity and charge of the molecules. This difference in reactivity is mainly due to the nature of the functional group of the thiols and to the chain length, which affects the diffusion speed. Therefore, it is crucial to characterize the surface after functionalization to examine the organization of the thiols and to confirm the formation of the SAM on the GaAs surface.

5.3 Characterization of SAMs on GaAs membrane

SAMs constitute the basis of the bio-interface, and a well-organized and dense SAM is required to ensure an effective and reproducible immobilization of ligands. Therefore, the characterization of this chemical interface is essential to better understand its organization, its composition, and its homogeneity. A systematic characterization of SAMs was carried out using contact angle measurements, Fourier-Transform Infrared (FTIR) spectroscopy and X-ray Photoelectron Spectroscopy (XPS). Going from macroscopic to microscopic scale, these techniques allow proving the presence of thiols on the surface (satisfactory functionalization of GaAs surface), examining their quality (organization, ratio, density).

5.3.1 Contact angle measurements on the SAM-coated membrane

The validation of the presence of the thiols on the GaAs surface can be obtained through measurements of surface energies. This technique makes it possible to evaluate the difference in wettability of the studied surface. This difference originates from the change of the surface chemical functional group ($-CH_3$, -COOH, -OH ...) which causes the inclination of the carbon chains composing the SAM and organizational defects.

Contact angle measurements were performed using the setup presented in Figure 46. The measurements were carried out in an enclosed chamber to control the evaporation conditions. A drop of 20 µl of deionized water was deposited on the surface of the samples using a micro-syringe, and the images were captured about 10 seconds later. The angle measurements were performed using the DropSnake plugin [194] on the ImageJ® software. For each measurement, the static contact angle is calculated to the right and to the left of the drop with a typical error of ± 3 °, and the results are then averaged. Measurements were carried out on membranes functionalized with MHDA/MUDO (1:9), and on freshly deoxidized GaAs membranes, considered as a reference to compare the difference in surface tensions. In each case, 3 samples were tested. Figure 47 shows an example of the droplet shape on each surface.

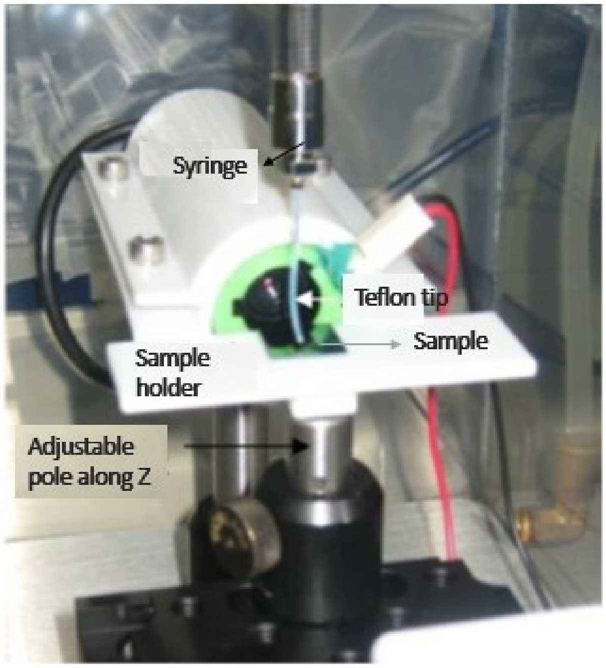

Figure 46. Contact angle measurement bench (modified from the LCSM training manual)

The contact angle measured on deoxidized GaAs is at 59 ° which is close to the 57 ° value reported by Huang et al. [75]. This minor difference in the contact angle measured on bare GaAs is probably due to the re-oxidation of the substrate before the measurements or the differences in surface conditions (polishing, cleaning and etching reagents, surface termination…) between different GaAs wafers.

The contact angle measured for GaAs functionalized with MHDA/MUDO (1:9) is of 71.5 ± 3 °. To assess the measured value, we compared it to the contact angles for GaAs surfaces functionalized with SAMs of pure MUDO and pure MHDA reported in a previous study in the group [12]. The reported angle for a GaAs surface functionalized with pure MUDO is 45 ± 2 °, which is expected due to the terminal hydroxyl group. On the other hand, the reported angle of GaAs surface functionalized with a SAM of pure MHDA is 90 ± 2 °, which is surprising since the carboxyl terminal group is hydrophilic. However, the combination of different parameters, such as the proximity of long hydrophobic carbon chains, the hydrophilic terminal groups as well as the pronounced inclination of this type of layer on the surface, can explain this intermediate value of surface tension for pure MHDA functionalization. Therefore, the measured angle for MHDA/MUDO (1:9) corresponds to a value between the reported angles for pure MUDO and MHDA. This value therefore corresponds to the presence of both types of molecules on the surface. Furthermore, it is close to the value reported for 3 % MHDA by Bienaimé et al., consolidating our findings.

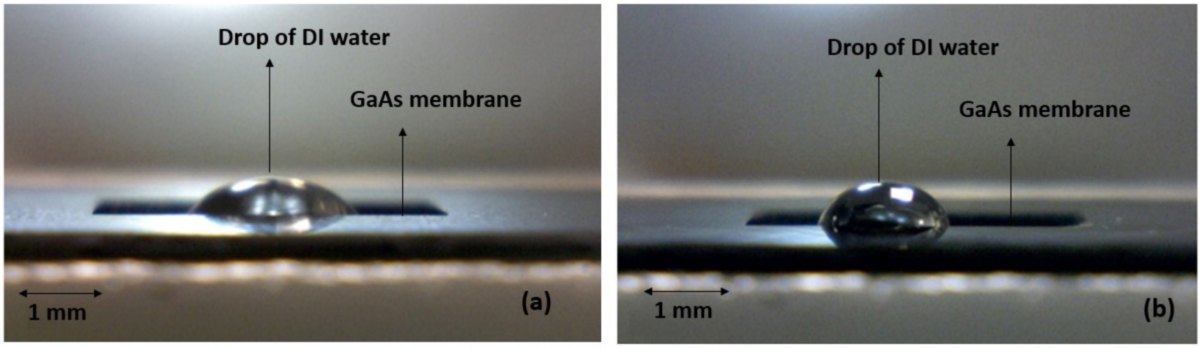

Figure 47: Photos of a 2 µl drop of deionized water on the surface of GaAs membrane (a) freshly deoxidized and (b) functionalized with MHDA/MUDO (1:9) (N = 6 samples)

The measurements of static contact angle remain difficult to reproduce from one device to another, and therefore the comparison with other authors is not accurate. By cons, we can validate the presence of thiols on the surface of the samples based on the hydrophilic or hydrophobic character that the surface should have. In our case, the difference in the wettability of the surfaces between bare and functionalized GaAs surface clearly shows a modification of the surface state due to the presence of molecules of MHDA and MUDO.

5.3.2 FTIR characterization of SAM on GaAs membrane

Within the previous thesis, FTIR has proved to be a characterization technique of choice for SAM, since it allowed to understand the formation kinetics of mixed SAMs of alkanethiols on GaAs. FTIR can provide information about the density, organization and proportions of the thiols within the SAM. In particular, the position of the νCH_2 bands shows the conformity of arrangement of the molecules constituting the SAM. The monolayers can thus be described according to the position of their peaks of methylenes. In order to prove the establishment of a mixed SAM of MHDA/MUDO on GaAs surface, the νCH_2 bands were examined using FTIR.

The FTIR measuring system is a Vertex 70v from Bruker Company equipped with a RockSolid interferometer and a wide-range Globar IR source covering 6000 to 10 cm^{-1}. The signal is collected with a liquid-nitrogen-cooled MCT (Mercury-Cadmium Telluride) IR detector, and a resolution of 4 cm^{-1}. Transmission spectra of chemically functionalized GaAs membranes are recorded with Bruker Vertex 70v spectrometer (512 scans) interfaced with a computer using OPUS Bruker Optics software. A reference for the measurements is provided via a freshly deoxidized GaAs membrane incubated in deoxygenated ethanol solution for 20 hours, then rinsed and dried under Nitrogen flow. Measurements are carried out under vacuum and spectra of SAMs were subtracted from the spectrum of the reference.

FTIR results for GaAs membranes showed a very high noise level compared with those obtained with bulk GaAs samples, which made it difficult to examine the CH_2 peaks relative to the SAM. The high noise in the spectrum (Figure 48) is probably caused by interference due to the low thickness of the membranes (down to 100 μm), which can be explained by the Fabry-Perot principle. It states that the varying transmission function of a standard is caused by the interference between the multiple reflections of light between the two reflecting surfaces. So, the interference pattern can be used to determine the refractive index of the film with the following expression:

$$n = k/(2\ \delta\upsilon\ t) \tag{5.1}$$

with t the sample thickness, k the number of fringes in the wavenumber region, and $\delta\nu$ the wavenumber region used [195].

Indeed, using the $\delta\nu$ and k from the FTIR spectra and GaAs refractive index ($n = 3.94$), we were able to recalculate the thickness of the measured sample. Moreover, the interference is less pronounced when the sample is thick, which explains why the signal noise was lower on the edge of the membrane (~360 μm) and negligible for bulk GaAs samples (~ 617 μm).

To solve the problem of interference, two solutions were tested: the first one consisted in tilting the sample during the measurement, which resulted in reduced signal intensity. The second method consisted of processing FTIR spectra/data using OriginPro 8 software. After determining the interference period, we calculated the corresponding frequency and we applied an FFT (Fast Fourier Transform) filter with a fixed value of the frequency, which allowed to subtract the noise from the signal. Figure 48 shows an example of processing an FTIR spectrum of a 220 μm thick functionalized membrane, displaying the symmetric (2851.6 cm^{-1}) and asymmetric (2922.8 cm^{-1}) CH_2 peaks. The presence of the CH_2 peaks confirms the presence of the thiols on the GaAs membrane.

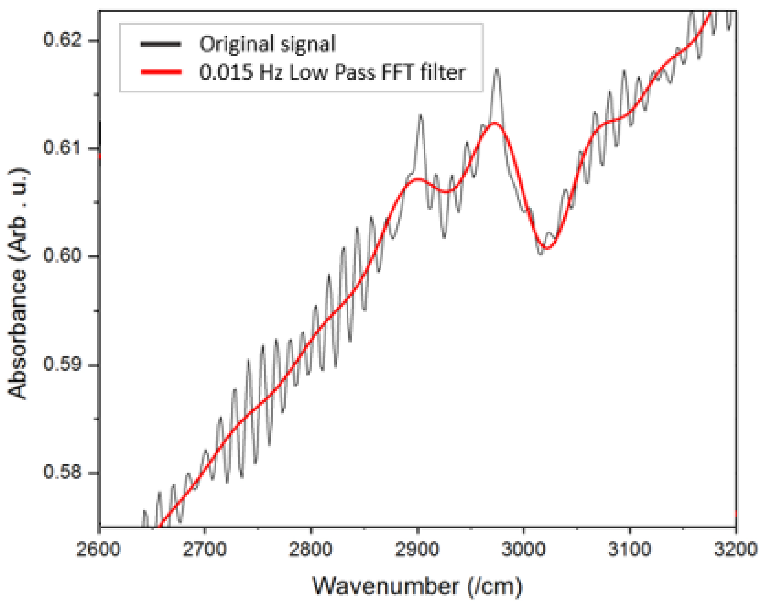

Figure 48: FTIR spectra of MHDA/MUDO (1:9) functionalized membrane (220 µm thickness)

Although FTIR is a technique of choice, we were not able to extract exact information about the organization and density of the SAM, even with the signal filtration. Therefore, we opted for a characterization using X-ray photoelectron spectroscopy (XPS), searching for a solid proof of the formation of MHDA/MUDO SAM on the GaAs membrane.

5.3.3 Proof of Ga-S and As-S covalent binding by XPS

XPS is a quantitative spectroscopic technique for the determination of the chemical composition of a material. The surface of the material is irradiated by X-rays which ionize the constitutive atoms by photoelectric effect. The photon interacts with the valence band by ejecting one of its electrons. XPS spectra show the number of electrons in counts per second (CPS) as a function of their binding energy. Since the binding energies are dependent on the electronic orbital of the ejected electron, the peaks obtained on the XPS spectrum correspond not only to a specific atom, but their position varies according to the nature of their bonds with the neighboring atoms. The intensities of photoelectrons are proportional to the concentration of the element from which it is ejected. By normalizing the number of electrons of each type detected by a certain sensitivity factor, it is possible to obtain the relative ratios between each atom and thus to obtain the chemical composition of the sample. X-rays can penetrate the surface of the sample over several micrometers, but only a fraction of electrons near the surface (~ 10 nm) has enough energy to be ejected without being scattered. This allows to characterize the surface with a high finesse.

We wish to demonstrate with this method the covalent binding of the sulfur atoms of the monolayer of alkanethiols on the GaAs membrane. For that, the analysis was carried out in the vacuum chamber of the XPS (Kratos Analytical, AXIS Ultra DLD) system under a pressure of 1×10^{-9} Torr. The data were collected for a takeoff angle of 60 ° with respect to the surface normal. In this configuration, the measured depth is reduced from 10 to 5 nm, allowing a better resolution and a finer characterization. The surface survey scans were observed with a 75 W Al Kα source operating in a constant energy mode at the 20 eV pass energy. The analyzed area was of dimensions 300 μm × 700 μm, and charge corrections were made using the adventitious saturated hydrocarbon at a peak energy of 285 eV. The XPS results were analyzed with CASA XPS 2.3.18. The relative sensitivity factors used for quantification purposes are the experimental values provided by Kratos Analytical for their instruments.

XPS survey spectra for bare (deoxidized) and chemically functionalized membranes are shown in Figure 49. The results are dominated, as expected, by C, O, Ga and As XPS features. While the adventitious saturated hydrocarbon is frequently the source of C 1s peak observed at 285 eV in deoxidized membranes, the significantly greater atomic concentration percentage of C (Table 16) in the sample coated with MHDA/MUDO (1:9) SAM formed in ethanol is consistent with the increased contribution from hydrocarbons present in the MHDA and MUDO thiols.

Table 16. Main elements detected on the surface of freshly deoxidized GaAs and MHDA/MUDO (1:9) SAM coated GaAs

		Freshly deoxidized GaAs		MHDA/MUDO (1:9) SAM-coated GaAs	
XPS peak	Binding energy (eV)	FWHM	% Atomic concentration	FWHM	% Atomic concentration
C 1s	285	2.4	21.2	2.6	43.6
O 1s	531	3.5	31.1	3.3	22.5
Ga 3d	19	2.5	26.3	2.7	20.9
As 3d	41	2.4	21.4	2.6	13

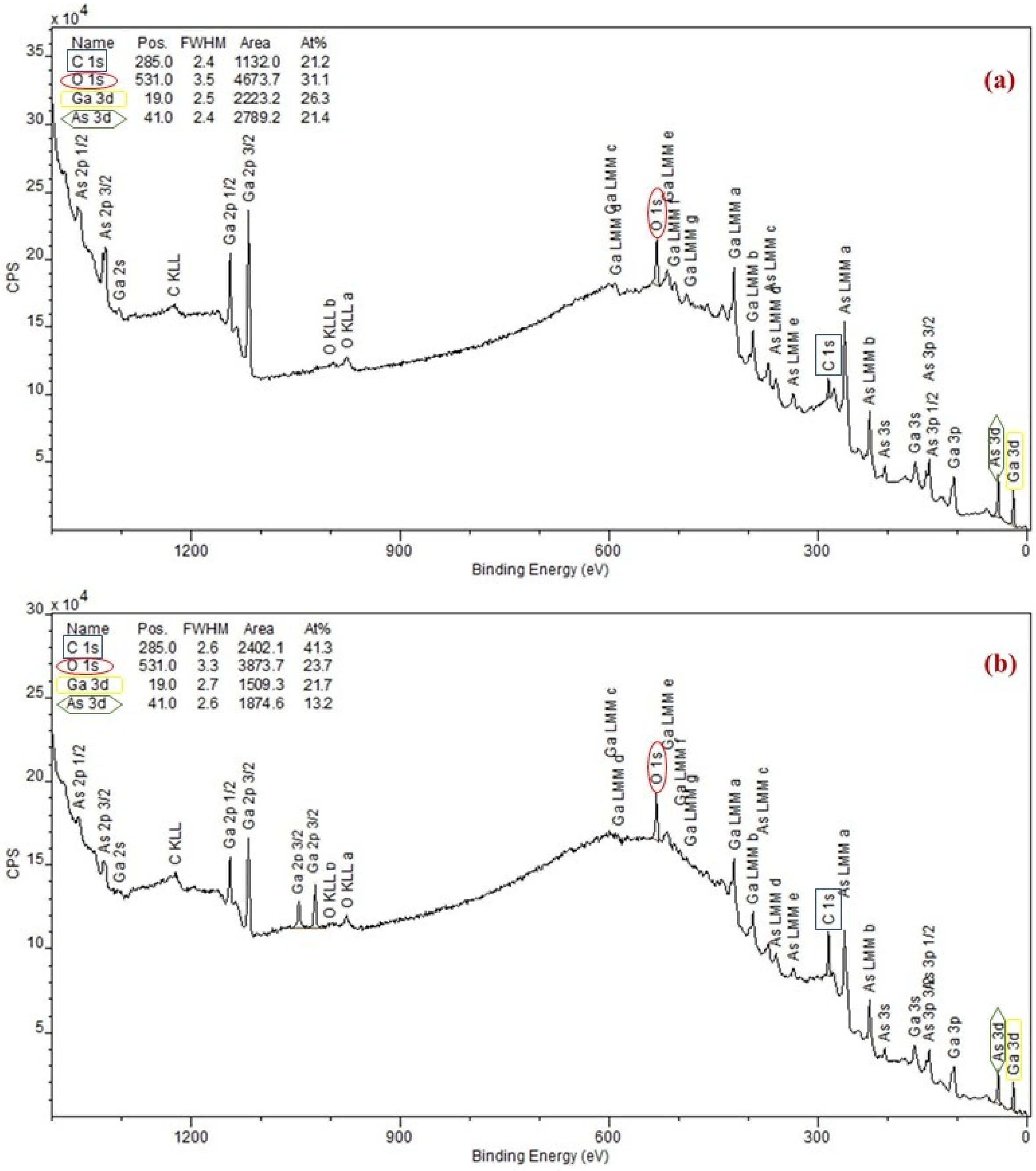

(a)

Name	Pos.	FWHM	Area	At%
C 1s	285.0	2.4	1132.0	21.2
O 1s	531.0	3.5	4673.7	31.1
Ga 3d	19.0	2.5	2223.2	26.3
As 3d	41.0	2.4	2789.2	21.4

(b)

Name	Pos.	FWHM	Area	At%
C 1s	285.0	2.6	2402.1	41.3
O 1s	531.0	3.3	3873.7	23.7
Ga 3d	19.0	2.7	1509.3	21.7
As 3d	41.0	2.6	1874.6	13.2

Figure 49. XPS spectra of (a) deoxidized GaAs membrane and (b) GaAs membrane functionalized with MHDA/MUDO (1:9)

High resolution XPS spectra were also obtained over shorter energy ranges. Spectra were obtained from the O 1s, C 1s, As 3d, Ga 3s, and Ga 3d core levels. Nevertheless, we are mainly interested in the C 1s, As 3d and Ga 3s levels. The parameters for their individual component peaks, e.g. branching ratio, binding energy, percentage of atomic concentration and FWHM are provided in Table 17.

Table 17. Parameters of the individual peaks determined for deoxidized GaAs and MHDA/MUDO (1:9) SAM coated GaAs

Branching ratio	Deoxidized GaAs			MHDA/MUDO (1:9) SAM-coated GaAs		
	Binding energy (eV)	FWHM (eV)	%At Conc	Binding energy (eV)	FWHM (eV)	%At Conc
C 1s C-C, C-H	284.8	1.2	21.1	285.1	1.2	35.3
C 1s C-O	286.3	1.2	2.5	286.5	1.2	3.9
C 1s COO				289.1	1.2	1.9
Ga 3s	160.2	3.2		160.1	2.9	
As plasmon	156.2	2.5		156.4	2.7	
S 2p3/2				161.9	1.6	
S 2p1/2				163.1	1.6	

The oxygen spectra were not evoked in this analysis since the increase of the O 1s peak can be at the same time related to the presence of hydrophilic functional groups carried by the MUDO and MHDA molecules (both containing oxygen atoms), and to the native oxidation of the GaAs surface. Therefore, we can not rely on the increase of the O 1s peak to prove the functionalization of GaAs surface.

The examination of the C 1s peak shows that the intensity is low (5.8×10^3 CPS) on bare GaAs surface, indicating that carbon contamination in the ambient air is low. After functionalization of the surface, its intensity increases strongly (2.7×10^4 CPS). The functionalized surface exhibits a pronounced peak with a binding energy of 285.1 eV, which is a value consistent with previous work [7], [12]. The presence of new contributions of higher energy is revealed, certainly induced by the presence of hydroxyl and carboxyl groups of MUDO and MHDA molecules. Indeed, the two peaks at 286.5 eV and 289.1 eV (Figure 50) correspond respectively to binding with the hydroxyl (OH) groups of MUDO and carboxyl (COOH) of MHDA.

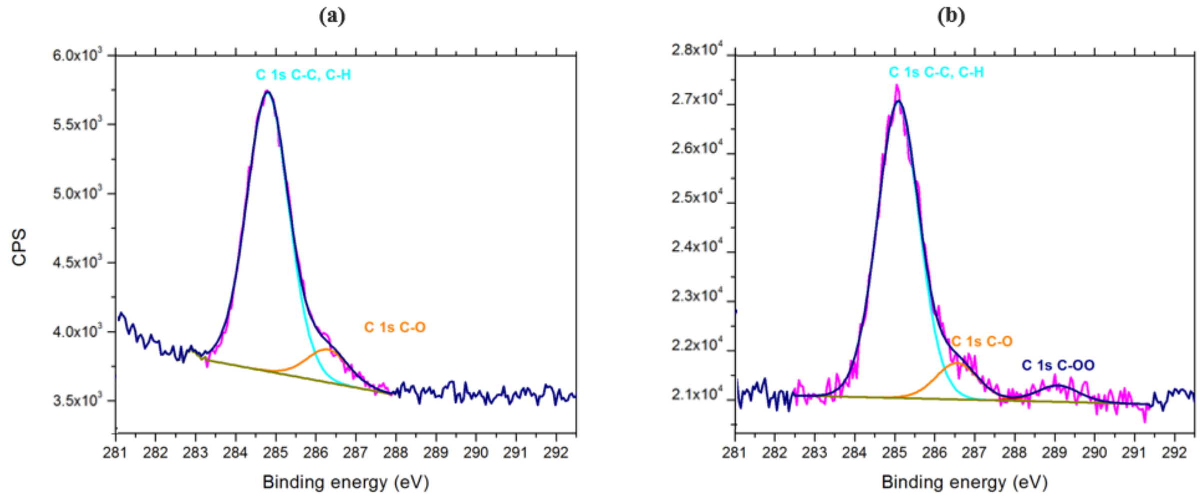

Figure 50. High-resolution C 1s XPS spectra of (a) deoxidized GaAs membrane and (b) MHDA/MUDO (1:9) SAM coated GaAs membrane

The Ga 3s and S 2p spectra overlap as shown in Figure 51. On deoxidized GaAs, the Ga 3s peak at 160.2 eV dominates different contributions. After functionalization, we observe an additional contribution between 160 and 164 eV that can be attributed to S 2p resulting from thiol species present on the surface, which is consistent with the creation of bonds between the sulfur of the thiol and the Ga and As atoms. The doublet S 2p consisting of two peaks at 161.9 eV and 163.1 eV, confirms the covalent attachment of thiols on the surface. These values are in reasonable agreement with the binding energies for bound thiolate (162.0 eV) and free thiols (163.5 eV) reported on gold [196], [197].

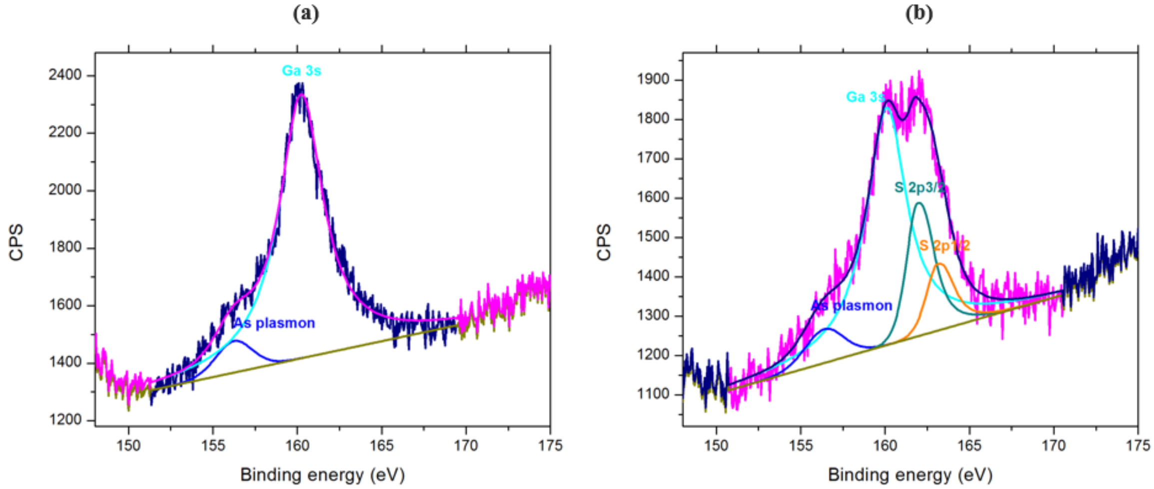

Figure 51. High-resolution XPS spectra for the S 2p and Ga 3s region of (a) deoxidized GaAs membrane and (b) MHDA/MUDO (1:9) SAM coated GaAs membrane

5.4 Activation of carboxyl groups present in the SAM

The principle of activation for the formation of a covalent bond with an amine group relates to the architectures composed of a carboxylic acid, e.g. MHDA. It is done by means of a reaction between EDC (1-ethyl-3-[3-dimethylaminopropyl]carbodiimide) and NHS (N-hydroxysuccinimide). Two aliquots containing NHS and EDC, prepared in deionized water, were mixed to obtain a total concentration of 1 M with NHS/EDC ratio of 1:4. The solution was used directly after mixing the reagents (unstable over time), and the sample was then incubated in the solution for activation for 30 minutes.

In a first step, the EDC molecule forms with the carboxyl groups an O-acylisourea intermediate which can react with a primary amine group (-NH_2) to form an amide bond. O-acylisourea is a highly unstable intermediate in aqueous solution; if this compound does not react rapidly with the primary amine, it can readily hydrolyse to regain its carboxyl form. For this reason, another compound, NHS, is used in conjunction with EDC. NHS is a relatively stable ester allowing the primary amine to be conjugated at physiological pH. Due to the steric hindrance of NHS molecules, the reaction with the carboxyl groups saturates when their number becomes too large at the surface [198].

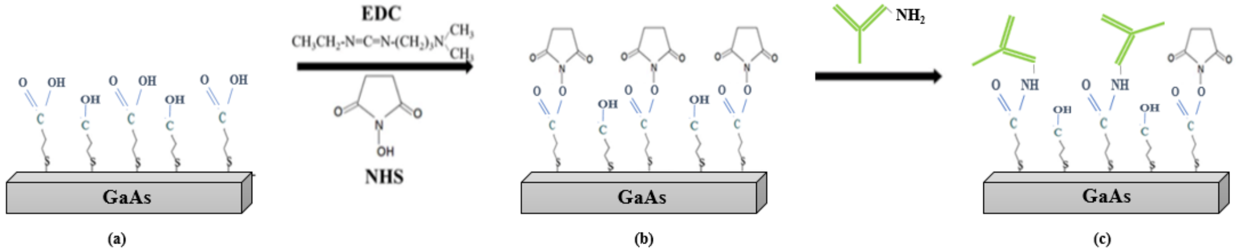

Figure 52. Schematic illustration of the ligands immobilization steps applied on the surface of GaAs: (a) formation of the SAM, (b) activation of the COOH group with NHS/EDC (1:4), (c) immobilization of the antibodies, modified from [199].

After the activation, the excess of unreacted NHS and EDC molecules was removed by rinsing the samples 5 times with DI water. The antibody was then fixed via its primary amine groups of lysine residues essentially.

5.5 Immobilization conditions of α-*E. coli* antibodies on GaAs surface

The effects of the concentration of the antibody, the incubation time and pH were studied on the immobilization efficiency of antibodies. For that, 2x2 mm^2 bulk double side polished GaAs samples (WV 23084/UN) were functionalized with MHDA/MUDO (1:9) at 2 mM. Then the COOH groups of MHDA were activated by incubation for 30 minutes in a mixture of NHS/EDC (1:4). After the activation, the membranes were incubated in antibodies against *E. coli* (α-*E. coli*) diluted in different buffers (PBS (1X), pH 7.4 or acetate, pH 4.5) and at different concentrations (2.5; 12.5; 25; 100 and 200 µg/ml) for different durations (0.5; 1; 2; 4 and 20 hours). The antibodies used in this work were unconjugated polyclonal IgG, purchased from ViroStat, Inc. (Portland, ME). Subsequently, the samples were thoroughly rinsed with PBS (1X) and TWEEN 20 (0.05 % V/V), then rinsed with deionized water to remove surface salts and dried under N_2 flow.

At this point, the samples are separated into two batches (A and B). Batch A undergoes FTIR measurements used to characterize the amide bands of the antibodies. The presence of immobilized antibodies on the surface was studied by examining the amide bands A, I, and II located in the regions of 3296.4 cm^{-1}, 1644.4 cm^{-1} and 1527.4 cm^{-1}, respectively. According to Bandekar et al., within the proteins, the amide band A is essentially due to the NH stretching vibrations, the amide I is rather associated with the C=O vibrations also in stretching, whereas the amide II is related to the modes of torsion of the NH bonds as well as modes of stretching of the CN bonds [200]. Therefore, in this study, the number of immobilized antibodies on the surface was quantified by calculating the integral of the amide bands A, I, and II.

As for batch B, the non-bound COOH groups of the constitutive samples were inactivated using ethanolamine (1 M, pH 8.5) for 30 min. After, the samples were exposed to GFP (Green fluorescent protein) *E. coli* bacteria solutions at 10^6 CFU/ml in PBS (1X) for 1 hour, then rinsed and dried. Finally, fluorescence measurements were performed, and images were taken using a GFP filter and 20X magnification. The number of bacteria captured on the surface was estimated using ImageJ software. For each couple of concentration and incubation time, 3 samples were tested to ensure the reproducibility.

5.5.1 Optimal concentration and duration for immobilization of α-*E. coli*

Figure 53 shows examples of FTIR spectra measured on SAM-coated GaAs surface after immobilization of α-*E. coli* at different concentrations of antibodies and time durations. Since the amide A peak is the most obvious and easy to analyze among the amide bands, we will limit the analysis to the integral of this peak.

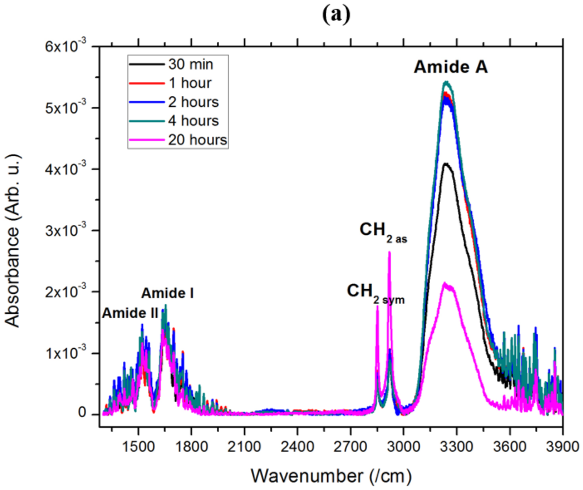

Figure 53. FTIR spectra measured on SAM-coated GaAs surface after immobilization of α-*E. coli* (a) at 200 µg/ml for different durations, (b) for 2 hours at various concentrations

The integral values for each antibody concentration and time duration are reported in the histogram of Figure 54. At low concentrations of antibodies, the highest absorbance intensity and integral were obtained when the sample was incubated in α-*E. coli* for 4 hours. However, when the concentration is increased, the absorbance intensity and the integral values were comparable for incubation times between 1 and 4 hours. Nevertheless, these values remain relatively low for 20 hours of incubation, suggesting that the efficiency of the antibody is deteriorated over time and eliminating this option. Therefore, if we use a high concentration of antibodies, the incubation time can be reduced significantly. Indeed, for a biosensor application, we are looking to reduce the analysis time. Hence, if we set the incubation time between 1 and 2 hours, we can choose, based on the fluorescence results, the concentration of antibodies allowing to capture the greatest number of bacteria on the surface.

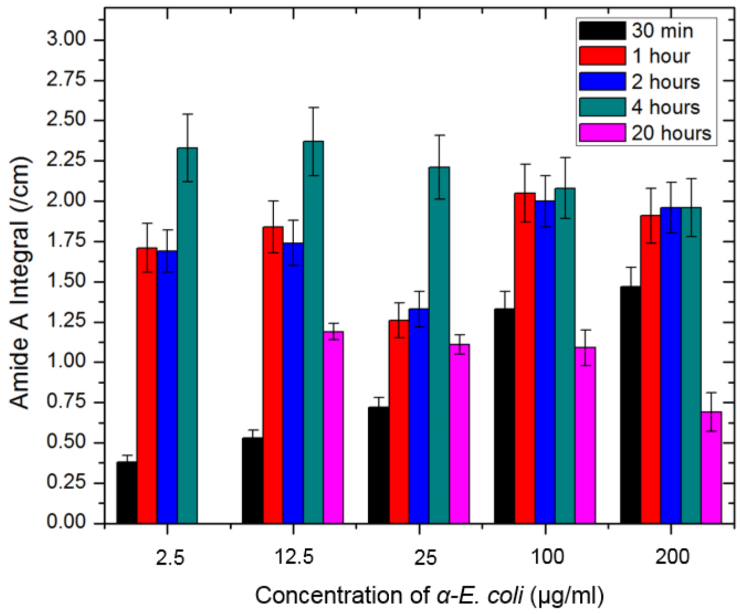

Figure 54. Integral of the amide A peak determined for different immobilization durations and concentrations of α-*E. coli* on the MHDA/MUDO (1:9) modified GaAs membrane

To assess the surface coverage with bacteria, fluorescence images were analyzed using ImageJ software and the number of *E. coli* captured on the surface was estimated for each concentration and incubation time. Some examples of the fluorescence images of bacteria captured on the surface by α-*E. coli* immobilized for the same concentration of antibodies but different incubation times, and at the same incubation time but for different concentrations are shown in Figure 55 and 56, respectively. It can be seen that both the concentration and the incubation time have an important impact on the efficiency of the capture of bacteria.

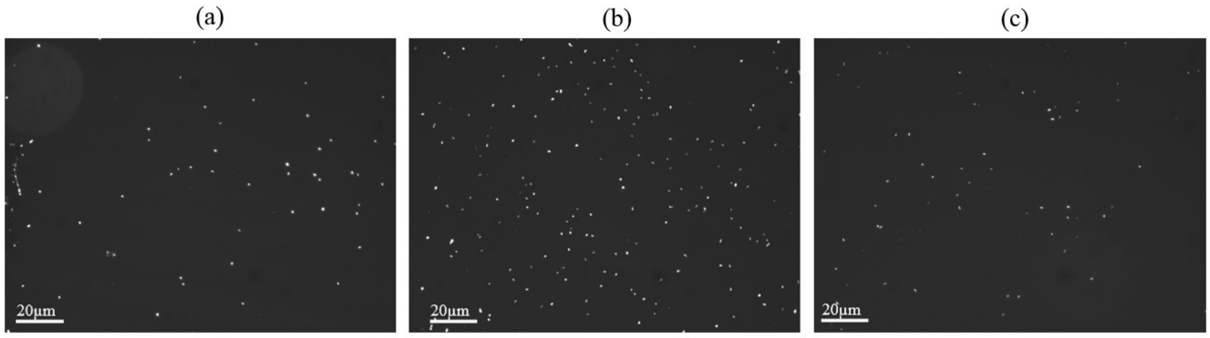

Figure 55. *E. coli* captured on the bio-functionalized GaAs membrane surface by α-*E. coli* immobilized at 25 μg/ml for (a) 30 min, (b) 1 hour and (c) 20 hours, measured by fluorescence microscopy (20X magnification, GFP filter)

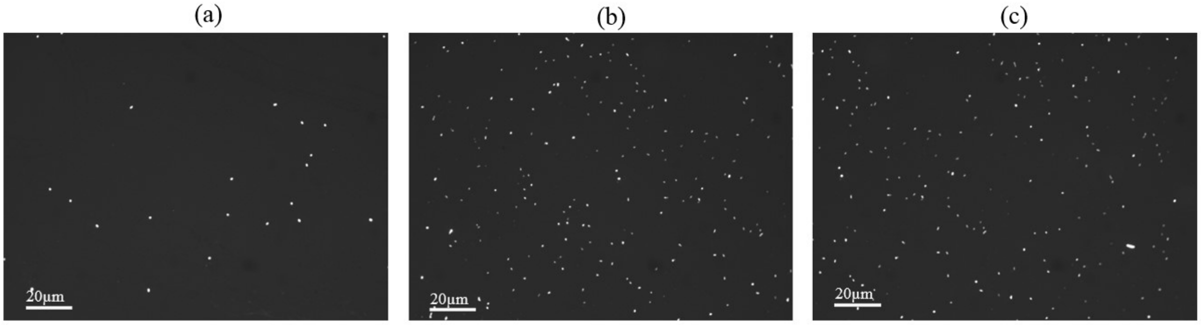

Figure 56. *E. coli* captured on the bio-functionalized GaAs membrane surface by α-*E. coli* immobilized for 1 hour at (a) 2.5 µg/ml, (b) 100 µg/ml (c) 200 µg/ml, measured by fluorescence microscopy (20X magnification, GFP filter)

The number of bacteria captured on the surface for each antibody concentration and incubation time, obtained from the fluorescence images, are shown in Figure 57. It is obvious that the greatest number of bacteria is captured by incubating the sample for 4 hours using 100 µg/ml. However, if we examine the high concentrations (100 and 200 µg/ml), we can see the number of captured bacteria is comparable either we incubate the sample for 1 or 2 hours. Therefore, we can opt for a concentration of 100 µg/ml and an incubation time of 1 hour, which does not consume too much time or material.

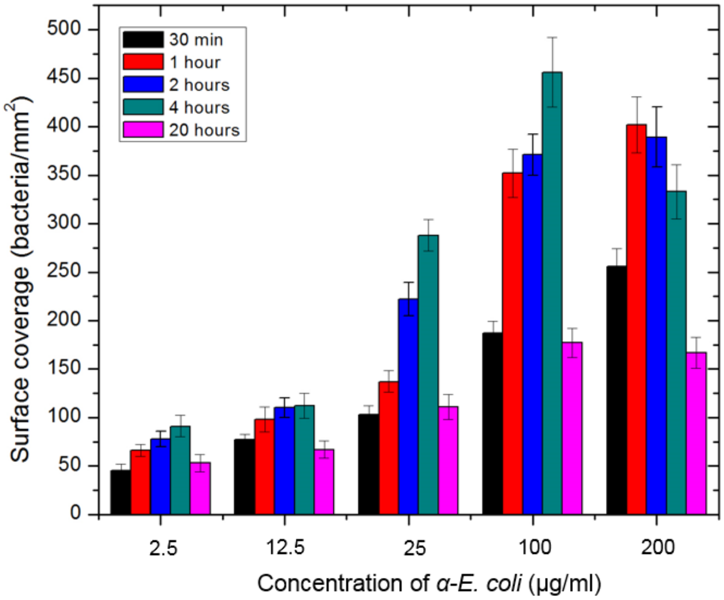

Figure 57. Number of captured *E. coli* bacteria on the bio-functionalized GaAs membrane surface for different concentration and incubation times of the antibodies

5.5.2 Impact of pH on the immobilization efficiency

To evaluate the effect of pH on the immobilization of antibodies, acetate (pH 4.5) and PBS (pH 7.4) buffers were used. The concentration of α-*E. coli* and the duration of incubation were set at 100 µg/ml and 1 hour, respectively. Three samples were measured per buffer and an example of the FTIR spectra in Figure 58 illustrate formation of peaks originating from the amide bands of the antibodies. It is obvious that the integral of the amide A peak is greater for PBS (2.22 ± 0.31) than for acetate (0.58 ± 0.09), which offers better immobilization conditions for antibodies.

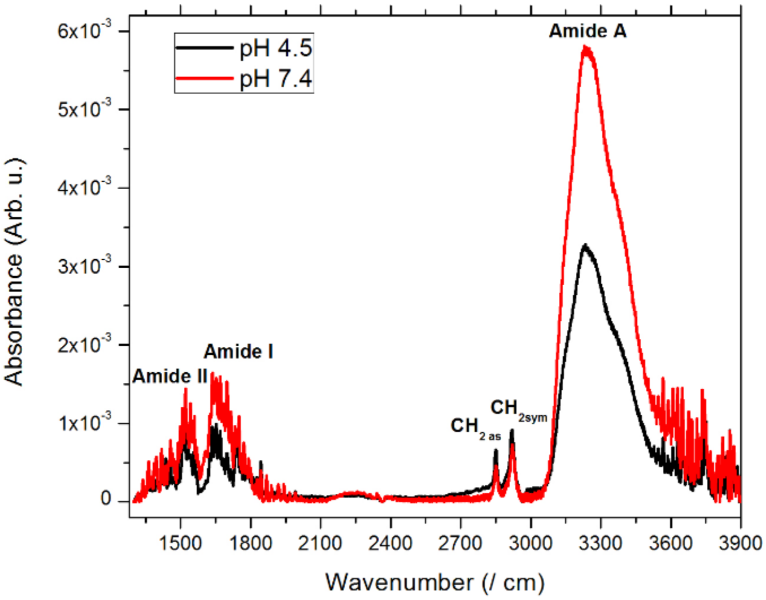

Figure 58. FTIR spectra of α-*E. coli* immobilized on MHDA/MUDO (1:9) SAM-coated GaAs surface following 1-hour exposure to 100 µg/mL antibody solutions at different pH conditions.

The fluorescence results in Figure 59 are in a reasonable agreement with the FTIR data, since the number of bacteria captured on the surface after the exposure to *E. coli* solution at 10^6 CFU/ml is greater when PBS buffer is used (456 ± 24 bacteria/mm^2) instead of the acetate buffer (143 ± 16 bacteria/mm^2).

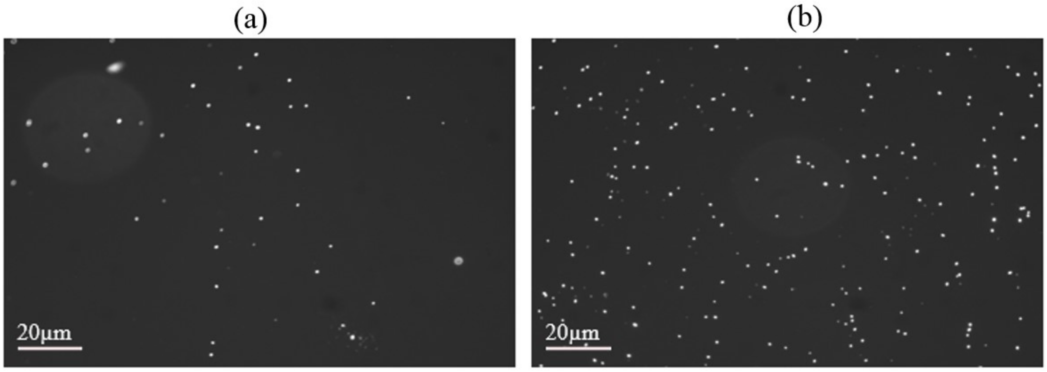

Figure 59. Fluorescence images (20X magnification) of GFP *E. coli* captured on the surface by antibodies immobilized in different buffers: (a) acetate (pH 4.5) and (b) PBS (pH 7.4) (N = 3 samples per buffer)

To summarize, FTIR and fluorescence results show higher FTIR peaks intensity and surface coverage with bacteria when the antibodies are immobilized in PBS (1X, pH 7.4). As for the concentration and incubation time, we have chosen 100 µg/ml and 1 hour, respectively.

5.6 Conclusion

In this chapter, we have presented the complete bio-functionalization protocol established for the immunocapture of the bacteria of interest: *E. coli.* This protocol employs a mixed SAM of alkanethiols of MHDA/MUDO (1:9) to immobilize antibodies against *E.* coli. Using contact angle measurements, FTIR and XPS, we validated the functionalization of GaAs membranes. Moreover, we tested different parameters for optimizing the immobilization of antibodies in terms of concentration, duration and pH. Our bio-interface is now ready to be confronted to the targeted bacteria and the performances of the biosensors can be evaluated.

Chapter 6: Testing ZnO/GaAs biosensor for detection of *E. coli*

After presenting the analytical and numerical modeling of the transducer, the microfabrication protocol and the realization of the bio-recognition interface, we will present in this chapter the measured parameters of the ZnO/GaAs biosensor subjected to different liquid environments, as well as the testing of its performances for the detection of *E. coli* in ideal (buffer) and complex liquid media.

As a first step, we present the methodology and measurement setup adopted for the electrical characterization of the sensor. The electrical measurements are conducted using a network analyzer and an electrical interface adapted to the device, and we focus on impedance measurements around the resonant frequency.

In a second part, we determine the impact of the environmental factors on the response of the sensor, such as the impedance dependence on the salt concentration (electrical conductivity) and pH of the surrounding environment, respectively.

We also evaluate the effectiveness of the bio-interface to capture the targeted bacteria. To quantify *E. coli* captured on bio-functionalized GaAs surface, electrical characterizations are performed at the resonant frequency. The number of bacteria captured on the surface is estimated by measuring the shift of the resonant frequency. In parallel, fluorescence measurements are carried out to evaluate the surface coverage and estimate the mass of captured bacteria. Detection tests are realized using solutions of different concentrations of *E. coli* diluted in PBS solution and the calibration curve of the biosensor is established. Controls with *Bacillus subtilis* are carried out to test the specificity of the bio-interface. Furthermore, detection tests in a more complex biological environment are performed where *Bacillus subtilis* and *E.* coli co-exist in a solution. These tests, combined with the correlation between electrical and fluorescence measurements, show a successful and specific capture of *E. coli* on the bio-interface. Finally, we discuss the possible optimization tracks for improving the performances of the biosensor.

6.1 Electrical characterization of ZnO/GaAs sensor

6.1.1. Measurements in air

After the fabrication of the devices, it was necessary to characterize them electrically in air and in liquid media. Therefore, we proceeded to electrical measurements to identify the resonant frequency of interest, using a network analyzer operating in impedance mode. In this mode of operation, the analyzer performs a frequency sweep at a maximum voltage of 1 V and outputs the amplitude and phase of the impedance for the chosen frequency range.

Depending on the availability of the equipment in the lab, several network analyzers were used during the thesis, that are listed below:

- HP 4194A impedance/gain-phase analyzer (10 kHz to 100 MHz): equipped with a GPIB port and interfaced with a computer through a GPIB/USB conversion module. A program in LabVIEW is used to communicate with the apparatus and receive the acquisitions. It is therefore possible to monitor the analyzer and perform automatic measurement sequences.
- Agilent N5232A PNA-L series network analyzer (300 kHz to 20 GHz): performs S-parameter measurements. Therefore, the data were extracted under Smith chart format which retrieves the resistance and reactance. Then, to retrieve the impedance phase φ and modulus |Z|, the data were converted using the following equations:

$$|\mathrm{Z}| = \sqrt{\mathrm{Resistance}^2 + \mathrm{Reactance}^2} \;; \qquad \tan\varphi = \frac{\mathrm{Reactance}}{\mathrm{Resistance}} \tag{6.1}$$

- Agilent E5061B ENA series network analyzer (5 Hz to 3 GHz): combines S-parameter measurements and impedance analysis. The data is directly extracted via its USB port.

The output of the measurement is a Bode impedance diagram representing the impedance modulus and phase as a function of the frequency of the sinusoidal excitation. Figure 60 shows an example of the measurement performed in air on a ZnO/GaAs sensor sample at the fundamental frequency.

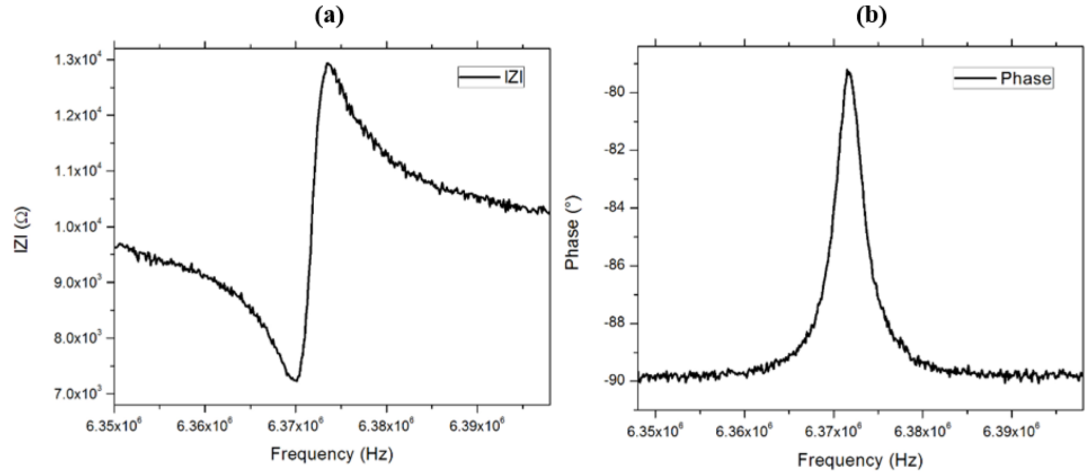

Figure 60. Modulus (a) and phase φ (b) of the impedance measured in air at the resonant frequency for a 220 µm ZnO/GaAs thick membrane

The quality factor Q was determined for each membrane by collecting the resonant frequencies f_r and anti-resonant frequencies f_a from the impedance modulus plot and using the equation:

$$Q = \frac{f}{\Delta f} \qquad \text{with} \qquad \Delta f = |f_r - f_a| \tag{6.2}$$

The membranes used in these measurements (wafer AXT – AV 503-93) had thicknesses between 195.5 ± 5.2 µm for the central membranes and 206.9 ± 13.7 µm for the ones near the edges, providing resonant frequencies ranging from 7.9 to 6.3 MHz. For a 200 µm membrane, the resonant frequency determined using this setup (6.66 MHz) was close to the one obtained by the FEM simulation in chapter 3 (7.94 MHz). Yet, the model needs to be improved to represent as close as possible the real structure of the sensor.

The corresponding quality factors varied between Q = 7000 and Q = 15000, depending on the electrode geometry and the roughness of the membrane. The obtained values indicate a significant improvement with respect to the quality factors obtained for GaAs sensor (without ZnO) developed in the previous thesis by V. Lacour (Q = 2759 to 4135).

The electrodes located on the top side of the sensor were connected to the analyzer through an electrical interface consisting of contact spring tips attached to a printed circuit board (PCB). The PCB was screwed to a plexiglass plate attached to a Y-axis displacement stage, fixed by two poles on a support as shown in Figure 61. The PCB was connected to the analyzer via SMA

(SubMiniature version A) coaxial connectors (characteristic impedance of 50 Ω). The circuit consists of a large ground plane to avoid the antenna effects.

The calibration of the analyzer is an essential step that we repeated prior to each measurement series or after any modification of the acquisition parameters (frequency range or number of points). It makes it possible to compensate for the impedances created by the connections and cables located between the analyzer and the device to be measured. The calibration was carried out via the "85052D" calibration kit, using its three standards corresponding to an ideal open circuit (zero admittance), an ideal closed circuit (zero impedance) and a circuit with a load of 50 Ω. We placed the standards at the end of the SMA cable to eliminate the parasitic capacitances related to the cables and interconnections as efficiently as possible.

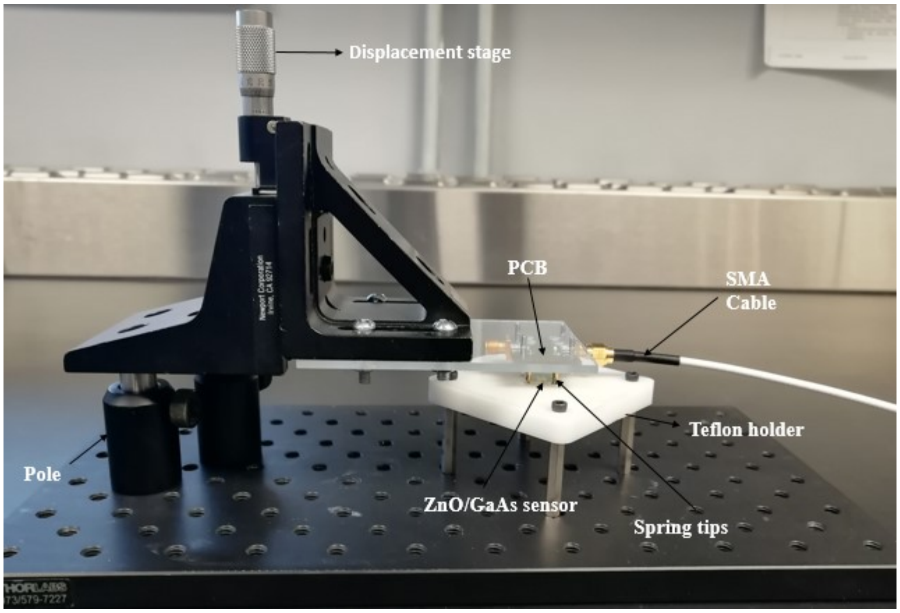

Figure 61. Electrical interface used for the determination of the resonance characteristics of ZnO/GaAs biosensor

6.1.2. Setup for the measurements in liquids

A fluidic module has been designed to perform the electrical measurements while the biosensor is supplied by the liquid solution to be tested. This module makes it possible to maintain the sample on a support made in Teflon which can be filled by any liquid. The sample is placed on top of a seal designed in Polydimethylsiloxane (PDMS) allowing the continuous circulation of the liquid on the membrane, as shown in Figure 62 (a). Seals of different thicknesses were made using the mold shown in Figure 62 (b) and tested, and the retained thickness was 0.7 µm.

The microfluidic tubes were positioned and held in place by a 4-way linear connector (Dolomite) placed at the bottom side of the Teflon support (Figure 62 (c)). Two holes of 0.6 µm in diameter were realized in the fluidic support in front of the microfluidic tubes, allowing the entry and exit of the liquid. A cover designed in plexiglass provided the necessary pressure for sealing (Figure 62 (d)). This cover comprised 4 openings allowing the contact between the spring tips of the PCB and the electrodes on the top side of the sample, thus enabling the electrical measurement while the biosensor is supplied with the liquid solution to be tested.

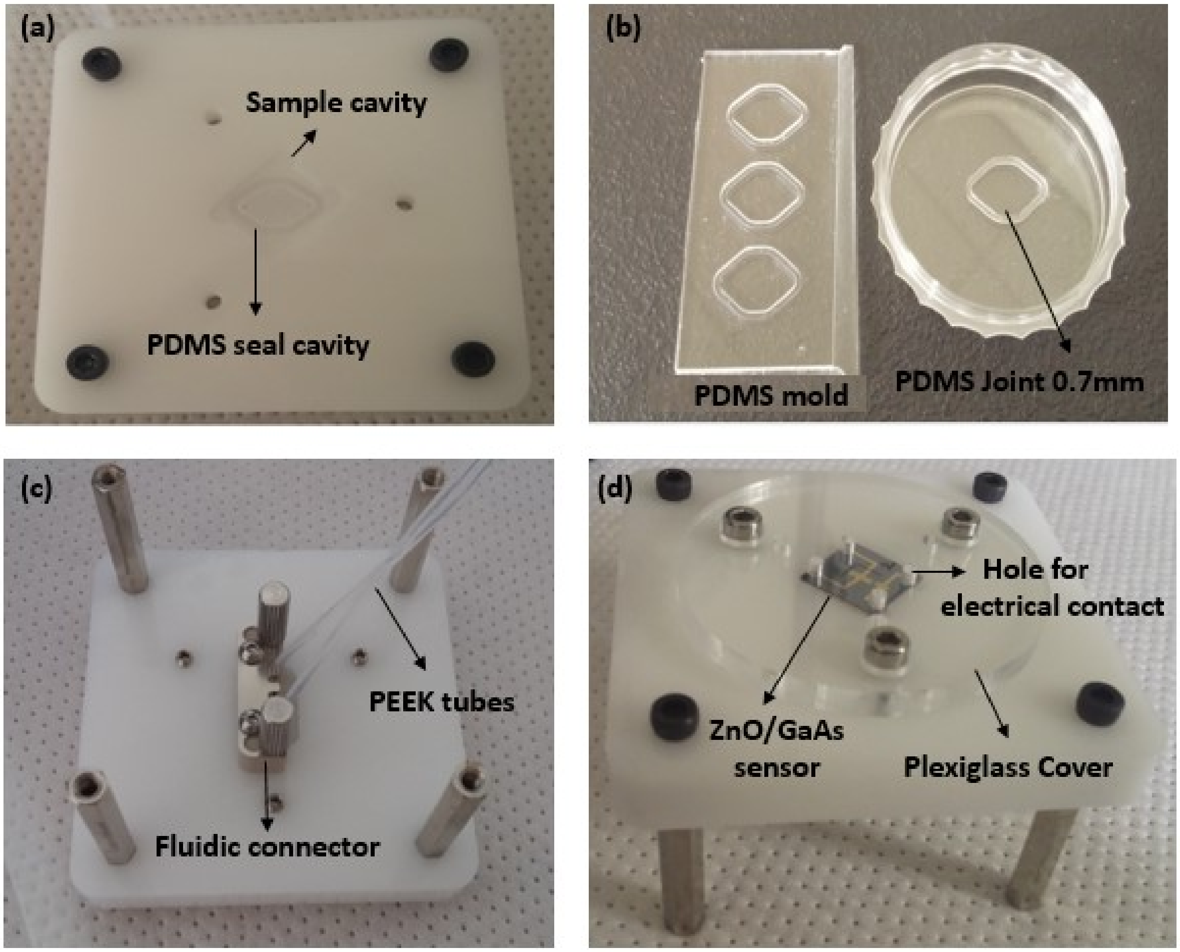

Figure 62. Fluidic module designed for electrical measurements on ZnO/GaAs biosensors in liquid media

The injection of liquid solution was carried out using a syringe pump Harvard Apparatus PHD 2000 and BD syringes of 5 ml, at a constant flow of 150 µl/min.

This fluidic module can moreover be used for the functionalization of the samples while protecting the top side. In fact, the materials in contact with liquids have a wide chemical compatibility (Teflon support, and PEEK tubes).

6.2 Effect of the physico-chemical properties of the liquid on the biosensor's response

The detection of the targeted bacteria needs to be done in complex liquid environments (river/drinking/waste water) or with biological fluids such as blood or urine, which can inevitably induce surface charge variations on the material. Moreover, the proposed architecture of the biosensor presented in section 2.6 separates the electrical interface from the sensing area making this structure beneficial for monitoring the electrical parameters (conductivity, resistivity, permittivity). This multi-parameter sensing requires a thorough understanding of the electrical contributions to the sensor's response. Therefore, in this section, we will investigate the impedance dependence due to the pH and NaCl concentration (electrical conductivity) variation of the fluid/electrolyte.

Furthermore, to highlight the impact of the surface functionalization and passivation on the frequency response of the sensor, electrical measurements were performed at different surface states, which were denoted as the following:

- Surface state A: Sensor with bare surface
- Surface state B: Sensor surface chemically functionalized with MHDA/MUDO (1:9)
- Surface state C: Sensor surface functionalized with MHDA/MUDO (1:9) and α-*E. coli* (100 µg/ml), then blocked with BSA (200 µg/ml, pH 5.2) and inactivated with ethanolamine (1 M, pH 7.5).

6.2.1. Impedance dependence to the electrolyte's conductivity

The influence of molecular electrical charges in liquids on the measured impedance spectrum was evaluated by changing the concentration of NaCl in water. The electrical measurements were performed at the fundamental frequency while introducing NaCl solutions prepared in DI water with concentrations ranging from 0 to 1 mol/l at the vicinity of the sensing surface, using the fluidic module presented in section 6.1.2. The reference frequency was obtained with DI water. The measurements were carried out in ascending order on three samples, in the three different surface states A, B and C. The impedance peak amplitudes (Δ lZl) as well as the variation in the impedance phase (Δφ) were plotted (Figure 63) as a function of the conductivity of the NaCl solution, which was calculated for each concentration using the linear relationship determined by Gavish and Promislow [201]:

$$\sigma = 0.06 + 9.5\ C \tag{6.3}$$

Where σ is the conductivity expressed in S/m and C is the concentration expressed in mol/l of the NaCl solution. The molar ionic strength I of the solution is a function of the concentration of all the present ions, and is determined by:

$$\mathrm{I} = \frac{1}{2}\sum_{i=1}^{n} c_i\, z_i^2 \tag{6.4}$$

Where c_i is the molar concentration of ion i (mol/l), z_i is the charge number of the ion, and the sum is taken over all ions in the solution. For a 1:1 electrolyte such as sodium chloride (NaCl), where each ion is singly-charged, the ionic strength is equal to the concentration.

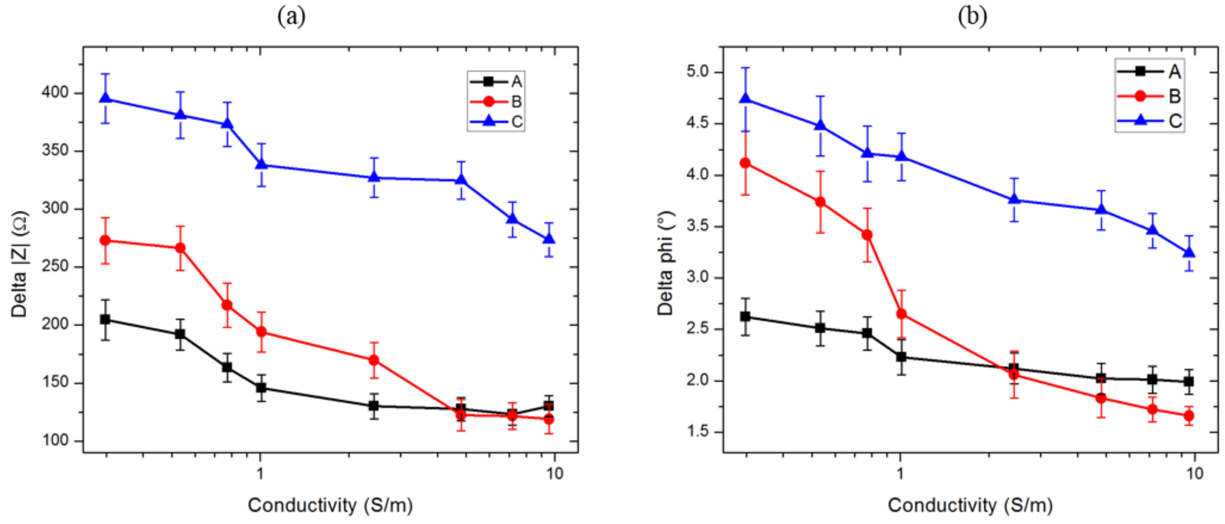

Figure 63. Impedance peak amplitude ΔlZl (a) and variation in the impedance phase Δφ (b) versus the conductivity σ of the NaCl solution for each of the surface states A (bare), B (chemically functionalized) and C (antibody coated + passivated). (N = 3 samples/surface state)

The reference measurements (with DI water) revealed a difference in the impedance peak amplitude and phase variation between the different surface states. Indeed, by comparison to bare surface the impedance peak amplitude is increased by 28 % when the surface is functionalized, and by 97 % when the antibody-coated surface is blocked using BSA. The higher ΔlZl and Δφ are due to the passivation of the surface, first with thiols then with BSA, which reduces the attenuation and losses due to the interaction with the liquid.

A rapid attenuation of the amplitude of the resonance peaks was observed with the addition of NaCl, for all surface states. However, this attenuation becomes less important as we go from surface A to B than C. The sensor with bare surface is very sensitive to the conductivity of the electrolyte. When it is chemically functionalized, ΔlZl and Δφ are slightly improved. A significant improvement is observed when the surface coated with antibodies is passivated with BSA. This dependence on the electrolyte's conductivity can limit the efficiency of the biosensor in liquid media. Indeed, the concentration of NaCl in a physiological solution, for example, is generally 0.15 mol/l giving a conductivity of 1.52 S/m. If we look up this value in the graphs of Figure 63, we would see that the amplitude of the signal has been already attenuated, and the efficiency of the sensor in its current configuration will be probably reduced in a physiological solution.

In these measurements, 5 electrode geometries were used (Figure 64). The geometries 1 and 2 have electrode widths of 1700 µm while the others have a width of 300 µm. Configurations 1, 2 and 3 have an inter-electrode distance or gap "g" of 200 µm while for geometries 4 and 5, the gap is 1600 µm. Finally, in the configuration 5, a metallized zone with a width of 1200 µm is placed between the two electrodes and spaced apart from each of them by 200 µm.

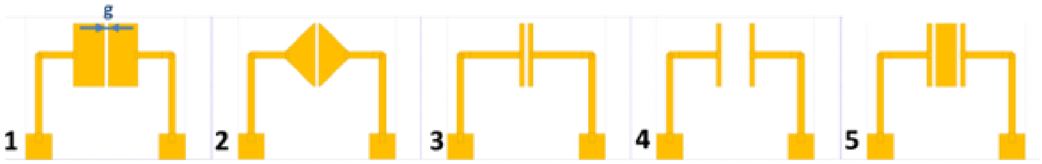

Figure 64. Geometries of the electrodes deposited on the top of ZnO films

To limit the impact of the NaCl concentration on the impedance phase and modulus, it is possible to reduce the penetration of the electric field into the medium, by reducing the gap between the electrodes. Different gap configurations were tested in chapter 3, using the Comsol model presented in section 3.6, and the variation of the gap was shown to affect the penetration of the electric field. Therefore, this aspect could be the subject of more in-depth numerical studies leading to reduce the impact of the conductivity of the tested liquid. It will be necessary to determine the optimal gap/thickness ratio of the membrane, in order to optimize the sensitivity of the device without being affected by the electrical parameters of the surrounding environment.

6.2.2. Effect of the fluid's pH on the biosensor resonant frequency

To determine the effect of the pH on the biosensor's response, different pH solutions (pH 4; 6; 7; 8 and 10) at constant ionic strength were introduced into the fluidic module. The reference frequency was obtained with pH 7. The impedance peak amplitudes (ΔlZl) and the variation in the impedance phase (Δφ) were recorded for the different pH and are shown in Figure 65.

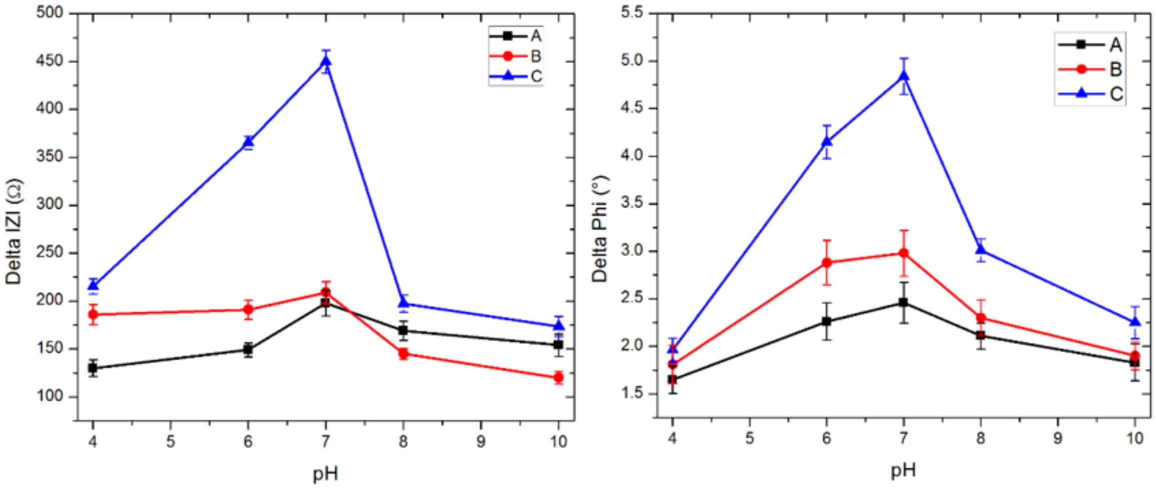

Figure 65. Impedance peak amplitudes (ΔlZl) and variation in the impedance phase (Δφ) versus the pH of the analyte for each of the surface states A (bare), B (chemically functionalized) and C (antibody coated + passivated). (N = 3 samples/surface state)

Low and high values of pH (4 and 10 respectively) induced important attenuation of ΔlZl and Δφ of the sensor with bare surface (35 % and 24 % respectively) compared to pH ranging between 6 and 8 (23 % and 14 % respectively), which was shown by the decrease of ΔlZl and Δφ. The chemical functionalization of the surface and the use of BSA for blocking after antibody immobilization increased the sensitivity of the response to pH, which was shown by the increase of the slope of the curves. Indeed, when the pH is modified, ΔlZl and Δφ drop significantly which is related to the sensitivity of BSA covering the surface to acidic and basic pH. This drop of ΔlZl and Δφ induces a loss of performance and sensitivity because the quality factor decreases. Thus, the solution's pH should be controlled to ensure a stable and reproducible response.

Furthermore, the peak amplitude and phase variation are the highest for the passivated surface at pH 7, which is very convenient for testing biological samples around physiological pH (pH = 7.4). However, around this pH, ΔlZl and Δφ change rapidly and significantly with pH variation. It is therefore necessary to have the control over the solution's pH.

6.3 Electrical measurements prior to exposure to *E. coli*

The detection and quantification of *E. coli* in the tested solution is done by determining the shift of the resonant frequency f_r associated with the mass variation caused by the immunocapture of *E. coli* on the surface. The value of the frequency shift Δf_r induced by an added mass Δm can be calculated using the Sauerbrey equation [119]:

$$\Delta f_r = \frac{-2\,\Delta m\,fr^2}{A\,V_s\,\rho} \tag{6.5}$$

Where A is the piezoelectrically active surface corresponding to the area between the electrodes (4 mm^2), ρ is the density of GaAs (5.307 g/cm^3) and V_s is the velocity of the quasi-shear wave.

By substituting the acoustic velocity by $V_s = \frac{n\,f_r}{2\,h}$ deduced from equation (3.25), the frequency shift at the fundamental rank (n = 1) can be expressed as the following:

$$\Delta f_r = \frac{-\,\Delta m\;f_r}{A\,h\,\rho} \tag{6.6}$$

To make sure that the recorded shift is only due to the capture of *E. coli*, electrical measurements were performed in air at the end of each phase of the bio-functionalization procedure as presented in Table 18. The detailed procedure for samples preparation and characterization performed in each phase is provided in Appendix B.

Table 18. Preparation and electrical measurements procedure for ZnO/GaAs biosensors performed at each of the bio-functionalization phases. The * sign indicates that the electrical measurements procedure is identical in each phase

Phase	Step	Objective	Tools & solutions	Parameters/Remarks
Sensor with Bare surface	Cleaning of the samples	Remove mineral and organic impurities from the surface of the samples	Immersion in successive baths of: -OptiClear -Acetone -Ethanol	5 min in each solvent under US, followed by drying under Nitrogen flow
	Electrical measurements*	Determine the resonance characteristics (frequency, impedance phase and modulus)	Network analyzer Cal kit 85052D Electrical interface	Calibration prior to measurements and after any modification of the acquisition parameters
Sensor with chemically functionalized surface	Deoxidation of GaAs	Remove the native oxide from GaAs surface to prevent the chemisorption of thiols on the surface	Ammonium hydroxide NH_4OH (28 %)	2 min followed by brief rinsing with degassed ethanol
	Chemical functionalization of GaAs at the bottom side of the sensor	Formation of SAM to graft ligands	-Sample holder -MHDA/MUDO (1:9) at 2 mM -Degassed ethanol	20 hours followed by rinsing with degassed ethanol and drying under Nitrogen flow
	Electrical measurements*			
Sensor with antibody-coated surface	NHS/EDC activation	Form a covalent bond between the carboxyl group of MHDA and the amine group	-NHS at 0.1 M -EDC at 0.4 M	-30 min in dark at room temperature -Rinsing (5 x 1 ml DI water)
	Antibody immobilization	Fix the antibodies via amine groups ($-NH_2$)	Unconjugated α-*E. coli* antibodies diluted in PBS (1X) at 100 µg/ml	1 hour in dark at room temperature followed by rinsing and drying
	Electrical measurements*			

Sensor after surface passivation	Passivation of the surface using BSA	Saturate the surface to block any unspecific adsorption reaction	BSA solution at 200 µg/ml, pH 5.5	30 min in dark at room temperature followed by rinsing and drying
	Electrical measurements*			
Sensor before exposure to *E. coli*	Inactivation of COOH groups	Inactivate free activated COOH groups to prevent their interaction with the analyte	Ethanolamine at 1 M, pH 8.5	30 min in dark at room temperature
	Electrical measurements*			

Since each phase induces a mass variation on the surface by addition or removal of material, the frequency shift was recorded after each phase to follow the variation of the resonant frequency. The measurements were repeated on 3 samples, and the associated frequency shifts for each phase are reported in Table 19.

The theoretical frequency shifts associated with each step were also determined using the surface coverage with the molecules (thiols, α-*E. coli*, BSA) and the corresponding added mass on the surface. The theoretical shift caused by the formation of the SAM of MHDA/MUDO (1:9) on the surface was calculated using equation (6.6) at the resonant frequency 6.35 MHz for a 220 µm thick membrane, based on the surface coverage with the constitutive alkanethiols determined within a previous study in the research group [202]. For MHDA (10 %) the surface coverage is 5 molecules/nm^2, adding a mass of 6.64 x 10^{-10} g. As for MUDO (90 %), the surface coverage is 5 molecules/nm^2 as well, which corresponds to an added mass of 8.3 x 10^{-9} g. The combination of the two thiols forming the SAM would generate a shift of 3.04 Hz.

The determination of the theoretical shifts related to the α-*E. coli* immobilization and BSA passivation was difficult, since it is strictly dependent on the efficiency of the antibodies immobilization and their surface coverage. Indeed, BSA is used to block the sites that have not interacted with an antibody. Therefore, the mass of BSA deposited on the surface is a function of the antibody immobilization efficiency. To have an estimation of the shifts, we calculated the frequency shift that would be observed if the surface was fully covered by a dense layer of α-*E. coli* or BSA. For that, the surface coverage was determined using the surface occupied by 1 molecule of α-*E. coli* or BSA, and by calculating how many molecules can fit in our 16 mm^2 membrane. The added mass on the surface was then calculated after determining the number of α-*E. coli* or BSA using the surface coverage. The comparison of the experimental and theoretical shifts allows to assess the quality of the immobilization and the percentage of surface coverage with both α-*E. coli* and BSA.

Table 19. Theoretical and experimental frequency shifts (Δf) determined after each phase of the bio-functionalization procedure of ZnO/GaAs biosensor (N = 3 samples)

Phase	Entity		Theoretical				Experimental Δf (Hz)
			Surface coverage (molecule/nm^2)	Added mass (g)		Theoretical Δf (Hz)	
Chemical functionalization	Thiols	MHDA (10 %)	5	6.64×10^{-10}	8.964×10^{-9}	-3.04	-15.5 ± 10.5
		MUDO (90 %)	5	8.30×10^{-9}			
Antibodies immobilization	α-*E. coli*		0.05	1.66×10^{-7}		-56.43	-27.1 ± 4.5
Passivation	BSA		0.2	3.32×10^{-7}		-112.85	-59.8 ± 11.3

According to these results, the ratio of the experimental to the theoretical shift for α-*E. coli* is between 40 to 58 %, which suggests that the antibodies cover 40 to 58 % of the surface. This immobilization rate seems reasonable, knowing that it is impossible to have a dense layer of antibodies covering the whole surface especially that we are working in static conditions. To increase this rate, the immobilization procedure could be improved by performing the exposures in dynamic conditions, under flow of solution or assisted by ultrasounds [203].

As for BSA, this ratio is between 43 to 63 %, which is in agreement with the role of BSA in blocking the sites that have not interacted with an antibody.

6.4 Methodology of measurements for detecting *E. coli*

After inactivation of the COOH groups with ethanolamine, the samples were exposed to bacterial solutions. The bacteria used in our experiments is GFP *E. coli* K12 (level 1), provided by the Department of Microbiology of the Faculty of Medicine at Université de Sherbrooke

(Prof. E. Frost). The information and the requirements regarding the preparation and manipulation of *E. coli* bacteria are provided in Appendix C.

For these measurements, we opted to perform the measurements in air. Therefore, the exposure of the biosensor surface to bacterial solutions was carried out in liquid medium while placing the samples in the holders presented in section 5.2.2. The volume of bacterial solutions used in all experiments was 1 ml. Then the samples were removed, rinsed and dried for electrical and fluorescence measurements. Although it was no longer possible to perform a real-time analysis, the bacteria were captured at different exposure times and concentrations, and on several sensors in parallel to achieve, as much as possible, an efficient and reproducible detection of *E. coli*.

The objective of the tests presented here is to establish the full-scale range of the biosensor by exposing it to increasing concentrations of *E. coli*. For that, we started by exposing 3 biosensor samples to *E. coli* at 10^4 CFU/ml for 1 hour. After the exposure to *E. coli*, the solutions were withdrawn and the samples were consecutively rinsed 3 times with PBS (1X), Tween 20 at 0.05 %, then DI water. After drying under nitrogen flow, the samples were removed from the holders to perform the electrical and fluorescence measurements. After the first round of measurements, the biosensor samples were placed again in the holders for regeneration using a commercial antigen-antibody dissociation kit, then electrical and fluorescence measurements are performed again to verify the removal of bacteria from the biosensors surface. Afterwards, the samples were re-exposed to *E. coli* at higher concentration (10^5 CFU/ml), and the same procedure was repeated until 10^8 CFU/ml. The bacterial solutions were obtained from cultures of *E. coli* at 10^9 CFU/ml (measured by optical density) at the end of the exponential phase or at the beginning of the stationary phase, by successive dilutions (1/10) in PBS (1X).

In this set of measurements, the sensor was exposed to solutions of *E. coli* of increasing concentrations through cycles of regeneration/re-exposure. This means that for concentrations greater than 10^4 CFU/ml, the sensor is exposed to the bacteria solution with regenerated surface. However, if the sensor surface was fresh and did not undergo regeneration, the response of the biosensor could be different. Therefore, to evaluate this effect, the sensor was solely exposed to one concentration at a time, referred to as “fresh sensor”.

6.4.1. Complementary fluorescence measurements on the biosensor surface after exposure to *E. coli*

In parallel, fluorescence microscopy was used to characterize the density and distribution of bacteria on the surface, to estimate and to try to correlate the number of bacteria captured on the surface. After each electrical measurement, the samples were placed on glass slides with the membrane facing up, for microscopic analysis. The visualization of bacteria on the surface was investigated using an Olympus IX71 fluorescence microscope which was equipped with a xenon arc lamp emitting at 470 and 490 nm. The microscope was connected to a DP71 digital camera and *in-situ* fluorescence images of the samples were taken by using Q-capture software. Six to eight images were collected per sample at different sites of the membranes with a magnification of 20X and three samples were tested per concentration.

The fluorescent images were analyzed with ImageJ software and the number of *E. coli* present on the samples was estimated for each concentration of bacteria. Then the mass of captured bacteria (m) was estimated using the following equation:

$$m = d \times m_{E.\ coli} \times A \tag{6.7}$$

Where d is the surface density ("bacteria"/mm^2) determined by the surface coverage with bacteria on the surface, $m_{E.\ coli}$ is the mass of 1 bacterium of *E. coli* (9.5×10^{-13} g [204]) and A is the area of the sensing surface (4 mm^2).

It is possible that the fluorescence images underestimated the number of bacteria. The reason might be related to the fact that a fluorescent spot can be associated with more than one bacterium (aggregation, colony…). Therefore, the reported numbers of "bacteria/mm^2" relate to at least 1 bacterium. A control with optical microscopy using 100X magnification was done in parallel (Figure 66) to make sure that the fluorescence images are representative of the surface.

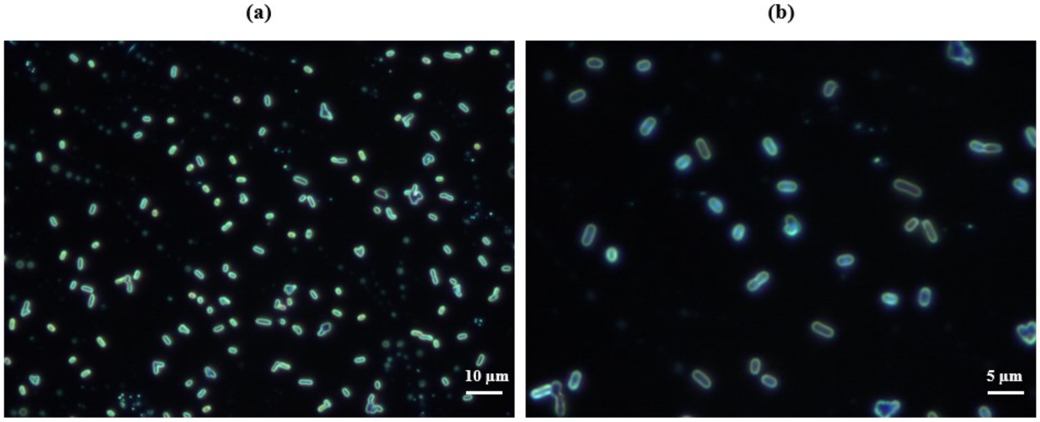

Figure 66. Optical images of GFP *E. coli* captured by α-*E. coli* immobilized on GaAs surface functionalized with MHDA/MUDO (1:9). Magnification: (a) 50X, (b) 100X

6.4.2. Regeneration procedure

After exposure of the sample to the bacterial solution, we wanted to prove the regenerability of the bio-interface to re-use the biosensor and reduce its operation cost. The chosen approach is a level 2 regeneration consisting in detaching the bacteria and conserving the bio-interface (i.e. the SAM and the antibodies). For this, we used a commercial antigen-antibody dissociation kit from bioWORLD (Catalog No. 21310002-1 (650161)). The kit contains two reagents for dissociating the antigen-antibody complex under normal or acidic conditions. In our case, we opted for an acidic dissociation at pH 2.

The kit was tested beforehand to make sure that the bacteria is efficiently removed and that the antibodies remain intact after exposure to pH 2. For that, we functionalized 4x4 mm^2 bulk double side polished GaAs samples with MHDA/MUDO (1 :9) at 2mM, and with α-*E. coli* antibodies via NHS/EDC activation. Then, the samples were separated into 2 batches denoted 1 and 2, each consisting of 3 samples. Batch 1 was dedicated for FTIR measurements (Figure 67) to characterize the amide peaks relative to the antibodies before and after exposure to the regeneration kit for 5 minutes.

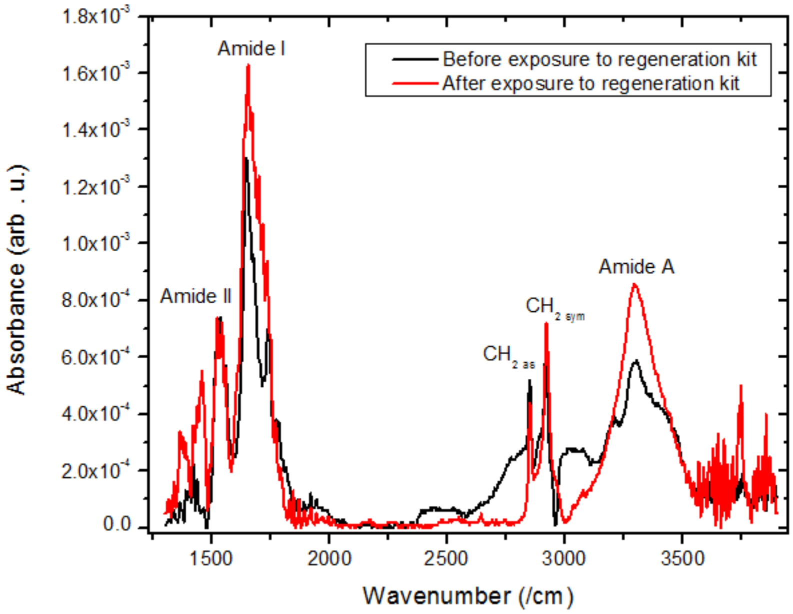

Figure 67: Regeneration efficiency tested by FTIR analysis of the CH_2 peaks and the amide bands of the antibodies before and after exposure to the regeneration kit (N = 3 samples)

FTIR results showed that the amide bands of the antibody were not affected by the low pH. Contrarywise, the amide A peak values (Table 20) showed that the absorbance intensity and integral of the peaks were enhanced after exposure to the regeneration kit, suggesting that the organisation of antibodies on the SAM-coated surface was improved. This result is in agreement with the literature [205]. According to Djoumerska-Alexieva et al., IgG molecules are exposed on a regular basis to acidic conditions during immunoaffinity purification procedures, as well as during the production of some therapeutic immunoglobulin preparations. This exposure was found to induce in them an increased functional antigen-binding affinity and an enhanced binding efficiency. On the other hand, the CH_2 peaks remained unchanged during this process, confirming that the thiols were intact after the regeneration. These results confirm the tested kit preserves the bio-interface.

Table 20. Amide A peak values of α-*E. coli* antibodies measured by FTIR before and after exposure to the regeneration kit (N = 3 samples)

Stage	Wavenumber (cm^{-1})	Absorbance (arb. u.)	Integral
Before regeneration	3312.6 ± 12.15	$4.6 \times 10^{-4} \pm 7.1 \times 10^{-5}$	0.21 ± 0.04
After regeneration	3314.1 ± 3.9	$8.2 \times 10^{-3} \pm 1.6 \times 10^{-5}$	0.30 ± 0.06

As for batch 2, the samples were exposed to GFP *E. coli* at 10^6 CFU/ml for 1 hour, and fluorescence images were taken. Later, the samples were exposed to the regeneration solution for 5 min, and another set of fluorescence measurements was performed. Then, a second exposure to *E. coli* at 10^6 CFU/ml was conducted for 1 hour, before taking a final set of fluorescence images. The cycles of exposure-regeneration were repeated 5 times to ensure the efficiency of the regeneration procedure.

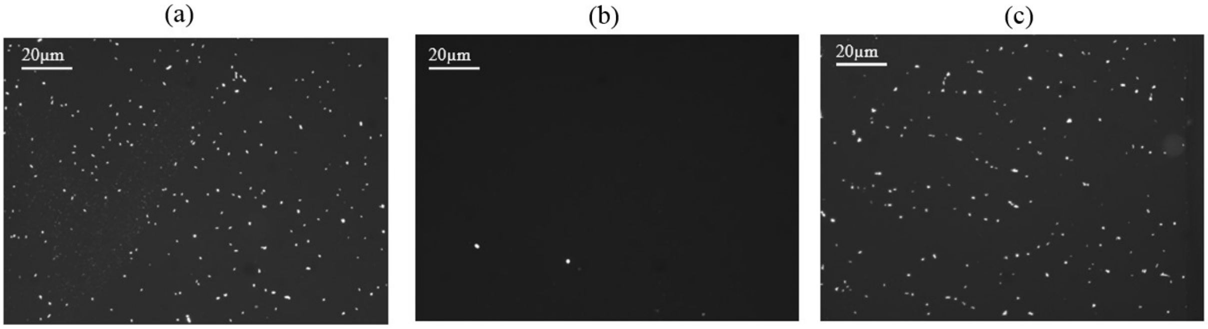

Figure 68: Efficiency of the regeneration kit investigated using fluorescence images (20X magnification) of captured bacteria (a) after the 1st exposure to *E. coli,* (b) after the exposure to the regeneration kit, (c) after the 5th exposure to *E. coli* (N = 3 samples)

The comparison of fluorescence data taken after each step showed an efficient bacteria removal and re-capture with this regeneration kit. The number of bacteria captured on the surface after the first exposure to *E. coli* at 10^6 CFU/ml was determined at 475 ± 23 “bacteria”/mm^2 (Figure 68). This number droped to 10 ± 5 “bacteria”/mm^2 after regeneration and went back to 456 ± 27 “bacteria”/mm^2 after the 5th exposure to *E. coli* at 10^6 CFU/ml.

Figure 69 shows the evolution of the number of “bacteria” captured on the surface after each cycle. This number slightly increased after the first exposure to the regeneration kit, which is in agreement with the FTIR data that showed better amide peak values of the antibodies (Table 20) after the first exposure. This number decreased slowly after each cycle but remained in the limit of the error of the initial number of captured bacteria. These results clearly show the capacity of the proposed kit to regenerate the surface of the biosensor while preserving the efficiency of the bio-interface for the capture of bacteria.

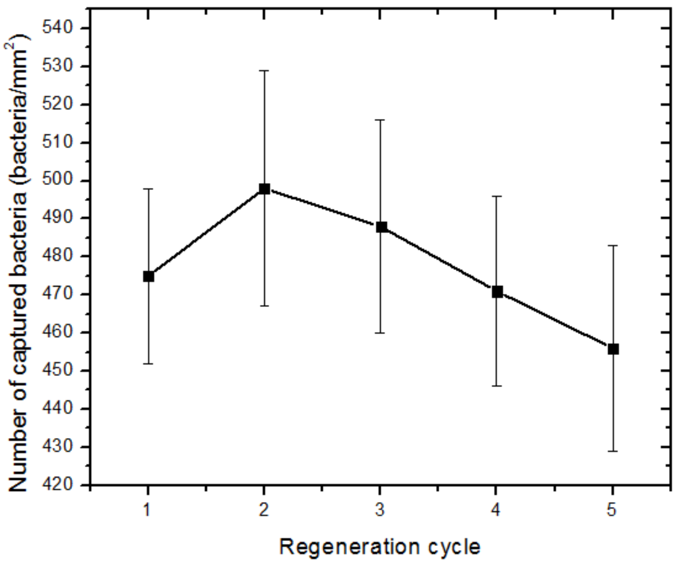

Figure 69. Number of bacteria captured by the bio-interface after each regeneration cycle

6.4.3. Specificity of the biosensor demonstrated by controls

To validate the specificity of the biosensor, two types of controls were carried out:

Control 1: It consisted of the immobilization of antibodies against *Bacillus subtilis* (α-*Bacillus subtilis*) instead of α-*E. coli* on the GaAs membranes and expose it to *E. coli*. The used antibodies were unconjugated polyclonal IgG, purchased from ViroStat, Inc. (Portland, ME). The membranes were chemically functionalized with MHDA/MUDO (1:9) according the procedure presented in section 5.2, then α-*Bacillus subtilis* were immobilized via NHS/EDC activation. After BSA passivation and inactivation of the COOH groups by ethanolamine, the membranes were successively exposed to solutions of *E. coli* of increasing concentrations (10^4 to 10^8 CFU/ml), for one hour for each concentration.

Control 2: It consisted of exposing GaAs membranes bio-functionalized with α-*E. coli* to *Bacillus subtilis* solutions instead of *E. coli*. The exposure was carried out using the same protocol as for of *E. coli*, by incubating the samples in solutions of *Bacillus subtilis* diluted in PBS (1X) at concentrations going from 10^4 to 10^6 CFU/ml for one hour for each concentration.

The controls were prepared and tested in parallel with the sensor samples, in the same conditions. Electrical and fluorescence measurements were performed as well.

6.5 Bio-detection results of *E. coli*

6.5.1. In ideal medium: Phosphate buffer saline

The immunocapture of *E. coli* by the bio-interface was quantified by determining the resulting frequency shifts measured after exposure of the biosensor to solutions of *E. coli* of different concentrations (Figure 70). In these measurements, the biosensor was exposed to *E. coli* through cycles of regeneration/re-exposure, referred to as "regenerated sensor" and with fresh surface referred to as "fresh sensor". The measurements with fresh sensors were performed for some concentrations only, due to the limited number of sensor samples.

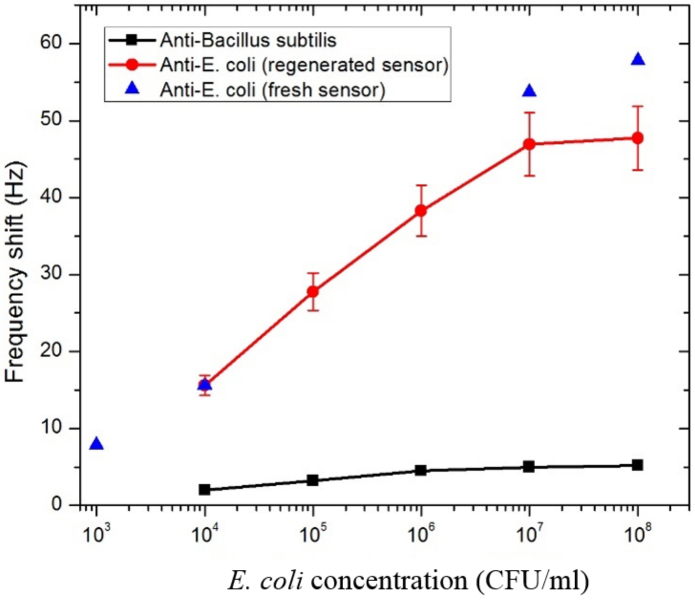

Figure 70. Frequency shifts measured on fresh and regenerated sensors bio-functionalized with α-*E. coli* (N=3) or α-*Bacillus subtilis* after exposure to different concentrations of *E. coli*

As shown in Figure 70, the measurement range of the biosensor was between 10^4 and 10^8 CFU/ml, with a linear region between 10^4 and 10^7 CFU/ml. One test was reported for the fresh sensor at 10^3, 10^7 and 10^8 CFU/ml. The shift observed at 10^4 CFU/ml is the same, since the measurements with regeneration were always started at this concentration. It can be seen that with the fresh sensor, higher frequency shifts and mass of captured bacteria are observed, which is expected since the bio-interface had not sustained any modification due to the regeneration.

The curve representing the frequency shift Δf versus the logarithm of the concentration of *E. coli* can be described using the following relation: Δf = a log [*E. coli*] + b, where a = 0.28

mHz/CFU.ml^{-1}. Further tests with lower concentrations are necessary to determine the lower limit of the full-scale range (LOD) and position ZnO/GaAs biosensor compared to others with respect to the detection limit.

The samples bio-functionalized with α-*Bacillus subtilis* antibodies showed very low frequency shits after exposure to *E. coli* solutions, compared with the shifts measured for the sensor samples bio-functionalized with α-*E. coli* antibodies, which validates the specificity of the bio-interface towards *E. coli.*

To assess the surface coverage with bacteria captured on ZnO/GaAs bio-functionalized surface, fluorescence images were taken immediately after electrical measurements, for each concentration of *E. coli.* Then, the mass of *E. coli* captured on the surface of ZnO/GaAs sensors bio-functionalized with α-*E. coli* was determined from the fluorescence images using equation (6.7) and the results are reported in Table 21.

Table 21. Surface density and mass of *E. coli* captured on the surface for different solutions estimated from fluorescence images

E. coli concentration (CFU/ml)	10^4	10^5	10^6	10^7	10^8
Surface density (“bacteria”/mm^2)	152 ± 12	292 ± 18	475 ± 23	598 ± 33	613 ± 37
Mass of *E. coli* captured on the surface (ng)	0.59 ± 0.05	1.11 ± 0.08	1.81 ± 0.14	2.27 ± 0.17	2.33 ± 0.18

Moreover, the fluorescence images showed a homogeneous bacteria distribution on the surface and an efficient capture of bacteria demonstrated by the surface coverage reported for each concentration of *E. coli.* Figure 71 shows the evolution of the surface density of bacteria for the different tested concentrations of *E. coli*.

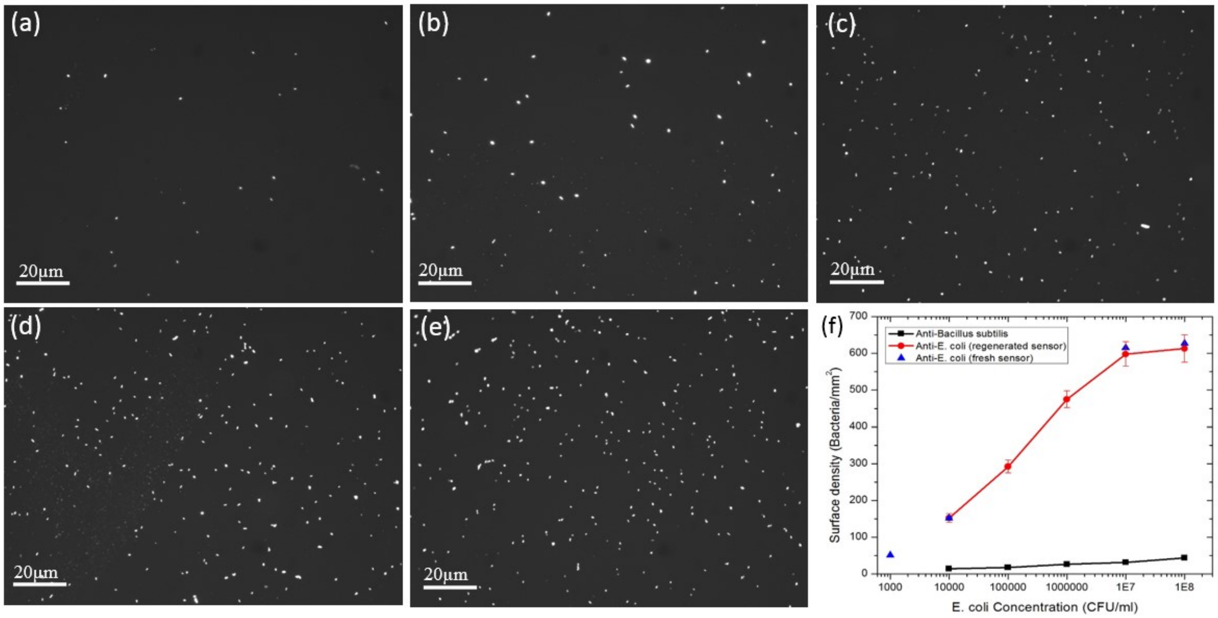

Figure 71. Surface density of GFP *E. coli* captured on ZnO/GaAs bio-functionalized surface observed by fluorescence microscopy (20X magnification) for different *E. coli* concentrations: (a) 10^4 CFU/ml, (b) 10^5 CFU/ml, (c) 10^6 CFU/ml, (d) 10^7 CFU/ml, (e) 10^8 CFU/ml, (f) Comparison of the surface density obtained on ZnO/GaAs surface bio-functionalized with α-*Bacillus subtilis* and with α-*E. coli* (N = 3)

The variation of the number of bacteria captured on the surface between *E. coli* concentrations of 10^7 and 10^8 CFU/ml is almost negligible as shown in Figure 71 (f), indicating that an equilibrium state is established. Indeed, since the exposure to bacteria is done in static conditions, an equilibrium is reached at a certain point, which could have been avoided if a flow or ultrasounds were employed.

On the other hand, the mass of bacteria captured on the surface was calculated from the frequency shifts using equation (6.6) and from the fluorescence data (Table 21). A gap was observed between the corresponding curves, as shown in Figure 72 (a). This gap could be explained by the fact that fluorescence images underestimate the number of bacteria captured on the surface by counting each fluorescent spot as one bacterium instead of an aggregation or a cluster of bacteria.

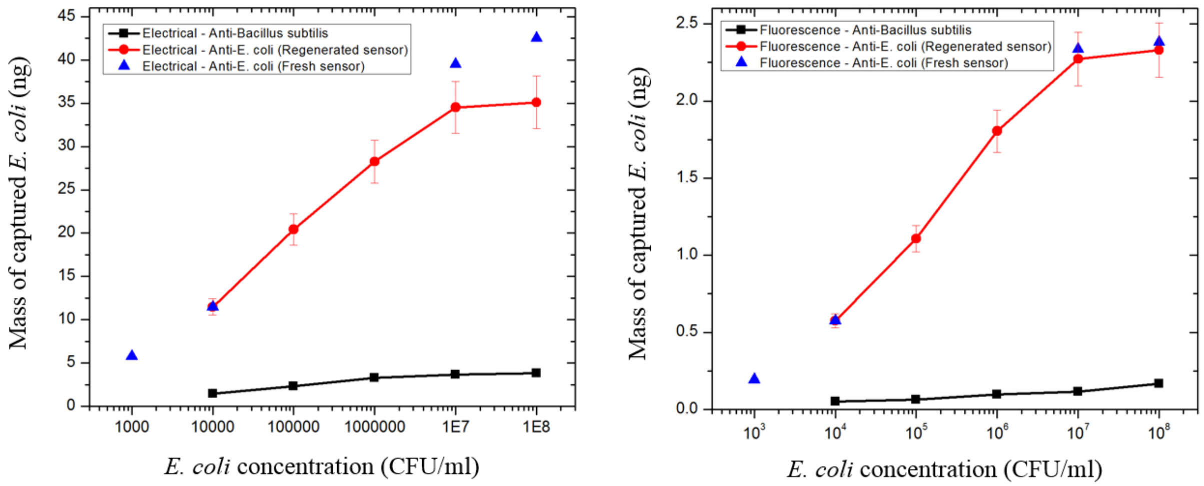

Figure 72. Mass of *E. coli* captured on the surface estimated by fluorescence and electrical measurements for fresh and regenerated ZnO/GaAs sensors bio-functionalized with α-*Bacillus subtilis* and α-*E. coli* (N=3)

Moreover, the specificity of the biosensor was demonstrated, once again, by the low frequency shifts (3.2; 7.7 and 15.5 Hz) determined after exposure of the sensors bio-functionalized with α-*E. coli* to solutions of *Bacillus Subtilis* at concentrations of 10^4; 10^5 and 10^6 CFU/ml, respectively.

6.5.2. In complex medium: in the presence of *Bacillus subtilis*

The challenge is to be able to recognize and quantify *E. coli* in the presence of other biological elements. To simulate the detection in a complex medium, we carried out detection tests in a mixture of *E. coli* at different concentrations and *Bacillus Subtilis* at a constant concentration of 10^6 CFU/ml, in PBS (1X). Figure 73 shows the frequency shifts obtained in comparison with ones determined in ideal medium.

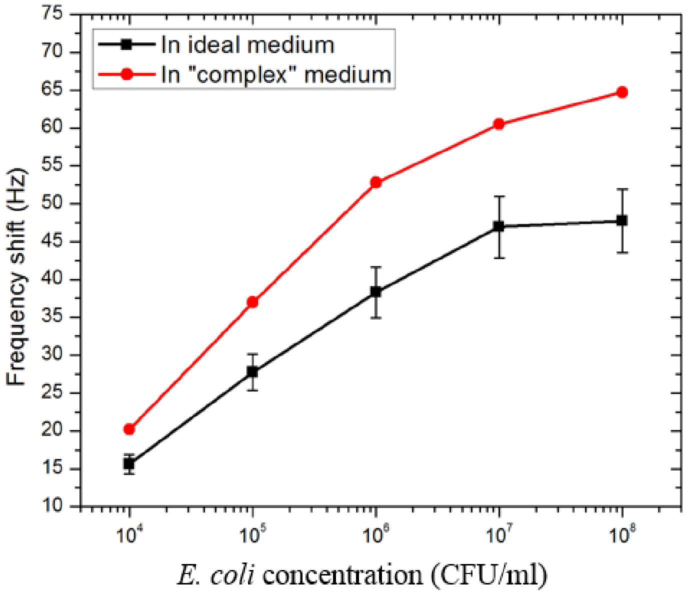

Figure 73. Frequency shifts reported for different concentrations of *E. coli* in a mixture containing *Bacillus subtilis* at 10^6 CFU/ml

The correlation of the frequency shifts obtained in ideal and complex medium shows the capacity of ZnO/GaAs biosensor to detect the targeted bacteria in the presence of a competitor. We succeeded to detect *E. coli* in the presence of *Bacillus Subtilis*, which indicates that the proposed biosensor has the potential to detect selectively *E. coli* bacteria in complex liquids. However, further detection tests in environments of increasing complexity need to be performed to simulate the detection in complex biological liquids.

6.6 Optimization tracks for ZnO/GaAs biosensor

6.6.1. NHS/EDC ratio

N-hydroxysuccinimide (NHS) is a well-known cross-linking agent for linking amine to carboxyl groups. This reagent is mostly used in conjunction with EDC to obtain an extremely reactive intermediate acid group. The commonly employed activation protocols use a ratio of (1:4) for (NHS/EDC) at 1 M. In this work, we were interested in determining the optimal ratio for these reagents to ensure an optimal SAM activation. Therefore, in this section various NHS/EDC mixtures were tested.

For this purpose, bulk double side polished GaAs samples of dimensions 4x4 mm^2 were functionalized with SAMs of MHDA/MUDO (1:9) at 2 mM. FTIR measurements were performed to qualify the organization of the SAMs. OPUS software of Bruker Optics Company, used for the measurement and control of the FTIR instrument, has been employed in the treatment and evaluation of the absorption spectra obtained. The positions of the CH_2 peaks as well as the absorbance values and integrals were noted. After, the COOH groups were activated by incubation of the samples in NHS/EDC solutions at ratios of (1:1), (1:2) and (1:4) for 30 minutes, and FTIR measurements were carried out to examine the C = O peaks. An example of the peaks relative to amide A for the different ratios of NHS/EDC is shown in Figure 74.

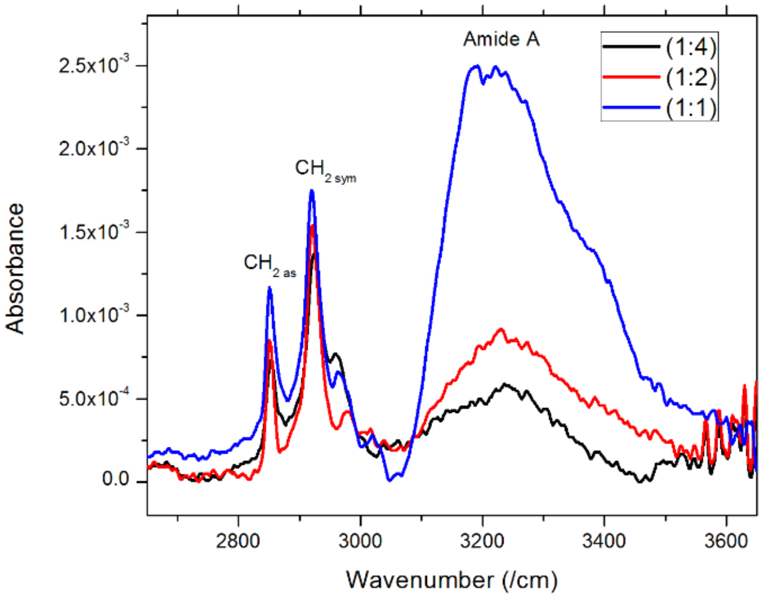

Figure 74. CH_2 and amide A peaks of bulk GaAs samples functionalized with MHDA/MUDO (1:9) and activated with different concentrations of NHS/EDC (N = 3 samples per ratio)

Three samples per ratio were measured and the number of antibodies immobilized on the surface was estimated by calculating the integral of the amide A bands (Table 22). The amide A peak values showed that using NHS/EDC (1:1) is better in terms of absorbance intensity and integral, which suggests that the number of antibodies immobilized on the surface is higher for this ratio. The results are similar for amide I and II.

Table 22. Amide A values revealed after GaAs membrane bio-functionalization with antibodies using different ratios of NHS/EDC (N = 3 samples per ratio)

(NHS/EDC) ratio	Wavenumber (cm^{-1})	Absorbance (arb. u.)	Integral
(1:4)	3256.6 ± 28.3	$1.4 \times 10^{-3} \pm 1.1 \times 10^{-4}$	0.49 ± 0.18
(1:2)	3262.3 ± 20.1	$1.6 \times 10^{-3} \pm 9.7 \times 10^{-4}$	0.55 ± 0.19
(1:1)	3246.1 ± 6.7	$21.6 \times 10^{-3} \pm 4.7 \times 10^{-4}$	0.69 ± 0.18

The transformation from carboxylic acid to amide takes place as the following: in the first step, EDC is attached with the acid, which is a slow process and therefore the totality of the acid will not be converted into O-acylisourea intermediate compound. For this reason, EDC is usually used in excess. In the second step, NHS intervenes very fast which results in complete conversion. In our case, the (1:1) ratio seems to be adequate for amide formation. It is probable that EDC reacts with the acid more efficiently on the solid substrate (particularly on GaAs surface) compared to the solution based organic reaction, therefore we do not need an excess of EDC. At higher ratios of EDC, there is a possibility of reversible reaction of the O-acylisourea intermediate with water which will form the acid again (amide will not be formed). This result is very beneficial to optimize the antibodies immobilization and reduce the cost of material used.

6.6.2. Exposure time to bacteria

To determine the adequate exposure time of the bio-interface to *E. coli*, we used fluorescence microscopy to determine the surface coverage with captured bacteria on the surface after incubation of bio-functionalized samples in GFP *E. coli* for durations going from15 minutes to 1 hour (3 samples per exposure time). The samples were chemically functionalized beforehand by a SAM of MHDA/MUDO (1:9) and α-*E. coli* were immobilized by activation with NHS/EDC (1:4). After the passivation of the surface with BSA and the inactivation of the activated carboxyl groups, the samples were exposed for different durations to *E. coli* at 10^5 and 10^6 CFU/ml. Figure 75 shows an example of the surface coverage in bacteria obtained for each exposure time.

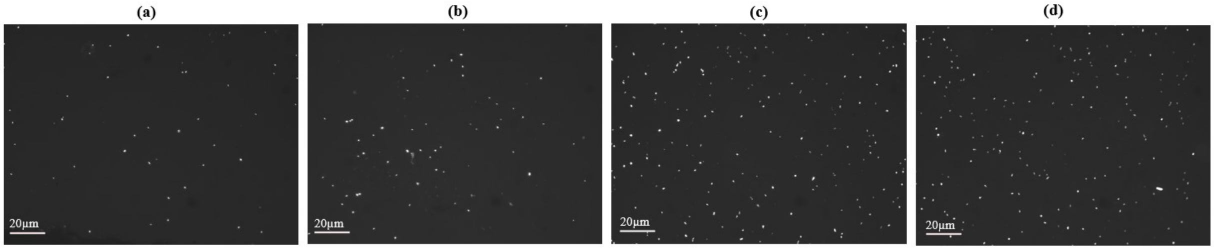

Figure 75. Fluorescence images (20X magnification) of ZnO/GaAs bio-functionalized samples after incubation in GFP *E. coli* at 10^6 CFU/ml for different durations: (a) 15 min, (b) 30 min, (c) 45 min, (d) 1 hour (N = 2 samples per exposure time and concentration)

The surface coverage for each exposure time was determined using ImageJ and the results are reported in Table 23. The highest surface coverage was obtained when the samples were incubated in the bacteria solution for 1 hour. However, the longer the incubation time, the higher is the possibility of non-specific interactions on the surface. For an incubation of 15 minutes, the number of captured bacteria is reduced to half when the concentration of *E. coli* in the tested solution is decreased of one order of magnitude. This means that if the concentration of *E. coli* in the initial solution was low, the number of captured bacteria on the biosensor's surface would be too low to quantify.

Table 23. Coverage density for different exposure times of the ZnO/GaAs biosensor to *E. coli* (N = 3 samples per exposure time and concentration)

E. coli concentration (CFU/ml)	Coverage density («bacteria»/mm^2)			
	15 min	30 min	45 min	1 hour
10^5	104 ± 11	173 ± 13	261 ± 19	292 ± 18
10^6	195 ± 14	281 ± 18	458 ± 24	475 ± 23

Among the tested durations, an exposure of 45 minutes to *E. coli* seems to be a reasonable compromise, since it allows an efficient capture of bacteria (comparable to 1 hour) while limiting the non-specific interactions. Further tests with other concentrations of *E. coli* are necessary to confirm these results.

Note that these results were obtained in static conditions, without any flow or agitation. Kardous et al., in our group, showed that the acoustic mixing during antibody binding at the biochips surface increases their bio-recognition performances of a mean factor of 2.7 and increases statistically the homogeneity of the response over all the surface of the chips [203]. Therefore, better performances of the sensor are expected in dynamic conditions.

6.7 Conclusion

In this chapter, we presented the methodology and setup for testing the ZnO/GaAs biosensor in various environments. The resonant frequency of shear mode obtained by electrical measurements in air were close to the values determined by FEM simulation in chapter 3.

The impact of the conductivity and pH of the electrolyte on the performance of the biosensor was examined. In perspective, the impact of these parameters on the resonance should be reduced or compensated for enhanced mass-sensing measurements. Therefore, it is necessary to consider more tests and simulations to determine the key parameters in the geometry of the biosensor to limit these effects.

We performed tests with bacterial solutions and determined the frequency shift and the surface coverage obtained by the capture of *E. coli* bacteria on the bio-interface. The results obtained by electrical measurements were correlated to those of fluorescence microscopy. The controls performed using *Bacillus subtilis* showed the specificity of the bio-interface to *E. coli*. The measurement range was 10^4 - 10^8 CFU/ml, with a linear region between 10^4 and 10^7 CFU/ml.

By comparing ZnO/GaAs BAW biosensor to the other sensors reported in section 2.2.4., it can be seen that it covers a wide measurement range. The lowest measured concentration of *E. coli* was 10^3 CFU/ml which suggests the possible application of the biosensor for the detection of *E. coli* in urine. For detection in water, further tests are required to assess the detection limit of the biosensor. Although the phases of sample preparation and incubation are time-consuming, the analysis time after exposure to bacteria is less than 5 minutes, which makes the biosensor suitable for the rapid detection of *E. coli*.

Although the performances of the developed biosensor are promising compared to others, the reduced performance due to the liquid will not be adequate to detect biological entities in liquid medium in the current configuration. The tests carried out in liquid showed the limitations of the biosensor to the possible variations of the electrical parameters or pH of the solution. However, based on the results obtained in this chapter, we can propose different strategies to improve the performance of the biosensor.

CONCLUSIONS AND PERSPECTIVES

The work presented in this manuscript focused on the fabrication, characterization and testing of a ZnO/GaAs-based bulk acoustic wave biosensor. This study was conducted for the development of a miniaturized biosensor for the detection and quantification of bacteria in complex liquid media. The field of application is large and targets clinical diagnostics, environmental monitoring and food industry.

The first chapter has presented the context of the research topic: it provided a brief presentation of the project and the preceding work carried out in the research teams of Besançon and Sherbrooke, as well as the objectives of the thesis.

The second chapter has introduced the bacterial threats to human health and the conventional biosensing approaches, while focusing on the pertinence of the developed biosensor compared to existing techniques applied to detect bacteria, and particularly *Escherichia coli*. We exploited the microfabrication, surface bio-functionalization and regeneration potentialities of GaAs, and we exposed the properties of ZnO thin films leading to the choice of this material. To improve the performances of the existing GaAs-based biosensor, a new architecture was designed combining these two materials: GaAs was retained for the sensing part in contact with the liquid and a piezoelectric ZnO thin film was added on top of the GaAs membrane to improve the electromechanical coupling.

The third chapter was devoted to the modeling of the bulk acoustic wave transducer. We presented the theoretical relations and analytical models allowing to understand the functioning of the transducer. After a brief overview on acoustic waves transduction, we recalled the tensorial expressions and the fundamental equations of piezoelectricity, leading to the development of the analytical model of the transducer. A simulation using finite elements method was carried out using Comsol Multiphysics® for the dimensioning of the ZnO/GaAs transducer. Using this model, we determined the resonance characteristics corresponding to shear mode of bulk acoustic waves and the displacement along the different axis of the structure. After testing different inter-electrode distances, a 500 µm gap was shown to be an optimal configuration to limit the penetration of the electrical field in the structure, especially in the case of measurement in liquid medium.

In the fourth chapter, we worked on the aspects of microfabrication of the transducer. Through an overview of the commonly used deposition techniques for ZnO thin films, reactive RF magnetron sputtering has been selected for the deposition of piezoelectric ZnO films on GaAs substrates. We investigated the use of a Platinum buffer layer for promoting the growth of ZnO on GaAs, using Ti or Ta adhesion layers. Structural (XRD, Raman) and topographic (AFM) characterization techniques have been used to determine the impact of the crystallographic orientation of the GaAs substrate on the ZnO films quality. The chemical interfaces between the deposited layers were studied using secondary ions mass spectrometry (SIMS), and ellipsometry was used to evaluate the thicknesses of ZnO films. In the last part, the different stages of microfabrication of the transducer were presented, including the realization of the electrodes and the micromachining of the GaAs membrane by chemical wet etching.

In the fifth chapter, we studied and characterized the bio-recognition interface of the biosensor realized on the GaAs membrane. The establishment and characterization of thiolates self-assembled monolayers on the GaAs membrane were analyzed using contact angle measurements, FTIR and XPS. We have chosen a mixed SAM architecture of MHDA/MUDO (1:9), which has proved to allow the immobilization of the ligands in a durable, robust and reproducible way. Furthermore, we have tested different conditions for ligands immobilization such as the concentration in ligands, the pH of the immobilization solution and the incubation time of the ligand on the membrane, in order to achieve a maximum of recognition sites on the surface, and therefore to improve the sensitivity of the detection.

Finally, chapter 6 was devoted to the testing of the biosensor in various media. We presented the experimental setup for electrical characterization of the devices, which allowed to characterize the frequency response of the transducer. Then, we studied the impacts of the environmental parameters on the response, such as the pH and the electrical conductivity of the electrolyte solution, which can critically influence the performance of the biosensor. We have successfully demonstrated the bio-detection of *E. coli* at different concentrations, over a dynamic range of 3 orders of magnitude, and correlated these results to the surface density of bacteria on the biosensor by fluorescence measurements. We have performed two types of controls that validated the specificity of the biosensor to the targeted bacteria. Through detection tests performed using the biosensor in ideal and complex medium, we determined the relation between the frequency shift and the concentration of *E. coli*. Despite the limitations in liquid medium observed in this chapter, the performances of the biosensor remain interesting.

In order to overcome these limitations and achieve better performances of the biosensor, several approaches can be adopted on the short and long term. First, the optimization tracks presented in section 6.6, concerning the NHS/EDC ratio and the exposure time to the antigen solution should be applied to improve the ligands immobilization and the immunocapture of bacteria. Moreover, the performances of the device can be improved by performing the chemical functionalization, the antibodies immobilization and the antigen exposure in dynamic conditions, to optimize the bio-recognition event.

Another perspective to this work is the optimization of the deposition of ZnO films on GaAs using the Pt buffer layer. As shown by XRD and AFM, this buffer improves the crystalline and structural quality of the films, in terms of texture, stress, roughness, etc., but it promotes the diffusion of Ga, interface layers (Ta, Ti) and ZnO itself into the Pt. Therefore, further optimization of the Pt/GaAs interface should be considered to stop the diffusion. This problem could be addressed in the future, by adjusting the deposition temperature to prevent this diffusion, or by adding an extra diffusion barrier at Pt/GaAs interface.

From a microfabrication point of view, the thinning of the substrate by chemical wet etching should be replaced with mechanical polishing in order to avoid surface defects before the micromachining of the membranes. This would allow to obtain flat membrane structures without roughness or surface defects.

Furthermore, it is necessary to make changes in the sensor structure to confine the vibrations in the membrane. A new structure trapping the waves under the membrane could be proposed using the same microfabrication techniques and integrating a fluidic cell.

Another improvement track could be to use the phenomena of coupling between different modes of resonance, which could lead to the generation of local resonances and eventually increase the sensitivity of the transducer. In the longer term, it would be interesting to extend this type of sensor in the form of a network in order to allow the simultaneous detection of several targeted molecules involved in the diagnosis of a disease.

CONCLUSIONS ET PERSPECTIVES

Le travail présenté dans ce manuscrit a porté sur la fabrication, la caractérisation et le test d'un biocapteur à ondes acoustiques de volume à base de ZnO/GaAs. Cette étude visait à développer un biocapteur miniaturisé pour la détection et la quantification de bactéries dans des milieux liquides complexes. Le champ d'application est large et vise le diagnostic clinique, la surveillance de l'environnement et l'industrie agroalimentaire.

Le premier chapitre a présenté le contexte du sujet de recherche : il a fourni une brève présentation du projet et des travaux précédents menés dans les équipes de recherche à Besançon et Sherbrooke, ainsi que les objectifs de la thèse.

Le deuxième chapitre a présenté les menaces bactériennes pour la santé humaine et les approches classiques de bio-détection, en se focalisant sur la pertinence du biocapteur développé par rapport aux techniques existantes pour la détection de bactéries, en particulier l'*Escherichia coli*. Nous avons exploité les potentialités de microfabrication, de fonctionnalisation biochimique et de régénération de surface du GaAs, et nous avons présenté les propriétés des films minces de ZnO qui ont conduit au choix de ce matériau. Pour améliorer les performances du biocapteur existant à base de GaAs, nous avons conçu une nouvelle architecture combinant ces deux matériaux : GaAs a été retenu pour la partie sensible en contact avec le liquide et un film mince piézoélectrique de ZnO a été ajouté sur la face avant de la membrane en GaAs pour améliorer le couplage électromécanique.

Le troisième chapitre a été consacré à la modélisation du transducteur à ondes acoustiques de volume. Nous avons présenté les relations théoriques et les modèles analytiques permettant de comprendre le fonctionnement du transducteur. Après un bref aperçu de la transduction acoustique, nous avons rappelé les expressions tensorielles et les équations fondamentales de la piézoélectricité, qui ont conduit au développement du modèle analytique du transducteur. Une simulation utilisant la méthode des éléments finis (FEM) a été réalisée avec le logiciel Comsol Multiphysics® pour le dimensionnement du transducteur ZnO/GaAs. En utilisant ce modèle, nous avons déterminé les caractéristiques à la résonance des modes de cisaillement des ondes acoustiques de volume et le déplacement le long des différents axes de la structure. Après avoir testé différentes distances inter-électrodes, un gap de 500 µm a présenté la configuration optimale pour limiter la pénétration du champ électrique dans la structure, en particulier dans le cas d'une mesure en milieu liquide.

Dans le quatrième chapitre, nous avons abordé les aspects de la microfabrication du transducteur. Après un aperçu des techniques de dépôt couramment utilisées pour les couches minces de ZnO, la pulvérisation réactive radio fréquence à effet magnétron a été sélectionnée pour le dépôt de couches minces piézoélectriques de ZnO sur des substrats en GaAs. Nous avons testé l'utilisation d'une couche intermédiaire en platine entre le ZnO et le GaAs pour favoriser la croissance, en utilisant des couches d'adhésion de Ti ou Ta. Des techniques de caractérisation structurale (DRX, Raman) et topographique (AFM) ont été utilisées pour déterminer l'impact de l'orientation cristallographique du substrat de GaAs sur la qualité des films de ZnO. Les les interfaces chimiques entre les différentes couches déposées ont été étudiées par spectrométrie de masse à ionisation secondaire (SIMS) et l'ellipsométrie a été utilisée pour évaluer les épaisseurs des films de ZnO. Dans une dernière partie, les différentes étapes de microfabrication du transducteur ont été présentées, y compris la réalisation des électrodes et l'usinage de la membrane en GaAs par gravure chimique humide.

Dans le cinquième chapitre, nous avons étudié et caractérisé la bio-interface de reconnaissance du biocapteur réalisée sur la membrane de GaAs. La formation et la caractérisation de monocouches auto-assemblées de thiols sur la membrane de GaAs ont été analysées par des mesures d'angle de contact, FTIR et XPS. Nous avons choisi une architecture de SAM mixte de MHDA/MUDO (1: 9), qui s'est révélée permettre l'immobilisation des ligands de manière durable, robuste et reproductible. De plus, nous avons testé différentes conditions de greffage de ligands, telles que la concentration en ligands, le pH de la solution de greffage et le temps d'incubation du ligand sur la membrane du capteur, afin de maximiser le nombre de sites de reconnaissance en surface et d'améliorer la sensibilité de détection.

Enfin, le chapitre 6 a été consacré aux tests du biocapteur dans divers environnements. Nous avons présenté le montage expérimental pour la caractérisation électrique des dispositifs, permettant de caractériser la réponse fréquentielle du transducteur. Ensuite, nous avons étudié les impacts des paramètres environnementaux sur la réponse, tels que le pH et la conductivité de la solution électrolytique, susceptibles d'influencer de manière critique les performances du biocapteur. Nous avons démontré avec succès la bio-détection d'*E. coli* à différentes concentrations, sur une gamme dynamique de 3 ordres de grandeur, et avons corrélé ces résultats à la densité surfacique en bactéries sur le biocapteur par des mesures de fluorescence. Nous avons effectué des contrôles qui ont validé la spécificité du biocapteur vis-à-vis de la bactérie ciblée. Grâce à des tests de détection réalisés en milieux idéal et complexe, nous avons déterminé la relation entre le décalage en fréquence et la concentration d'*E. coli*. Malgré les limitations en milieu liquide observées dans ce chapitre, les performances du biocapteur restent toutefois prometteuses.

Pour surmonter ces limitations et obtenir de meilleures performances du biocapteur, plusieurs approches peuvent être adoptées à court et à long terme. Premièrement, les pistes d'optimisation présentées dans la section 6.6 concernant le ratio de NHS/EDC et le temps d'exposition à la solution d'antigène doivent être considérées pour améliorer le greffage des ligands et l'immunocapture des bactéries à la bio-interface, respectivement. De plus, les performances du dispositif peuvent être améliorées en effectuant la fonctionnalisation chimique, le greffage d'anticorps et l'exposition à l'antigène dans des conditions dynamiques, afin d'optimiser l'événement de bio-reconnaissance.

Une autre perspective de ce travail est l'optimisation du dépôt de films de ZnO sur GaAs en utilisant une couche intermédiaire de Pt. Comme l'ont montré les caractérisations DRX et AFM, cette couche de Pt améliore la qualité cristalline et structurale des films, en termes de texture, de contraintes et de rugosité, mais elle favorise l'inter-diffusion de Ga, Ta, Ti et de ZnO lui-même. Par conséquent, une étude plus poussée de l'interface Pt/GaAs devrait être envisagée pour arrêter la diffusion. Ce problème pourrait être résolu à l'avenir, en ajustant la température de dépôt, ou en ajoutant une barrière de diffusion supplémentaire à l'interface Pt/GaAs.

Du point de vue de la microfabrication, l'amincissement du substrat par voie chimique devrait être remplacé par un polissage mécanique afin d'éviter les défauts de surface avant le micro-usinage des membranes. Cela permettrait d'obtenir des structures membranaires planes sans rugosité ni défauts de surface.

De plus, il est nécessaire d'apporter des modifications à la structure du capteur afin de confiner les vibrations dans la membrane. Une nouvelle structure piégeant les ondes sous la membrane pourrait être proposée en utilisant les mêmes techniques de microfabrication et en intégrant une cellule fluidique.

Une autre piste d'amélioration pourrait être l’utilisation des phénomènes de couplage entre différents modes de résonance, ce qui pourrait conduire à la génération de résonances locales et éventuellement à augmenter la sensibilité du transducteur. A plus long terme, il serait intéressant d'étendre ce type de capteur sous forme de réseau afin de permettre la détection simultanée de plusieurs molécules ciblées impliquées dans le diagnostic d'une maladie.

Appendix A: JCPDS cards

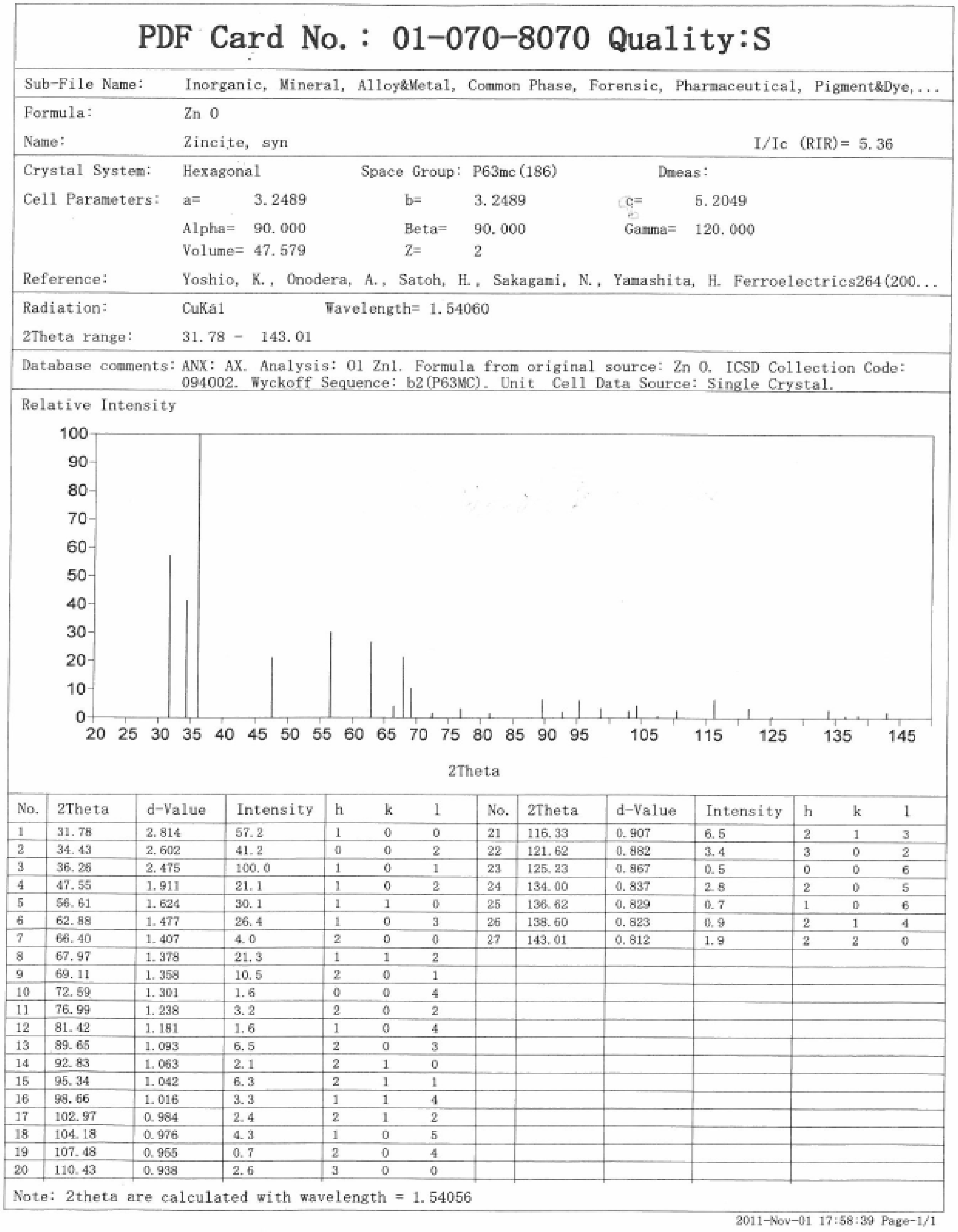

PDF Card No.: 01-070-8070 Quality:S

Sub-File Name: Inorganic, Mineral, Alloy&Metal, Common Phase, Forensic, Pharmaceutical, Pigment&Dye,...

Formula: Zn O

Name: Zincite, syn I/Ic (RIR)= 5.36

Crystal System: Hexagonal Space Group: P63mc(186) Dmeas:

Cell Parameters: a= 3.2489 b= 3.2489 c= 5.2049

Alpha= 90.000 Beta= 90.000 Gamma= 120.000

Volume= 47.579 Z= 2

Reference: Yoshio, K., Onodera, A., Satoh, H., Sakagami, N., Yamashita, H. Ferroelectrics264(200...

Radiation: CuKá1 Wavelength= 1.54060

2Theta range: 31.78 - 143.01

Database comments: ANX: AX. Analysis: O1 Zn1. Formula from original source: Zn O. ICSD Collection Code: 094002. Wyckoff Sequence: b2(P63MC). Unit Cell Data Source: Single Crystal.

No.	2Theta	d-Value	Intensity	h	k	l
1	31.78	2.814	57.2	1	0	0
2	34.43	2.602	41.2	0	0	2
3	36.26	2.475	100.0	1	0	1
4	47.55	1.911	21.1	1	0	2
5	56.61	1.624	30.1	1	1	0
6	62.88	1.477	26.4	1	0	3
7	66.40	1.407	4.0	2	0	0
8	67.97	1.378	21.3	1	1	2
9	69.11	1.358	10.5	2	0	1
10	72.59	1.301	1.6	0	0	4
11	76.99	1.238	3.2	2	0	2
12	81.42	1.181	1.6	1	0	4
13	89.65	1.093	6.5	2	0	3
14	92.83	1.063	2.1	2	1	0
15	95.34	1.042	6.3	2	1	1
16	98.66	1.016	3.3	1	1	4
17	102.97	0.984	2.4	2	1	2
18	104.18	0.976	4.3	1	0	5
19	107.48	0.955	0.7	2	0	4
20	110.43	0.938	2.6	3	0	0
21	116.33	0.907	6.5	2	1	3
22	121.62	0.882	3.4	3	0	2
23	125.23	0.867	0.5	0	0	6
24	134.00	0.837	2.8	2	0	5
25	136.62	0.829	0.7	1	0	6
26	138.60	0.823	0.9	2	1	4
27	143.01	0.812	1.9	2	2	0

Note: 2theta are calculated with wavelength = 1.54056

2011-Nov-01 17:58:39 Page-1/1

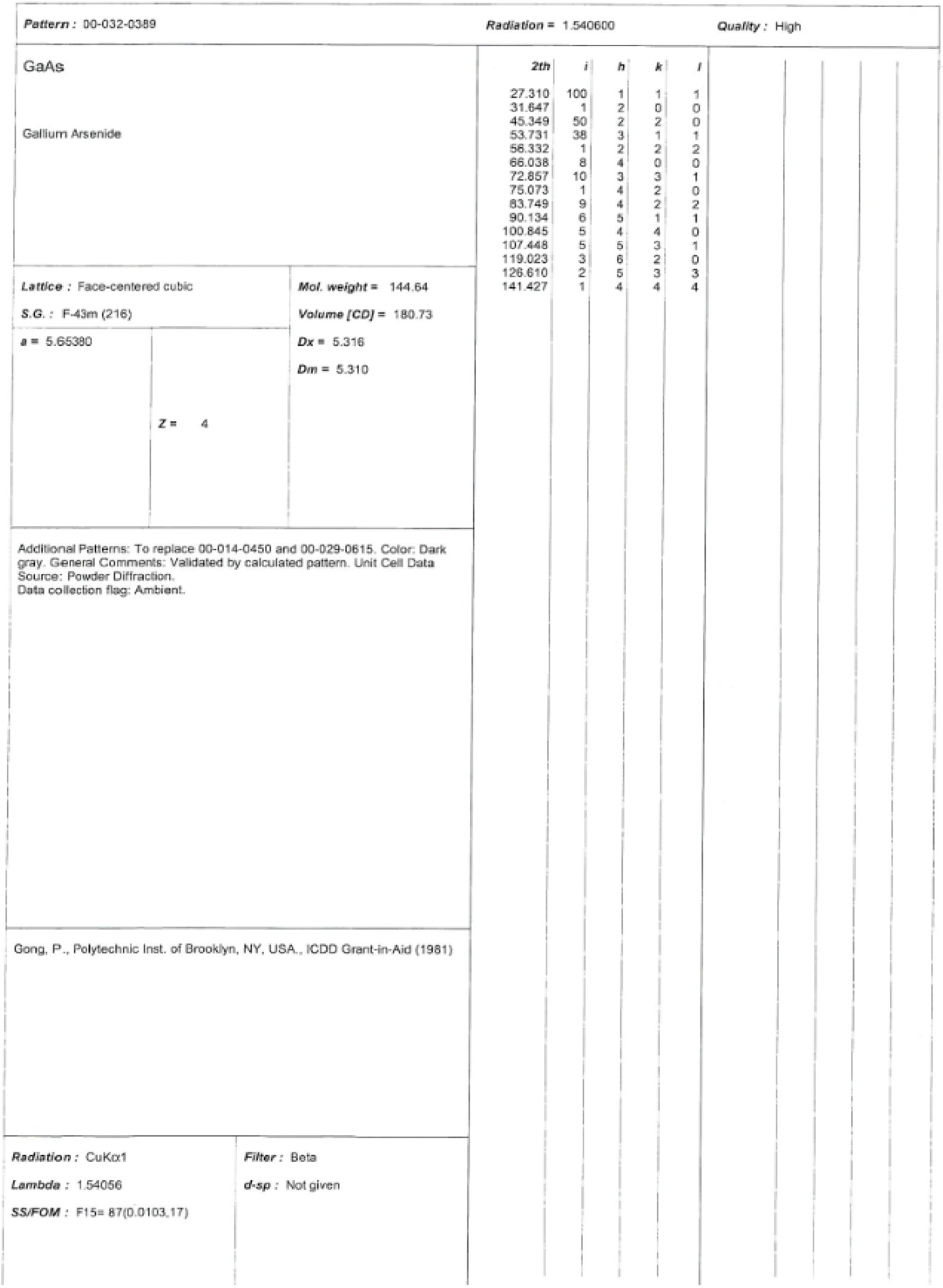

Pattern : 00-032-0389

Radiation = 1.540600

Quality : High

GaAs

Gallium Arsenide

2th	i	h	k	l
27.310	100	1	1	1
31.647	1	2	0	0
45.349	50	2	2	0
53.731	38	3	1	1
56.332	1	2	2	2
66.038	8	4	0	0
72.857	10	3	3	1
75.073	1	4	2	0
83.749	9	4	2	2
90.134	6	5	1	1
100.845	5	4	4	0
107.448	5	5	3	1
119.023	3	6	2	0
126.610	2	5	3	3
141.427	1	4	4	4

Lattice : Face-centered cubic

S.G. : F-43m (216)

a = 5.65380

Z = 4

Mol. weight = 144.64

Volume [CD] = 180.73

Dx = 5.316

Dm = 5.310

Additional Patterns: To replace 00-014-0450 and 00-029-0615. Color: Dark gray. General Comments: Validated by calculated pattern. Unit Cell Data Source: Powder Diffraction.
Data collection flag: Ambient.

Gong, P., Polytechnic Inst. of Brooklyn, NY, USA., ICDD Grant-in-Aid (1981)

Radiation : CuKα1

Lambda : 1.54056

SS/FOM : F15= 87(0.0103,17)

Filter : Beta

d-sp : Not given

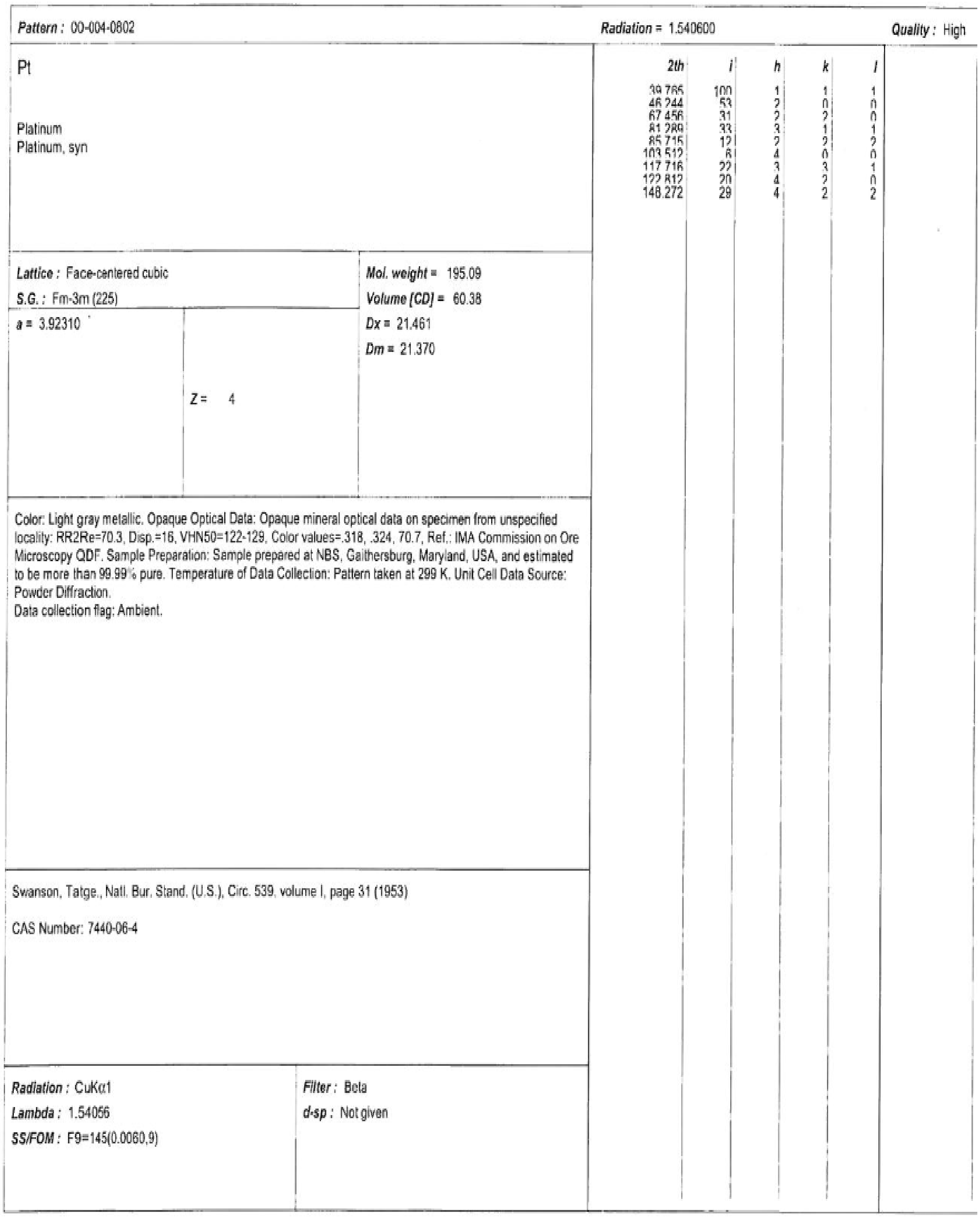

Pattern : 00-004-0802

Radiation = 1.540600

Quality : High

Pt

Platinum
Platinum, syn

2th	i	h	k	l
39.765	100	1	1	1
46.244	53	2	0	0
67.456	31	2	2	0
81.289	33	3	1	1
85.715	12	2	2	2
103.512	6	4	0	0
117.716	22	3	3	1
122.812	20	4	2	0
148.272	29	4	2	2

Lattice : Face-centered cubic
S.G. : Fm-3m (225)

a = 3.92310

Z = 4

Mol. weight = 195.09
Volume [CD] = 60.38
Dx = 21.461
Dm = 21.370

Color: Light gray metallic. Opaque Optical Data: Opaque mineral optical data on specimen from unspecified locality: RR2Re=70.3, Disp.=16, VHN50=122-129, Color values=.318, .324, 70.7, Ref.: IMA Commission on Ore Microscopy QDF. Sample Preparation: Sample prepared at NBS, Gaithersburg, Maryland, USA, and estimated to be more than 99.99% pure. Temperature of Data Collection: Pattern taken at 299 K. Unit Cell Data Source: Powder Diffraction.
Data collection flag: Ambient.

Swanson, Tatge., Natl. Bur. Stand. (U.S.), Circ. 539, volume I, page 31 (1953)

CAS Number: 7440-06-4

Radiation : CuKα1
Lambda : 1.54056
SS/FOM : F9=145(0.0060,9)

Filter : Beta
d-sp : Not given

Appendix B: Samples preparation & characterization procedure prior to exposure to *E. coli*

Phase	Step	Objective	Tools & solutions	Parameters/Remarks
Characterisation of the sensor with bare surface	Cleaning of the samples	Remove mineral and organic impurities from the surface of the samples	Immersion in successive baths of: -OptiClear -Acetone -Ethanol	1) Immersion for 5 min in each solvent under US 2) Drying under Nitrogen flow
	Electrical measurements	Determine the resonance characteristics (frequency, impedance phase and modulus)	-Network analyzer -Cal kit 85052D -Electrical interface	Calibration prior to measurement series and after modification of the acquisition parameters
Characterisation of the sensor with chemically functionalized surface	Degassing of ethanol	Remove the oxygen from ethanol to prevent re-oxidation of GaAs	-Anhydrous ethanol -Nitrogen flow -Erlenmeyer -Electrode	1 hour
	Cleaning of the samples	Remove mineral and organic impurities from the surface of the samples	Immersion in successive baths of: -OptiClear -Acetone -Ethanol	1) Immersion for 5 min in each solvent under US 2) Drying under Nitrogen flow
	Deoxidation of GaAs	Remove the native oxide from the GaAs surface to prevent the chemisorption of thiols on the surface	Ammonium hydroxide NH_4OH (28 %)	1) Incubation for 2 min 2) Brief rinsing with degassed ethanol

	Chemical functionalization of GaAs at the bottom side of the sensor	Formation of SAMs to graft ligands	-Sample holder -MHDA/MUDO (1:9) at 2mM -Degassed ethanol	1) Sonicate for 1 min after mixing for homogenization 2) Incubate for 20 hours in dark at RT
	Rinsing	Remove physiosorbed thiols	-Degassed ethanol -Nitrogen gun	1) Rinsing (2x, 1st time under US) with degassed ethanol 2) Drying under Nitrogen flow
	Electrical measurements	Determine the frequency shift due to thiols adsorption	-Network analyzer -Cal kit 85052D -Electrical interface	Calibration
Characterisation of the sensor with antibody-coated surface	EDC/NHS activation	Form a covalent bond between carboxyl group and amine group	-EDC at 0.4M -NHS at 0.1M	1) Incubation for 30 min in dark at RT 2) Rinsing (5 x with DI water)
	Antibodies immobilization	Fix the antibodies via amine groups (-NH_2)	Unconjugated polyclonal α-*E. coli* IgG diluted in PBS (1X) at 100 µg/ml	1 hour in dark at RT
	Rinsing and drying	Remove traces of salts and PBS	- PBS (1X) -Tween20 at 0.05 %	1) Siphon the solution 2) Rinse 3x with PBS 3) Rinse 3x with Tween 20 at 0.05 % 4) Rinse 3x with deionized water
	Electrical measurements	Determine the frequency shift due to α-*E. coli*	-Network analyzer -Cal kit 85052D -Electrical interface	Calibration
Characterisation of the sensor with passivated surface	Passivation of the surface using BSA	Saturate the surface to block any unspecific adsorption reaction	BSA solution (200 µg/ml, pH 5.5)	1) Incubation for 30 min in dark at RT 2) Rinsing & drying

	Rinsing and drying	Remove traces of BSA	- PBS (1X) -Tween20 at 0.05 %	1) Siphon the solution 2) Rinse 3x with PBS 3) Rinse 3x with Tween 20 at 0.05 % 4) Rinse 3x with deionized water
	Electrical measurements	Determine the frequency shift due to BSA fixation	-Network analyzer -Cal kit 85052D -Electrical interface	Calibration
Characterisation of the sensor before exposure to *E. coli*	Inactivation of COOH groups	Inactivate free COOH functions to prevent their interaction with the analyte	Ethanolamine at 1 M, pH 8.5	Incubation for 30 min in dark at RT
	Rinsing and drying	Remove traces of ethanolamine	- PBS (1X) -Tween20 at 0.05 %	1) Siphon the solution 2) Rinse 3x with PBS 3) Rinse 3x with Tween 20 at 0.05 % 4) Rinse 3x with deionized water
	Electrical measurements	Determine the frequency shift prior to exposure	-Network analyzer -Cal kit 85052D -Electrical interface	Calibration

Note that during the incubation steps, the samples are placed in the holders as described in section 5.2.2., in order to protect the ZnO thin films and the electrodes during the exposure to the different biochemical solutions used.

Appendix C: Preparation & manipulation of *E. coli*

Escherchia coli (*E. coli*) K12 is considered as non-pathogenic bacteria under the guidelines of the NIH (National Institutes of Health, USA). These micro-organisms are classified under the containment 1 (manipulated in Level laboratories) under the European Federation of Biotechnology Guidelines (Frommer et al., 1989).

Culture and Storage

Bacteria are stored in 30% glycerol solution at - 80 °C. At each manipulation, a new culture is started by streaking on LB-Agar plates. After 24 hours of culture at 37 °C, an isolated colony of *E. coli* is transferred to LB broth (40 mL) which allows its growth overnight. In the next morning, the optical density (OD) is measured to determine the concentration of the culture (0.1 OD corresponds to 10^8 CFU/ml). The fresh culture is then aliquoted and stored at 50 % Glycerol and - 20 °C in freezer placed in local P2-1174 of the LCSM.

Transportation between locals and intra-university

In accordance with the biosafety procedure of Université de Sherbrooke, level 1 containment bacteria are transported in double containers in the case of intra-LCSM transportation (a primary container such as a sample holder and a secondary container like a saddle bag), and in triple containers for transportation between the university and 3IT. The transportation between premises must be minimal. The outside of the containers must not be in contact with the bacteria.

Waste management

Single-use Eppendorf tubes are used in all experiments. At the end of the manipulation, all the material exposed to bacteria is decontaminated with bleach (1 %) for at least 1 hour. After, the material used is considered as domestic waste, and the surfaces are decontaminated with ethanol.

Handling conditions:

- Wear lab coat, gloves and goggles.
- Place used consumables (Eppendorf tubes, gloves...) in the dedicated waste containers.
- Decontaminate the benches with ethanol (70 %). All the material exposed to the bacteria must be decontaminated by autoclaving.

LIST OF REFERENCES

[1] B. W. Blais, J. Leggate, J. Bosley, and A. Martinez-Perez, “Comparison of fluorogenic and chromogenic assay systems in the detection of *Escherichia coli* O157 by a novel polymyxin-based ELISA,” Lett. Appl. Microbiol., vol. 39, no. 6, pp. 516–522, Dec. 2004.

[2] J. Castillo, S. Gáspár, S. Leth, M. Niculescu, A. Mortari, I. Bontidean, V. Soukharev, S. A. Dorneanu, A. D. Ryabov, and E. Csöregi, “Biosensors for life quality,” Sens. Actuators B Chem., vol. 102, no. 2, pp. 179–194, Sep. 2004.

[3] J. H. T. Luong, K. B. Male, and J. D. Glennon, “Biosensor technology: Technology push versus market pull,” Biotechnol. Adv., vol. 26, no. 5, pp. 492–500, Sep. 2008.

[4] V. Perumal and U. Hashim, “Advances in biosensors: Principle, architecture and applications,” J. Appl. Biomed., vol. 12, no. 1, pp. 1–15, Jan. 2014.

[5] E. B. Bahadır and M. K. Sezgintürk, “Applications of commercial biosensors in clinical, food, environmental, and biothreat/biowarfare analyses,” Anal. Biochem., vol. 478, pp. 107–120, Jun. 2015.

[6] C. I. L. Justino, A. C. Duarte, and T. A. P. Rocha-Santos, “Critical overview on the application of sensors and biosensors for clinical analysis,” TrAC Trends Anal. Chem., vol. 85, pp. 36–60, Dec. 2016.

[7] A. Bienaime, “Microcapteur en arséniure de gallium pour la détection de molécules dans un fluide,” Université de Franche-Comté, 2012.

[8] A. Bienaime, L. Liu, C. Elie-Caille, and T. Leblois, “Design and microfabrication of a lateral excited gallium arsenide biosensor,” Eur. Phys. J. Appl. Phys., vol. 57, no. 02, p. 21003, 2012.

[9] A. Bienaime, C. Elie-Caille, and T. Leblois, “Micro structuration of GaAs surface by wet etching: towards a specific surface behavior,” J. Nanosci. Nanotechnol., vol. 12, pp. 6855–6863, 2012.

[10] A. Bienaime, T. Leblois, N. Gremaud, M. J. Chaudon, M. El Osta, D. Pecqueur, P. Ducoroy and C. Elie-Caille, “Influence of a thiolate chemical layer on GaAs (100) biofunctionalization: an original approach coupling atomic force microscopy and mass spectrometry methods,” Materials, vol. 6, no. 11, pp. 4946–4966, Oct. 2013.

[11] A. Bienaime, T. Leblois, G. Lucchi, V. Blondeau-Patissier, P. Ducoroy, W. Boireau and C. Elie-Caille, “Reconstitution of protein monolayer on thiolates functionalized GaAs surface,” Int. J. Nanosci., vol. 11, no. 04, p. 1240018, May 2012.

[12] V. Lacour, “Optimisation d’un microcapteur GaAs à ondes acoustiques et de sa biointerface pour la détection de pathogènes en milieu liquide,” Université de Franche-Comté, 2016.

[13] V. Lacour, C. Elie-Caille, T. Leblois, and J. J. Dubowski, “Regeneration of a thiolated and antibody functionalized GaAs (001) surface using wet chemical processes,” Biointerphases, vol. 11, no. 1, p. 019302, Mar. 2016.

[14] V. Lacour, K. Moumanis, W. M. Hassen, C. Elie-Caille, T. Leblois, and J. J. Dubowski, “Formation kinetics of mixed self-assembled monolayers of alkanethiols on GaAs(100),” Langmuir, Nov. 2017.

[15] V. Lacour, A. Bienaime, J.-F. Manceau, T. Leblois, and J. J. Dubowski, “Design and experimental studies of Gallium Arsenide bulk acoustic wave transducer under lateral field excitation,” in 2014 European Frequency and Time Forum (EFTF), Neuchatel, Switzerland, 2014, pp. 163–166.

[16] T. Leblois and V. Lacour, “Thermal and conductivity dependence of GaAs based acoustic biosensors,” in 2016 IEEE International Ultrasonics Symposium (IUS), Tours, France, 2016, pp. 1–4.

[17] O. Lazcka, F. J. D. Campo, and F. X. Muñoz, “Pathogen detection: A perspective of traditional methods and biosensors,” Biosens. Bioelectron., vol. 22, no. 7, pp. 1205–1217, 2007.

[18] W. Bereket, K. Hemalatha, B. Getenet, T. Wondwossen, A. Solomon, A. Zeynudin, and S. Kannan, “Update on bacterial nosocomial infections,” Eur Rev Med Pharmacol Sci., vol. 16, no. 8, pp. 1039-1044, 2012

[19] E. Scallan, R. M. Hoekstra, and F.J. Angulo, “Foodborne illness acquired in the United States–major pathogens,” Emerg. Infect. Dis., vol. 17, no. 1, pp. 7–15, Jan. 2011.

[20] P. A. D. Grimont, “Taxonomie des *Escherichia*,” Médecine Mal. Infect., vol. 17, pp. 6–10, Mar. 1987.

[21] B. Decludt, P. Bouvet, P. Mariani-Kurkdjian, F. Grimont, P.A.D. Grimont, B. Hubert, and C. Loirat, “Haemolytic uraemic syndrome and Shiga toxin-producing *Escherichia coli* infection in children in France,” Epidemiol. Infect., vol. 124, no. 2, pp. 215–220, Apr. 2000.

[22] https://www.cdc.gov/ecoli/2018/o26-09-18/index.html

[23] Recommandations au sujet de la qualité des eaux utilisées à des fins récréatives au Canada – Troisième édition (page 9).

[24] C. Rock and B. Rivera, “Water Quality, *E. coli* and Your Health,” Arizona Cooperative Extension, AZ1624, 2014.

[25] https://www.glowm.com/lab_text/item/94

[26] A. van Belkum, G. Durand, M. Peyret, S. Chatellier, G. Zambardi, J. Schrenzel, D. Shortridge, A. Engelhardt, and W. M. Dunne, “Rapid clinical bacteriology and its future impact,” Ann Lab Med., vol. 33, no. 1, pp.14-27, Jan. 2013.

[27] D. M. Olive and P. Bean, “Principles and applications of methods for DNA-based typing of microbial organisms,” J. Clin. Microbiol., vol. 37, p. 9, 1999.

[28] S. Kawasaki, P. M. Fratamico, N. Horikoshi, Y. Okada, K. Takeshita, T. Sameshima, and S. Kawamoto, “Multiplex real-time Polymerase Chain Reaction assay for simultaneous detection and quantification of *Salmonella* species, *Listeria monocytogenes*, and *Escherichia coli* O157:H7 in ground pork samples,” Foodborne Pathog. Dis., vol. 7, no. 5, pp. 549–554, May 2010.

[29] C. Piñero-Lambea, G. Bodelón, R. Fernández-Periáñez, A. M. Cuesta, L. Álvarez-Vallina, and L. Á. Fernández, “Programming controlled adhesion of *E. coli* to target surfaces,

cells, and tumors with synthetic adhesins," ACS Synth. Biol., vol. 4, no. 4, pp. 463–473, Apr. 2015.

[30] A. F. Collings and F. Caruso, "Biosensors: recent advances," Rep. Prog Phys, vol. 60, pp. 1397–1445, 1997.

[31] J. H. T. Luong, A. Mulchandani, and G. G. Guilbault, "Developments and applications of biosensors," Trends Biotechnol., vol. 6, no. 12, pp. 310–316, 1988.

[32] G. G. Guilbault and J. G. Montalvo Jr, "Urea-specific enzyme electrode," J. Am. Chem. Soc., vol. 91, no. 8, pp. 2164–2165, 1969.

[34] A. P. F. Turner, "Biosensors: sense and sensibility," Chem. Soc. Rev., vol. 42, no. 8, p. 3184, 2013.

[34] S. Rodriguez-Mozaz, M. J. Lopez de Alda, and D. Barceló, "Biosensors as useful tools for environmental analysis and monitoring," Anal. Bioanal. Chem., vol. 386, no. 4, pp. 1025–1041, Oct. 2006.

[35] P. Mehrotra, "Biosensors and their applications – A review," J. Oral Biol. Craniofacial Res., vol. 6, no. 2, pp. 153–159, May 2016.

[36] K. Kalantar-zadeh, "Sensors Characteristics," in Sensors, Boston, MA: Springer US, 2013, pp. 11–28.

[37] D. Ivnitski, I. Abdel-Hamid, P. Atanasov, and E. Wilkins, "Biosensors for detection of pathogenic bacteria," Biosens. Bioelectron., vol. 14, no. 7, pp. 599–624, Oct. 1999.

[38] R. Monošík, M. Streďanský, and E. Šturdík, "Biosensors – classification, characterization and new trends," Acta Chim. Slovaca, vol. 5, no. 1, Jan. 2012.

[39] D. Grieshaber, R. MacKenzie, J. Voros, and E. Reimhult, "Electrochemical Biosensors – Sensor Principles and Architectures," p. 59, 2008.

[40] M. Barreiros dos Santos, J. P. Agusil, B. Prieto-Simón, C. Sporer, V. Teixeira, and J. Samitier, "Highly sensitive detection of pathogen *Escherichia coli* O157:H7 by electrochemical impedance spectroscopy," Biosens. Bioelectron., vol. 45, pp. 174–180, Jul. 2013.

[41] Z. Muhammad-Tahir and E. C. Alocilja, "A conductometric biosensor for biosecurity," Biosens. Bioelectron., vol. 18, no. 5–6, pp. 813–819, May 2003.

[42] M. Varshney, L. Yang, X.-L. Su, and Y. Li, "Magnetic nanoparticle-antibody conjugates for the separation of *Escherichia coli* O157: H7 in ground beef," J. Food Prot., vol. 68, no. 9, pp. 1804–1811, 2005.

[43] C. Ercole, M.Del Gallo, M. Pantalone, S. Santucci, L. Mosiello, C. Laconi, A. Lepidi, "A biosensor for *Escherichia coli* based on a potentiometric alternating biosensing (PAB) transducer," 2002.

[44] D. Grieshaber, R. MacKenzie, J. Voros, and E. Reimhult, "Electrochemical biosensors – sensor principles and architectures," 2008.

[45] R. Monošík, M. Stred'anský, and E. Šturdík, "Application of electrochemical biosensors in clinical diagnosis," J. Clin. Lab. Anal., vol. 26, no. 1, pp. 22–34, Jan. 2012.

[46] X. Fan, I. M. White, S. I. Shopova, H. Zhu, J. D. Suter, and Y. Sun, “Sensitive optical biosensors for unlabeled targets: A review,” Anal. Chim. Acta, vol. 620, no. 1-2, pp. 8–26, 2008.

[47] J. Homola, “Present and future of surface plasmon resonance biosensors,” Anal. Bioanal. Chem., vol. 377, no. 3, pp. 528–539, Oct. 2003.

[48] S.-J. Chen, F. C. Chien, G. Y. Lin, and K. C. Lee, “Enhancement of the resolution of surface plasmon resonance biosensors by control of the size and distribution of nanoparticles,” Opt. Lett., vol. 29, no. 12, p. 1390, Jun. 2004.

[49] A. D. Taylor, J. Ladd, Q. Yu, S. Chen, J. Homola, and S. Jiang, “Quantitative and simultaneous detection of four foodborne bacterial pathogens with a multi-channel SPR sensor,” Biosens. Bioelectron., vol. 22, no. 5, pp. 752–758, Dec. 2006.

[50] https://www.biocompare.com/Editorial-Articles/41803-Surface-Plasmon-Resonance-SPR-and-Other-Options-for-Label-free-Detection/

[51] P. Damborsky, J. vitel, and J. Katrlik, “Optical biosensors,” Essays Biochem., vol. 60, no. 1, pp. 91–100, Jun. 2016.

[52] X. Muñoz-Berbel, N. Vigués, A. T. A. Jenkins, J. Mas, and F. J. Muñoz, “Impedimetric approach for quantifying low bacteria concentrations based on the changes produced in the electrode–solution interface during the pre-attachment stage,” Biosens. Bioelectron., vol. 23, no. 10, pp. 1540–1546, May 2008.

[53] E. C. Alocija, E. Lansing, and S. Radke, “Impedimetric biosensor and its use for rapid detection of bacterial pathogens in solution,” Mar. 2005.

[54] S. Chemburu, E. Wilkins, and I. Abdel-Hamid, “Detection of pathogenic bacteria in food samples using highly-dispersed carbon particles,” Biosens. Bioelectron., vol. 21, no. 3, pp. 491–499, Sep. 2005.

[55] M. Hnaiein, W.M. Hassen, A. Abdelghani, C. Fournier-Wirth, J. Coste, F. Bessueille, D. Leonard, N. Jaffrezic-Renault, “A conductometric immunosensor based on functionalized magnetite nanoparticles for *E. coli* detection,” Electrochem. Commun., vol. 10, no. 8, pp. 1152–1154, Aug. 2008.

[56] A. G. Gehring, D. L. Patterson, and S.-I. Tu, “Use of a light-addressable potentiometric sensor for the detection of *Escherichia coli* O157:H7,” Anal. Biochem., vol. 258, no. 2, pp. 293–298, May 1998.

[57] E. Nazemi, S. Aithal, W. M. Hassen, E. H. Frost, and J. J. Dubowski, “GaAs/AlGaAs heterostructure based photonic biosensor for rapid detection of *Escherichia coli* in phosphate buffered saline solution,” Sens. Actuators B Chem., vol. 207, pp. 556–562, Feb. 2015.

[58] F. P. Mathew, D. Alagesan, and E. C. Alocilja, “Chemiluminescence detection of *Escherichia coli* in fresh produce obtained from different sources,” Luminescence, vol. 19, no. 4, pp. 193–198, Jul. 2004.

[59] M. Magliulo, P. Simoni, M. Guardigli, E. Michelini, M. Luciani, R. Lelli, A. Roda, “A rapid multiplexed chemiluminescent immunoassay for the detection of *Escherichia coli* O157:H7, *Yersinia enterocolitica*, *Salmonella typhimurium* , and *Listeria monocytogene* pathogen bacteria,” J. Agric. Food Chem., vol. 55, no. 13, pp. 4933–4939, Jun. 2007.

[60] X. L. Su and Y. Li, “A self-assembled monolayer-based piezoelectric immunosensor for rapid detection of *Escherichia coli* O157:H7,” Biosens. Bioelectron., vol. 19, no. 6, pp. 563–574, Jan. 2004.

[61] C. Poitras and N. Tufenkji, “A QCM-D-based biosensor for *E. coli* O157:H7 highlighting the relevance of the dissipation slope as a transduction signal,” Biosens. Bioelectron., vol. 24, no. 7, pp. 2137–2142, Mar. 2009.

[62] E. Berkenpas, P. Millard, and M. Pereira da Cunha, “Detection of *Escherichia coli* O157:H7 with langasite pure shear horizontal surface acoustic wave sensors,” Biosens. Bioelectron., vol. 21, no. 12, pp. 2255–2262, Jun. 2006.

[63] N. Moll, E. Pascal, D. H. Dinh, J.P. Pillot, B. Bennetau, D. Rebiere, D. Moynet, Y. Mas, D. Mossalayi, J. Pistre, and C. Dejous, “A Love wave immunosensor for whole *E. coli* bacteria detection using an innovative two-step immobilisation approach,” Biosens. Bioelectron., vol. 22, no. 9–10, pp. 2145–2150, Apr. 2007.

[64] B. Kannan, D. E. Williams, C. Laslau, and J. Travas-Sejdic, “A highly sensitive, label-free gene sensor based on a single conducting polymer nanowire,” Biosens. Bioelectron., vol. 35, no. 1, pp. 258–264, May 2012.

[65] R. Koncki, “Recent developments in potentiometric biosensors for biomedical analysis,” Anal. Chim. Acta, vol. 599, no. 1, pp. 7–15, Sep. 2007.

[66] K. R. Rogers and M. Mascini, “Biosensors for field analytical monitoring,” Field Anal. Chem. Technol., vol. 2, no. 6, pp. 317–331, 1998.

[67] J. Wang, 1996. Electrochemical transduction. In: Taylor, R.F., Schultz, J.S. (Eds.), Handbook of Chemical and Biological Sensors. IOP Publishing Ltd., Bristol, pp. 119–133.

[68] J. Chawich, P. Boiteux, C. Elie-caille, and T. Leblois, “Specificity and sensitivity characterization of a gallium arsenide resonant bio-sensor,” 2018 IEEE International Ultrasonics Symposium (IUS), Kobe, Japan, pp. 1–4, 2018.

[69] K. Hjort, “Gallium arsenide micromechanics : a comparison to silicon and quartz,” presented at the Gallium Arsenide Applications Symposium. GAAS 1994, Turin, Italy, 1994.

[70] T. Glinsner, T. Luxbacher, P. Lindner, C. Schaefer, R. Michaels, J. Palensky, V. Dragoi, and M. Reiche, “Reversible and permanent wafer bonding for GaAs processing,” GaAs MANTECH Inc, 2001.

[71] C. R. Tellier, G. Huve, and T. Leblois, “Micromachining of GaAs structures with an acidic hydrogen peroxide solution,” Sens. Actuators Phys., vol. 127, no. 1, pp. 179–193, 2006.

[72] C. D. Thurmond, “GaAs Oxidation and the Ga-As-O Equilibrium Phase Diagram,” J. Electrochem. Soc., vol. 127, no. 6, p. 1366, 1980.

[73] O. Voznyy and J. J. Dubowski, “Structure of Thiol Self-Assembled Monolayers Commensurate with the GaAs (001) Surface,” Langmuir, vol. 24, no. 23, pp. 13299–13305, Dec. 2008.

[74] O. Voznyy and J. J. Dubowski, “Adsorption Kinetics of Hydrogen Sulfide and Thiols on GaAs (001) Surfaces in a Vacuum,” J. Phys. Chem. C, vol. 112, no. 10, pp. 3726–3733, 2008.

[75] X. Huang, N. Liu, K. Moumanis, and J. J. Dubowski, “Water-Mediated Self-Assembly of 16-Mercaptohexadecanoic Acid on GaAs (001),” J. Phys. Chem. C, vol. 117, no. 29, pp. 15090–15097, Jul. 2013.

[76] J. A. Goode, J. V. H. Rushworth, and P. A. Millner, “Biosensor regeneration: a review of common techniques and outcomes,” Langmuir, vol. 31, no. 23, pp. 6267–6276, Jun. 2015.

[77] Ö. Ümit, D. Hofstetter, and H. Morkoc, “ZnO devices and applications: a review of current status and future prospects,” Proc. IEEE, vol. 98, no. 7, pp. 1255–1268, 2010.

[78] C. Jagadish and S. J. Pearton, “Zinc oxide bulk, thin films and nanostructures: processing, properties, and applications,” 1st ed. Elsevier, 2006.

[79] D. Royer and E. Dieulesaint, Elastic Waves in Solids I: Free and Guided Propagation, vol. 1. Springer, 2000.

[80] H. Morkoç and Ü. Özgür, “Zinc oxide: fundamentals, materials and device technology,” Weinheim: Wiley-VCH, 2009.

[81] Ü. Özgür, Ya. I. Alivov, C. Liu, A. Teke, M. A. Reshchikov, S. Doğan, V. Avrutin, S.-J. Cho, and H. Morkoç “A comprehensive review of ZnO materials and devices,” J. Appl. Phys., vol. 98, no. 4, p. 041301, Aug. 2005.

[82] H.-K. Kim, K.-K. Kim, S.-J. Park, T.-Y. Seong, and Y. S. Yoon, “Thermally stable and low resistance Ru ohmic contacts to n-ZnO,” Jpn. J. Appl. Phys., vol. 41, no. Part 2, No. 5B, pp. L546–L548, May 2002.

[83] X. L. Xu, S. P. Lau, J. S. Chen, Z. Sun, B. K. Tay, and J. W. Chai, “Dependence of electrical and optical properties of ZnO films on substrate temperature,” Mater. Sci. Semicond. Process., vol. 4, no. 6, pp. 617–620, Dec. 2001.

[84] Z. L. Wang, “Zinc oxide nanostructures: growth, properties and applications,” J. Phys. Condens. Matter, vol. 16, no. 25, pp. R829–R858, Jun. 2004.

[85] D.-S. Liu, C.-Y. Wu, C.-S. Sheu, F.-C. Tsai, and C.-H. Li, “The preparation of piezoelectric ZnO films by RF magnetron sputtering for layered surface acoustic wave device applications,” Jpn. J. Appl. Phys., vol. 45, no. 4B, pp. 3531–3536, Apr. 2006.

[86] L. Mai, V.-S. Pham, and G. Yoon, “ZnO-based film bulk acoustic resonator devices on a specially designed Bragg reflector,” Appl. Phys. A, vol. 95, no. 3, pp. 667–671, Jun. 2009.

[87] S. Krishnamoorthy and A. A. Iliadis, “Development of high frequency ZnO/SiO_2/Si Love mode surface acoustic wave devices,” Solid-State Electron., vol. 50, no. 6, pp. 1113–1118, Jun. 2006.

[88] Y. Q. Fu, J.K. Luo, N.T. Nguyen, A.J. Walton, A.J. Flewitt, X.T Zu, Y. Li, G. McHale, A. Matthews, E. Iborra, H. Du, W.I. Milne, “Advances in piezoelectric thin films for acoustic biosensors, acoustofluidics and lab-on-chip applications,” Prog. Mater. Sci., vol. 89, pp. 31–91, Aug. 2017.

[89] P. Muralt, “Recent progress in materials issues for piezoelectric MEMS,” J. Am. Ceram. Soc., vol. 91, no. 5, pp. 1385–1396, May 2008.

[90] P. Muralt, “PZT thin films for microsensors and actuators: Where do we stand?,” IEEE Trans. Ultrason. Ferroelectr. Freq. Control, vol. 47, no. 4, pp. 903–915, Jul. 2000.

[91] P. K. Panda and B. Sahoo, “PZT to lead free piezo ceramics: A review,” Ferroelectrics, vol. 474, no. 1, pp. 128–143, Jan. 2015.

[92] A. Khan, Z. Abas, H. Soo Kim, and I.-K. Oh, “Piezoelectric thin films: an integrated review of transducers and energy harvesting,” Smart Mater. Struct., vol. 25, no. 5, p. 053002, May 2016.

[93] M. A. Fraga, H. Furlan, R. S. Pessoa, and M. Massi, “Wide bandgap semiconductor thin films for piezoelectric and piezoresistive MEMS sensors applied at high temperatures: an overview,” Microsyst. Technol., vol. 20, no. 1, pp. 9–21, Jan. 2014.

[94] N. Ledermann, P. Muralt, J. Baborowski, S. Gentil, K. Mukati, M. Cantoni, A.Seifert, and N. Setter, “{1 0 0}-Textured, piezoelectric $Pb(Zr_x, Ti_{1-x})O_3$ thin films for MEMS: integration, deposition and properties,” Sens. Actuators Phys., vol. 105, no. 2, pp. 162–170, Jul. 2003.

[95] Y. Yoshino, “Piezoelectric thin films and their applications for electronics,” J. Appl. Phys., vol. 105, no. 6, p. 061623, Mar. 2009.

[96] S. A. Kumar and S. Chen, “Nanostructured zinc oxide particles in chemically modified electrodes for biosensor applications,” Anal. Lett., vol. 41, no. 2, pp. 141–158, Feb. 2008.

[97] S. Bensmaine, L. Le Brizoual, O. Elmazria, J. J. Fundenberger, and B. Benyoucef, “Deposition of ZnO inclined c -axis on silicon and diamond by r.f. magnetron sputtering,” Phys. Status Solidi A, vol. 204, no. 9, pp. 3091–3095, Sep. 2007.

[98] P. Wang, H. Du, S. Shen, M. Zhang, and B. Liu, “Deposition, characterization and optimization of zinc oxide thin film for piezoelectric cantilevers,” Appl. Surf. Sci., vol. 258, no. 24, pp. 9510–9517, Oct. 2012.

[99] K. B. Sundaram and A. Khan, “Characterization and optimization of zinc oxide films by r.f. magnetron sputtering,” Thin Solid Films, vol. 295, no. 1–2, pp. 87–91, Feb. 1997.

[100] G. Sai Krishna Santosh and H. B. Nemade, “Investigation of properties of surface acoustic waves generated by periodically patterned ZnO on silicon substrate,” Ultrasonics, vol. 59, pp. 40–44, May 2015.

[101] R. S. Gonçalves, P. Barrozo, G. L. Brito, B. C. Viana, and F. Cunha, “The effect of thickness on optical, structural and growth mechanism of ZnO thin film prepared by magnetron sputtering,” Thin Solid Films, vol. 661, pp. 40–45, Sep. 2018.

[102] M. Soylu, A. A. Al-Ghamdi, O. A. Al-Hartomy, F. El-Tantawy, and F. Yakuphanoglu, “The electrical characterization of ZnO/GaAs heterojunction diode,” Phys. E Low-Dimens. Syst. Nanostructures, vol. 64, pp. 240–245, Nov. 2014.

[103] J. Jou, M. Han, and D. Cheng, “Substrate dependent internal stress in sputtered zinc oxide thin films,” J. Appl. Phys., vol. 71, no. 9, pp. 4333–4336, May 1992.

[104] J. Pedrós, L. García-Gancedo, C. J. B. Ford, C. H. W. Barnes, J. P. Griffiths, G. A. C. Jones, and A. J. Flewitt, “Guided propagation of surface acoustic waves and piezoelectric field enhancement in ZnO/GaAs systems,” J. Appl. Phys., vol. 110, no. 10, p. 103501, Nov. 2011.

[105] Y.-C. Huang, L.-W. Weng, W.-Y. Uen, S.-M. Lan, Z.-Y. Li, S.-M. Liao, T.-Y. Lin, and T.-N. Yang, “Annealing effects on the p-type ZnO films fabricated on GaAs substrate by

atmospheric pressure metal organic chemical vapor deposition," J. Alloys Compd., vol. 509, no. 5, pp. 1980–1983, Feb. 2011.

[106] M. K. Ryu, S. H. Lee, M. S. Jang, G. N. Panin, and T. W. Kang, "Postgrowth annealing effect on structural and optical properties of ZnO films grown on GaAs substrates by the radio frequency magnetron sputtering technique," J. Appl. Phys., vol. 92, no. 1, pp. 154–158, Jul. 2002.

[107] H. K. Kim and M. Mathur, "Thermally stable ZnO films deposited on GaAs substrates with a SiO_2 thin buffer layer," Appl. Phys. Lett., vol. 61, no. 21, pp. 2524–2526, Nov. 1992.

[108] W.-C. Shih and M.-S. Wu, "Growth of ZnO films on GaAs substrates with a SiO_2 buffer layer by RF planar magnetron sputtering for surface acoustic wave applications," J. Cryst. Growth, vol. 137, pp. 319-325, 1994.

[109] Y. Kim, W. D. Hunt, F. S. Hickernell, and R. J. Higgins, "Surface acoustic wave properties of ZnO films on {001}-cut <110>-propagating GaAs substrates," J. Appl. Phys., vol. 75, no. 11, pp. 7299–7303, Jun. 1994.

[110] A. B. M. A. Ashrafi, A. Ueta, A. Avramescu, H. Kumano, and I. Suemune, "Growth and characterization of hypothetical zinc-blende ZnO films on GaAs(001) substrates with ZnS buffer layers," Appl. Phys. Lett., vol. 76, no. 5, pp. 550–552, Jan. 2000.

[111] K. Zhao, L. Ye, M. C. Tamargo, and A. Shen, "Plasma-assisted MBE growth of ZnO on GaAs substrate with a ZnSe buffer layer," Phys. Status Solidi C, vol. 9, no. 8–9, pp. 1809–1812, Aug. 2012.

[112] S. Agouram, M. C. Martínez-Tomás, and V. Muñoz-Sanjosé, "ZnO films grown by MOCVD on GaAs substrates: Effects of a Zn buffer deposition on interface, structural and morphological properties," J. Cryst. Growth, vol. 311, no. 8, pp. 2564–2571, Apr. 2009.

[113] E. A. Cerda-Méndez, D. Krizhanovskii, K. Biermann, R. Hey, P. V. Santos, and M. S. Skolnick, "Effects of the piezoelectric field on the modulation of exciton–polaritons by surface acoustic waves," Superlattices Microstruct., vol. 49, no. 3, pp. 233–240, Mar. 2011.

[114] S. J. Jiao, P. D. Batista, K. Biermann, R. Hey, and P. V. Santos, "Electrical detection of ambipolar acoustic carrier transport by surface acoustic waves," J. Appl. Phys., vol. 106, no. 5, p. 053708, Sep. 2009.

[115] O. D. D. Couto, F. Iikawa, J. Rudolph, R. Hey, and P. V. Santos, "Anisotropic Spin Transport in (110) GaAs Quantum Wells," Phys. Rev. Lett., vol. 98, no. 3, Jan. 2007.

[116] D. J. Rogers, F. Hosseini Teherani, T. Monteiro, M. Soares, A. Neves, M. Carmo, S. Pereira, M. R. Correia, A. Lusson, E. Alves, N. P. Barradas, J. K. Morrod, K. A. Prior, P. Kung, A. Yasan, and M. Razeghi, "Investigations of p-type signal for ZnO thin films grown on (100) GaAs substrates by pulsed laser deposition," Phys. Status Solidi C, vol. 3, no. 4, pp. 1038–1041, Mar. 2006.

[117] H. F. Liu, A. S. W. Wong, G. X. Hu, and H. Gong, "Observation of interfacial reactions and recrystallization of extrinsic phases in epitaxial grown ZnO/GaAs heterostructures," J. Cryst. Growth, vol. 310, no. 19, pp. 4305–4308, Sep. 2008.

[118] A. A. Vives, Ed., Piezoelectric Transducers and Applications. Berlin, Heidelberg: Springer Berlin Heidelberg, 2008.

[119] M. Thompson, A. L. Kipling, W. C. Duncan-Hewitt, L. V. Rajaković, and B. A. Čavić-Vlasak, “Thickness-shear-mode acoustic wave sensors in the liquid phase. A review,” The Analyst, vol. 116, no. 9, pp. 881–890, 1991.

[120] D. S. Ballantine, Ed., Acoustic wave sensors: theory, design, and physico-chemical applications. San Diego: Academic Press, 1997.

[121] V. Ferrari and R. Lucklum, “Overview of Acoustic-Wave Microsensors,” in Piezoelectric transducers and applications, A. A. Vives, Ed. Berlin, Heidelberg: Springer Berlin Heidelberg, 2008, pp. 39–62.

[122] M. J. Vellekoop, “Acoustic wave sensors and their technology,” Ultrasonics, vol. 36, no. 1–5, pp. 7–14, Feb. 1998.

[123] K. Länge, B. E. Rapp, and M. Rapp, “Surface acoustic wave biosensors: a review,” Anal. Bioanal. Chem., vol. 391, no. 5, pp. 1509–1519, Jul. 2008.

[124] H. Nakahata, S. Fujii, K. Higaki, A. Hachigo, H. Kitabayashi, S. Shikata and N. Fujimori, “Diamond-based surface acoustic wave devices,” Semicond. Sci. Technol., vol. 18, no. 3, pp. S96–S104, Mar. 2003.

[125] M. Kaspar, H. Stadler, T. Weiß, and C. Ziegler, “Thickness shear mode resonators (‘mass-sensitive devices’) in bioanalysis,” Fresenius J. Anal. Chem., vol. 366, no. 6–7, pp. 602–610, Mar. 2000.

[126] J. Du, G. L. Harding, J. A. Ogilvy, P. R. Dencher, and M. Lake, “A study of Love-wave acoustic sensors,” Sens. Actuators Phys., vol. 56, no. 3, pp. 211–219, Sep. 1996.

[127] I. Gammoudi, H. Tarbague, A. Othmane, D. Moynet, D. Rebière, R. Kalfat, and C. Dejous, “Love-wave bacteria-based sensor for the detection of heavy metal toxicity in liquid medium,” Biosens. Bioelectron., vol. 26, no. 4, pp. 1723–1726, Dec. 2010.

[128] S. Lee, K.-B. Kim, and Y.-I. Kim, “Love wave SAW biosensors for detection of antigen-antibody binding and comparison with SPR biosensor,” Food Sci. Biotechnol., vol. 20, no. 5, pp. 1413–1418, Nov. 2011.

[129] S. J. Martin, A. J. Ricco, T. M. Niemczyk, and G. C. Frye, “Characterization of SH acoustic plate mode liquid sensors,” Sens. Actuators, vol. 20, no. 3, pp. 253–268, Dec. 1989.

[130] V. E. Sakharov, S. A. Kuznetsov, B. D. Zaitsev, I. E. Kuznetsova, and S. G. Joshi, “Liquid level sensor using ultrasonic Lamb waves,” Ultrasonics, vol. 41, no. 4, pp. 319–322, Jun. 2003.

[131] J. F. Rosenbaum, Bulk acoustic wave theory and devices. Boston: Artech House, 1988.

[132] X. Zhang, W. Xu, A. Abbaspour-Tamijani, and J. Chae, “Thermal analysis and characterization of a high Q Film Bulk Acoustic Resonator (FBAR) as biosensers in liquids,” in micro electro mechanical systems, 2009. MEMS 2009. IEEE 22nd International Conference on, 2009, pp. 939–942.

[133] C. Steinem and A. Janshiff, Piezoelectric sensors, vol. 5. Springer, 2007.

[134] J.-J. Rousseau and A. Gibaud, Cristallographie géométrique et radiocristallographie: cours et exercices corrigés. Paris: Dunod, 2007.

[135] W. Wang, C. Zhang, Z. Zhang, T. Ma, and G. Feng, "Energy-trapping mode in lateral-field-excited acoustic wave devices," Appl. Phys. Lett., vol. 94, no. 19, p. 192901, May 2009.

[136] A. Dickherber, C. D. Corso, and B. Hunt, "Lateral Field Excitation (LFE) of Thickness Shear Mode (TSM) acoustic waves in Thin Film Bulk Acoustic Resonators (FBAR) as a potential biosensor".

[137] T. Voglhuber-Brunnmaier, R. Beigelbeck, and B. Jakoby, "Semi-numeric boundary element method for piezoelectric fluid sensors using a fourier spectral approach," in IEEE Sensors 2014 Proceedings, Valencia, Spain, 2014, pp. 594–597.

[138] J. Soderkvist and K. Hjort, "The piezoelectric effect of GaAs used for resonators and resonant sensors," J. Micromechanics Microengineering, vol. 4, no. 1, pp. 28–34, Mar. 1994.

[139] S. Adachi, "GaAs, AlAs, and $Al_xGa_{1-x}As$: Material parameters for use in research and device applications," J. Appl. Phys., vol. 58, no. 3, pp. R1–R29, Aug. 1985.

[140] T. B. Bateman, "Elastic Moduli of Single-Crystal Zinc Oxide," J. Appl. Phys., vol. 33, no. 11, pp. 3309–3312, Nov. 1962.

[141] A. Janotti and C. G. Van de Walle, "Fundamentals of zinc oxide as a semiconductor," Rep. Prog. Phys., vol. 72, no. 12, p. 126501, Dec. 2009.

[142] H. Li, J. Wang, H. Liu, H. Zhang, and X. Li, "Zinc oxide films prepared by sol–gel method," J. Cryst. Growth, vol. 275, no. 1–2, pp. e943–e946, Feb. 2005.

[143] Z. R. Khan, M. S. Khan, M. Zulfequar, and M. Shahid Khan, "Optical and structural properties of ZnO thin films fabricated by sol-gel method," Mater. Sci. Appl., vol. 02, no. 05, pp. 340–345, 2011.

[144] B. Cao, W. Cai, H. Zeng, and G. Duan, "Morphology evolution and photoluminescence properties of ZnO films electrochemically deposited on conductive glass substrates," J. Appl. Phys., vol. 99, no. 7, p. 073516, Apr. 2006.

[145] S. Sanchez, C. Lévy-Clément, and V. Ivanova, "Electrochemical deposition of ZnO thin films and nanowires for photovoltaic applications," J. Electrochem. Soc., vol. 159, no. 12, pp. D705–D712, 2012.

[146] N. Lehraki, M. S. Aida, S. Abed, N. Attaf, A. Attaf, and M. Poulain, "ZnO thin films deposition by spray pyrolysis: Influence of precursor solution properties," Curr. Appl. Phys., vol. 12, no. 5, pp. 1283–1287, Sep. 2012.

[147] A. Ashour, M. A. Kaid, N. Z. El-Sayed, and A. A. Ibrahim, "Physical properties of ZnO thin films deposited by spray pyrolysis technique," Appl. Surf. Sci., vol. 252, no. 22, pp. 7844–7848, Sep. 2006.

[148] Y. Ma, G. Du, J. Yin, T. Yang, and Y. Zhang, "Structural and optoelectrical properties of ZnO thin films deposited on GaAs substrate by metal-organic chemical vapour deposition (MOCVD)," Semicond. Sci. Technol., vol. 20, no. 12, pp. 1198–1202, Dec. 2005.

[149] A. Hongsingthong, I. Afdi Yunaz, S. Miyajima, and M. Konagai, “Preparation of ZnO thin films using MOCVD technique with D_2O/H_2O gas mixture for use as TCO in silicon-based thin film solar cells,” Sol. Energy Mater. Sol. Cells, vol. 95, no. 1, pp. 171–174, Jan. 2011.

[150] J. Malm, E. Sahramo, J. Perälä, T. Sajavaara, and M. Karppinen, “Low-temperature atomic layer deposition of ZnO thin films: Control of crystallinity and orientation,” Thin Solid Films, vol. 519, no. 16, pp. 5319–5322, Jun. 2011.

[151] Y.-S. Min, C.-J. An, S.-K. Kim, J.-W. Song, and C.-S. Hwang, “Growth and characterization of conducting ZnO thin films by atomic layer deposition,” Bull. Korean Chem. Soc., vol. 31, no. 9, pp. 2503–2508, Sep. 2010.

[152] G. Gordillo and C. Caldero, “Properties of ZnO thin films prepared by reactive evaporation,” Sol. Energy Mater., p. 10, 2001.

[153] J. A. Alvarado, A. Maldonado, H. Juarez, M. Pacio, and R. Perez, “Characterization of nanostructured ZnO thin films deposited through vacuum evaporation,” Beilstein J. Nanotechnol., vol. 6, pp. 971–975, Apr. 2015.

[154] M. G. Tsoutsouva, C. N. Panagopoulos, D. Papadimitriou, I. Fasaki, and M. Kompitsas, “ZnO thin films prepared by pulsed laser deposition,” Mater. Sci. Eng. B, vol. 176, no. 6, pp. 480–483, Apr. 2011.

[155] R. Ondo-Ndong, G. Ferblantier, M. Al Kalfioui, A. Boyer, and A. Foucaran, “Properties of RF magnetron sputtered zinc oxide thin films,” J. Cryst. Growth, vol. 255, no. 1–2, pp. 130–135, Jul. 2003.

[156] W. L. Dang, Y. Q. Fu, J. K. Luo, A. J. Flewitt, and W. I. Milne, “Deposition and characterization of sputtered ZnO films,” Superlattices Microstruct., vol. 42, no. 1–6, pp. 89–93, Jul. 2007.

[157] J. Molarius, J. Kaitila, T. Pensala, and M. Ylilammi, “Piezoelectric ZnO films by rf sputtering,” J. Mater. Sci. Mater. Electron., vol. 14, no. 5–7, pp. 431–435, 2003.

[158] P. J. Kelly and R. D. Arnell, “Magnetron sputtering: a review of recent developments and applications,” Vacuum, vol. 56, no. 3, pp. 159–172, 2000.

[159] S. Bensmaine and B. Benyoucef, “Effect of the temperature on ZnO thin films deposited by r.f. magnetron.,” Phys. Procedia, vol. 55, pp. 144–149, 2014.

[160] Y. Waseda, E. Matsubara, and K. Shinoda, X-Ray diffraction crystallography: introduction, examples and solved problems. Heidelberg [Germany] ; New York: Springer, 2011.

[161] S. Maniv, W. D. Westwood, and E. Colombini, “Pressure and angle of incidence effects in reactive planar magnetron sputtered ZnO layers,” J. Vac. Sci. Technol., vol. 20, no. 2, pp. 162-170, 1982.

[162] H. F. Pang, G. A. Zhang, Y. L. Tang, Y. Q. Fu, L. P. Wang, X. T. Zu, F. Placido, “Substrate-tilt angle effect on structural and optical properties of sputtered ZnO film,” Appl. Surf. Sci., vol. 259, pp. 747–753, Oct. 2012.

[163] A. Bartasyte, “Stress effects and phase transitions in PbTiO3 thin films deposited by MOCVD,” Institut national polytechnique de Grenoble, 2007

[164] A. Bartasyte V. Plausinaitiene, A. Abrutis, T. Murauskas, P. Boulet, S. Margueron, J. Gleize, S. Robert, V. Kubilius, and Z. Saltyte, “Residual stresses and clamped thermal expansion in $LiNbO_3$ and $LiTaO_3$ thin films,” Appl. Phys. Lett., vol. 101, no. 12, p. 122902, Sep. 2012.

[165] S. Kuprenaite, S. Margueron, M. Raschetti, C. Millon, T. Baron, W. Daniau, S. Ballandras, B. Gautier, D. Albertini, and P. Boulet, “Effect of $LiNbO_3$ polarity on the structural, optical and acoustic properties of epitaxial ZnO and $Mg_xZn_{1-x}O$ films,” J. Phys. Appl. Phys., vol. 51, no. 48, p. 484003, Dec. 2018.

[166] A. Kudelski, “Raman spectroscopy of surfaces,” Surf. Sci., vol. 603, no. 10–12, pp. 1328–1334, Jun. 2009.

[167] C. A. Arguello, D. L. Rousseau, and S. P. da S. Porto, “First-order Raman effect in wurtzite-type crystals,” Phys. Rev., vol. 181, no. 3, p. 1351, 1969.

[168] T. C. Damen, S. P. S. Porto, and B. Tell, “Raman effect in zinc oxide,” Phys. Rev., vol. 142, no. 2, p. 570, 1966.

[169] I. Zardo, S. Conesa-Boj, F. Peiro, J. R. Morante, J. Arbiol, E. Uccelli, G. Abstreiter, and A. Fontcuberta i Morral “Raman spectroscopy of wurtzite and zinc-blende GaAs nanowires: Polarization dependence, selection rules, and strain effects,” Phys. Rev. B, vol. 80, no. 24, 2009.

[170] Y. Zhang, H. Jia, R. Wang, C. Chen, X. Luo, and D. Yu, “Low-temperature growth and Raman scattering study of vertically aligned ZnO nanowires on Si substrate,” Appl. Phys. Lett., vol. 83, no. 22, pp. 4631–4633, Dec. 2003.

[171] A. Bartasyte, S. Margueron, J. Kreisel, P. Bourson, O. Chaix-Pluchery, L. Rapenne-Homand, J. Santiso, C. Jimenez, A. Abrutis, F. Weiss, and M. D. Fontana “Residual stress estimation in ferroelectric $PbTiO_3$ thin films by Raman spectroscopy,” Phys. Rev. B, vol. 79, no. 10, Mar. 2009.

[172] A. Alessandrini and P. Facci, “AFM: a versatile tool in biophysics,” Meas. Sci. Technol., vol. 16, no. 6, pp. R65–R92, Jun. 2005.

[173] https://pharm.virginia.edu/facilities/atomic-force-microscope-afm/

[174] G. R. Fox, S. Trolier-McKinstry, S. B. Krupanidhi, and L. M. Casas, “$Pt/Ti/SiO_2/Si$ substrates,” J. Mater. Res., vol. 10, no. 6, pp. 1508–1515, 1995.

[175] E.R. Amstalden van Hove, D.F. Smith, and R.M.A. Heeren, “A concise review of mass spectrometry imaging,” J. Chromatogr. A, vol.1217, pp. 3946–3954, 2010.

[176] D. Touboul, F. Kollmer, E. Niehuis, A. Brunelle, and O. Laprévote, “Improvement of biological time-of-flight-secondary ion mass spectrometry imaging with a bismuth cluster ion source,” J. Am. Soc. Mass Spectrom., vol. 16, no. 10, pp. 1608–1618, Oct. 2005.

[177] T. Maeder, L. Sagalowicz, and P. Muralt, “Stabilized Platinum electrodes for ferroelectric film deposition using Ti, Ta and Zr adhesion layers,” Jpn. J. Appl. Phys., vol. 37, no. Part 1, No. 4A, pp. 2007–2012, Apr. 1998.

[178] D. J. Schroeder, G. D. Berry, and A. A. Rockett, “Gallium diffusion and diffusivity in $CuInSe_2$ epitaxial layers,” Appl. Phys. Lett., vol. 69, no. 26, pp. 4068–4070, Dec. 1996.

[179] T. Y. Tan, S. Yu, and U. Gösele, “Determination of vacancy and self-interstitial contributions to gallium self-diffusion in GaAs,” J. Appl. Phys., vol. 70, no. 9, pp. 4823–4826, Nov. 1991.

[180] D. E. Aspnes, “Spectroscopic ellipsometry - Past, present, and future,” Thin Solid Films, vol. 571, pp. 334–344, Nov. 2014.

[181] K. Sato and S. Adachi, “Optical properties of ZnTe,” J. Appl. Phys., vol. 73, no. 2, pp. 926–931, Jan. 1993.

[182] V. Srikant and D. R. Clarke, “On the optical band gap of zinc oxide,” J. Appl. Phys., vol. 83, no. 10, pp. 5447–5451, May 1998.

[183] W. L. Bond, “Measurement of the Refractive Indices of Several Crystals,” J. Appl. Phys., vol. 36, no. 5, pp. 1674–1677, May 1965.

[184] V. Lebec, S. Boujday, C. Poleunis, C.-M. Pradier, and A. Delcorte, “Time-of-Flight Secondary Ion Mass Spectrometry investigation of the irientation of adsorbed antibodies on SAMs correlated to biorecognition tests,” J. Phys. Chem. C, vol. 118, no. 4, pp. 2085–2092, Jan. 2014.

[185] M. R. Aziziyan, W. M. Hassen, D. Morris, E. H. Frost, and J. J. Dubowski, “Photonic biosensor based on photocorrosion of GaAs/AlGaAs quantum heterostructures for detection of *Legionella pneumophila*,” Biointerphases, vol. 11, no. 1, p. 019301, Mar. 2016.

[186] C. C. Chang, P. H. Citrin, and B. Schwartz, “Chemical preparation of GaAs surfaces and their characterization by Auger electron and Xray photoemission spectroscopies,” J. Vac. Sci. Technol., vol. 14, no. 4, pp. 943-952, 1977.

[187] M. V. Lebedev, E. Mankel, T. Mayer, and W. Jaegermann, “Etching of GaAs(100) with aqueous Ammonia solution: A synchrotron-photoemission spectroscopy study,” J. Phys. Chem. C, vol. 114, no. 49, pp. 21385–21389, Dec. 2010.

[188] M. Reth, “Matching cellular dimensions with molecular sizes,” Nat. Immunol., vol. 14, p. 765, Jul. 2013.

[189] K. Bonroy, F. Frederix, G. Reekmans, E. Dewolf, R. De Palma, G. Borghs, P. Declerck, and B. Goddeeris, “Comparison of random and oriented immobilisation of antibody fragments on mixed self-assembled monolayers,” J. Immunol. Methods, vol. 312, no. 1–2, pp. 167–181, May 2006.

[190] E. Briand, M. Salmain, J.-M. Herry, H. Perrot, C. Compère, and C.-M. Pradier, “Building of an immunosensor: How can the composition and structure of the thiol attachment layer affect the immunosensor efficiency?,” Biosens. Bioelectron., vol. 22, no. 3, pp. 440–448, Sep. 2006.

[191] F. Frederix, K. Bonroy, W. Laureyn, G. Reekmans, A. Campitelli, W. Dehaen, and G. Maes, “Enhanced performance of an affinity biosensor interface based on mixed self-assembled monolayers of thiols on gold,” Langmuir, vol. 19, no. 10, pp. 4351–4357, 2003.

[192] L. Huang, G. Reekmans, D. Saerens, J.-M. Friedt, F. Frederix, L. Francis, S. Muyldermans, A. Campitelli, and C. Van Hoof, “Prostate-specific antigen immunosensing based on mixed self-assembled monolayers, camel antibodies and colloidal gold enhanced sandwich assays,” Biosens. Bioelectron., vol. 21, no. 3, pp. 483–490, Sep. 2005.

[193] V. Silin, H. Weetall, and D. J. Vanderah, “SPR Studies of the nonspecific adsorption kinetics of human IgG and BSA on gold surfaces modified by Self-Assembled Monolayers (SAMs),” J. Colloid Interface Sci., vol. 185, no. 1, pp. 94–103, Jan. 1997.

[194] A. F. Stalder, G. Kulik, D. Sage, L. Barbieri, and P. Hoffmann, “A snake-based approach to accurate determination of both contact points and contact angles,” Colloids Surf. Physicochem. Eng. Asp., vol. 286, no. 1–3, pp. 92–103, Sep. 2006.

[195] Y. A. Bioud, A. Boucherif, A. Belarouci, E. Paradis, S. Fafard, V. Aimez, D. Drouin, and R. Ares, “Fast growth synthesis of mesoporous germanium films by high frequency bipolar electrochemical etching,” Electrochimica Acta, vol. 232, pp. 422–430, Apr. 2017.

[196] H. Rieley, G. K. Kendall, F. W. Zemicael, T. L. Smith, and S. Yang, “X-ray studies of Self-Assembled Monolayers on Coinage Metals. 1. Alignment and photooxidation in 1,8-Octanedithiol and 1-Octanethiol on Au,” Langmuir, vol. 14, no. 18, pp. 5147–5153, Sep. 1998.

[197] Y. Jun, X.-Y. Zhu, and J. W. P. Hsu, “Formation of Alkanethiol and Alkanedithiol monolayers on GaAs(001),” Langmuir, vol. 22, no. 8, pp. 3627–3632, Apr. 2006.

[198] S. Sam, L. Touahir, J. Salvador Andresa, P. Allongue, J.-N. Chazalviel, A. C. Gouget-Laemmel, C. Henry de Villeneuve, A. Moraillon, F. Ozanam, N. Gabouze, and S. Djebbar “Semiquantitative study of the EDC/NHS activation of acid terminal groups at modified porous silicon surfaces,” Langmuir, vol. 26, no. 2, pp. 809–814, Jan. 2010.

[199] J. Bart, R. Tiggelaar, M. Yang, S. Schlautmann, H. Zuilhof, and H. Gardeniers, “Room-temperature intermediate layer bonding for microfluidic devices,” Lab. Chip, vol. 9, no. 24, p. 3481, 2009.

[200] J. Bandekar, “Amide modes and protein conformation,” Biochim. Biophys. Acta BBA - Protein Struct. Mol. Enzymol., vol. 1120, no. 2, pp. 123–143, Apr. 1992.

[201] N. Gavish and K. Promislow, “Dependence of the dielectric constant of electrolyte solutions on ionic concentration: a microfield approach,” Phys. Rev. E, vol. 94, no. 1, Jul. 2016.

[202] F. Remy-Martin, M. El Osta, G. Lucchi, R. Zeggari, T. Leblois, S. Bellon, P. Ducoroy, and W. Boireau, “Surface plasmon resonance imaging in arrays coupled with mass spectrometry (SUPRA-MS): proof of concept of on-chip characterization of a potential breast cancer marker in human plasma,” Anal. Bioanal. Chem., vol. 404, no. 2, pp. 423–432, Aug. 2012.

[203] F. Kardous, A. Rouleau, B. Simon, R. Yahiaoui, J. F. Manceau, and W. Boireau, “Improving immunosensor performances using an acoustic mixer on droplet microarray,” Biosens. Bioelectron., vol. 26, no. 4, pp. 1666–1671, Dec. 2010.

[204] F.C. Neidhardt, *Escherichia coli* and *Salmonella* : Cellular and Molecular Biology. Vol 1. pp. 14, ASM Press 1996. .

[205] I. K. Djoumerska-Alexieva, J. D. Dimitrov, E. N. Voynova, S. Lacroix-Desmazes, S. V. Kaveri, and T. L. Vassilev, “Exposure of IgG to an acidic environment results in molecular modifications and in enhanced protective activity in sepsis: Molecular modifications in low pH-exposed IgG,” FEBS J., vol. 277, no. 14, pp. 3039–3050, Jul. 2010.